Imperial College London

Combined musculoskeletal and finite element modelling of the lumbar spine and lower limbs

Clément D. Favier

A dissertation submitted in part fulfilment of the requirements of the degree of Doctor of Philosophy

Imperial College London
Department of Civil and Environmental Engineering

October 2019

I declare that, except where reference is explicitly made to the work of others, this dissertation is the result of my own work and has not been submitted for any other degree at Imperial College London or any other institution.

Clément D. Favier

The author can be contacted at clement.favier13@imperial.ac.uk
A high resolution version of this thesis is available online
under the same Creative Commons license:
https://imperialcollegelondon.box.com/v/ClementFavier-PhDThesis

Acknowledgements

My first thoughts go to my supervisors, Andrew Phillips and Alison McGregor. The first time I came to Imperial College was for a 4 month internship during my second year of engineering school. At the time, I was just a mechanical engineering student, eager to put my freshly acquired knowledge into practice. You both gave me this opportunity when you asked me to develop a new perturbation platform for the lab. Six years later, the platform is still used everyday by the research teams and a paper has just been published (eventually). And I am completing a PhD in biomechanical engineering. This was not part of my original plan, but I discovered research and biomechanics in your group, and realised mechanical engineering would not be enough. Thank you for trusting me from the beginning. I have always been able to count on your support and valuable advice. Thank you for all the enriching conversations (including anti-Brexit talks Andrew) and for encouraging me to share my research internationally multiple times and blossom as a researcher.

I want to acknowledge the Department of Civil and Environmental Engineering at Imperial College London for the award of a Skempton scholarship to fund this project.

I want to thank Anantharaman Gopalakrishnan, Luca Modenese, Claire Villette and Dan Zaharie for sharing their knowledge, experience and office with me. You have been great colleagues during the past four years, and will remain close friends for years to come.

I am grateful to the imaging team at Charing Cross hospital for their assistance with the MRI scanning protocol. In particular, I want to thank Mary Finnegan for her help and patience during the long hours staring at the MRI screen. A special thank also goes to Adam, Arnault, Birana, Clément, Etienne and Luca for their invaluable input.

The past four years would not have been the same without the colleagues and friends I met at Imperial, and the great work atmosphere in Office 326. Thank you all for the kung fu fighting, tennis smashing, rock climbing, beer drinking and bananagramming.

My thoughts also go to my closest friends and family, whose contribution to my life extends beyond the support they gave me during the PhD. A special mention goes to Andreas Fieber. Thank you vollpfosten for being a fantastic flatmate, and introducing me to the finest German vocabulary and gastronomy. Kaiserschmarrn forever changed my way of skiing.

My final thanks go to my parents, brother and sister. Mam, Dad, je ne serais pas là sans votre confiance, vos encouragements et vos sacrifices. Merci pour votre patience et votre soutiens moral et financier depuis toutes ces années. Thib et Roro, vous avez toujours été présents dans les bons et les mauvais moments. Je suis fier de vous avoir à mes côtés. Bisous les gros, je vous aime.

Abstract

Bone health deterioration is a major public health issue increasing the risk of fragility fracture with a substantial associated psychosocioeconomic impact. In the lumbar spine, physical deconditioning associated with ageing and chronic pain is a potential promoter of bone structural degradation. General guidelines for the limitation of bone loss and the management of pain have been issued, prescribing a healthy lifestyle and a minimum level of physical activity. However, there is no specific recommendation regarding targeted activities that can effectively maintain lumbar spine bone health in populations at risk.

The aim of this thesis was to develop a new predictive computational modelling framework for the study of bone structural adaptation to healthy and pathological conditions in the lumbar spine. The approach is based on the combination of a musculoskeletal model of the lumbar spine and lower limbs with structural finite element models of the lumbar vertebrae. These models are built with bone and muscle geometries derived from healthy individuals. Based on daily living activities, musculoskeletal simulations provide physiological loading conditions to the finite element models. Cortical and trabecular bone are modelled with shell and truss elements whose thicknesses and radii are adapted to withstand the physiological mechanical environment using a strain driven optimisation algorithm.

This modelling framework allows to generate healthy bone architecture when a loading envelope representative of a healthy lifestyle is applied to the vertebrae, and identify influential activities. Prediction of bone remodelling under altered loading scenarios characteristic of lumbar pathologies can also be achieved.

The modelling approach developed in this thesis is a powerful tool for the investigation of bone remodelling in the lumbar spine. Preliminary results indicate that locomotion activities are insufficient to maintain lumbar spine bone health. Specific recommendations to limit the effect of physical deconditioning related to muscle weakening back pain are suggested. The approach is also promising for the investigation of other lumbar pathologies such as age related osteoporosis and scoliosis.

Contents

List of Figures

List of Tables

Chapter 1

Introduction

1.1 Context of the research

Bone health relates to the capacity of bone to resist the loads applied to it. Osteoporosis is a bone health condition influenced by structural properties of bone associated with the density and thickness of its internal architecture. Affecting more than 200 million people worldwide (Reginster & Burlet 2006), osteoporosis is considered to be a major public health issue, as a deficient bone structure leads to an increased risk of fragility fractures. Kanis & Johnell (2004) estimated the number of osteoporotic fractures in Europe at 3.79 million in 2000, costing more than 30 billion euros. This figure is expected to more than double by 2050. Besides being financially costly, osteoporotic fractures have a negative psychological and sociological impact. They are often associated with reduced quality of life (Gold 2003) including stress (Roberto 1989), depression (Gold et al. 1989) and psychiatric consequences (Gold et al. 1991), and increased mortality risk (Cooper et al. 1993, Center et al. 1999, Teng et al. 2008).

It is widely accepted that bone optimises its structure to withstand the mechanical loads it is subjected to. Bone apposition occurs when the structure is over stimulated, while bone resorption is observed when bone is under stimulated. This process is called bone remodelling, and was theorised by Frost (1987, 2003) in the Mechanostat principle. Following this principle, sedentary behaviours and low physical activity levels are often considered as a cause of osteoporosis (Lau & Guo 2011), and exercise is usually recommended for the management of this condition (Nelson et al. 2007, Sinaki et al. 2010, Rossini et al. 2016, Benedetti et al. 2018).

In the lumbar spine, there is also evidence that osteoporosis is associated with back pain (Nakamura 2003, de-las Peñas et al. 2011, Chou et al. 2013, Al-Saeed et al. 2013). Although osteoporotic vertebral fractures are described as a cause of low back pain (Francis et al. 2007), it remains unclear if pain could also be a cause of bone degradation.

The fear-avoidance model (Vlaeyen & Linton 2000, Leeuw et al. 2006) is often used to describe the behaviour of patients who avoid activities which they do not feel comfortable in performing. This behaviour can lead to physical inactivity and deconditioning. This phenomenon can be observed in patients with low back pain (Gatchel et al. 2016) who

adopt different mobility strategies (Hodges & Richardson 1996, Hodges & Richardson 1997, Hodges & Richardson 1998, McGregor & Hukins 2009) and reduce their physical activity level (Mayer et al. 1985, Weiner et al. 2003, Kothe et al. 2007, Hoffman et al. 2010, Bjoernsdottir et al. 2012). The inverse phenomenon has also been observed, as Steele et al. (2014) demonstrated that physical deconditioning can be a cause of low back pain. Since deconditioning can be a cause or a consequence of pain, physical reconditioning is recommended both in preventive and rehabilitative treatments (Verbunt et al. 2010) following guidelines for healthy active lifestyle (Haskell et al. 2007).

There appears to be an interlink between lumbar spine bone health, low back pain and physical activity levels. Figure 1.1 presents a causal loop diagram of this interconnection. In this diagram, bone health, back pain, and activity can all be seen as a cause and a consequence of each other. In order to avoid pain, patients with low back pain will modify their mobility strategies. Because bone adapts to its mechanical environment, altered mobility strategies can influence bone loss. In turn, osteoporotic bone structure will induce pain when failing at microscopic and macroscopic levels.

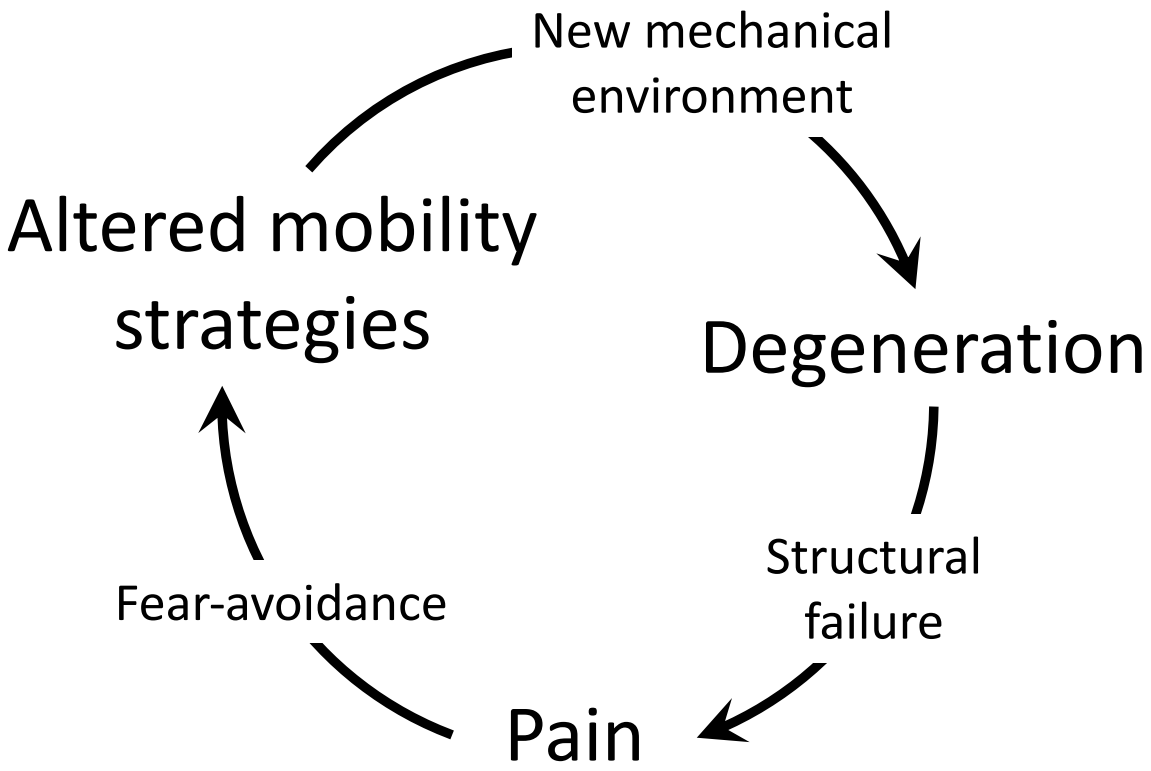

Figure 1.1: Causal loop diagram of the interconnection between lumbar spine bone health, low back pain, and physiscal activity.

This interconnection loop can be initiated by different factors. Tissue damage is known as a potential cause of pain (Wall 1979). Altered mobility strategies can arise with fear-avoidance behaviours induced by the fear of future injuries (Vlaeyen et al. 1999), or simply with ageing which is often associated with reduced physical capacities (Milanovic et al. 2013). Bone degeneration in specific areas can potentially be induced by surgical procedures such as implants, internal fixations or cement augmentations, which create a new mechanical environment for the bone (Uppin et al. 2003, Legroux-Gerot et al. 2004, Liu et al. 2011, Kiapour et al. 2012, Longo et al. 2014, Li et al. 2017). It can also be triggered by hormonal changes such as menopause (Melton et al. 2009, Tella & Gallagher 2014). Finally, injury can also initiate the loop at all stages.

This intricate interconnection loop implies that specific treatments should be developed to help patients slowing down the degenerative process. For both low back pain and osteoporosis, treatment and rehabilitation guidelines in the literature recommend to maintain muscular strength and general fitness. Walking is often considered as the standard to evaluate activity level of patients (Haskell et al. 2007) and physical exercises are usually aimed at reducing the fall events in the population at risk (Madureira et al. 2006). These exercises maintain muscle strength but tend to focus on the lower limbs. More specific exercises may be needed to prevent bone loss in the spine (Sinaki et al. 2010).

1.2 Thesis aims and objectives

To understand the changes in lumbar spine bone health and propose specific exercise recommendations to prevent regional osteoporosis and its associated risks, it is important to investigate the structure of the lumbar vertebrae and their adaptation to loading conditions representative of healthy and pathological mechanical environments. Traditional clinical studies allow direct observation of a pathology among cohorts of patients. However, this is also their main limiting factor. To obtain significant results and reduce the influence of inter-subject variability, large cohorts have to be monitored over decades. Computational modelling is an attractive alternative to clinical studies as it allows time-dependent scenarios to be tested in a few hours.

The aim of this thesis is to develop a new computational modelling approach for the investigation of bone structural adaptation in the lumbar spine under healthy and pathological conditions. The thesis is organised in eight Chapters, including the present Introduction.

Chapter 2 describes the musculoskeletal anatomy of the lumbar spine and reviews common computational modelling techniques used to study the architecture of lumbar vertebrae. A predictive mesoscale modelling approach is introduced as an alternative to these modelling techniques. This new approach combines a detailed musculoskeletal model of the lumbar spine and the lower limbs with structural finite element models of the lumbar vertebrae. A strain driven adaptation algorithm developed by Phillips et al. (2015) based on the Mechanostat principle (Frost 1987, Frost 2003) is used to iteratively adapt the geometry of trabecular and cortical bone in the finite element model to the loading environment derived from the musculoskeletal simulations. The work presented in this thesis takes full advantage of the predictive approach by applying it to healthy volunteers and investigating a different scenario of a pathological condition. While experimental data was collected on six healthy volunteers, the full modelling framework has been developed for one of the volunteers in this thesis.

Chapter 3 presents the protocol used to acquire and process experimental data on healthy volunteers for a range of activities representative of daily living. The collected data

include motion capture and ground reaction forces needed for musculoskeletal simulations. Electromyography (EMG) is also recorded to assess the muscle activations predicted by the model.

Chapter 4 describes the magnetic resonance imaging (MRI) and segmentation protocols developed to produce bone and muscle geometries necessary to build the subject-specific musculoskeletal and finite element models. A localisation method is used to ensure consistency between the experimental data described in Chapter 3 and medical images, which are recorded from the same healthy volunteers.

In Chapter 5, a musculoskeletal model of the lumbar spine and lower limbs is developed from the geometries segmented in Chapter 4 for one of the healthy volunteers. Muscle insertions and paths are also based on the same scans and specific to the healthy volunteers. Musculoskeletal simulations described in Chapter 2 are performed for the activities recorded in Chapter 3. Joint reaction forces obtained for these activities are assessed against in-vivo measurements from the literature. Estimated muscle activations are also compared to the EMG signals recorded in Chapter 3.

In Chapter 6, structural mesoscale finite element models of the lumbar vertabrae are developed. The adaptation algorithm described in Chapter 2 is used to optimise the architecture of these models to a loading scenario representative of a healthy lifestyle. Selected activities include tasks involving the lower limbs, movements of the spine in all degrees of freedom and lifting tasks involving flexion and twisting of the spine. Loading conditions for the finite element models based on these activities were obtained in Chapter 5. The adapted models are compared to clinical observations reported in the literature.

Chapter 7 investigates the influence of different activities on the architecture of the lumbar vertebrae. Two cases are studied to compare the spine-based activities with lower limb-based activities. A pathological condition scenario is also simulated by adapting healthy models previously obtained in Chapter 6 to an altered loading condition potentially induced by low back pain.

Finally, concluding remarks are made in Chapter 8.

Chapter 2

Combined computational modelling framework for the lumbar vertebrae

This Chapter details the anatomy of the lumbar spine necessary to model the musculoskeletal system in the context of this study. It introduces the modelling framework and describes the modelling techniques used.

2.1 Introduction

As stated in Chapter 1, it is of importance to study the evolution of the structures of the lumbar vertebra in order to understand the potential long term effects of low back pain and lumbar pathologies on bone health. There are different approaches to study spine mechanics, which can be divided in three categories: in-vivo, in-vitro, and in-silico.

In-vivo approaches consist in measuring data directly on a subject via instrumented implants, sensors, or medical imaging. Instrumented implants allow direct measurement of the internal loads acting on a joint ((Rohlmann et al. 2008, Rohlmann et al. 2014)). Sensors like electromyography (EMG) electrodes can measure muscle activations during movements ((Lee et al. 2018)). Strain gauges can be fitted on the surface of the bone to measure strains during movements ((Yang et al. 2011, Nazer et al. 2012)). Body range of motion can be investigated using static imaging ((Fujii et al. 2007)), while fluoroscopy ((Breen et al. 2012)), motion capture ((Pal et al. 2007, Rozumalski et al. 2008, Papi et al. 2019)) and wearable technology such as inertial measurement units ((Papi et al. 2017)) can measure body kinematics. Although these in-vivo methods allow direct measurements on the subject of interest, it is difficult to draw conclusions at a population scale from such studies due to inter-patient variability and small cohorts. The potential risks associated with some invasive or radiative in-vivo approaches are usually justified for patients in need of treatment only. This means data are generally collected from patients who are or were suffering from pathologies or injuries. These data are unlikely to be representative of a healthy population, making it hard to study the evolution of a pathology from the beginning. In some cases where pre-pathology data are available, it still takes months or years to study the evolution of a pathology and the effects of a treatment.

In-vitro approaches can be a useful alternative to in-vivo. These can use the same measurement techniques as in-vivo studies, but on cadaveric material. This allows researchers to test different hypotheses getting around ethical, cost and time constraints. However, such studies can only focus on the region of interest, dissecting out the other structures of the body that may have played a role and influenced the data ((Panjabi et al. 1982, Wilke et al. 1996, Gilbertson et al. 2000, Yeager et al. 2015, Ghezelbash

et al. 2019)). Cadaveric material also means active contribution of tissues cannot be evaluated.

In-silico approaches use numerical models to reproduce in-vivo situations. Advances in computer performance over the past decades allow time-dependent hypotheses to be investigated in a relatively short time, without putting a patient at risk. As opposed to in-vivo studies, it is possible to measure data anywhere, without using a sensor or implant that may alter the subject's behaviour. However, computational models are not fully self-sufficient as they still require input data for simulations which usually come from in-vivo or in-vitro studies. Another limitation of these computational models is the need for validation. Before using such a model, it is necessary to make sure the output data are in agreement with what would be observed in-vivo, for every activity of interest (Hicks et al. 2015). This implies some in-vivo or in-vitro data are also required for validation of the in-silico estimations prior to using the model for a study.

Due to the complexity of the structures of the spine, in-vivo studies of the lumbar spine are not as common as for other parts of the body such as the hip or the knee. The nature of the intervertebral joints with multiple degrees of freedom, the unique structure of the intervertebral discs, the complex shape of the facet joints and processes and the proximity of the spinal chord make it hard to place sensors or instrumented implants without altering the natural biomechanics. To overcome this limitation, computational models appear to be a valuable solution. They can estimate intervertebral disc pressure without using a needle on a patient, predict vertebral compression forces without using an instrumented vertebral body replacement implant which reduces the range of motion, assess cortical and trabecular bone strains which cannot be measured directly, and even predict the bone adaptation to its mechanical environment.

This Chapter presents the in-silico techniques chosen to model the spine in the context of this study. The anatomy of importance for the chosen lumbar spine modelling approach is described in Section 2.2. Section 2.3 describes the modelling pipeline used to predict bone structure. Finally, musculoskeletal modelling and finite element adaptation are introduced in Sections 2.4 and 2.5 respectively.

2.2 Anatomy of the human spine

The main function of the spine is to bear the load of the body, whilst allowing flexibility and balance at the same time, and protection of the spinal cord. The spine has a wide range of motion in the three anatomical planes (Figure 2.1). In the sagittal plane, forward and backward bending are called flexion and extension of the spine respectively. Lateral bending (right or left) refers to movements in the coronal plane, and axial rotation (right or left) refers to movements in the transverse plane. To look at the spine in more detail, it is common to consider spinal units (an intervertebral disc between two vertebrae). At this level, coupling between the three basic rotations is observed during spine movements (Panjabi, Yamamoto, Oxland & Crisco 1989). Small displacements in the three translational degrees of freedom also occur, but are limited by the vertebral anatomy and the vertebral ligaments. These displacements are neglected in the modelling approach presented here.

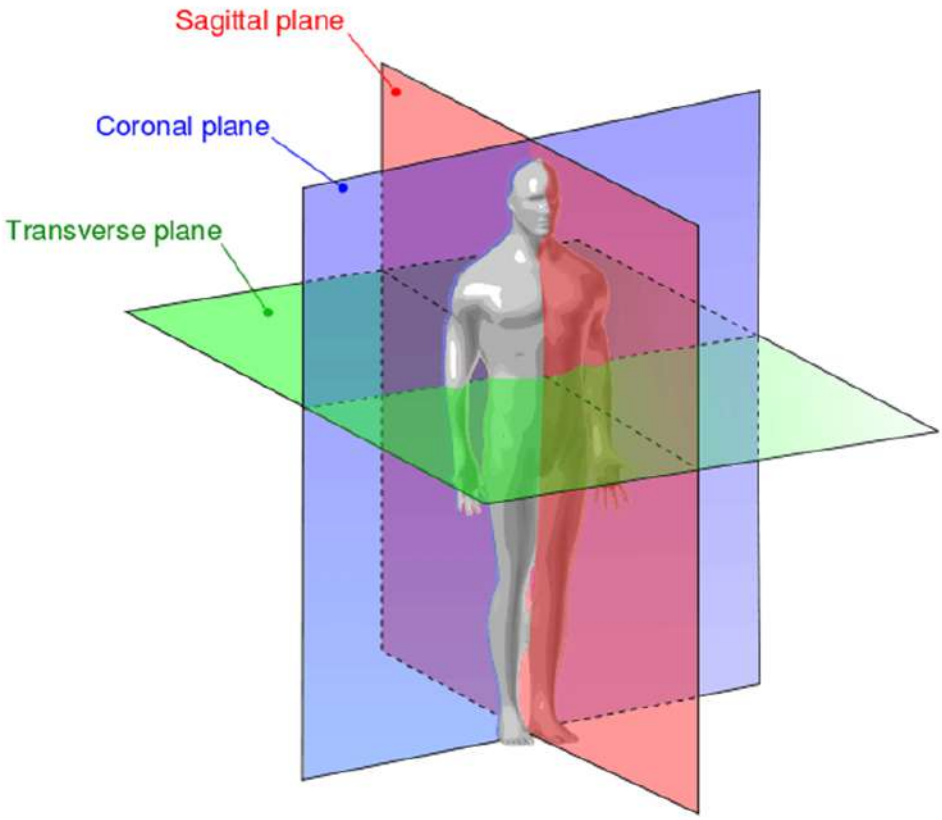

Figure 2.1: Anatomical planes. (Credits Bouza / CC-BY-3.0)

2.2.1 Skeletal anatomy

The human spine is composed of 33 vertebrae and can be divided into five regions (Figure 2.2). At the most distal part, the coccyx and sacrum are part of the pelvic ring. The coccyx is a vestigial human anatomical trait (Mukhopadhyay et al. 2012) composed of four fused vertebrae. As all mammals, the human embryo has a tail. With human evolution, this tail has lost its original balancing function and disappears after about 10 weeks of gestation (Fallon & Simandl 1978), but the coccyx remains to serve as attachment site for some of the pelvic ligaments and muscles. Superior to the coccyx, the sacrum is typically composed of five vertebrae which fuse together during growth to form a single bone by the age of 30 (Gokaslan & Hsu 2012). Linked to the pelvic ring by the lumbosacral joint (also called L5-S1 joint), the articulated spine is composed of five lumbar (L5 to L1), twelve thoracic (T12 to T1) and seven cervical (C7 to C1) vertebrae separated from one another by intervertebral discs.

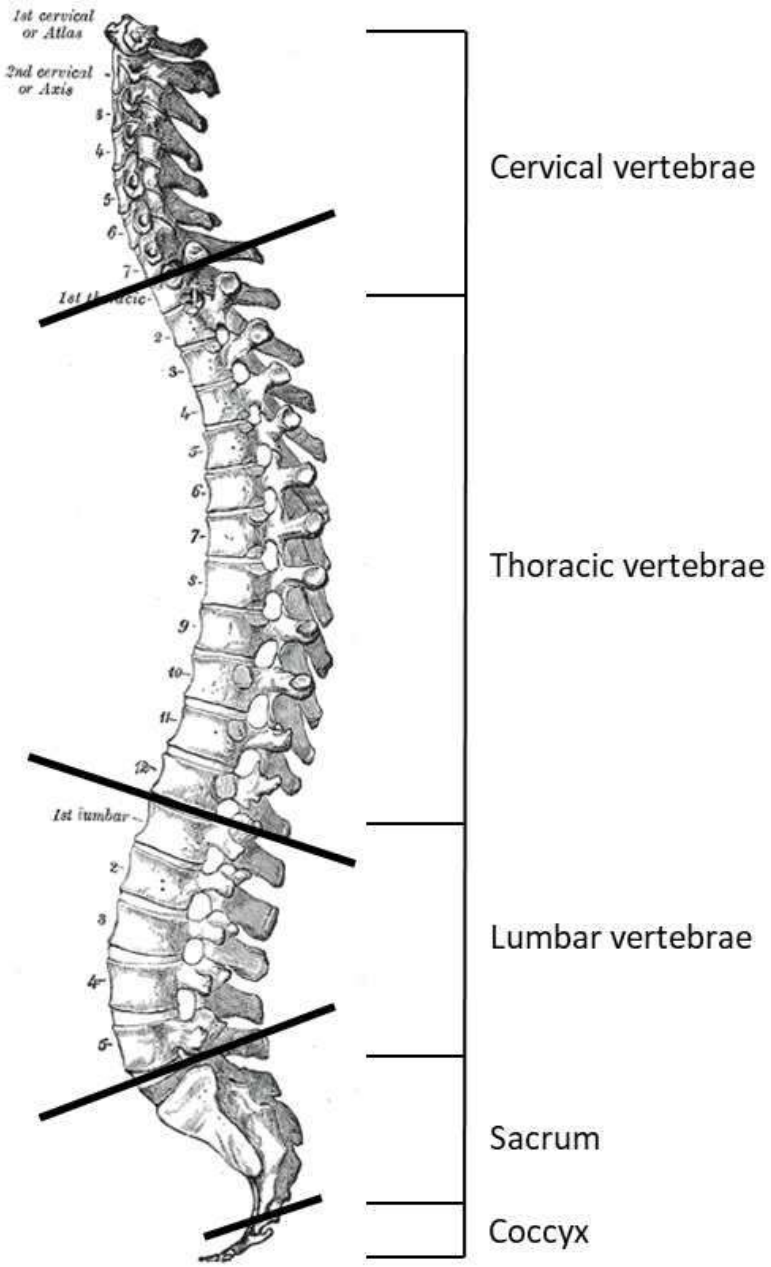

Figure 2.2: Left view of the human skeletal spine (adapted from Gray (1862)).

2.2.1.1 Anatomy of the pelvic ring

The pelvic ring is made of the sacrum, the coccyx, and the two hip bones (hemipelves). Each hip bone is composed of the pubis, the ischium and the ilium, which fuse together during adolescence (Figure 2.3). The pelvic ring is held together by strong ligaments which allow little movement between the different bones. The sacrum is attached to the two hip bones with the sacroiliac ligaments, the sacrospinous ligaments and the sactrotuberous ligaments, forming the sacroiliac joint. The two hip bones are also attached anteriorly by fibrous ligaments forming the pubic symphisis joint (Figure 2.4).

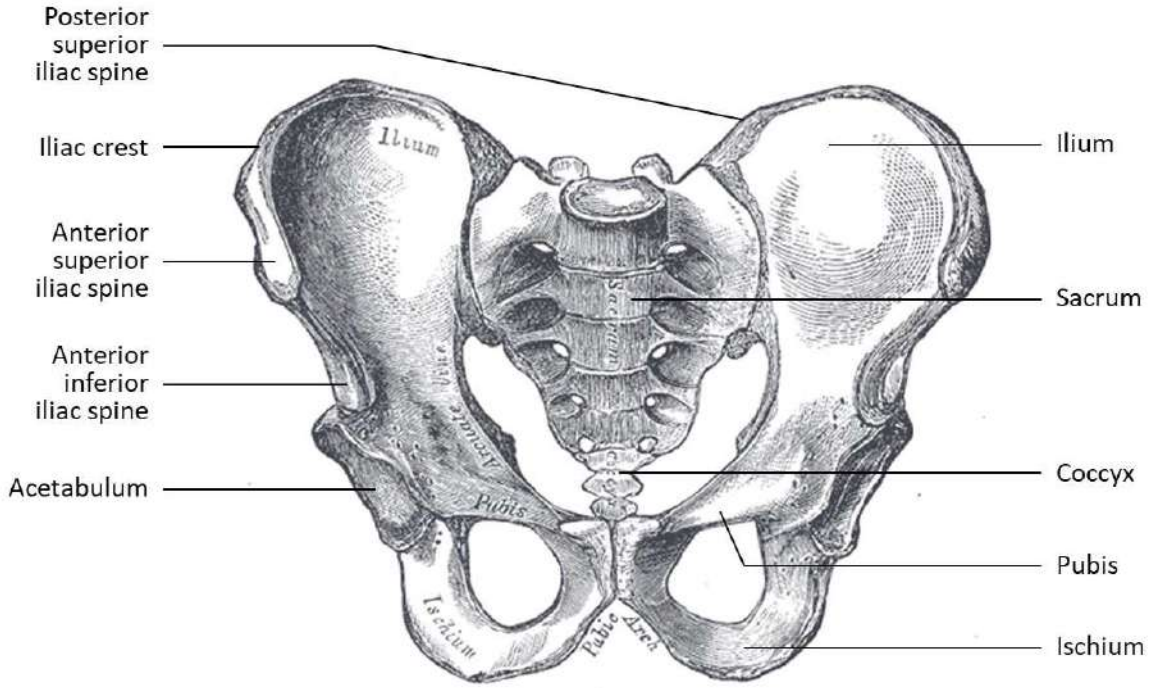

Figure 2.3: Anatomy of the pelvic ring (adapted from Gray (1862)).

The pelvic ring distributes the weight from the upper body to the lower limbs through the lumbosacral joint and the hip joints. It also protects the pelvic viscera and provides attachments for the muscles of the lower limbs and the lumbar spine.

Note that the male and female pelvic ring anatomies differ largely. The female pelvis has wider hip bones and pelvic canal as it is optimised for childbirth (Figure 2.5). A different pelvic shape can influence joint locations and muscle lines of action and will have to be accounted for in a modelling approach.

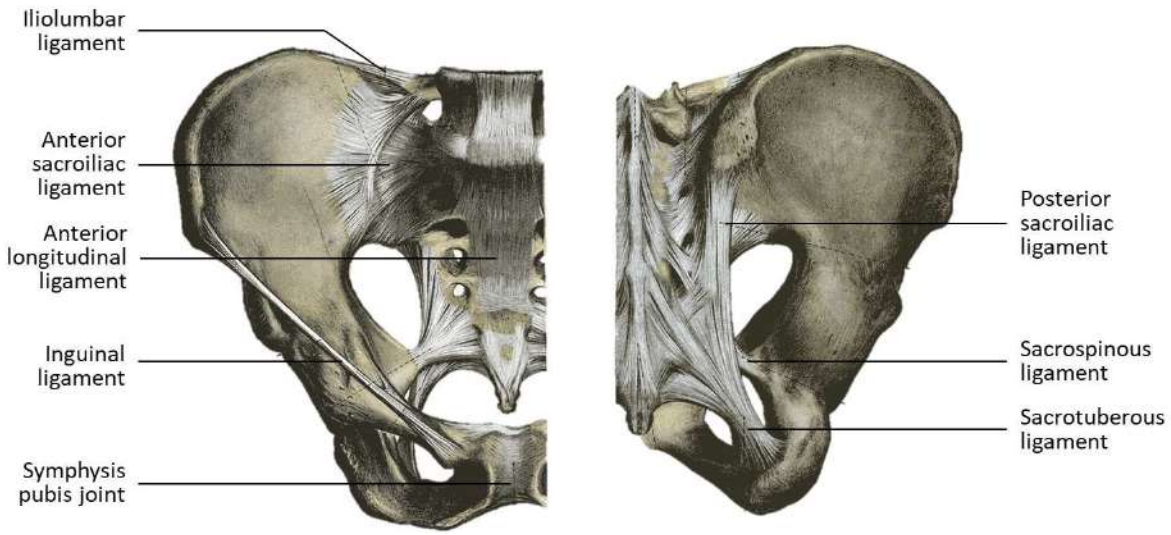

Figure 2.4: Ligaments of the pelvic ring (adapted from Gray (1862)).

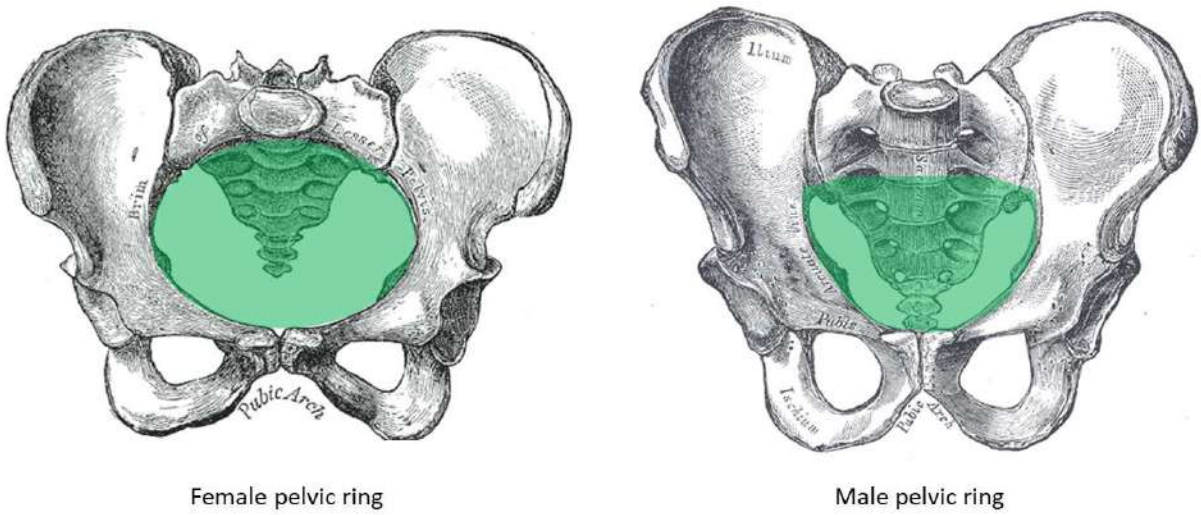

Figure 2.5: Skeletal differences between the male and female pelvic rings (adapted from Gray (1862)). The pelvic canal is highlighted in green.

2.2.1.2 Anatomy of the lumbar vertebrae

Like most bones, vertebrae are made of porous trabecular bone surrounded by a cortical bone layer. The posterior part of the vertebra, the vertebral arch, is composed of the pedicle and lamina which protect the spinal cord. Several processes emerge from this arch. Articular processes guide the spine during motion with facet joints, while spinous and transverse processes are attachment points for spinal muscles and ligaments (Figure 2.6). At each vertebral level, nerves come out of the spinal cord through the intervertebral foramen (Figure 2.7). The anterior part of the vertebra, the vertebral body, primarily bears the vertical compressive load.

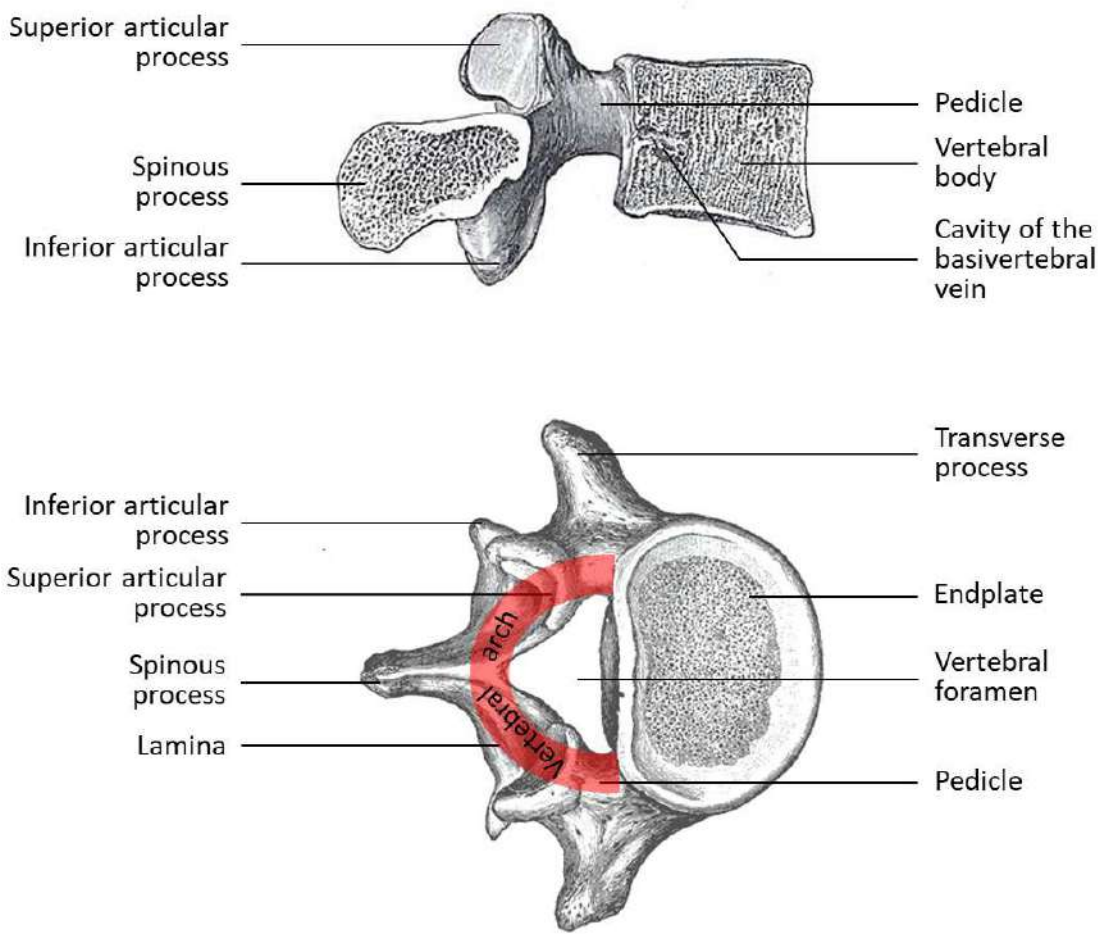

Figure 2.6: Anatomy of a vertebra (adapted from Gray (1862)). Top: right cut view. Bottom: top view.

The distal and proximal surfaces of the vertebral body are endplates. Located between two endplates of two successive vertebrae, the intervertebral disc allows translation and

rotation in six degrees of freedom between vertebrae (Figure 2.7). It is composed of an outer ring made of several layers of collagen fibres, the annulus fibrosus, surrounding an inner gel nucleus, the nucleus pulposus, which spreads the load evenly across the disc. The annulus fibrosus is made of 15 to 25 fibrocartilage layers composed of 20 to 60 type I collagen fibers each. These collagen fibers run obliquely from one vertebra to the next. The nucleus pulposus is mostly composed of a proteoglycan gel held together by a network of type II collagen fibers (Newell et al. 2017).

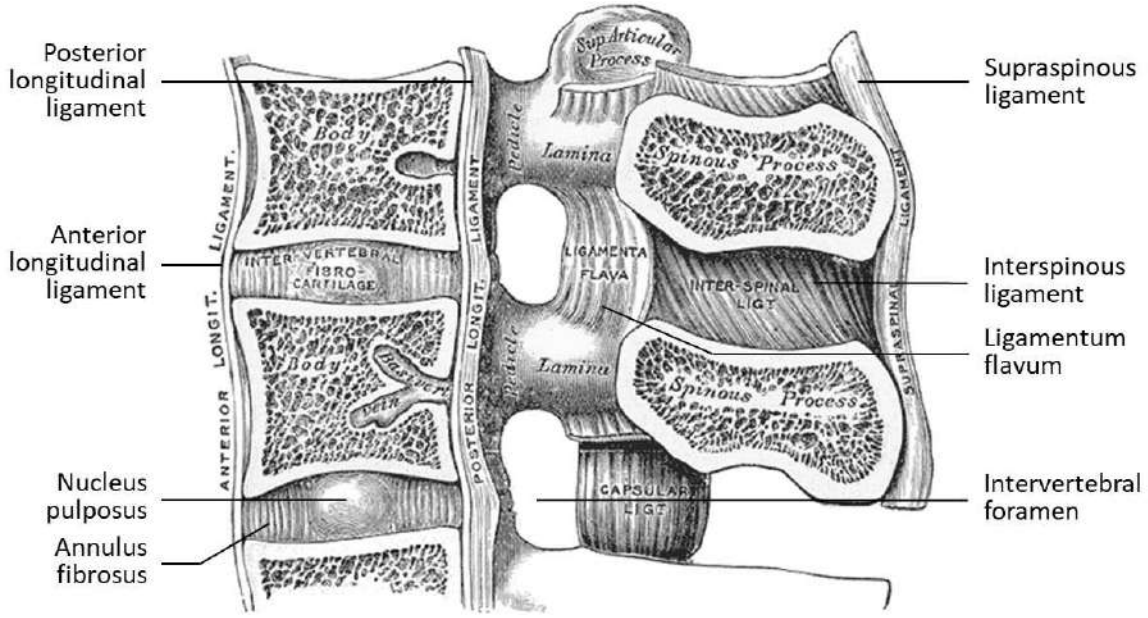

Figure 2.7: Vertebral ligaments and intervertebral discs in a spinal unit (adapted from Gray (1862)).

Every vertebra is linked to one another by five ligaments (Figure 2.7). The anterior and posterior longitudinal ligaments wrap around the vertebral bodies and span the entire spine. The supraspinous ligament also spans the spine along its entire length, attaching to the posterior tip of spinous processes. Two adjacent vertebrae are also connected by the ligamentum flavum attaching to the laminae, and the interspinous ligament linking the spinous processes. The interspinous ligament merges anteriorly with the ligamentum flavum and posteriorly with the supraspinous ligament.

2.2.2 Muscle anatomy

The spine musculature is very complex, with muscles of various sizes, shapes and functions. Goff (1972) classified muscles based on their functions in two categories: mobilisers which create the movement and stabilisers which control the movement by maintaining the alignment of the joints. Bergmark (1989) later classified muscles into local and global systems based on their attachment sites. Muscles having their origin or insertions at the vertebrae form the local system, while muscles transferring the load between the pelvis and the thoracic spine are part of the global system. From these concepts a new functional classification was proposed by Mottram & Comerford (1998), sorting muscles into three categories: local stabilisers, global stabilisers and global mobilisers.

In this study, the main focus is on the lumbar spine, from the pelvis to the first lumbar vertebra. Muscles of the lower limbs and the thoracic spine are also of interest as they play a role in locomotion and balance strategies, but are not described in this review.

2.2.2.1 Global mobility muscles of the lumbar spine

The global mobilisers of the spine are usually recruited to produce large ranges of motion in a given direction (Gibbons & Comerford 2001). These muscles include the erector spinae and the rectus abdominis. The erector spinae is the largest muscle group of the lumbar spine. It is composed of three bundles of muscles (iliocostalis, longissimus and spinalis) spanning the lumbar, thoracic and cervical spine (Figure 2.8). Its main function is to extend the spine, but it can also help to rotate or stiffen the back. It is enclosed in the thoracolumbar fascia, a membrane which wraps around muscles of the back and attaches to the spinous processes of the vertebrae (Figure 2.9 and 2.10). Muscles of the abdomen also merge into this fascia. Among the abdomen muscles (Figure 2.11), the rectus abdominis is the only global mobiliser, which acts primarily as a flexor of the spine. The other abdomen muscles are mostly used to stabilise the spine.

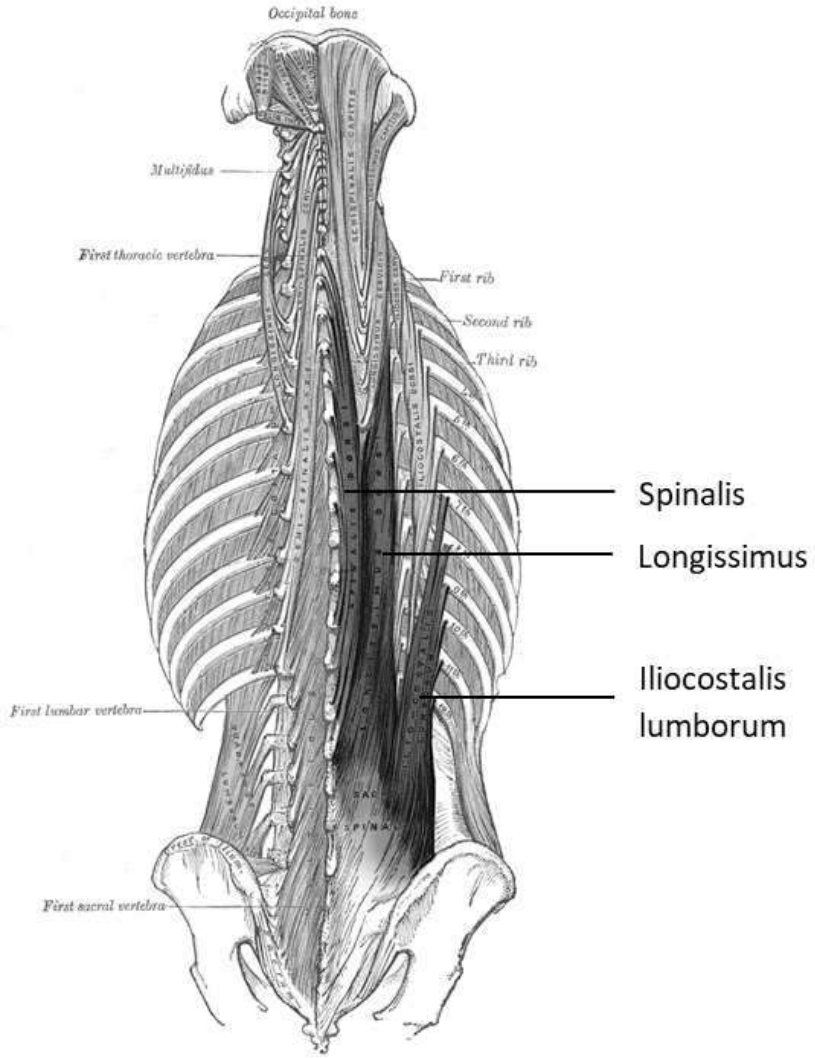

Figure 2.8: Muscles of the erector spinae (adapted from Gray (1862)).

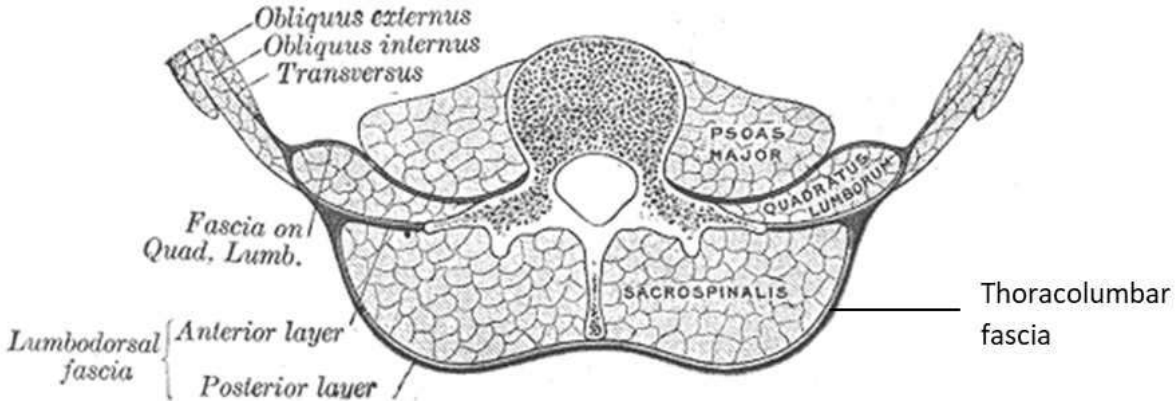

Figure 2.9: Transverse view of the lumbar region (adapted from Gray (1862)).

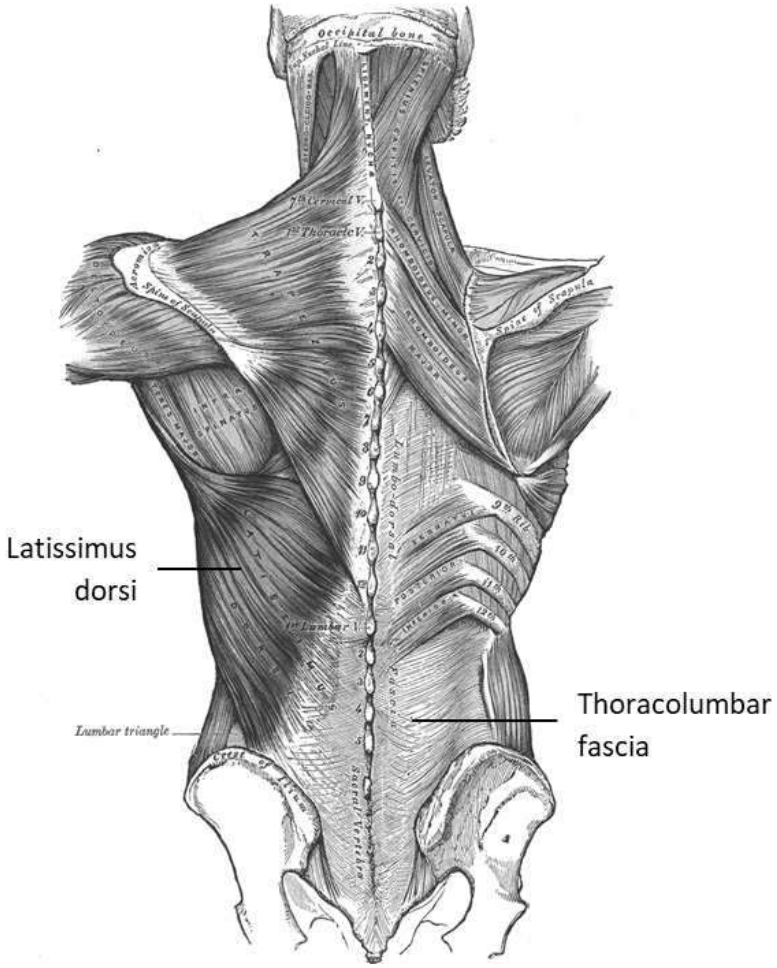

Figure 2.10: Dorsal view of the superficial muscles of the back (adapted from Gray (1862)).

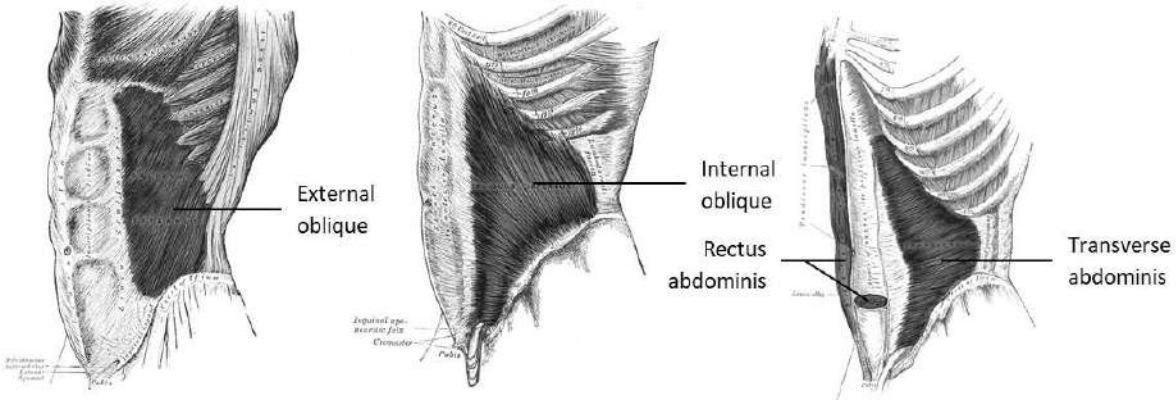

Figure 2.11: Muscles of the abdomen (adapted from Gray (1862)).

2.2.2.2 Global stability muscles of the lumbar spine

The global stabilisers of the lumbar spine control the range of motion (Gibbons & Comerford 2001). These muscles are the internal obliques, external obliques, and quadratus

lumborum (McGill et al. 1996). The obliques are thin layers of muscles arranged into a wall (Figure 2.11) linking the pelvis, ribcage and lumbar spine via the thoracolumbar fascia (Figure 2.9 and 2.10). They control the axial rotation movements of the spine. The quadratus lumborum links the ribcage to the iliac crest on the pelvis (Figure 2.12) and mainly helps to control lateral bending of the spine. It also attaches to the lumbar vertebrae, which suggests it can act as a local stabiliser.

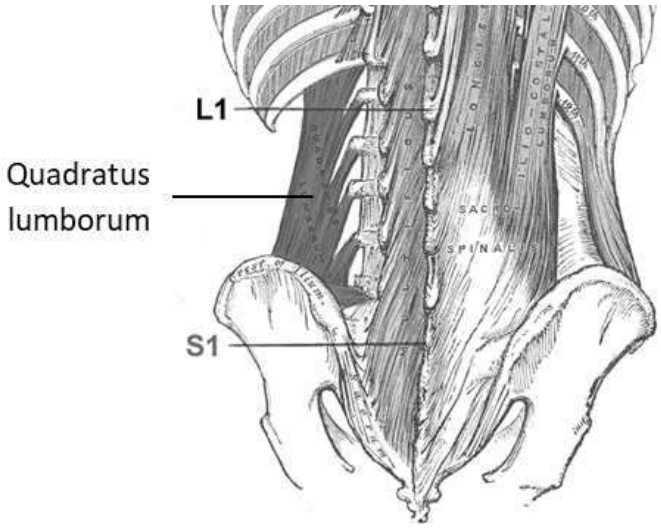

Figure 2.12: Quadratus lumborum (adapted from Gray (1862)).

2.2.2.3 Local stability muscles of the lumbar spine

Local stabilisers of the spine do not produce large movements of the spine (Gibbons & Comerford 2001). It has been suggested that these muscles control the lumbar curvature (Bergmark 1989). They include the multifidus, the rotatores, and the minor deep intrinsic muscles (Macintosh & Bogduk 1986, Panjabi, Abumi, Duranceau & Oxland 1989, Rosatelli et al. 2008, Ward et al. 2009). The multifidus is a succession of short muscle bundles linking vertebrae together, attaching to their processes (Figure 2.13). It spans the three regions of the spine, from the sacrum to the skull. The rotatores and the other deep intrinsic muscles link adjacent vertebrae by their spinous or transverse processes. These short muscles are believed to also have a proprioceptive role (McGill 2004). The transverse abdominis (Figure 2.11) is also considered to be a local stabiliser (Hodges & Richardson 1996, Hodges & Richardson 1997). It can increase intra-abdominal pressure which is

believed to help unloading the spine. The psoas major is a fusiform muscle attaching to the five lumbar vertebrae and merging with the iliacus to form the iliopsoas, attaching to the lesser trochanter of the femur (Figure 2.14). It is considered to be a hip flexor, but can also act as a stabiliser of the lumbar spine (Nachemson 1966, Nachemson 1968, Arbanas et al. 2009).

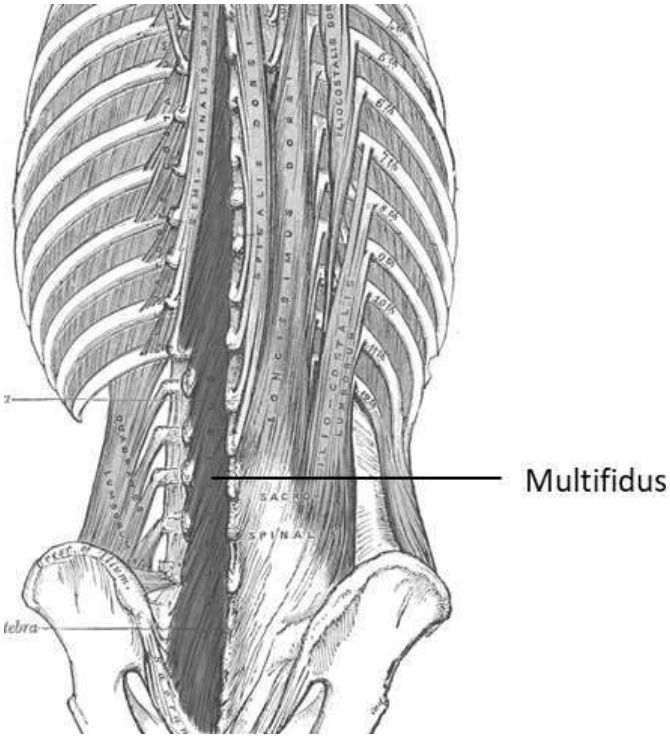

Figure 2.13: Multifidus (adapted from Gray (1862)).

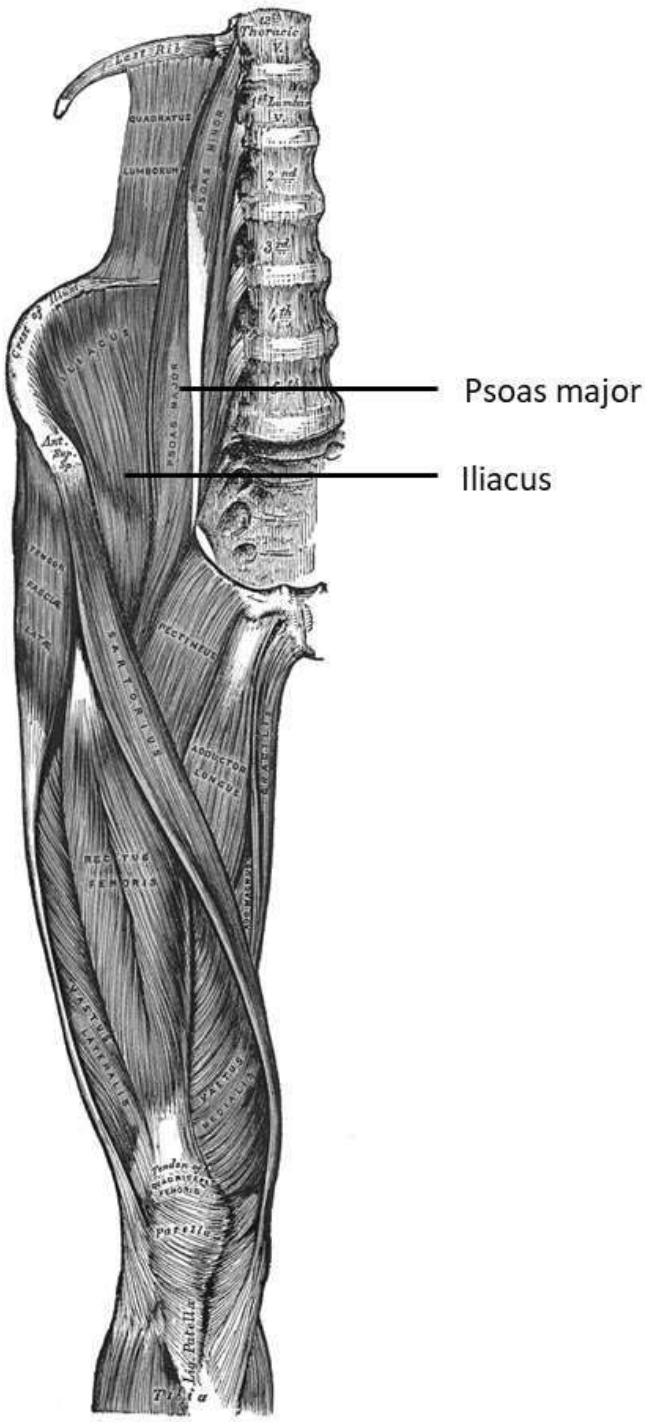

Figure 2.14: Muscles of the right lower limb and hip (adapted from Gray (1862)).

2.3 Computational modelling of the lumbar spine

This study is focused on the lumbar pathologies potentially promoted by the mechanical environment the spine is subjected to. However, studying a pathological population involves more care and more complicated ethical implications. As mentioned in the introduction of this Chapter, computational modelling offers the possibility of testing time-dependent hypotheses without putting the patient at risk. This means one can develop a model of a patient and investigate the influence of different treatments or rehabilitation techniques only with computational simulations.

2.3.1 Existing finite element models

The finite element method is a modelling technique which consists in discretising a volume or structure of interest into a finite number of elements connected to each other through nodes. Instead of solving the equilibrium equations over the entire volume, approximated equilibrium equations are associated with each element based on the forces applied at each node. To obtain solutions across an element and ensure continuity between adjacent elements, shape functions are used to interpolate the results at the nodes. The theory and concepts associated with the method are described in the work of Zienkiewicz (1967, 1977, 2000). The matrix formulation of the method is convenient for numerical implementation, which helped in making it available to the research community and the industry.

2.3.1.1 Continuum finite element modelling at different scales

The finite element method was originally applied in the aeronautic industry by Turner et al. (1956), but the first mention of the method under this name came four years later (Clough 1960). It was later transferred to other engineering fields. In biomechanics, the method was first used to study the stress field within a femur by Rybicki et al. (1972). With the advances in computer technology and the development of user-friendly software packages, more complex systems can be modelled and finite element models of the spine have been developed for a variety of applications. From single vertebrae to several spinal

units, models have been developed to investigate the kinematics and material properties of the spine (Shirazi-Adl 1994, Little et al. 2008, Zanjani-Pour et al. 2018, Tsouknidas et al. 2012) and answer clinical questions related to the mechanical causes of low back pain (Nabhani & Wake 2002), the effect of disc degeneration (Homminga et al. 2012, Park et al. 2013), the influence of disc replacement on the adjacent vertebrae (Polikeit et al. 2003) and the spine kinematics (Zander et al. 2009, Schmidt et al. 2010), the increased risk of fracture with ageing and osteoporosis (Homminga et al. 2001, Homminga et al. 2004, Eswaran et al. 2007, Badilatti et al. 2016, Allaire et al. 2018, Nakashima et al. 2018), or the outcome of different spinal surgery procedures and specific treatments (Tsubota et al. 2003, Ayturk & Puttlitz 2011, Liu et al. 2011, Kiapour et al. 2012, Li et al. 2017, Badilatti et al. 2017, van Rijsbergen et al. 2018).

As shown in Section 2.2 the vertebra has a convoluted shape compared to long bones such as the femur. In addition, bone tissue is a complex composite structure. At macroscale, two types of bone can be observed (Figure 2.15). Cortical bone is a dense external layer of bone usually enclosing a porous bone structure filled with bone marrow. This porous structure is called cancellous or trabecular bone. It is made of a network of 100 to 300 μm thick rods and plates (Rho et al. 1998, Keaveny et al. 2002). In the lumbar vertebrae, cortical thickness ranges between 250 and 380 μm in the anterior wall and 200 and 320 μm in the posterior wall of the vertebral body (Ritzel et al. 1997), while the cortical thickness of the endplates varies between 580 and 900 μm (Edwards et al. 2001). At microscale and sub-microscale both types of bones are made of thin 6 μm thick sheets called lamellae composed of 50 nm large unidirectionally oriented mineralised collagen fibers (Rho et al. 1998, Keaveny et al. 2002, Reznikov et al. 2014). At this scale the two bone types only differ in the structural organisation of the lamellae.

To increase the accuracy of simulations, most of the finite element models of the spine are based on medical images of the patients. Bone geometry is usually derived from 3D images, and discretised in a finite number of volumetric elements to create continuum models. Depending on the resolution and the type of imaging, it may be possible to capture the boundary between cortical and trabecular bone and the architecture of trabecular bone. At macroscale, the volumetric elements representing bone are larger than the size of a single trabecula and are assigned specific material properties

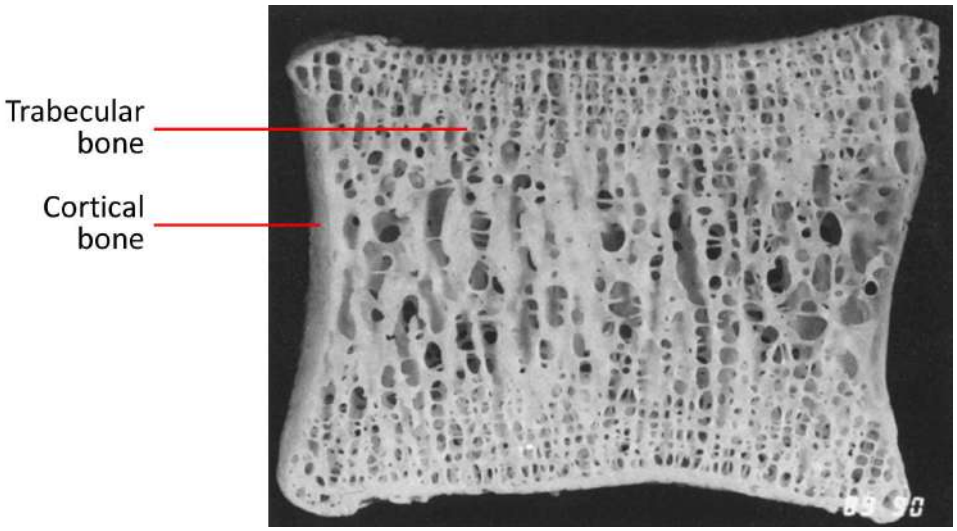

Figure 2.15: Trabecular and cortical bone in a vertebra slice (adapted by permission from Springer Nature Customer Service Centre GmbH: Springer Nature, Anatomy and Embryology, *Three-dimensional photographic study of cancellous bone in human fourth lumbar vertebral bodies*, Jayasinghe et al., © 2014).

representative of the overall behaviour of the porous structure (Shirazi-Adl 1994, Hominga et al. 2001, Nabhani & Wake 2002, Polikeit et al. 2003, Little et al. 2008, Ayturk & Puttlitz 2011, Homminga et al. 2012, Tsouknidas et al. 2012, Park et al. 2013, Li et al. 2017, Allaire et al. 2018, Zanjani-Pour et al. 2018, Nakashima et al. 2018, van Rijsbergen et al. 2018). When clinical computed tomography (CT) scans are available, material properties of bone can be derived from the grey values, assuming these values are related to bone density and bone density is related to the Young's modulus (Homminga et al. 2001, Ayturk & Puttlitz 2011, Homminga et al. 2012, Allaire et al. 2018). With the development of micro-CT scanners, it is possible to acquire images at a resolution higher than the size of individual trabeculae, and produce microscale continuum finite element models (Homminga et al. 2004, Eswaran et al. 2007, Badilatti et al. 2015, Badilatti et al. 2016, Badilatti et al. 2017). In these models, the trabeculae and the cortex are usually discretised into small volumetric elements the size of a voxel, which ensures an accurate representation of the vertebral architecture (Figure 2.16). This approach is considered as the gold standard in specimen-specific modelling (Pahr & Zysset 2009, Zapata-Cornelio et al. 2017).

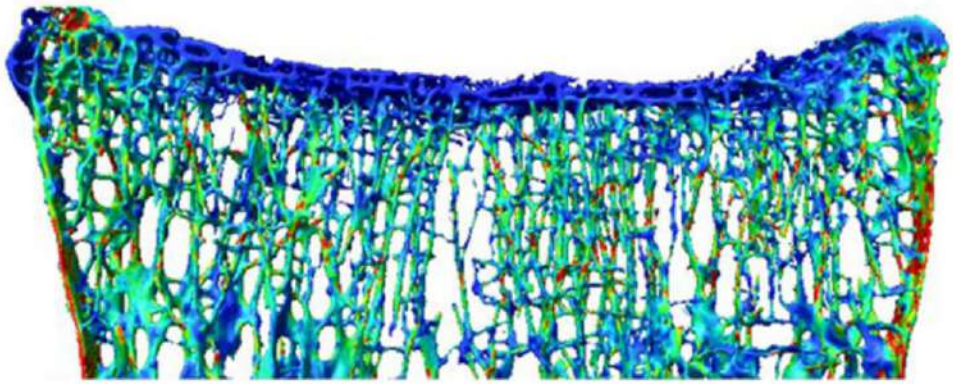

Figure 2.16: Example of a microscale finite element model. Coronal slice of L2 adapted by permission from SAGE Publications: Proceedings of the Institution of Mechanical Engineers, Part H: Journal of Engineering in Medicine, *Computational modeling of long-term effects of prophylactic vertebroplasty on bone adaptation*, Badilatti et al., © 2017).

2.3.1.2 Simulation of bone remodelling

The current study focuses on the evolution of lumbar bone architecture in pathological conditions. Despite the number of existing patient-specific CT and μCT-based continuum finite element models of the lumbar spine, very few have investigated bone architectural adaptation. Bone constantly adapts in response to the mechanical loading applied to it. This response called bone remodelling occurs at a cellular level and results in either bone resorption (loss of bone material) or bone deposition (gain of bone material) visible at macroscale (Hill 1998, Robling et al. 2006, Rucci 2008, Kular et al. 2012). Bone remodelling is believed to be driven by fluid flow at the cellular level. Frost (1987, 2003) proposed a mechanical surrogate to this fluid motion driver in his Mechanostat principle (Figure 2.17). This principle states that bone adapts towards a target stimulus state potentially driven by strain or stress. Following this theory, bone deposition occurs if strains or stresses are higher than a definite target, and bone resorption if strains or stresses are lower than the target. Frost (1987, 2003) also hypothesised the existence of a lazy zone around the target where bone remodelling would not be triggered. This principle is in agreement with observations of functional adaptation among professional athletes who have higher bone mineral density in their dominant limb (Krahl et al. 1994, Kannus 1995, Pollock et al. 1997, Bennell et al. 1997, Andreoli et al. 2001), or astronauts who experience bone loss after long spaceflights (LeBlanc et al. 2000, Lang et al. 2004).

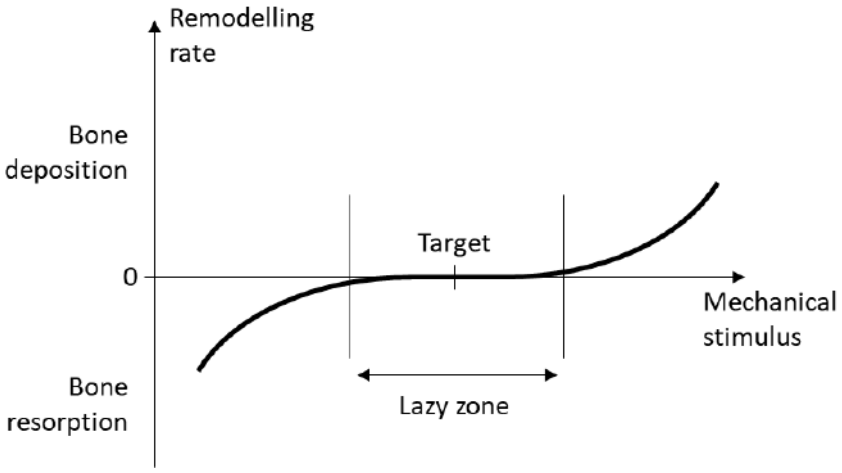

Figure 2.17: Illustration of the principle of Mechanostat suggested by Frost (1987, 2003).

Homminga et al. (2012) have applied this principle in combination with their macroscale CT-based subject-specific finite element model of the lumbar spine to study the influence of disc degeneration on the vertebral structure. They used strain energy density to drive bone remodelling under a vertical compressive load of 500 N. van Rijsbergen et al. (2018) adopted the same approach to investigate disc and bone remodelling after spinal fusion. These two macroscale continuum finite element studies simulate bone remodelling by adapting the Young's modulus of the trabecular bone elements. The obtained material properties vary across the vertebra, representing the dominant stiffness direction. In a bone with clear orientation of the trabecular trajectories, this macroscale approach will give reasonable results (Zaharie & Phillips 2019). In the current study however, it is important to capture the complete trabecular architecture to understand the consequences of lumbar pathologies on the vertebral structures. A more detailed representation of trabecular bone was achieved by Tsubota et al. (2003) using a microscale continuum model of a half vertebra to study fatigue fracture as a cause of fixation screw loosening. They chose a stress driven approach to model bone adaptation under vertical compression. Although the model was able to capture the remodelling of individual trabeculae, it had been artificially generated from a single cross-sectional photograph (L 1990), producing a completely axisymmetric vertebra. To the author's knowledge, Badilatti et al. (2015) have developed the most realistic model of a full lumbar vertebra. Based on μCT images, this microscale continuum model is composed of 365 millions of finite elements at a resolution of 43.5 μm. Strain energy density was used to drive bone remodelling under a combinaison of three 1000 N loads in vertical compression and shear in the transverse

plane. Badilatti et al. (2015) reported a run time of 8 hours on a supercomputer with 1024 CPUs for this particular loading scenario originally used to study bone remodelling with aging. The model was also used in osteoporosis (Badilatti et al. 2016) and bone graft (Badilatti et al. 2017) case studies.

2.3.1.3 Limitations of existing approaches

CT-based patient-specific continuum finite element modelling approaches appear to be the state-of-the-art when investigating bone architectural adaptation in lumbar spine pathologies. However, there are a number of limitations associated with this approach which cannot be neglected in the context of this study.

At macroscale, such approaches can predict dominant stiffness adaptation but the resolution of these models is not sufficient to investigate the architecture and behaviour of individual trabecula. Microscale continuum models allow a more detailed representation of the architecture of the bone. However, they are extremely computationally demanding compared to macroscale models. Structural finite element modelling is an attractive alternative to continuum modelling. Instead of discretising bone into volumetric elements, this modelling approach uses 1D and 2D elements to represent the architecture of bone. Trabecular bone can be modelled with beam or truss elements while shell elements can be used for the cortex. This mesoscale approach, where one element is approximately the size of one trabecula, allows a detailed representation of bone architecture while remaining computationally efficient. Apart from a few studies investigating structural stiffness (Goda & Ganghoffer 2015, Mondal et al. 2019), structural modelling is not commonly used in the lumbar spine despite its advantages.

Another significant limitation of published studies modelling bone adaptation in the vertebra is the very simplified loading used in the simulations. It has been shown that physiological loading and boundary conditions are crucial in finite element modelling of bone tissue (Bitsakos et al. 2005, Speirs et al. 2007, Phillips 2009). However existing finite element studies of bone remodelling in the lumbar vertebrae have used simple uni-directional load cases barely representative of intervertebral joint reaction forces (Tsubota et al. 2003, Homminga et al. 2012, Badilatti et al. 2015, Badilatti et al. 2016, Badilatti

et al. 2017, van Rijsbergen et al. 2018). None of these studies have considered the effect of muscle forces or the loading variations induced by different activities. In the current study, this limitation will be addressed using musculoskeletal modelling to obtain physiologically accurate loading conditions for the finite element simulations.

Subject-specific modelling is essential to ensure accurate, detailed and valuable simulation results, especially when studying the bone architecture. At macroscale, subject-specific spine models use clinical CT images to derive bone material properties from grey values (Homminga et al. 2001, Ayturk & Puttlitz 2011, Homminga et al. 2012, Allaire et al. 2018). At microscale, bone architecture is obtained from μCT scans and uniform material properties can be applied to all elements (Homminga et al. 2004, Eswaran et al. 2007, Badilatti et al. 2015, Badilatti et al. 2016, Badilatti et al. 2017). However, computed tomography is an imaging technique based on the radiation absorption levels of the different tissues. Obtaining CT-scans of in-vivo vertebrae will therefore expose the subject to a high level of radiations. Radiation exposure is only ethically acceptable for a patient in need for such imaging diagnosis. Developing a model from patient images implies the model would be specific to that particular patient and as such not transferable to other patients with different medical histories. Alternatively, considering that bone adapts to the mechanical environment it is subjected to, a predictive modelling approach based on the Mechanostat principle (Frost 1987, Frost 2003) will produce a bone architecture representative of a healthy vertebra if adapted to a loading scenario representative of daily living. With this approach, a healthy model can be created from an initial outer bone geometry, before simulating other scenarios that could lead to pathological conditions. This initial geometry can be based on a healthy subject using medical imaging techniques with low to zero radiation doses such as MRI, allowing the study of lumbar pathologies irrespective of patients' individual characteristics and medical history. The resolution of such a model will vary between macroscale and microscale, depending on the initial parameters and modelling choices.

The different concepts mentioned here to overcome limitations of the current state-of-the-art modelling approaches for bone remodelling in the spine are combined in a modelling pipeline described in the following Section.

2.3.2 A new combined multiscale modelling approach for the lumbar spine

The modelling approach used in this study to investigate bone adaptation to different loading scenarios is based on a combination of two modelling techniques. A musculoskeletal model of the full body is used at macroscale to predict muscle and joint reaction forces for a given activity performed by the subject. These forces are then used as loading conditions in a mesoscale finite element model of the lumbar vertebrae. An optimisation algorithm adapts the structural properties of the model to the applied loads to simulate functional adaptation of bone. This algorithm is described in Section 2.5. The modelling framework is shown in Figure 2.18.

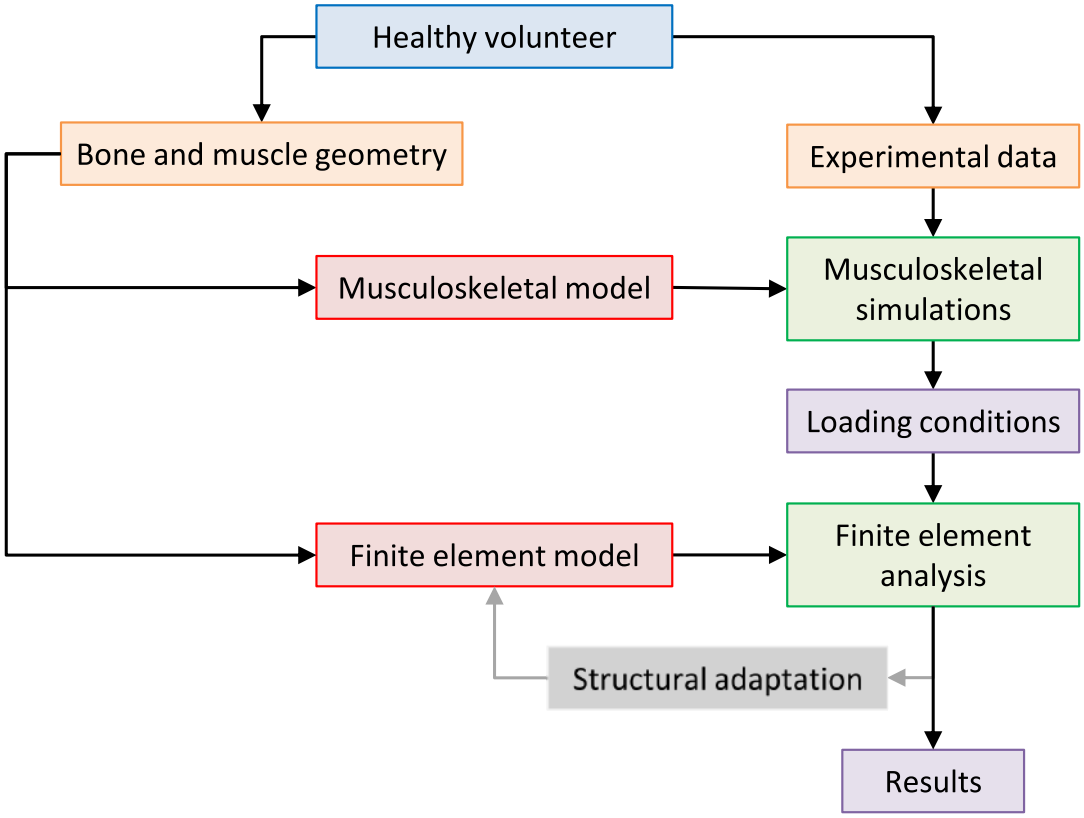

Figure 2.18: Combined modelling framework used to investigate bone structural adaptation to its mechanical loading. In orange are the data collected from the healthy volunteer (in blue). The models developed in this study are in red. Model simulations are in green and simulation outputs are in purple. The adaptation algorithm is in grey.

This framework has been used in the Structural Biomechanics Group at Imperial College London on the femur, tibia and fibula (Phillips 2009, Phillips et al. 2015) and on the pelvis (Phillips et al. 2007, Zaharie & Phillips 2018, Zaharie & Phillips 2019). It is now applied to the lumbar vertebrae. Previous studies within the group used scaled generic musculoskeletal models to obtain the loading conditions necessary in the finite element models. The current study uses a musculoskeletal model specific to the subject being tested. The advantages of this approach are explained in Section 2.4. It is also important to note that the musculoskeletal model developed in this study has a detailed representation of the lower limbs and the lumbar spine, and could potentially be used in lower limb studies.

2.3.3 Recruitment of healthy volunteers

The modelling approach in this study is based on healthy subjects. A protocol was developed to recruit a maximum of 30 healthy volunteers. Inclusion criteria were based on age, physical capabilities, and medical history. Volunteers had to be between 20 and 45 years old, able to stand, walk and lift weights of 5 kg without assistance, with no history of back pain and no musculoskeletal deformity which could potentially alter the biomechanics of the lumbar spine and the lower limbs. Deformities include scoliosis, Pagets disease, fracture or tumour which may have the potential for example to affect weight bearing, posture, strength and sensation. Exclusion criteria were strict and consisted of the following:

- History of hip, lower limb, or back surgery
- Current or past injury to the lower extremity or the back
- Current or past pregnancy
- MRI contraindication (participants with a pacemaker, cochlear implant or metal implants are excluded, as mentioned in the protocol of the imaging facility)
- Neurological disease or balance disorders
- Uncorrected vision problem

- Systemic infection
- Cardiovascular disorders
- Subjects who do not have a strong command of the English language
- Subjects using medication or substances which influence the ability to use equipment or drive safely

The study was granted ethical approval by the NHS Health Research Authority (REC reference: 17/HRA/0465) and the Imperial College Research Ethics Committee (ICREC reference: 17IC3811) (letters attached in Appendix A). Six healthy male volunteers aged between 22 and 38 were recruited (Table 2.1). All volunteers gave written informed consent for the study. Due to the differences between male and female skeletal anatomy of the pelvis (described in Section 2.2), it was decided to first limit the study to a male anatomy before extending the project to female subjects.

Table 2.1: Age, height and weight of the six male volunteers recruited for the study

Subject	**Age**	**Height** (cm)	**Weight** (kg)
1	26	175	67.8
2	27	169	64.4
3	25	175	74.0
4	38	179	88.2
5	29	172	58.3
6	22	168	51.4

2.4 Musculoskeletal modelling concepts

Musculoskeletal modelling is the study of internal forces of the musculoskeletal system such as muscle forces or joint reaction forces, with computational tools based on the theory of multibody dynamics. In a standard approach, bones are considered to be rigid bodies, which means they cannot deform under loading. Articular joints are idealised. They have six or less degrees of freedom to account for rotations and translations in the three orthogonal planes. A muscle is typically modelled with one or more straight line musculotendon actuators which attach to the bones at origin and insertion point(s). These straight line geometries can be enhanced with via points and wrapping surfaces to ensure a realistic muscle moment arm. To account for the physiological properties of the muscle, different mechanical musculotendon models are available. These models are usually based on the Hill-type model. Common parameters are the maximum isometric force, the optimal fiber length, the pennation angle at optimal fiber length, and the tendon slack length (Figure 2.19).

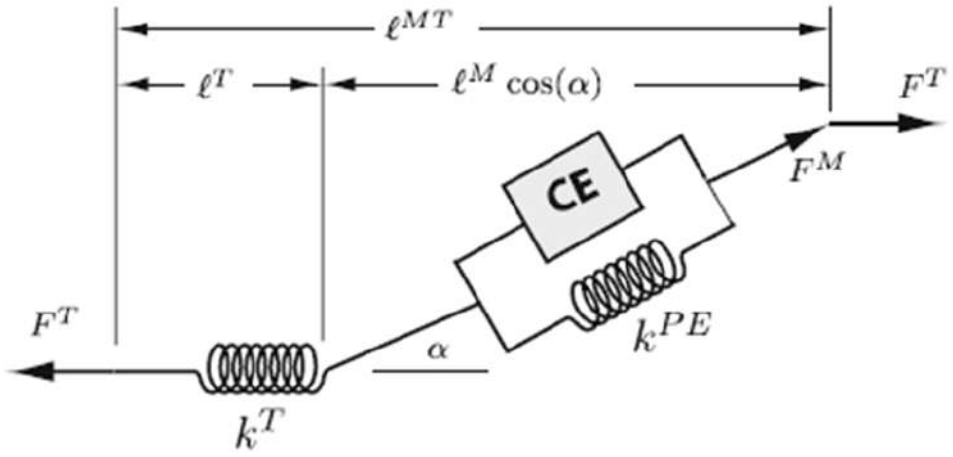

Figure 2.19: Hill-type muscle model (adapted from (Delp et al. 1990), © 1990 IEEE). F^M is the muscle force and F^T is the tendon force, α is the pennation angle, l^M is the muscle fiber length, l^T is the tendon length and l^{MT} is the musculotendon actuator length. CE is the contractile element, k^{PE} is the passive shape factor and k^T is the tendon stiffness.

2.4.1 Existing musculoskeletal models

Musculoskeletal models have been developed for a wide range of applications. Depending on the application, the model can be generic or subject-specific. It can represent the full body or focus only on a region of the anatomy. It can also be publicly available on an open source platform or developed on a commercial platform. The advantages and disadvantages of these modelling choices in regard to the lumbar spine are discussed below.

2.4.1.1 Generic and subject-specific models

Generic models are usually based on an idealised but potentially unrealistic bone geometry (Figure 2.20) (de Zee et al. 2007, Christophy et al. 2012). Muscle attachments and parameters are derived from cadaveric data sets (Bogduk, Macintosh & Pearcy 1992, Bogduk, Pearcy & Hadfield 1992, Bogduk et al. 1998, Bogduk & Endres 2005, Macintosh & Bogduk 1986, Macintosh & Bogduk 1987, Macintosh & Bogduk 1991, Santaguida & McGill 1995, Stokes & Gardner-Morse 1999, Wilkenfeld et al. 2006, Hansen et al. 2006, Phillips et al. 2008). The main advantage of such models is their symmetry. They can be scaled to match the morphology of the subject of the study. However, scaling is sensitive to the operator's choices, and does not take into account any bone and muscle defects or specific shapes. Considering the scope of the current study, bone geometries of generic models are not detailed enough to be used for finite element modelling. An alternative to generic models are subject-specific models (Figure 2.21) (Dao et al. 2014). These models are based on data sets derived from the volunteer or patient of interest. They can therefore capture every detail of the bone and muscle geometries. However, these models are often focused on a pathological population and cannot be scaled to be used in other studies.

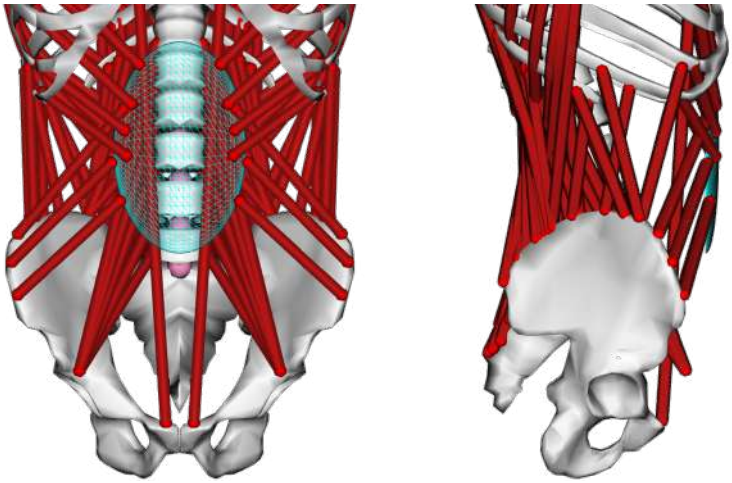

Figure 2.20: Front (left) and side (right) views of a generic musculoskeletal model of the lumbar spine (Christophy et al. 2012).

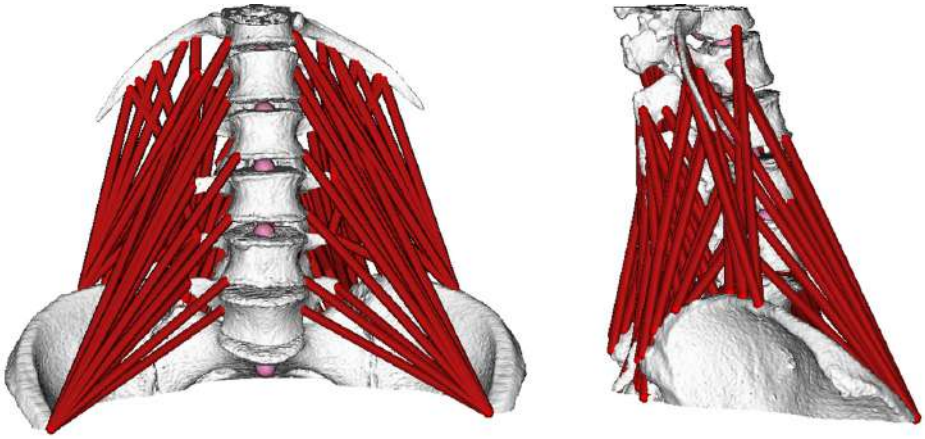

Figure 2.21: Front (left) and side (right) views of a subject-specific musculoskeletal model of the lumbar spine. Reprinted by permission from Springer Nature Customer Service Center GmbH: Springer Nature, *Advances in Intelligent Systems and Computing* by Dao et al., © 2014.

2.4.1.2 Full body and region models

Musculoskeletal models are often developed to answer a research question relative to a particular movement or pathology. This results in models of isolated body regions (Delp et al. 1990, Vasavada et al. 1998, Holzbaur et al. 2005, Arnold et al. 2009, Hamner et al. 2010, Modenese et al. 2011, Christophy et al. 2012). However, the influence of other body segments on the region of interest can be important, especially in movements engaging the whole body. It is common practice to build upon existing models and combine models of different regions (Senteler et al. 2015, Bruno et al. 2015, Raabe & Chaudhari 2016, Actis et al. 2018, Beaucage-Gauvreau et al. 2019). For example, Senteler et al. (2015) have combined the neck model from Vasavada et al. (1998) with the shoulder model of Holzbaur et al. (2005) and an improved version of the lumbar spine model from Christophy et al. (2012) to investigate intervertebral reaction forces during lifting tasks. There are also examples of full body models where lower limbs and spine models are merged together. To investigate jogging biomechanics, Raabe & Chaudhari (2016) have combined the lumbar spine model from Christophy et al. (2012) with the lower limb models from Hamner et al. (2010) and Arnold et al. (2009). Actis et al. (2018) have also combined the model from Christophy et al. (2012) with the lower limb model from Delp et al. (1990) to investigate back pain in amputees. The main limitation of such combined models is the inconsistency of the data sets they are built on. In the instance of combined full body models (Raabe & Chaudhari 2016, Actis et al. 2018, Beaucage-Gauvreau et al. 2019), lower limbs and spine models are built from different data sets, meaning the shape of the pelvis is different between the two sets, potentially resulting in a misrepresentation of the location of the hip joints relative to the L5-S1 joint and an inaccurate representation of the muscle anatomy. Modelling the spine-pelvis-hip complex accurately is of particular importance when studying balance strategies potentially linked to back pain (Shum et al. 2007), and it was decided that the approach of combining generic regional models was inappropriate for the current study.

2.4.1.3 Open source and commercial modelling platforms

In the biomechanics research community, shareable data is key to advances in the field. Musculoskeletal models can be developed on open-source platforms such as OpenSim (Delp et al. 2007), and made available to the community. Besides being free to use, these platforms benefit from a large community of users who provide support on the forums and share new or updated models. Commercial platforms like AnyBody Technology (Aalborg, Denmark) also exist. They provide a professional customer service which can be more appropriate for industry and clinical applications.

2.4.2 Musculoskeletal approach for the current study

2.4.2.1 Musculoskeletal modelling choices

In this study, muscle and joint reaction forces are estimated with the musculoskeletal model and used as input for the finite element model. These forces must be consistent with the anatomy of the subject to ensure reliable results from the finite element analysis. This implies detailed bone geometry and muscle representation are needed in the musculoskeletal model at the lumbar levels. The joint locations and muscle paths also have to be consistent throughout the whole body to ensure an appropriate and physiologically feasible model of the subject. For these reasons, a full body musculoskeletal model was developed in OpenSim 3.3 from a single data set specific to the subject (Chapter 5). Acquisition of the data set is described in Chapter 4.

2.4.2.2 Musculoskeletal simulation pipeline

For this study, muscle activations and joint reaction forces are estimated from the subject's movements and the external forces. Chapter 3 explains how this data was collected. Using the movement data, inverse kinematics simulations are performed to get all the joint angles during motion. These angles along with external forces data are used in an inverse dynamics analysis to compute the forces and moments needed at each joints. Inverse dynamics uses the Newton-Euler equations based on the motion of the model (positions,

velocities, and accelerations) and the mass properties of each segment. At each frame of the motion, Equation 2.1 must be satisfied.

$$M(q)\ddot{q} + C(q, \dot{q}) + G(q) = \tau \tag{2.1}$$

$q, \dot{q}, \ddot{q}$ are the vectors of generalized positions, velocities, and accelerations, respectively. $M(q)$ is the mass matrix of the system. $C(q, \dot{q})$ is the vector of Coriolis and centrifugal forces. $G(q)$ is the vector of gravitational forces. τ is the vector of generalized forces.

To estimate muscle forces, a constrained optimisation problem described in Equations 2.2 to 2.5 has to be solved. In the following Equations, i is the muscle number and j is the degree of freedom number. Equation 2.2 is the minimization of the cost function, where n is the number of muscles, F is the vector of forces exerted by every muscle, F_i is the force exerted by the muscle i and F^{iso}_{Maxi} is the maximal isometric force developed by the muscle i. Equation 2.3 is the constraint of the minimization problem, M_{arm} being the moment arm matrix, and τ being the vector of joint moments. Equation 2.4 expresses the boundaries within the force that can be calculated. Equation 2.5 is the calculation of the moment arm matrix, q being the vector of all joint coordinates with q_j being the coordinate of the degree of freedom j, and l_i being the length of muscle i as a function of all joints. In OpenSim, the static optimization tool performs its own inverse dynamics simulation before solving the optimization problem.

$$\min \sum_{i=1}^{n} \left(\frac{F_i}{F^{iso}_{Maxi}} \right)^2 \tag{2.2}$$

Subject to:

$$M_{arm_{ji}} F_i = \tau_i \tag{2.3}$$

$$0 \leq F_i \leq F^{iso}_{Maxi} \tag{2.4}$$

With:

$$M_{arm_{ji}} = \frac{\partial l_i(q)}{\partial q_j} \tag{2.5}$$

In OpenSim 3.3, a joint reaction analysis tool is available to compute the resultant joint loads. The tool uses a free body diagram approach where the reaction force and moment at a joint must equilibrate the equation of motion for the attached rigid body (Equation 2.6).

$$R_{i+1} = M(q)\ddot{q} - (F_{external} + F_{muscles} + R_i) \tag{2.6}$$

where R_{i+1} and R_i are the reaction loads at the proximal and distal joint of a given segment respectively. $\ddot{q}$ is the vector of generalized accelerations and $M(q)$ is the mass matrix of that segment. $F_{external}$ is the sum of all external loads such as the ground reaction forces and moments, and $F_{muscles}$ is the sum of all muscle loads applied to the segment.

The algorithm starts with the most distal segment where $R_i = 0$ and the process is then repeated with the next segment until all segments of the kinematic chain are balanced. A detailed description of the tool is available in the supplementary data of Steele et al. (2012).

2.5 Mesoscale structural finite element adaptation

Structural finite element approaches are a computationally efficient alternative to microscale continuum modelling of bones (Pothuaud et al. 2004, van Lenthe et al. 2006, Zaharie & Phillips 2019). These models use idealised elements like shells and beams to model the structure of the bone. Such elements allow finite element modelling of the whole bone at macroscale while capturing its complex microscale architecture. This level of modelling is called mesoscale. In structural approaches, material properties are usually the same for all the elements. The geometric properties of the elements are the primary difference between cortical and trabecular bone. In the context of this study where the structural behaviour of the vertebrae is investigated under different loading scenarios, a mesoscale structural finite element approach was chosen to capture the structural changes of bone while remaining computationally efficient.

2.5.1 Initial bone geometry

Subject-specific continuum finite element approaches commonly used in biomechanics are usually based on CT scans. A macroscale continuum model would derive material properties from the grey values of clinical CT images. A microscale model would rely on the segmentation of μCT images of trabecular bone to get a realistic geometry. In the current study, a mesoscale structural approach is used, which only requires the outside shape of the bone to produce a subject-specific model. A randomised cloud of nodes evenly spaced is assigned to the bone volume. Nodes on the outside are used to build shell elements of the cortex while all the other nodes are linked to their closest neighbours, forming a network of truss elements representing the trabecular bone. An initial thickness is assigned to all the cortical shells and an initial radius is assigned to all the trabecular trusses. Material properties assigned to each element are characteristic of bone tissue, with a Young's Modulus of 18 GPa and a Poisson's ratio of 0.3 (Turner et al. 1999), and kept constant throughout the adaptation. The elements' section properties are adapted to resist the load applied to the vertebra with a bone adaptation algorithm described in the next Section. This algorithm based on the Mechanostat principle (Frost 1987, Frost 2003)

drives bone adaptation towards a target strain of 1250 $\mu\epsilon$ (Aamodt et al. 1997). This combination of bone material properties and target strain has yielded physiologically reasonable results for studies of the femur (Phillips 2012, Phillips et al. 2015) and pelvis (Zaharie & Phillips 2018, Zaharie & Phillips 2019), and is expected to produce a trabecular and cortical structure characteristic of a healthy vertebra when a range of load cases representative of daily living activities is applied (Chapter 6, Section 6.3).

2.5.2 Bone adaptation algorithm

The bone adaptation algorithm used in this study was developed in the Structural Biomechanics Group at Imperial College London (Phillips 2012, Phillips et al. 2015). It is used in its structural finite element modelling version, where trabecular bone is modelled as a network of truss elements, and cortical bone as shell elements. More details on the mesoscale structural finite element models of the lumbar vertebrae can be found in Chapter 6. With this approach, the same bone material properties are assigned to all the elements. Shell thickness and truss cross-sectional area are optimised in the simulation of bone remodelling. The algorithm follows the Mechanostat hypothesis (Frost 1987, Frost 2003), optimising bone towards a target strain in an iterative process. This process is implemented with a combination of MATLAB (The MathWorks, Inc., USA) and Python (Python Software Foundation, Beaverton, OR, USA) scripts, and successive finite element models are run using the Abaqus/Standard solver (Dassault Systèmes, Vélizy-Villacoublay, France).

At each iteration i, bone is subjected to a loading scenario of n load cases representing a combination of different activities. The maximum absolute strain for each element j is extracted and compared to the target strain. Equation 2.7 defines the maximum absolute strain in truss elements.

$$|\epsilon_{i,j}|_{max} = max\left(|\epsilon_{11,j,\lambda}|\right) \tag{2.7}$$

where $\epsilon_{11,j,\lambda}$ is the axial strain in element j for the load case λ, with $\lambda = 1, ..., n$.

Equation 2.8 defines the maximum absolute strain in shell elements.

$$|\epsilon_{i,j}|_{max} = max\left(\left|\epsilon^{b}_{max,j,\lambda}\right|, \left|\epsilon^{b}_{min,j,\lambda}\right|, \left|\epsilon^{t}_{max,j,\lambda}\right|, \left|\epsilon^{t}_{min,j,\lambda}\right|\right) \tag{2.8}$$

where $\epsilon^{b}_{max,j,\lambda}$,$\epsilon^{b}_{min,j,\lambda}$,$\epsilon^{t}_{max,j,\lambda}$,$\epsilon^{t}_{min,j,\lambda}$ are the maximum and minimum principal strains in the bottom and top surfaces of the shell element j for the load case λ, with $\lambda = 1, ..., n$.

The strain ranges associated with the Mechanostat (Frost 1987, Frost 2003) are given in Equation 2.9. The target strain was given a value of $\epsilon_t = 1250\ \mu\epsilon$ (Aamodt et al. 1997, Phillips 2012).

$$\phi_{i,j} = \begin{cases} 1, \text{ for } 0\mu\epsilon \leq |\epsilon_{i,j}|_{max} \leq 250\mu\epsilon & \text{(Dead zone)} \\ 1, \text{ for } 250\mu\epsilon < |\epsilon_{i,j}|_{max} < 1000\mu\epsilon & \text{(Bone resorption)} \\ 0, \text{ for } 1000\mu\epsilon \leq |\epsilon_{i,j}|_{max} \leq 1500\mu\epsilon & \text{(Lazy zone)} \\ 1, \text{ for } |\epsilon_{i,j}|_{max} > 1500\mu\epsilon & \text{(Bone deposition)} \end{cases}. \tag{2.9}$$

Note the presence of a dead zone where bone is taken to resorp completely. In the initial model, a randomised network of truss elements is created, resulting in a number of trusses in excess of that required. Trusses that are not needed to bear the load applied to the bone will fall in this dead zone.

For iteration $i + 1$, the cross-sectional area of each truss element and the thickness of each shell element are adjusted using Equations 2.10 and 2.11 respectively. Adaptation of trabecular bone was given preference compared to adaptation of cortical bone at each iteration in order to avoid oscillation of the shell element thicknesses in the initial iterations.

$$A_{i+1,j} = \begin{cases} A_{i,j}\frac{|\epsilon_{i,j}|_{max}}{\epsilon_t} & \text{if } \phi_{i,j} = 1 \\ A_{i,j} & \text{if } \phi_{i,j} \neq 1 \end{cases} \tag{2.10}$$

where $A_{i,j}$ is the cross section area of truss element j.

$$T_{i+1,j} = \begin{cases} \frac{T_{i,j}}{2}\left(1 + \frac{|\epsilon_{i,j}|_{max}}{\epsilon_t}\right) & \text{if } \phi_{i,j} = 1 \\ T_{i,j} & \text{if } \phi_{i,j} \neq 1 \end{cases} \tag{2.11}$$

where $T_{i,j}$ is the thickness of shell element j.

2.6 Conclusion

This Chapter introduced the modelling concepts used in this study. A modelling framework based on young healthy volunteers and combining musculoskeletal and finite element modelling techniques was presented to investigate structural adaptation of the lumbar vertebrae under various loading scenarios. The collection of experimental data and medical images on the recruited volunteers is described in Chapter 3 and 4 respectively. The musculoskeletal modelling challenges and simulation pipeline have been presented. A detailed description of the development of the full body subject-specific musculoskeletal model is made in Chapter 5. The development of the mesoscale structural finite element models of the lumbar vertebrae is described in Chapter 6.

Chapter 3

Acquisition of experimental data on healthy subjects

Chapter 2 introduced the computational modelling framework that will be used to study the adaptation of bone structure in the lumbar vertebrae under various loading conditions. This Chapter explains the need for experimental data in computational simulations and presents the lab protocol used in this project.

3.1 Introduction

Chapter 2 introduced computational modelling as a tool to calculate variables that are difficult to measure with conventional sensors. However, computational models still require non-invasive in-vivo measurements as an input to ensure conclusions drawn from the simulation results are physiologically feasible to allow transfer to clinical applications. In this study, all the simulations in the modelling pipeline presented in Chapter 2 are based on the movements of the subjects and the external forces applied to the body. These measurements are collected on six healthy young males with no history of back pain as described in Chapter 2. The volunteers were asked to perform daily living activities in the safe environment of the Human Biodynamics Lab at Imperial College Research Labs at Charing Cross Hospital (London, UK). These activities are described in Section 3.2. Motion capture and forceplates used to record movements and ground reaction forces respectively are discussed in Section 3.3. Electromyography was also used to record muscle activations on the volunteers for model validation. The method is described in Section 3.4. Ethical approval for this study was granted by the NHS Health Research Authority (REC reference: 17/HRA/0465) and the Imperial College Research Ethics Committee (ICREC reference: 17IC3811). Informed consent was given by the volunteers.

3.2 Recorded activities

This study intends to predict bone adaptation to its loading environment. The starting point is to predict bone structure for a normal scenario where bone can be considered healthy. For this purpose it is necessary to use load cases that are representative of daily living. Morlock et al. (2001) used a portable monitoring system to identify frequent daily living activities for hip replacement patients and found that sitting, standing, walking, lying supine and stair climbing were the most common. The five following tasks were therefore considered in the current study: walking, stair ascent, stair descent, sit-to-stand and stand-to-sit. These activities mainly involve the lower limbs. However, the lumbar spine is not believed to have evolved primarily for locomotion, although it facilitates the movements of the lower limbs. It supports the upper body like a column while providing sufficient degrees of freedom to bend in all directions for balance strategies or low reach during lifting tasks. According to the functional adaptation of bone described by Frost (1987, 2003), the structure of lumbar vertebrae should be optimised to withstand loads in these scenarios. To test this hypothesis and predict vertebral architecture with the modelling pipeline, a loading envelope of the spine representative of a healthy lifestyle is needed. Activities involving spine movements were therefore considered in the current study. Along with the five locomotion activities mentioned previously, basic movements of the spine involving bending in all directions were recorded as a baseline. More demanding tasks representative of the activity level of a young healthy male were also included. These tasks involved lifting and carrying a 5 kg box. A full range of lifting tasks including bending and twisting of the spine from standing and sitting postures was recorded. All activities are listed in Table 3.1. For each activity the participants had a few practice trials before recording three trials for the study.

Table 3.1: List of all activities performed in the Human Biodynamics Lab by each participant.

Activity	Movement	Description
Core activities	Walking	Level walking at self selected speed ⋆
	Stair ascent	Walking up stairs ⋆
	Stair descent	Walking down stairs ⋆
	Sit-to-stand	Standing up form a chair ⋆
	Stand-to-sit	Sitting down on a chair from a standing position ⋆
Basic spine movements	Upright standing	Static upright standing, self selected pose ⋆
	Flexion	Slow forward flexion of the spine from upright standing to maximum flexion ⋆
	Extension	Slow backward extension of the spine from upright standing to maximum extension ⋆
	Lateral bending	Slow lateral bending of the spine from upright standing to maximum bending ∗⋆
	Axial rotation	Slow axial rotation of the spine from upright standing to maximum rotation ∗⋆
Lifting activities (standing)	From floor to chest	Picking up a box on the floor and holding it in front of the chest ∗†
	From chest to floor	Putting a box down on the floor from a holding position ∗†
	From floor to table	Picking up a box on the floor and putting it on a table ∗†※
	From table to floor	Picking up a box on a table and puting it down on the floor ∗†※
	From floor to floor	Moving a box on the floor, from one side to the other ∗
Lifting activities (sitting)	From floor to chest	Picking up a box on the floor and holding it in front of the chest ∗†
	From chest to floor	Putting a box down on the floor from a holding position ∗†
	From floor to table	Picking up a box on the floor and putting it on a table ∗†※
	From table to floor	Picking up a box on a table and putting it down on the floor ∗†※
	From floor to floor	Moving a box on the floor, from one side to the other ∗

For all trials, a 245 x 180 x 160 mm plastic box containing a 5 kg weight was used.

∗Trials were recorded for the left and right sides.

⋆Activities were performed with and without carrying a box.

†The box was located in turn to the front and to the side of the subject.

※The table was located in turn to the front and to the side of the subject.

3.3 Motion capture

Movements of the subjects were tracked with optical motion capture. The system available at the Human Biodynamics Lab uses ten infrared cameras (Vicon T160, sampling rate 100 Hz, Oxford Metric, Oxford, UK) to triangulate the position of experimental markers in space. Markers are 14 mm diameter spheres covered with reflective tape and mounted on a plastic base which was directly taped on the subject's skin with double sided tape (Figure 3.1). The markers were placed to track the body segments of importance for the musculoskeletal model: head and neck, upper torso (T1 to T7), lower torso (T8 to T12), lumbar spine (L1 to L5), pelvis, arms, forearms, thighs, shanks and feet. For each segment a minimum of three non-aligned markers are required to track its 3D position and orientation. Individual markers were placed on most of the anatomical landmarks identified in the recommendations of the International Society of Biomechanics (Wu et al. 2002, Wu et al. 2005). Clusters of markers were also used on the lower limbs and spine to limit the effect of skin artifacts that can impact the position of individual markers (Figure 3.2). The spine segments were tracked with three-marker clusters each. The center of these clusters was aligned with spinous processes. A cluster was considered at L5 level but was found to be in the way of markers on the posterior superior iliac spines. As explained in Chapter 5, these lumbar markers are not needed for the musculoskeletal simulations. The full marker set was composed of 77 markers (Table 3.2). Three markers were also used to track the box (Figure 3.3).

Figure 3.1: 14 mm spherical marker covered with reflective tape and mounted on a plastic base.

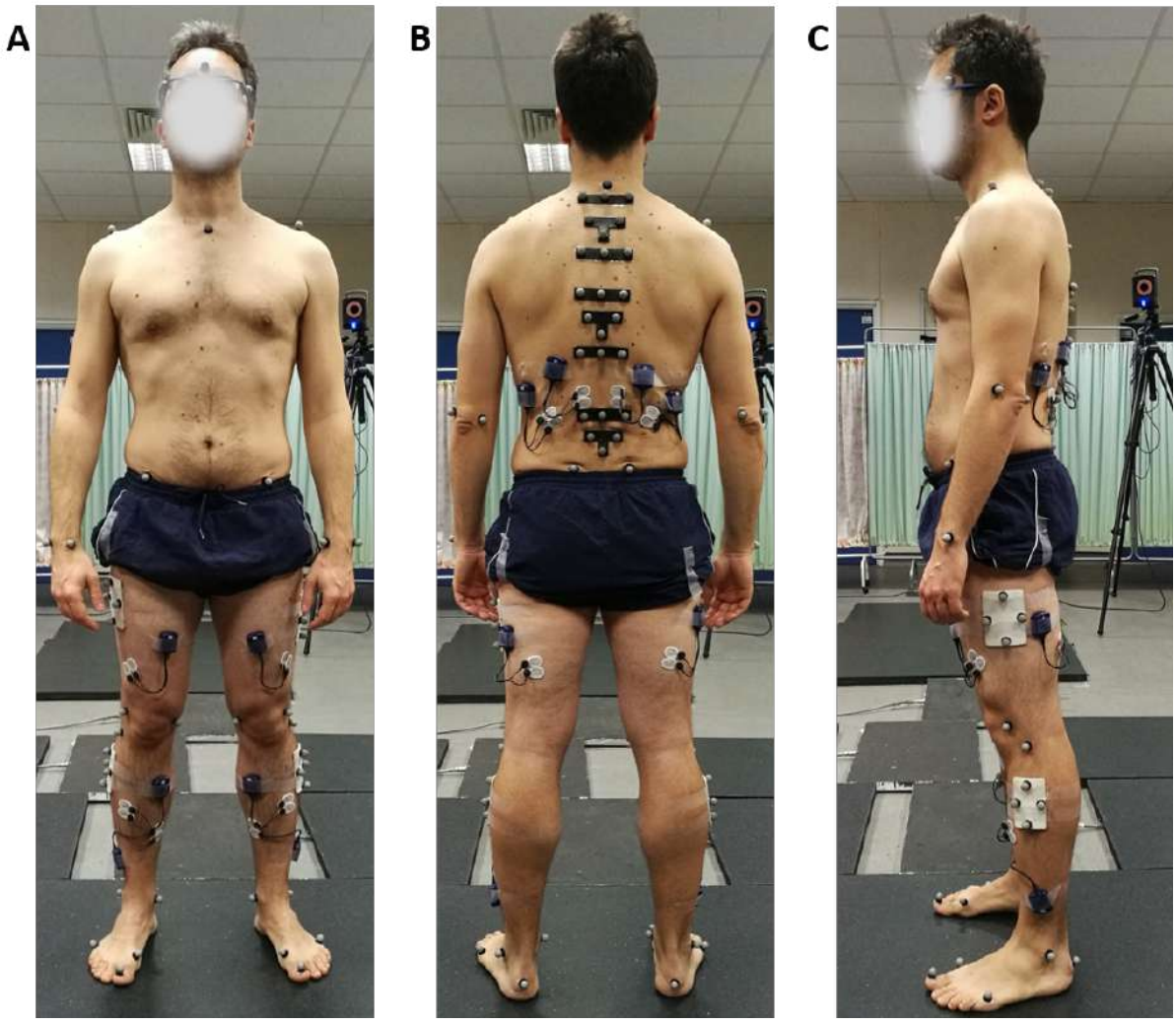

Figure 3.2: (A) Front, (B) back and (C) side views of the marker set used for motion capture.

Figure 3.3: 5 *kg* box with three markers used for the lifting activities.

Table 3.2: Full body marker set.

	Marker name	Marker position	Marker name	Marker position
Head	LTEMP	Left temporal	RTEMP	Right temporal
	NOSE	Forehead, top of the nose		
Thorax	CERV7	Spinous process of C7	STERN	Top of sternum
	LACRO	Left acromion	RACRO	Right acromion
Pelvis	LASIS	Left anterior superior iliac spine	RASIS	Right anterior superior iliac spine
	LPSIS	Left posterior superior iliac spine	RPSIS	Right anterior superior iliac spine
Upper limbs	LELME	Left elbow medial epicondyle	RELME	Right elbow medial epicondyle
	LELLA	Left elbow lateral epicondyle	RELLA	Right elbow lateral epicondyle
	LWRUL	Left wrist ulna	RWRUL	Right wrist ulna
	LWRRA	Left wrist radius	RWRRA	Right wrist radius
Lower limbs	LTHI1	Left thigh cluster proximal	RTHI1	Right thigh cluster proximal
	LTHI2	Left thigh cluster posterior	RTHI2	Right thigh cluster posterior
	LTHI3	Left thigh cluster distal	RTHI3	Right thigh cluster distal
	LTHI4	Left thigh cluster anterior	RTHI4	Right thigh cluster anterior
	LKCOM	Left knee medial condyle	RKCOM	Right knee medial condyle
	LKCOL	Left knee lateral condyle	RKCOL	Right knee lateral condyle
	LKFIB	Left knee fibula head	RKFIB	Right knee fibula head
	LSHA1	Left shank cluster proximal	RSHA1	Right shank cluster proximal
	LSHA2	Left shank cluster posterior	RSHA2	Right shank cluster posterior
	LSHA3	Left shank cluster distal	RSHA3	Right shank cluster distal
	LSHA4	Left shank cluster anterior	RSHA4	Right shank cluster anterior
	LANTI	Left ankle tibia (medial malleolus)	RANTI	Right ankle tibia (medial malleolus)
	LANFI	Left ankle fibula (lateral malleolus)	RANFI	Right ankle fibula (lateral malleolus)
	LHEEL	Left foot heel	RHEEL	Right foot heel
	LMET1	Left foot head of first metatarsal	RMET1	Right foot head of first metatarsal
	LMET5	Left foot head of fifth metatarsal	RMET5	Right foot head of fifth metatarsal
	LTOE	Left foot top of hallux	RTOE	Right foot top of hallux
Spine	FT11	T1 flat cluster left marker	FT81	T8 flat cluster left marker
	FT12	T1 flat cluster middle marker	FT82	T8 flat cluster middle marker
	FT13	T1 flat cluster right marker	FT83	T8 flat cluster right marker
	TT31	T3 triangular cluster left marker	TT101	T10 triangular cluster left marker
	TT32	T3 triangular cluster right marker	TT102	T10 triangular cluster right marker
	TT33	T3 triangular cluster bottom marker	TT103	T10 triangular cluster bottom marker
	FT51	T5 flat cluster left marker	FT121	T12 flat cluster left marker
	FT52	T5 flat cluster middle marker	FT122	T12 flat cluster middle marker
	FT53	T5 flat cluster right marker	FT123	T12 flat cluster right marker
	FL11	L1 flat cluster left marker	TL31	L3 triangular cluster left marker
	FL12	L1 flat cluster middle marker	TL32	L3 triangular cluster right marker
	FL13	L1 flat cluster right marker	TL33	L3 triangular cluster bottom marker

Ground reaction forces and moments were measured with three forceplates (Type 9286BA, sampling rate 1000 Hz, Kistler Instruments Ltd., Hook, UK) which could be

moved into different configurations depending on the activities. For walking tasks, the three forceplates were positioned on the floor, one after the other, with the middle one shifted to one side so they would lie directly under the feet at each step. An experimental staircase was used for the stairs activities. Forceplates were placed on three consecutive steps. Steps were 15 *cm* high and 25 *cm* deep, resulting in a 36.8° slope. For the sitting activities, one of the forceplates was placed on a 51 *cm* high stool and the two other under each foot. A 70 *cm* table was positioned in front, to the right, or to the left of the seat depending on the tasks. For the standing activities, only two forceplates were used under each foot.

Motion capture and ground reaction force data were collected with Vicon Nexus 1.8.5 (Oxford Metric, Oxford, UK). Markers sometimes flicker during data collection, resulting in gaps in marker trajectories. Post processing was done in Nexus, where markers were first labelled. Gaps in marker trajectories were then identified and filled. Trajectories were filtered with a Butterworth filter (zero phase low-pass, 4^{th} order, cutoff frequency 6 Hz) following recommendations from Winter et al. (1974). Filtered marker data and analog signals from the forceplates were exported in .C3D files. Using MATLAB (The MathWorks, Inc., USA) and the publicly available Biomechanical ToolKit (Barre & Armand 2014), forceplate data were filtered (zero phase low-pass Butterworth, cutoff frequency 30 Hz (Eng & Winter 1995)) and resampled at 100 Hz to match the marker data sample rate. The .TRC and .MOT files containing the marker trajectories and ground reaction forces respectively, required for musculoskeletal simulations in OpenSim were finally produced.

3.4 Electromyography

In this study, kinematics and external forces are the only input needed to run musculoskeletal simulations which estimate muscle activations and joint reaction forces for given activities. To validate the musculoskeletal model, it is necessary to compare these estimations with in-vivo measurements and other studies (Hicks et al. 2015). Joint reaction forces are impossible to measure without any invasive procedure. Muscle activations however can be measured in the Human Biodynamics Lab with a non-invasive technique.

To control body movements, the central nervous system sends action potentials to the muscles via motor neurons to induce muscle contraction. Once the action potential reaches the muscle, it travels from the neuromuscular junction to the end of the muscle fiber, altering the electrical potential of the muscle membrane as it propagates. These electrical potential changes can be measured with electrodes in a process called electromyography (EMG) (Winter 2009). There are three types of EMG: surface electromyography (sEMG) where electrodes are mounted on the skin over a muscle, subcutaneous electromyography where fine wires are inserted under the skin over a muscle, and intramuscular electromyography where a needle is inserted in the muscle between the fibers (Konrad 2006). The latter two techniques are invasive, and usually used to measure activations of individual muscle fibers. For the current study, it is more relevant to capture a more diffuse measure of muscle activity and to avoid invasive measurements. sEMG was therefore chosen to record muscle activations of 14 muscles of the lower limbs and lumbar spine. Electrodes were placed bilaterally on the soleus, tibialis anterior, vastus medialis, biceps femoris, rectus abdominis, longissimus and iliocostalis following the SENIAM project (Surface Electromyography for the Non-Invasive Assessment of Muscles) guidelines (Hermens et al. 1999) for the spine and lower limbs (Figure 3.4), and recommendations from Ng et al. (1998) for the abdominal muscles. After the locations of the electrodes were identified, the subject's skin was shaved and cleaned with alcohol wipes to reduce skin impedance. Pairs of self-adhesive electrodes coated with wet gel (Neuroline 720 00-S/25, Ambu A/S, Ballerup, Denmark) were mounted on the skin with an inter-electrode distance of 20 mm. Snap-on transmitters were attached to the electrodes and taped on the skin (Figure 3.5). EMG data was recorded using a sixteen channel wireless

system (Myon320, Myon AG, Schwarzenberg, Switzerland) at a 1000 Hz sampling rate and synchronized with the motion capture and ground reaction forces signals in Nexus (Oxford Metric, Oxford, UK).

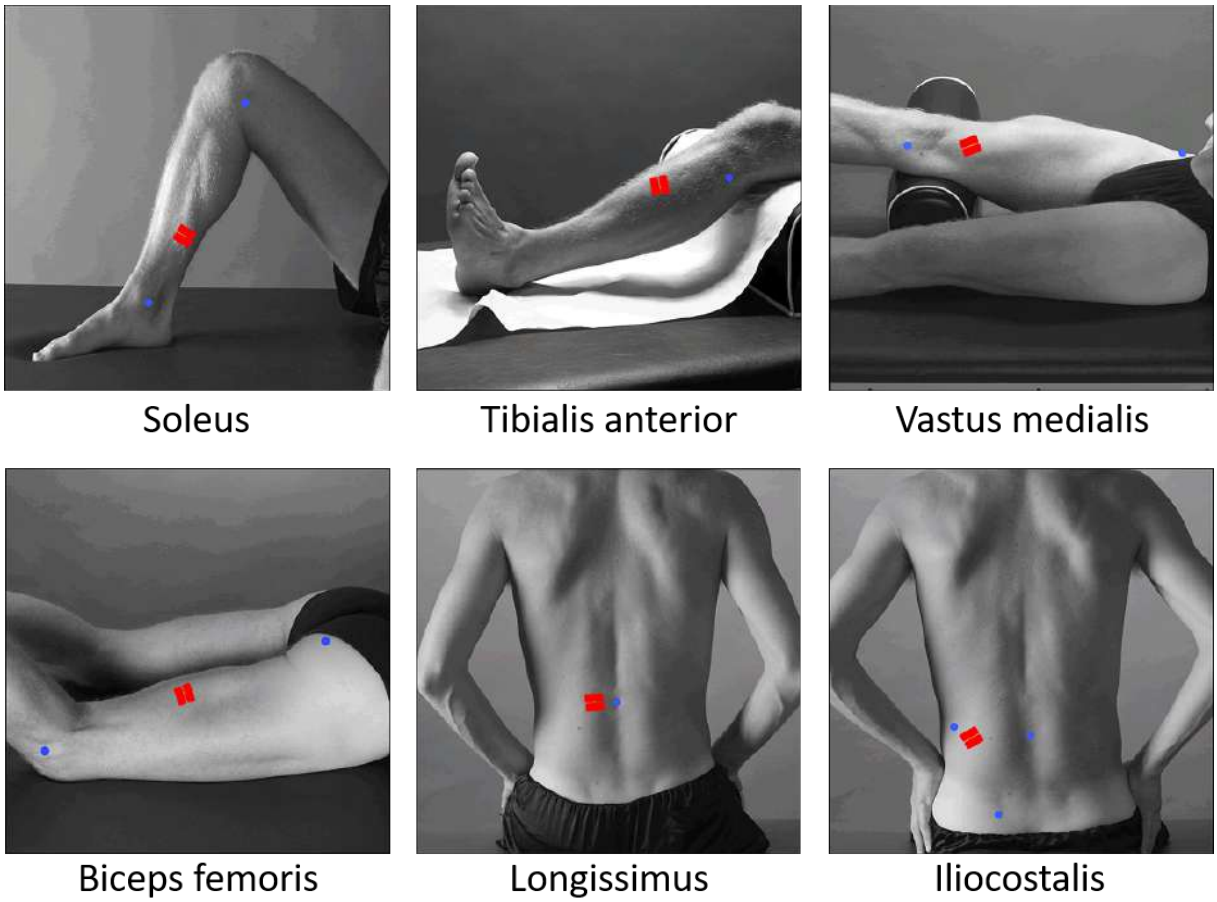

Figure 3.4: Positioning of the sEMG electrodes. The blue dots represent anatomical landmarks. The red rectangles show the position of the electrodes. Images adapted from http://www.seniam.org/.

Figure 3.5: Skin mounted sEMG electrodes with snap-on transmitter.

3.5 Discussion

The purpose of this PhD thesis is to create and validate a modelling pipeline capable of predicting bone structure of the lumbar vertebrae in young healthy individuals. This pipeline is therefore based on healthy volunteers with no history of back pain or lumbar pathologies. For all participants, body kinematics, ground reaction forces, and EMG of 14 muscles were recorded using non-invasive pain free techniques for a range of activities involving locomotion and lifting tasks in different positions, which are believed to constitute the mechanical loading envelope of the spine of a healthy young male. This constitutes a very detailed data set which can also be beneficial to other studies, but there are limitations to the techniques employed in this study.

If calibrated properly, motion capture can be very accurate, but its value can be reduced by factors such as marker placement or skin movements. To overcome any modelling error due to marker placement, a localisation technique based on medical imaging is used in this study, described in Chapter 4. Skin artifacts are a common problem, especially when tracking the spine. Although it takes close to one hour to prepare a participant with all the markers for motion capture, the detailed marker set used here limits the impact of such artifacts, as explained in Chapter 5, Section 5.1.4.

EMG recordings are not necessary to use the modelling pipeline, but were needed to verify that the model predicts a similar muscle activation pattern for a given activity. Being non-invasive, sEMG was chosen to be used on different muscles of the lower limbs and lumbar spine. However sEMG is more sensitive to cross-talk than wire EMG (Solomonow et al. 1994). Cross-talk happens when myoelectric signals of neighbouring muscles are picked up by the electrodes. This interference depends on the proximity of agonist muscles (Winter et al. 1994), the amount of subcutaneous adipose tissue (Solomonow et al. 1994, Kuiken et al. 2003) and the skin movements for large range of motion activities. For some of the subjects, the sEMG signals recorded on the abdominal muscles were noisy and muscle activation was not recorded. This noise was attributed to the cross-talk phenomenon and these signals were discarded for the model validation.

Chapter 4

Model geometry from magnetic resonance imaging

Chapter 2 introduced different modelling techniques that can be used to evaluate mechanical quantities that can not be measured otherwise. This Chapter discusses the importance of medical imaging in the development of such models, and presents the imaging protocol used in this project.

4.1 Introduction

As discussed in Chapter 2, most of the musculoskeletal models publicly available are generic models. In these models, bone geometries, joint locations, muscle insertions, muscle paths and physiological parameters all come from different datasets based on cadaveric dissections. Although this is a very accurate manner to obtain these parameters in different regions of the body, it results in inconsistent models when these datasets are merged together. For example, it is very common to combine a lower limb model with a spine model to study the lumbar spine, or an arm model with a neck and thorax model to study the shoulder. However, these combined models potentially misrepresent the hip joint or the shoulder joint, as well as the muscles spanning these joints. Another limitation of generic musculoskeletal models is the simplified bone geometry used. In a rigid body model, the 3D representation of bone is for visualisation purposes only and a detailed bone geometry is not needed. In this study however, the musculoskeletal model is used to get the loading conditions necessary for a finite element analysis of the lumbar vertebrae. This implies a refined representation of the bones, joints and muscles is needed.

subject-specific models have the potential to overcome these limitations. They are usually based on medical images and measurements from the same subject, which ensures consistency throughout the model.

4.2 Medical imaging

Medical imaging historically started in 1895 when Wilhelm Rontgen accidentally discovered x-rays (short for unknown radiation) as he was experimenting with a cathode vacuum tube. He then imaged the bones of his wife's hand and wedding ring to create the first x-ray image (Rontgen 1896). After World War I, x-rays became popular even outside the medical field, and were used for commercials such as balls and shoes. Although radiation safety procedures started to be implemented in the 1930s, it is only in the late 1940s that health risks of radiation exposure began to be quantified. It is now known that radiation exposure can lead to adverse effects like cancer. Techniques have evolved since then and the radiation dose needed for medical images has reduced but computed tomography (CT) and plain x-ray radiography are still used if justified by the medical condition. In the present study, the models are built from healthy volunteers so imaging techniques involving radiation will not be approved. Radiation exposure can be avoided using alternative imaging techniques. For pediatric and prenatal populations, ultrasound has become the standard. Instead of using x-rays, it emits sound waves and captures the echoes returning from the different tissues, just like a sonar. These echoed waves are then mapped to form an image that can be used for diagnosis. However, this technique is limited to small regions and it is difficult to reconstruct detailed 3D geometries from the images. Another imaging technique that does not involve radiation is magnetic resonance imaging (MRI). MRI was originally called nuclear magnetic resonance imaging (NMRI) but the term 'nuclear' was often negatively misinterpreted, and eventually discarded. Nuclear magnetic resonance (NMR) is a technique based on the magnetic properties of the nuclei of atoms. It uses a strong external magnetic field to align the nuclear magnetic moments parallel to the direction of the applied field. Short electromagnetic pulses of predefined resonance frequencies are then used to force the nuclear magnetic moments into a perpendicular plane. Each nucleus responds to a specific resonance frequency, providing information on the type and position of the atoms. The technique was first described by Isidor Isaac Rabi in 1938 (Rabi et al. 1938). Applications in the medical field arose in the 1950s with one-dimensional NMR spectra. In 1971, Raymond Damadian proposed to use the technique to distinguish cancerous tissue from normal tissue (Damadian 1971). Two years later, Paul Lauterbur demonstrated how to obtain images from NMR (Laut-

erbur 1973). The first human MRI acquisition took 5 hours. Since then, MRI technology and imaging techniques have evolved, allowing acquisition of high resolution images in a few minutes. Images obtained from MRI scans usually consist of a stack of slices of a given thickness. These slices are made of voxels (volumetric pixels) and form a 3D image which can be used to reconstruct 3D geometries of the different tissues. Because of the absence of radiation, the acceptable acquisition time and the 3D high resolution images, MRI was chosen to acquire full body images for this study.

4.3 MRI scan protocol

An MRI scanning protocol was developed to acquire anatomical images of the full body with a focus on the lumbar spine and pelvis. To build the musculoskeletal and finite element models, it is necessary to identify bones, muscles, fat and other soft tissues from the scans for the spine and pelvis region. A 3D T1-weighted VIBE (volumetric interpolated breath-hold examination) sequence was used to acquire high resolution images from the C7 vertebra to the mid femur. This sequence provides a fast acquisition at high resolution. It is usually used for the evaluation of soft tissues and vasculature simultaneously in the abdomen and chest. It is also very useful to acquire fast scans from uncooperative patients. In this study, the full body is scanned and a fast acquisition is key to ensure a reasonable time in the scanner. The signal was received through a spine coil and two body matrix coils, with MRI protocol settings as follow: axial field of view 450x450 mm with a pixel size of 1.41x1.41 mm, slice thickness 1 mm, slice increment 1 mm. The lower limbs are made of long bones less complex than the vertebrae and head and neck are not the focus of this study. Therefore, a lower resolution acquisition was selected for these regions. A 3D T1-weighted TSE (Turbo Spin Echo) sequence was used to acquire low resolution images of the head, neck and lower limbs. This type of sequence is very common for classic musculoskeletal imaging. Acquisition takes longer than the T1-weighted VIBE sequence but for this low resolution scan, the slice thickness and slice increment were increased. The signal was received through a head coil and two matrix body coils, with MRI protocol settings as follow: axial field of view 470x470 mm with a pixel size of 1.47x1.47 mm, slice thickness 6 mm, slice increment 9.6 mm. This sequence was sufficient to distinguish muscle contours and bone geometry of the lower limbs. Axial images of the subjects in the supine position were acquired using a 3T Siemens Verio MRI scanner (Siemens AG, Erlangen, Germany) at the Charing Cross Hospital imaging facility (London, UK). Scanning was done in axial blocks of 224 and 22 slices for the high and low resolution acquisitions respectively, with an overlap of 50 mm between adjacent blocks (Figure 4.1). The full body scans consisted of 3 to 4 high resolution blocks and 7 to 8 low resolution blocks, depending on the height of the subject. These blocks were axially coincident and only moved along the longitudinal axis to facilitate image processing. Because the scanner table could not slide far enough in the scanner bore to scan the whole

body in one acquisition, the subject had to do two sets of scans. The first one was head first, to acquire the whole spine down to mid thighs. The second one was feet first to scan the rest of the lower limbs at low resolution. To ensure consistency between the first and second sets of scans, the legs of the subject were positioned using a rope and sand bags. The overlap between the first and second sets was also doubled. The total acquisition time for the full body is approximately 45 minutes. Ethical approval was granted by the NHS Health Research Authority (REC reference: 17/HRA/0465) and the Imperial College Research Ethics Committee (ICREC reference: 17IC3811). Informed consent was given by the volunteers.

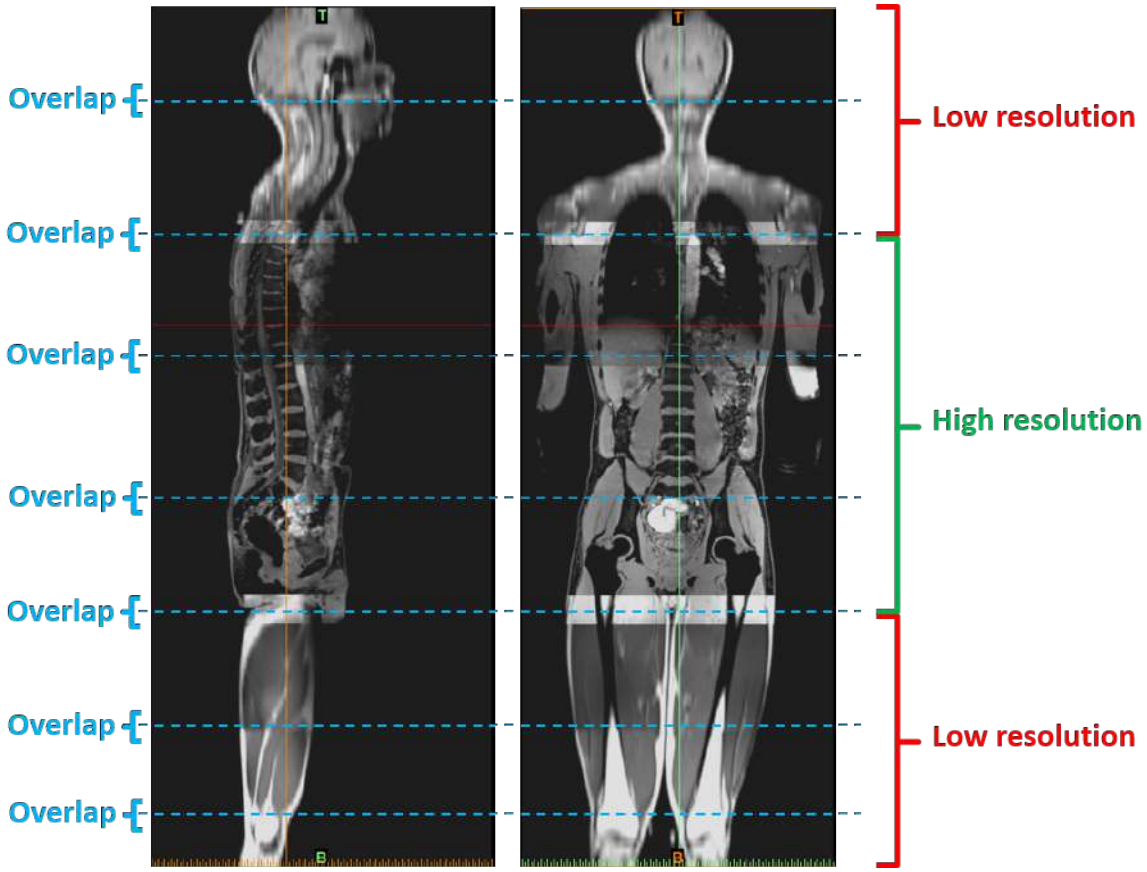

Figure 4.1: Merged high and low resolution blocks. The blue dash lines indicate the location of the overlap between two blocks.

4.4 Localisation technique

Chapter 3 explained how movement and muscle activations were recorded in the motion capture lab. To ensure a high accuracy in the musculoskeletal simulations, it is important to know the exact position of the reflective markers and the sEMG electrodes relative to the underlying soft tissues and bones. However, sEMG electrodes contain metallic parts which present a danger in the MRI scanner due to the strong magnetic field and have to be removed prior to MRI scanning. Reflective markers are made of plastic and would not be visible in the MRI scans. There exist a few substances that form a strong contrast during MRI imaging, and can be used as fiducial markers. A common example is fish oil capsules or bath oil beads. In this study, cod liver oil capsules available in drug stores as food supplement are used. 500 mg capsules are used to represent reflective markers and 1000 mg capsules are used to mark the position of sEMG electrodes (Figure 4.2). The motion capture lab and the imaging facility are in the same hospital site but not in the same building. The subjects had to put on clothes to walk across between buildings. In the motion capture lab, marker and electrode positions were marked on the skin with a surgical pen. In the imaging center changing room, cod liver oil capsules were directly taped onto the skin at the indicated locations with the same surgical tape previously used in the motion capture lab (Figure 4.3). Capsules placed on the spine were embedded in a custom made foam pad (Figure 4.4) to ensure comfort and prevent the capsules from bursting when the subject is lying in a supine position in the scanner. The capsules were located in the MRI scans (Figure 4.5) and their position relative to the segment they were attached to was calculated when building the musculoskeletal model.

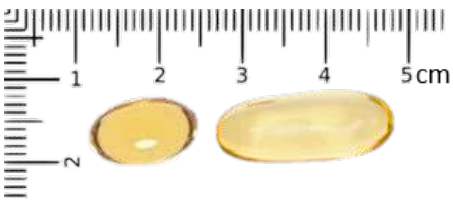

Figure 4.2: Cod liver oil capsules available in drug stores as food supplement. 500 mg capsule on the left and 1000 mg capsule on the right.

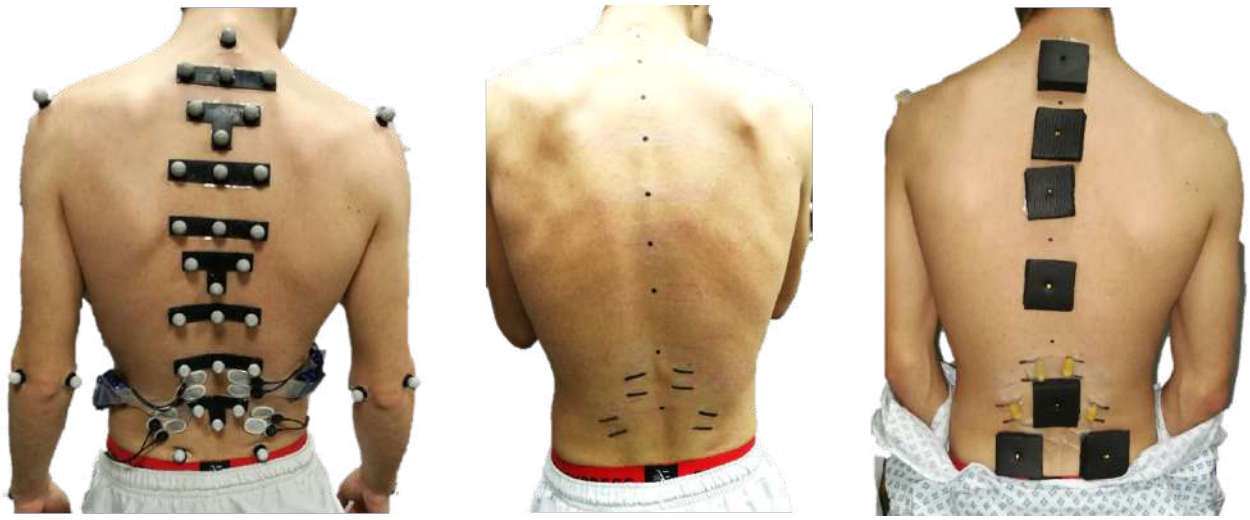

Figure 4.3: Reflective markers from the motion capture lab are replaced with cod liver oil capsules for the MRI scans. Left: Reflective markers and sEMG electrodes. Middle: marker and electrode positions marked with a surgical pen. Right: Cod liver oil capsules.

Figure 4.4: Cod liver oil capsule embedded in a foam pad for spine markers.

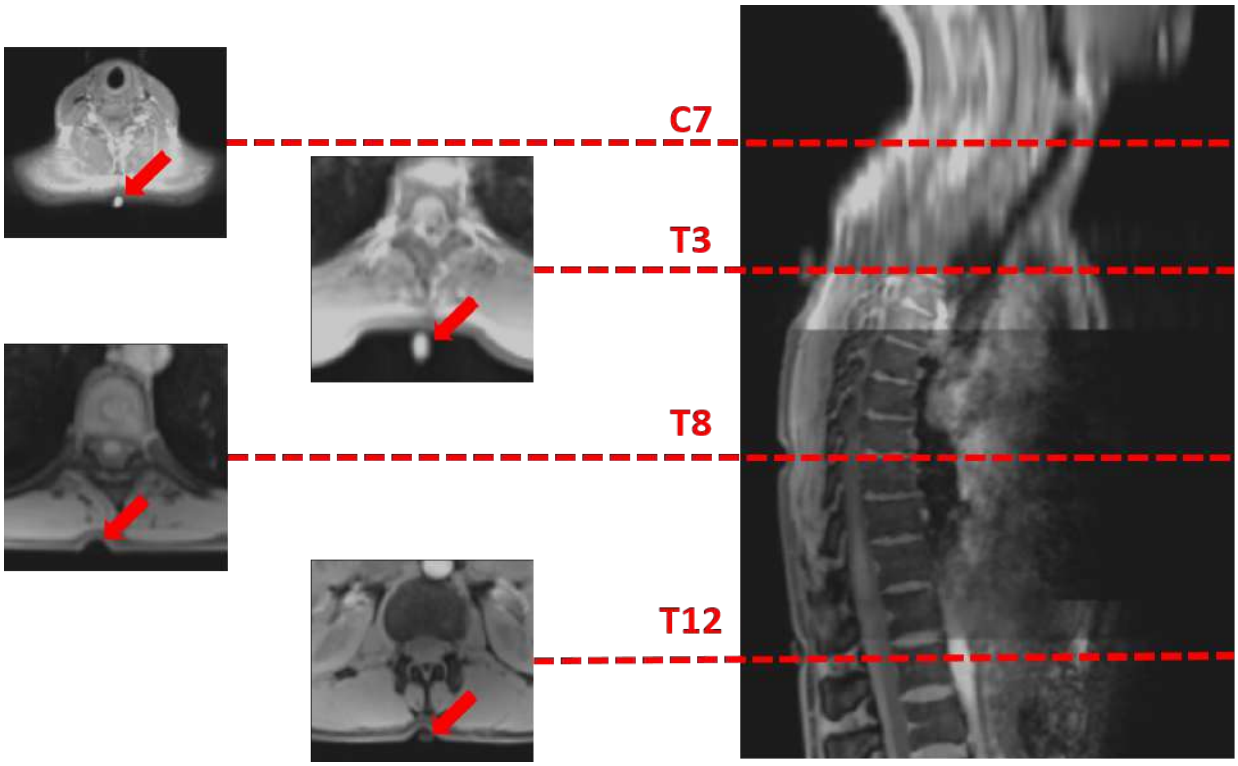

Figure 4.5: Locating cod liver oil capsules in an the MRI scans. Example shown for the thoracic spine.

4.5 Image processing

Mimics (Mimics Research 19.0, Materialise NV, Leuven, Belgium) was used for image processing. The high and low resolution blocks were merged into one single full body file. The acquisition method with the image stacks already axially coincident made image registration straightforward. The overlap of 50 mm between sections was treated with the fusion method 'Average' in Mimics.

To build the musculoskeletal and finite element models, accurate 3D bone geometry is required. Muscle geometry is also needed to identify muscle attachment areas on bones and muscle paths. These 3D geometries are obtained by segmenting the scans. Different sequences were used and grey values were found to be close to each other for the different tissues in the VIBE sequence which made threshold-based segmentation inefficient (Figure 4.6). Bones and muscles of the spine and lower limbs were therefore segmented manually in Mimics. The 3D geometry of bones and muscles was reconstructed form the segmented slices. The wrapping and smoothing tools were used to refine the bone geometries (Figure 4.7). Visual verification was carried out by superimposing 3D contours on 2D images (Figure 4.8). 3D bone and muscle geometries (Figure 4.9) were exported in STL files to build the musculoskeletal and finite element models. This is described in Chapter 5 and 6 respectively.

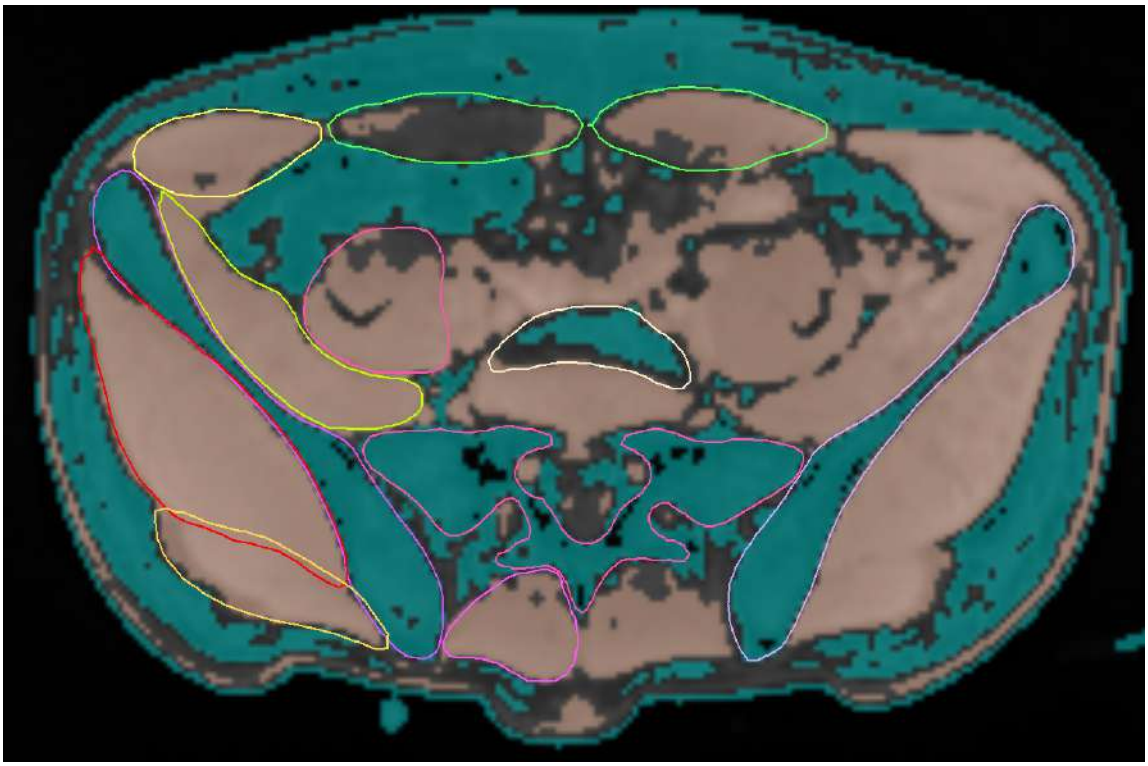

Figure 4.6: Manual and threshold-segmentation methods. The blue mask corresponds to bone tissue obtained with threshold-based segmentation. The red mask corresponds to muscle tissue obtained with threshold-based segmentation. The lines of different colors are the contours of the bone and muscle tissue obtained with a manual segmentation.

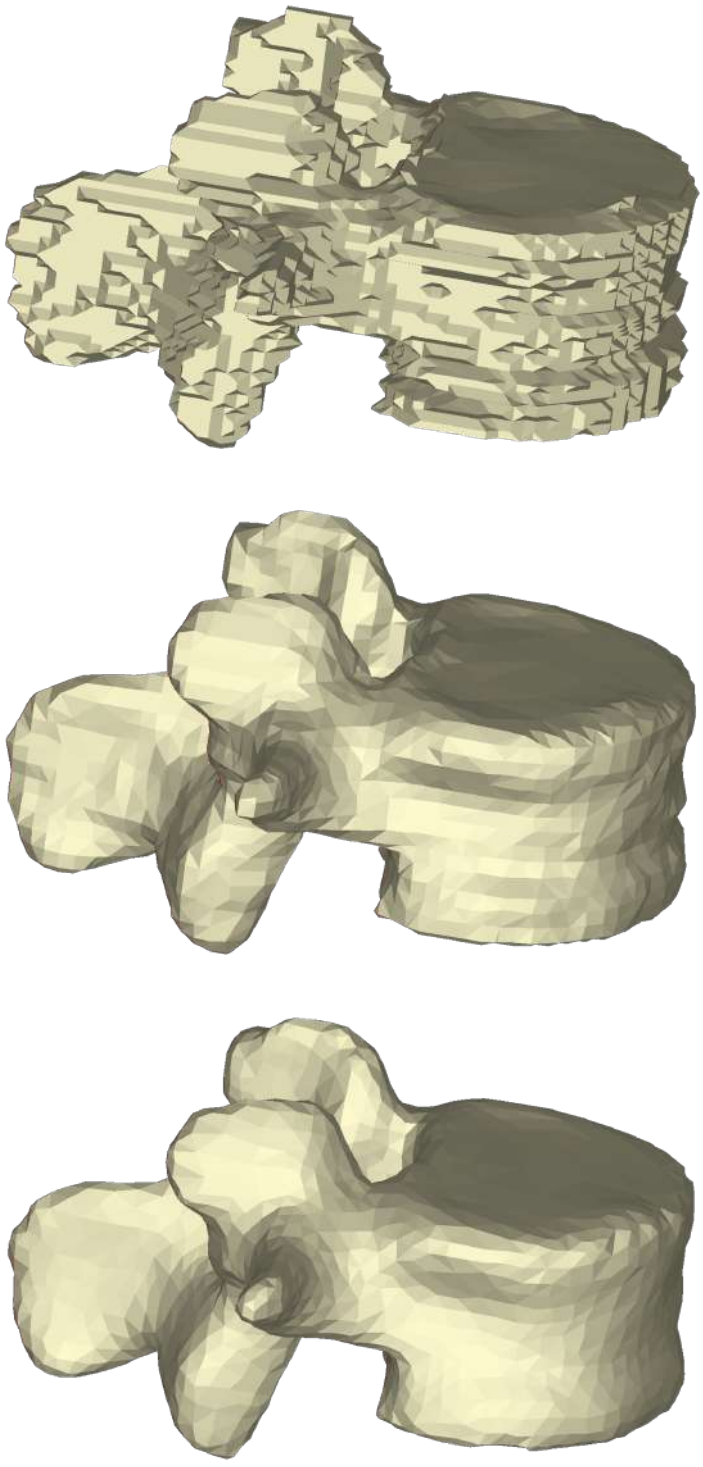

Figure 4.7: Example of the three steps to obtain the 3D geometry of L4. Top: 3D geometry reconstructed from the manual segmentation. Middle: 3D geometry after wrapping. Bottom: 3D geometry after smoothing.

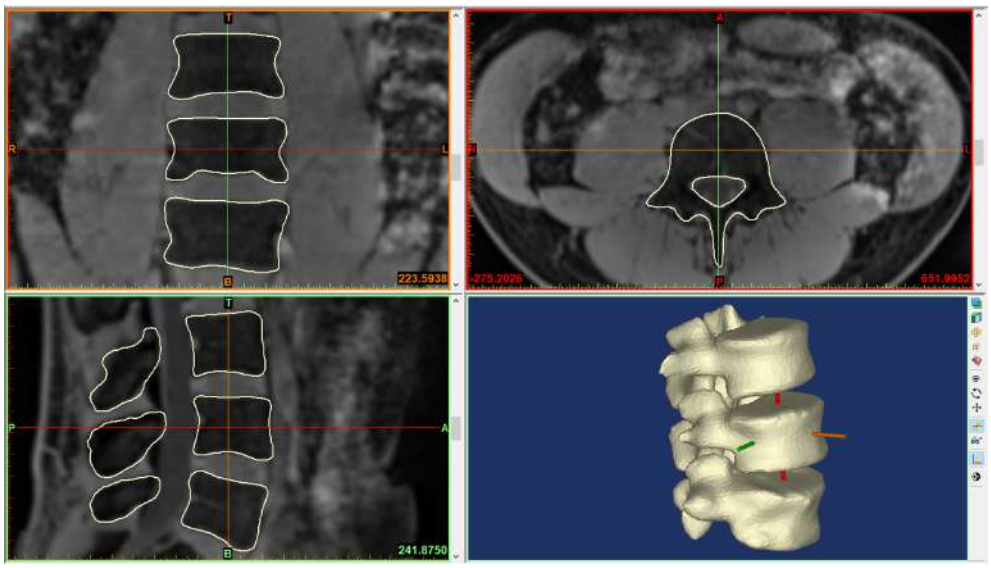

Figure 4.8: Contours of the final 3D geometries are superimposed on the MRI scans for a visual verification.

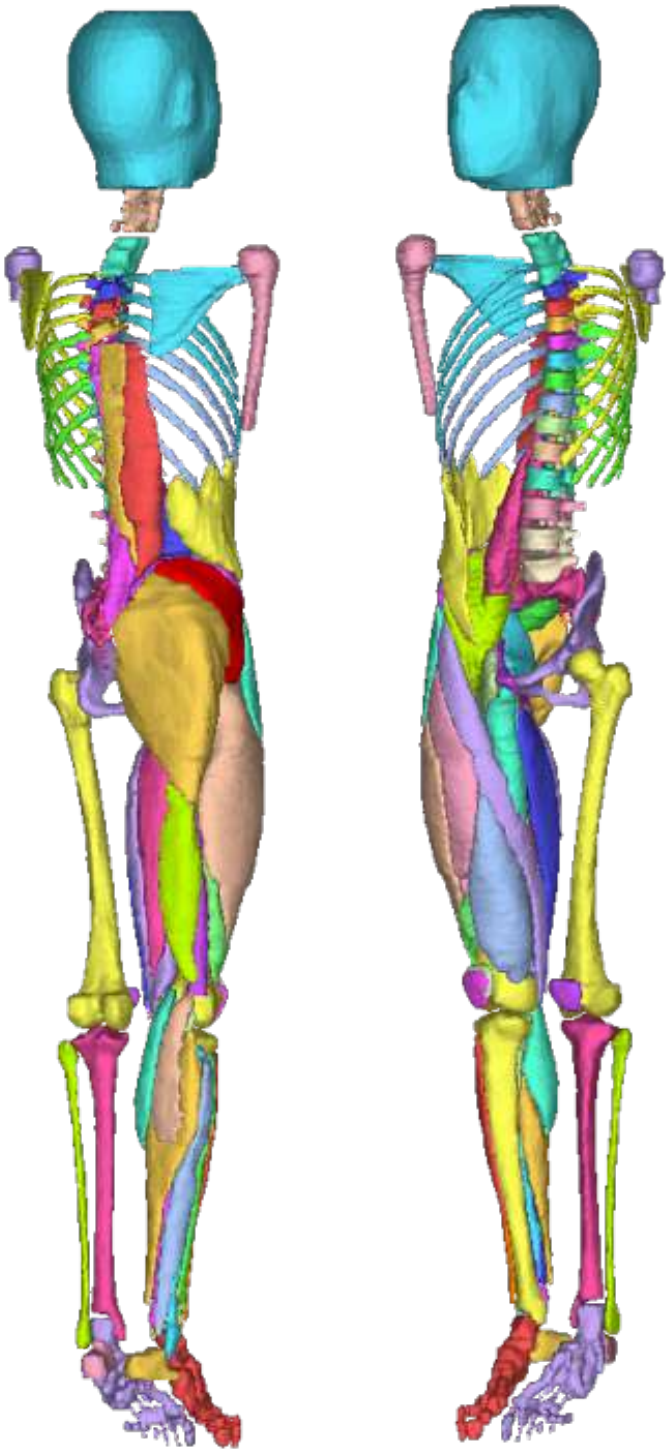

Figure 4.9: Geometries of the bones and the right hand side muscles.

4.6 Limitations of the MRI approach

MRI was used to obtain the detailed representation of bones and muscles needed for this study. Although MRI is a useful tool to visualise and model the different tissues of the human body without putting the subject at risk, the position of the subject in the scanner is a limiting factor for this study. Because the subject is lying supine, the shape of the muscles he is resting on are slightly altered. This is mainly the case for the gluteus muscles and for the erector spinae in the thoracic region to a lesser extent (Figure 4.10). The use of foam pads around the spine cod liver oil capsules also alters muscle shape (Figure 4.11). This is to be considered when building the musculoskeletal model in Chapter 5.

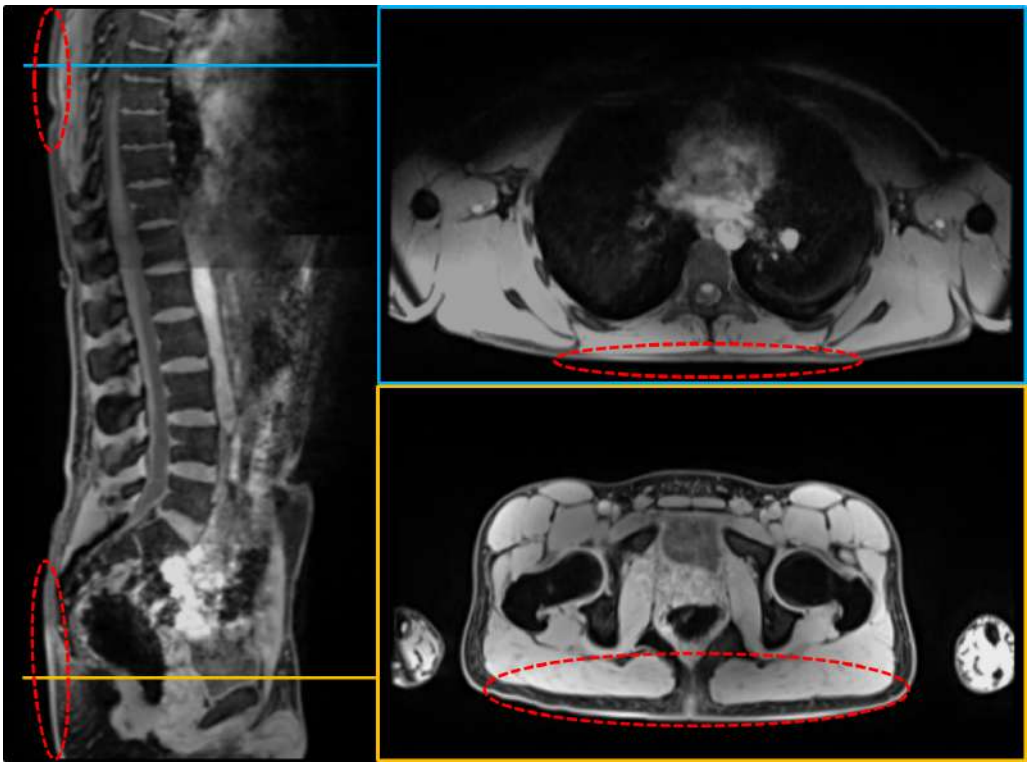

Figure 4.10: Muscles are flatten at the contact points with the table. Flattened muscles are highlighted (in red dash lines) in the pelvic region (yellow frame) and in the T7 region (blue frame).

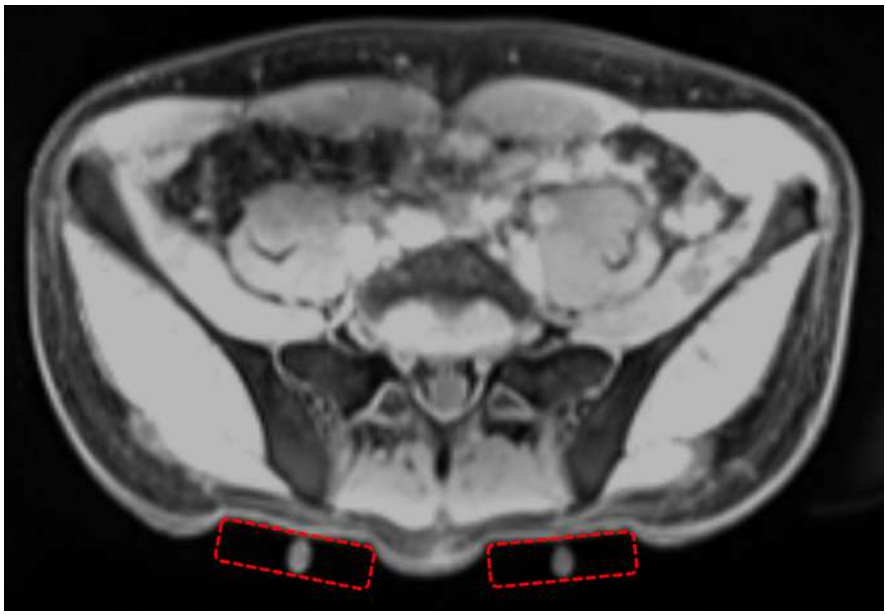

Figure 4.11: Deformation of the spine soft tissues due to the foam pads. Foam is not visible on the MRI scans, but the shape of the pad is indicated with a red dash line.

The altered muscle shape is not the only limitation of supine MRI scans. The curvature of the spine changes between upright and supine positions, particularly for patients with a pathological spine and degenerated intervertebral discs. Clinical studies have highlighted the importance of upright MRI for dynamic assessment of the spine in a weight-bearing position (Alyas et al. 2008, Tarantino et al. 2012, Splendiani et al. 2015). Upright MRI is also of interest to assess inter-segmental mobility in the spine, as it allows acquisitions with a flexed spine (McGregor et al. 2001, Koenig & Vitzthum 2001). However, the resolution of upright MRI scanners is lower than the resolution of traditional supine scanners due to the open magnet. For the current study, this resolution would have been even lower due to the inevitable small movements the subject would have made to maintain his balance, especially with the long acquisition time required for the full body. A supine MRI was preferred to ensure all the details of the spine were captured. The young healthy population of this study was assumed to have minor spine shape changes between supine and upright positions (Andreasen et al. 2007, Meakin et al. 2009, Brink et al. 2016).

The limited size of the MRI coils resulted in a very distorted image at the edge of the MRI scanning area. Arms of the subjects could not be segmented. This is addressed in Chapter 5 when building the musculoskeletal model. The low resolution scans were

sufficient to obtain an accurate bone and muscle geometry in the lower limbs. For the cervical spine and head, it was more difficult to segment the vertebrae and skull with precision. Since this area is not the focus of the study, the cervical spine and head were roughly segmented. Apart from the cervical spine region, bones were very clearly defined on the MRI scans and easy to segment manually. However, it was sometimes difficult to identify clearly the boundaries and insertions of all muscles at first sight during the manual segmentation. An atlas for muscle imaging (Fleckenstein et al. 1996) was used to help in this process, but the obtained muscle geometries are still subject to the operator's choices.

It is also important to note that this approach takes a lot of time. Manual segmentation takes between one and two weeks to obtain the full body geometries needed for this study. Total scanning time for one subject was around 45 min. Given the high resolution of the full body scans, this is acceptable for a healthy volunteer but would be too long for a patient with pain for instance. In the context of this study where pathological conditions are simulated on healthy models, this limitation is not a problem. However this means the current modelling framework based on full body MRI scans will not be easily transferable to clinical studies.

Chapter 5

Development of the musculoskeletal model

This Chapter presents the development of the musculoskeletal model based on one of the healthy volunteers (26 yo, 175 cm, 67.8 kg). The model was developed in OpenSim (Delp et al. 2007), an open-source platform for musculoskeletal modelling, and is available online. https://simtk.org/projects/llsm

5.1 Building the musculoskeletal model

5.1.1 Skeletal model

To ensure consistency throughout the model, bone geometry was segmented manually in Mimics (Mimics Research 19.0, Materialise NV, Leuven, Belgium) from full-body MRI scans of one of the healthy volunteers following the method described in Chapter 4. Each bone or group of bones was exported as an STL file. At this stage, bones were defined in the reference system of the MRI scanner.

In OpenSim, the skeleton is modelled as a chain of rigid bodies linked to each other with joints. Joints between two rigid bodies are defined with a pair of location and orientation vectors to position the joint in the parent rigid body, and another pair of location and orientation vectors to position the joint in the child rigid body (Figure 5.1). This joint definition can make it difficult to visualise the actual position of the joint in the final model. To avoid any confusion, coordinate systems for each rigid body in this model are defined to be coincident with the parent joint location, meaning the location and orientation vectors for the child rigid body are set to zero in the joint definition. This means coordinate systems of each bone must be moved from the scanner reference system to the parent joint location. This is done in 3-matic (3-matic Research 11.0, Materialise NV, Leuven, Belgium) using the rotation and translation tools with some of the shape analysis tools to locate bone landmarks that will help defining joints.

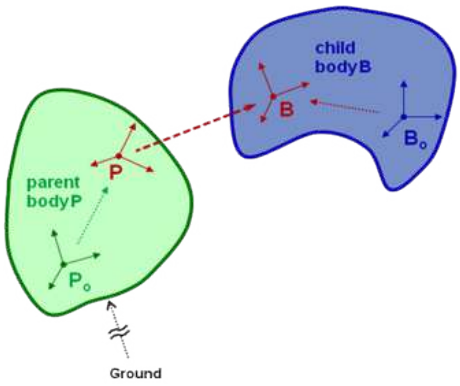

Figure 5.1: Definition of a joint between a parent and a child body. The P_0P vectors position the joint in the parent body. The B_0B vectors position the joint in the child body. The joint defines the kinematic relationship between the frames B and P. Image taken from https://simtk-confluence.stanford.edu

The final model is composed of 22 rigid bodies: one pelvis, two femura, two patellae, two tibiae and fibulae, two hind feet, two mid feet, five lumbar vertebrae and one lower torso, one upper torso, one head, two humeri, and two radii and ulnae plus hands. Pelvis and sacrum are considered as one rigid body, as well as tibia and fibula. The hind foot is composed of the talus and the calcaneus. The mid foot includes the cuboid, cuneiforms and navicular, plus the metatarsal bones and phalanxes. Toes are not articulated. The lower torso is composed of vertebrae T12 to T8 and the associated ribs. It is attached to L1 with a weld joint. The upper torso is composed of vertebrae T7 to T1 and the associated ribs and scapulae. The head is made of the seven cervical vertebrae and the skull. Radius, ulna and hand are considered as one rigid body. The hand is made of the carpal and metatarsal bones and phalanxes. These rigid bodies are articulated with 17 joints for a total of 43 degrees of freedom: hips (three rotations each), knees (one rotation each) and ankles (two rotations each) for the lower limbs, shoulders (three rotations each) and elbows (two rotations each) for the upper limbs, five lumbar joints (three rotations each), T7-T8 joint (three rotations) and C7-T1 joint (three rotations) for the spine.

5.1.1.1 Lower limbs

Bone coordinate systems and joint definitions for the lower limbs are adapted from the recommendations of the International Society of Biomechanics (Wu et al. 2002). The main modifications were made for the knee joint and the tibia coordinate system to ensure consistency with the other segments.

The pelvis coordinate system is defined such that the origin is the midpoint of the left and right anterior superior iliac spines. The Z axis is the line defined by the two anterior superior iliac spines, pointing dextro-laterally. The X axis is orthogonal to the Z axis, lying in the plane defined by the two anterior superior iliac spines and the midpoint of the two posterior inferior iliac spines, and pointing anteriorly. The Y axis is the line orthogonal to both the X and Z axes, pointing proximally (Figure 5.2). The pelvis is composed of the sacrum and the two hip bones. Due to the limited amount of movement allowed by the ligaments of the pelvic ring (Chapter 2, Section 2.2.1.1), the sacroiliac joint is considered rigid in the musculoskeletal model.

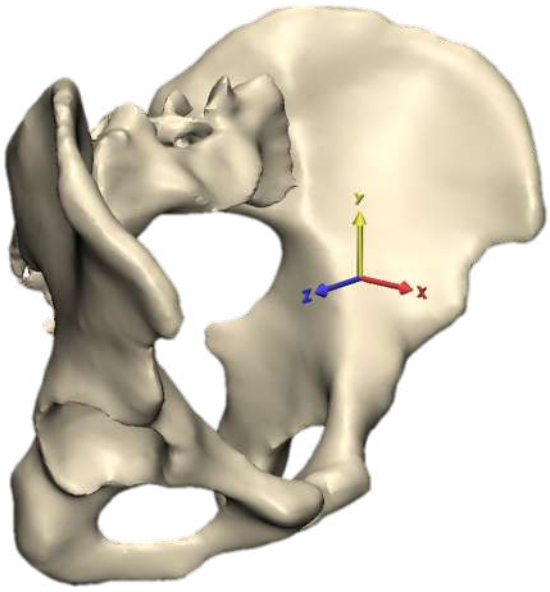

Figure 5.2: Coordinate system of Pelvis and sacrum in the OpenSim configuration. The X axis is in red, the Y axis in yellow, and the Z axis in blue.

The femur coordinate system is defined with the origin coincident with the center of a sphere fitted on the femoral head. The Y axis is defined by the line joining the origin and the midpoint between the lateral and medial epicondyles of the femur, and pointing proximally. The Z axis is orthogonal to the Y axis, lying in the plane defined by the femur epicondyles and the origin, and pointing dextro-laterally. The X axis is the line orthogonal to the Y and Z axes, pointing anteriorly (Figure 5.3).

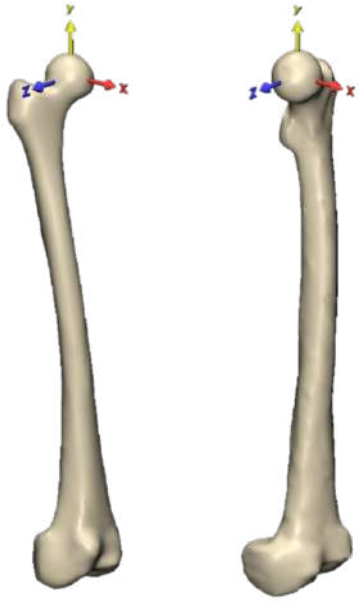

Figure 5.3: Coordinate systems of the right femur (left) and the left femur (right) in the OpenSim configuration. The X axis is in red, the Y axis in yellow, and the Z axis in blue.

The patella coordinate system is defined with the origin centered on the plateau, at the most proximal end. The Y axis is the line joining the tip of the apex and the origin, pointing proximally. The Z axis is orthogonal to the Y axis, lying in the plane defined by the Y axis and the lateral crest, and pointing dextro-laterally. The X axis is orthogonal to the Y and Z axes, pointing anteriorly (Figure 5.4).

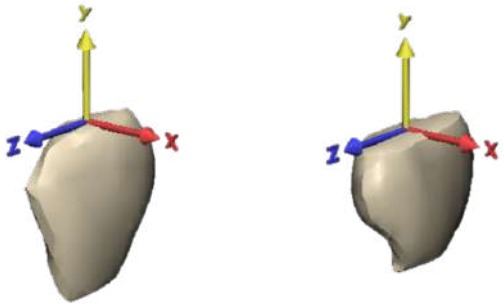

Figure 5.4: Coordinate systems of the right patella (left) and the left patella (right) in the OpenSim configuration. The X axis is in red, the Y axis in yellow, and the Z axis in blue.

The tibia coordinate system is defined with the origin coincident with the midpoint of the lateral and medial epicondyles of the femur. The Y axis is defined by the line joining

the origin and the midpoint between the lateral malleolus of the fibula and the medial malleolus of the tibia, pointing proximally. The Z axis is orthogonal to the Y axis, lying in the plane defined by the two malleoli and the origin, and pointing dextro-laterally. The X axis is the line orthogonal to the Y and Z axes, pointing anteriorly (Figure 5.5).

Figure 5.5: Coordinate systems of the right tibia and fibula (left), and the left tibia and fibula (right) in the OpenSim configuration. The X axis is in red, the Y axis in yellow, and the Z axis in blue.

The foot coordinate system is defined with the origin coincident with the midpoint of the lateral malleolus of the fibula and the medial malleolus of the tibia. The X axis is parallel to the line joining the calcaneus tuberosity and the second distal phalanx, pointing distally. The Y axis is orthogonal to the X axis, lying in the plane defined by the X axis and the origin, and pointing proximally. The Z axis is the line orthogonal to the X and Y axis, pointing dextro-laterally. Both the hind foot and the mid foot use this coordinate system (Figure 5.6).

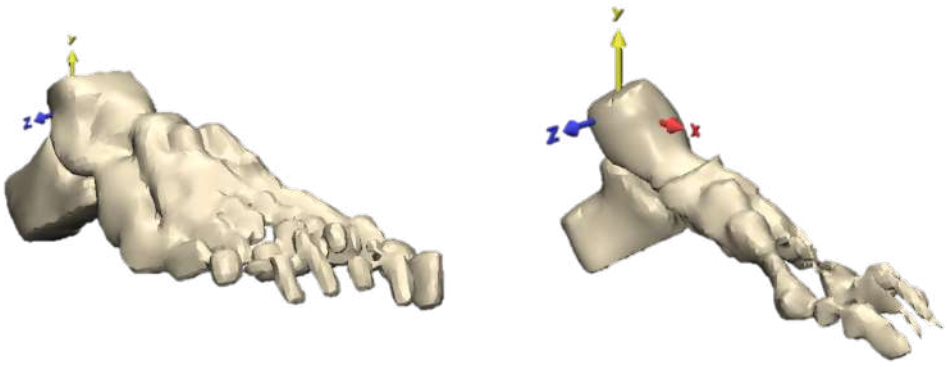

Figure 5.6: Coordinate systems of the right foot (left) and the left foot (right) in the OpenSim configuration. The X axis is in red, the Y axis in yellow, and the Z axis in blue.

The hip joint is modelled as a spheroid joint which allows rotations in the three planes. The hip center of rotation is coincident with the origin of the femur coordinate system. The adduction-abduction, internal-external rotation, and flexion-extension axes are coincident with the X, Y and Z axes of the femur coordinate system respectively.

The knee joint is modelled as a pivot joint which allows one rotation. The knee center is coincident with the origin of the tibia coordinate system. The flexion-extension axis is coincident with the Z axis of the tibia coordinate system.

The patellofemoral joint is modelled following the same approach as Modenese et al. (2011). It is a pivot joint which allows one rotation along the axis of the cylinder whose surface fits the femoral condyles. This axis is distinct from the knee axis of rotation. The patella moves relative to the femur as a function of the knee angle, in the plane orthogonal to the cylinder axis and coincident with the origin of the patella coordinate system in the neutral position of the MRI scan.

The ankle joint complex is modelled with a pivot joint between the tibia and the hind foot, and a pivot joint between the hind foot and the mid foot. The centre of the pivot joint between the tibia and the hind foot is coincident with the origin of the hind foot coordinate system. This joint allows one rotation along the axis defined by the center of the two malleoli. This rotation axis is distinct from the hind foot Z axis. The centre of the pivot joint between the hind foot and the mid foot is coincident with the origin of the

hind foot coordinate system. The rotation axis of this joint is coincident with the X axis of the mid foot.

5.1.1.2 Spine

Unlike synovial joints where cartilage surfaces move against each other making it easy to predict the type of motion, intervertebral joints are made of an intervertebral disc lying between adjacent vertebrae allowing movement in the six degrees of freedom. Wu et al. (2002) recommend to position the intervertebral joint at the centre of the intervertebral disc. However, the intervertebral disc is not a perfect cylinder, and the intervertebral movements are restricted by facet joints in the dorsal part of the vertebrae. Pearcy & Bogduk (1988) evaluated the position of the flexion-extension axis of rotation for the five lumbar vertebrae in ten normal individuals using lateral radiographs. They provide a method to locate these axes of rotation based on the anatomy of the vertebra. In the present musculoskeletal model, the vertebrae coordinate systems and joint definitions for the lumbar spine are based on this approach (Figure 5.7).

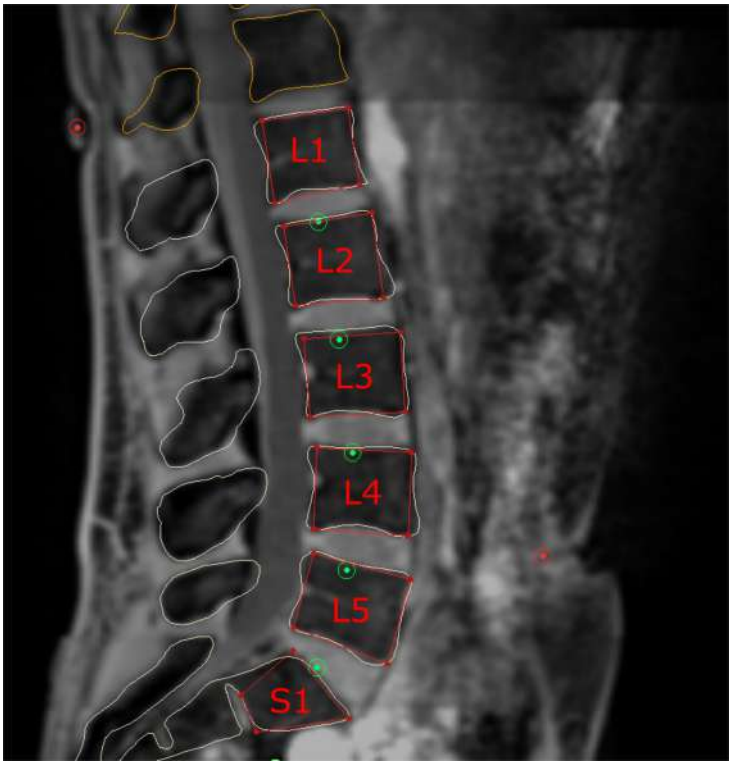

Figure 5.7: Location of the lumbar joint centers in the sagittal plane (in green) based on the method described by Pearcy & Bogduk (1988).

For each lumbar vertebra, the origin of the coordinate system of the child segment is located at the intersection of the flexion-extension axis of rotation with the parent segment as defined by Pearcy & Bogduk (1988) with the mid sagittal plane. The X axis is in the mid sagittal plane, parallel to the proximal endplate plane of the parent vertebra as defined by Pearcy & Bogduk (1988), and pointing anteriorly. The Y axis is in the mid sagittal plane, orthogonal to the X axis, and pointing proximally. The Z axis is orthogonal to the X and Y axes, pointing dextro-laterally (Figure 5.8). X, Y and Z axes are therefore the lateral bending, axial rotation and flexion-extension axes respectively.

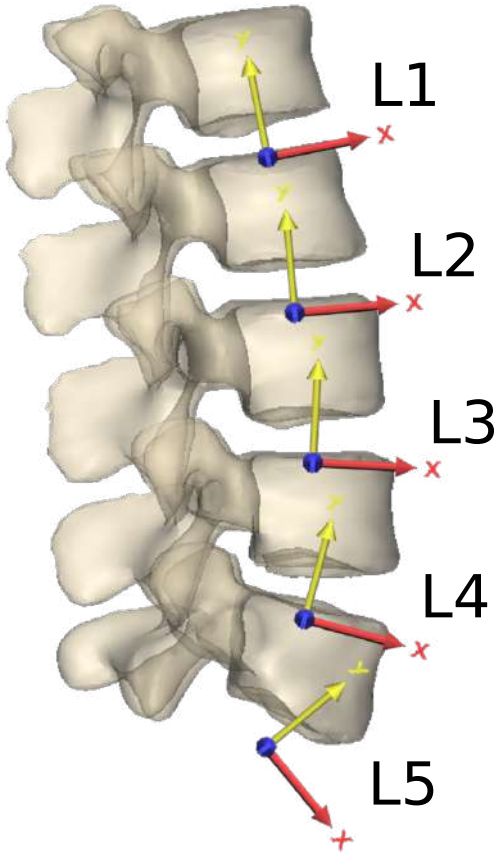

Figure 5.8: Coordinate systems of the lumbar vertebrae in the OpenSim configuration. The X axis is in red, the Y axis in yellow, and the Z axis in blue.

For the lower torso, upper torso and head segments, less anatomical accuracy is needed as these are not part of the region of interest. The origins of the coordinate systems can be defined following the recommendations from Wu et al. (2002). The origin of the coordinate system for the upper torso is located at the center of the T7-T8 intervertebral disc, and

the origin of the coordinate system for the head is located at the center of the C7-T1 intervertebral disc. The X, Y and Z axes of these rigid bodies are parallel to the X, Y and Z axes of the pelvis in the MRI scan configuration.

To simplify the model, intervertebral joints were modelled with spheroid joints allowing the three rotations and neglecting translations. Each lumbar intervertebral joint centre is coincident with the origin of the vertebra. The lateral bending axis is coincident with the X axis, the axial rotation axis is coincident with the Y axis, and the flexion-extension axis is coincident with the Z axis.

T7-T8 and C7-T1 joints are also modelled with spheroid joints. Joint centre, lateral bending axis, axial rotation axis and flexion-extension axis of T7-T8 and C7-T1 joints are coincident with the origin, X, Y and Z axes of the upper torso and head segments respectively.

5.1.1.3 Upper limbs

Since the upper limbs of the subjects were close to the edge of the scanner table and out of range of the coils, it was not feasible to segment the bone geometry for the upper limbs from the MRI scans. The geometry was therefore imported from the musculoskeletal model of Rajagopal et al. (2016), and scaled to match the subject's anatomy using the OpenSim scaling tool. The shoulder joint was visible on the MRI scans, making it possible to link the generic upper limb geometry to the segmented torso. Coordinate systems of the humerii, ulnae, radii, and hands remained the same as the model from Rajagopal et al. (2016). The origin of the coordinate system of the humerus is coincident with the centre of a sphere fitted on the humeral head segmented from MRI scans.

Joint definitions were also kept unchanged, apart from the radioulnar and the wrist joints. The radioulnar joint allows the forearm to rotate along its longitudinal axis and the wrist joint allows the hand to rotate in the three directions. The hand, the radius and the ulna were merged into one single rigid body. A degree of freedom was added at the elbow joint to account for the forearm axial rotation. This reduces the complexity of the model while keeping the same level of mobility. The three rotations of the wrist were

removed as they are not needed in the present study. The shoulder is modelled with a spheroid joint to allow rotations in the three planes. The shoulder centre of rotation is coincident with the origin of the humerus. The elbow complex is modelled with two pivot joints to account for forearm flexion and axial rotation.

5.1.1.4 Inertia properties

The method presented here is based on the simplistic assumption that bone and soft tissue are two homogeneous materials. This hypothesis is assumed to give an acceptable approximation of the segments mass and inertia properties.

Soft tissues were segmented as one single material for each body segment and exported as STL files (Figure 5.9). The same transformation matrices were applied in 3-Matic to have bone and corresponding soft tissues in the same coordinate systems. Bone geometries were imported in Solidworks (Solidworks 2019, Dassault Systemes S.A., France) with their corresponding soft tissue parts. Two new materials were created and added to the Solidworks library. A material with a density of 1.92 g/cm^3 representative of cortical bone was initially applied to bone parts, while a material with a density of 1.05 g/cm^3 was applied to soft tissue parts. These values are taken from the International Commission on Radiation Units and Measurements' report 46 by White et al. (1992). The bone and soft tissue parts were made into a Solidworks assembly, and the mass properties tool was used to obtain the mass, center of mass and matrix of inertia for each body segment. Mass and inertia properties of the upper limbs were scaled from Rajagopal et al. (2016). Total body mass obtained with this method was compared against the actual body mass of the subject. Because bone is made of cortical and trabecular bone, it was necessary to adjust the initial bone density. The bone density was therefore adjusted so the sum of all segments' computed values matched the total measured value. The final bone density was 1.5 g/cm^3. Mass, centre of mass, and inertia tensor of each segment were exported from Solidworks and implemented in the musculoskeletal model. A description of these properties is available in Appendix B.

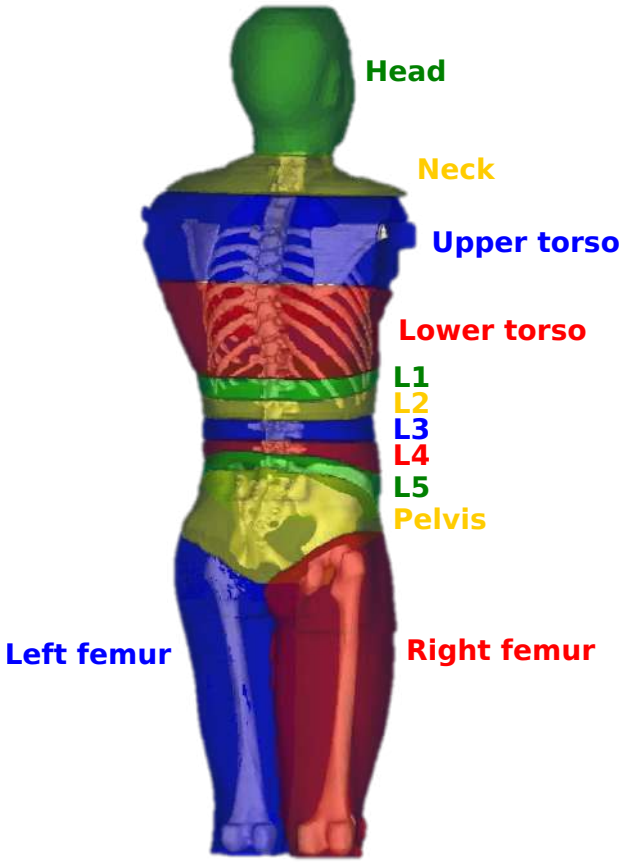

Figure 5.9: Segmentation of soft tissues corresponding to each body segment.

5.1.2 Musculotendon model

The model includes 538 musculotendon actuators to represent 92 muscles of the lower limbs and lumbar spine (Figure 5.10). These actuators were adapted from existing musculoskeletal models (Modenese et al. 2011, Christophy et al. 2012, Bruno et al. 2015). They are implemented with the Thelen model (Thelen 2003) available in OpenSim and defined with parameters common to every Hill-type models (Zajac 1989) (Chapter 2, Section 2.4, Figure 2.19): the maximum isometric force, the optimal fiber length, the pennation angle at optimal fiber length, and the tendon slack length. On the MRI scans, it is difficult to identify the fiber orientation and the limit between muscles and tendons. Physiological muscle parameters were therefore adapted from generic models. Pennation angles from the generic models were kept the same in the new model. Tendon slack lengths and optimal fiber lengths were scaled to match the new muscle morphology.

Maximum isometric force is usually calculated as proportional to the muscle physiological cross sectional area (PCSA) using a fixed maximum tetanic stress (Equation 5.1). The reported range for the maximum tensile stress varies between 20 N/cm^2 and 140 N/cm^2 (Haxton 1944, Bogduk, Macintosh & Pearcy 1992, Buchanan 1995, Maganaris et al. 2001, Holzbaur et al. 2005). A maximum tensile stress of 100 N/cm^2 was chosen to allow simulation of lifting tasks (Bruno et al. 2015, Beaucage-Gauvreau et al. 2019) and maximum isometric forces where adapted accordingly. A description of musculotendon properties is available in Appendix B.

$$F_{max}^{iso} = PCSA \times \sigma_{Tmax} \tag{5.1}$$

where F_{max}^{iso} is the maximum isometric force, $PCSA$ is the physiological cross sestion area and σ_{Tmax} is the maximum tensile stress.

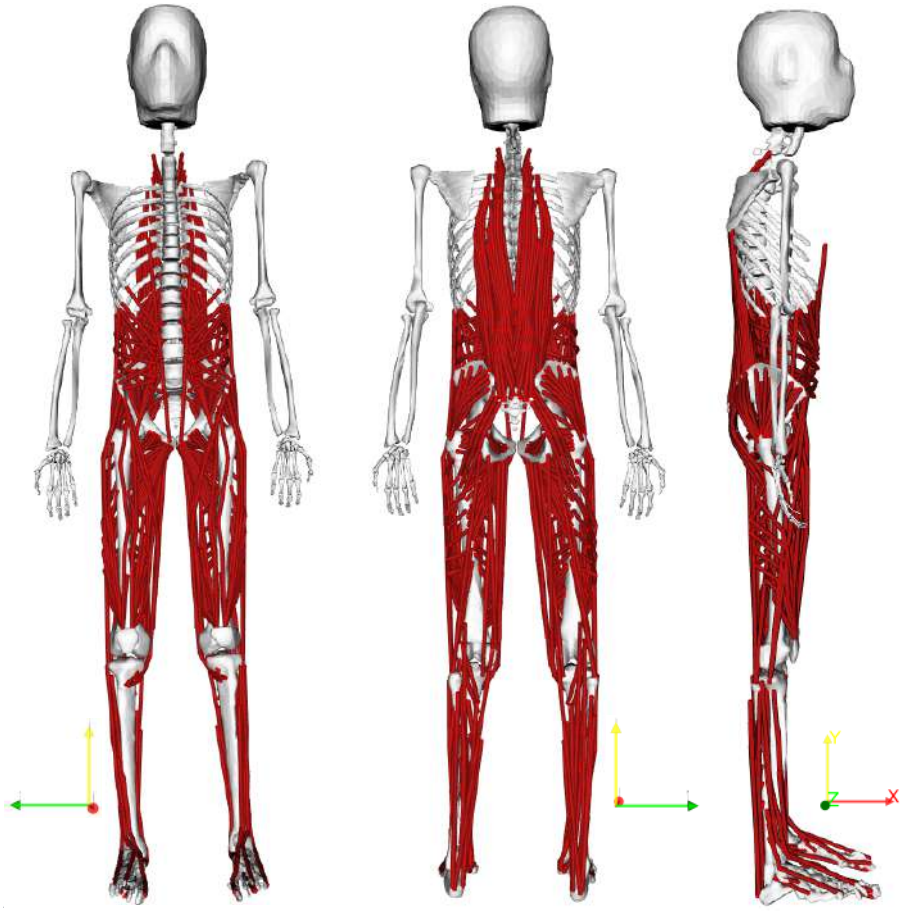

Figure 5.10: Musculoskeletal model with 22 rigid bodies and 538 musculotendon actuators.

Muscle geometries were also adapted to the subject-specific bone geometry by deriving muscle insertions, attachments and path points from the MRI scans of the healthy volunteer. In Mimics, muscle insertions and attachments were marked on the axial slices for each body segment. Figure 5.11 shows the the example of the pelvis. The coordinates of these points were then exported in a CSV file and processed with MATLAB (The MathWorks, Inc., USA). Using the same transformation matrices as in 3-Matic, the muscle insertions and attachments were transformed to the coordinate system of the body segment they belong to. These new coordinates were finally implemented in the model through the OpenSim API. Existing muscle path points and via points were also adapted to the subject-specific geometry using the same method, to ensure muscle moment arms are consistent with the rest of the model. Figure 5.12 shows the example of L3. The OpenSim musculotendon paths overlaying the muscle geometry for each muscle group of the lumbar spine are presented in Appendix B.

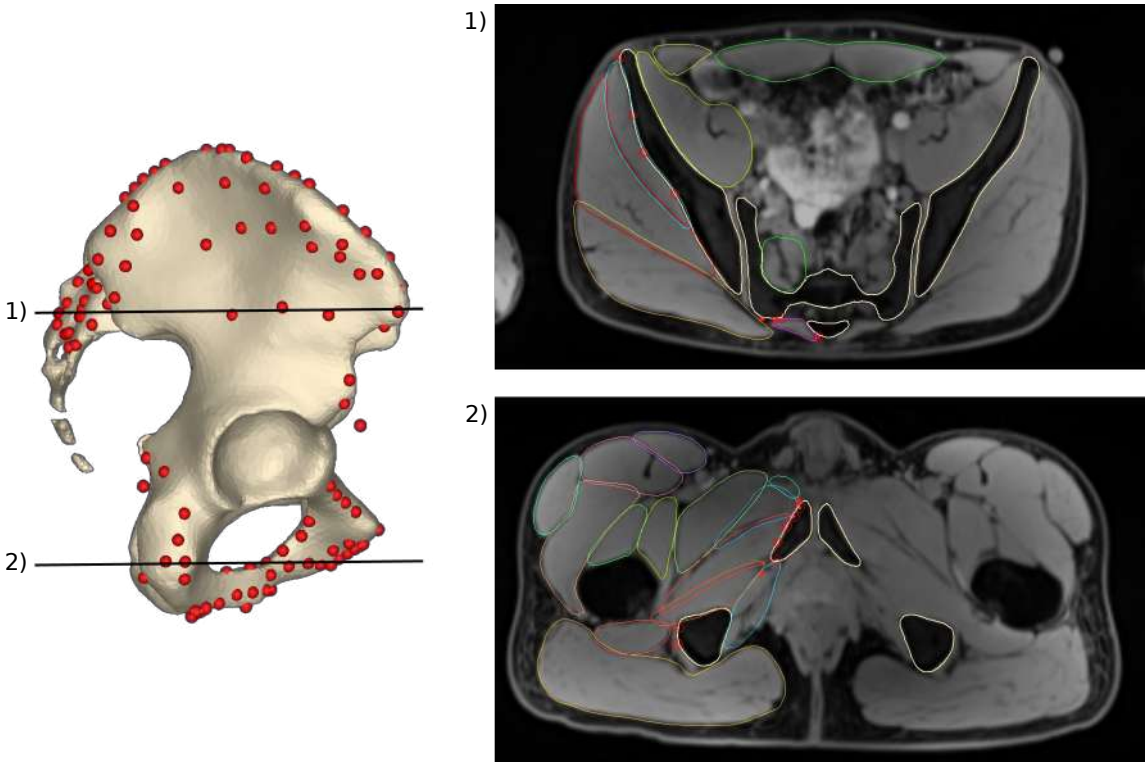

Figure 5.11: Muscle insertions (red dots) on the right pelvis determined on MRI axial slices (right) and visualized on the 3D geometry (left).

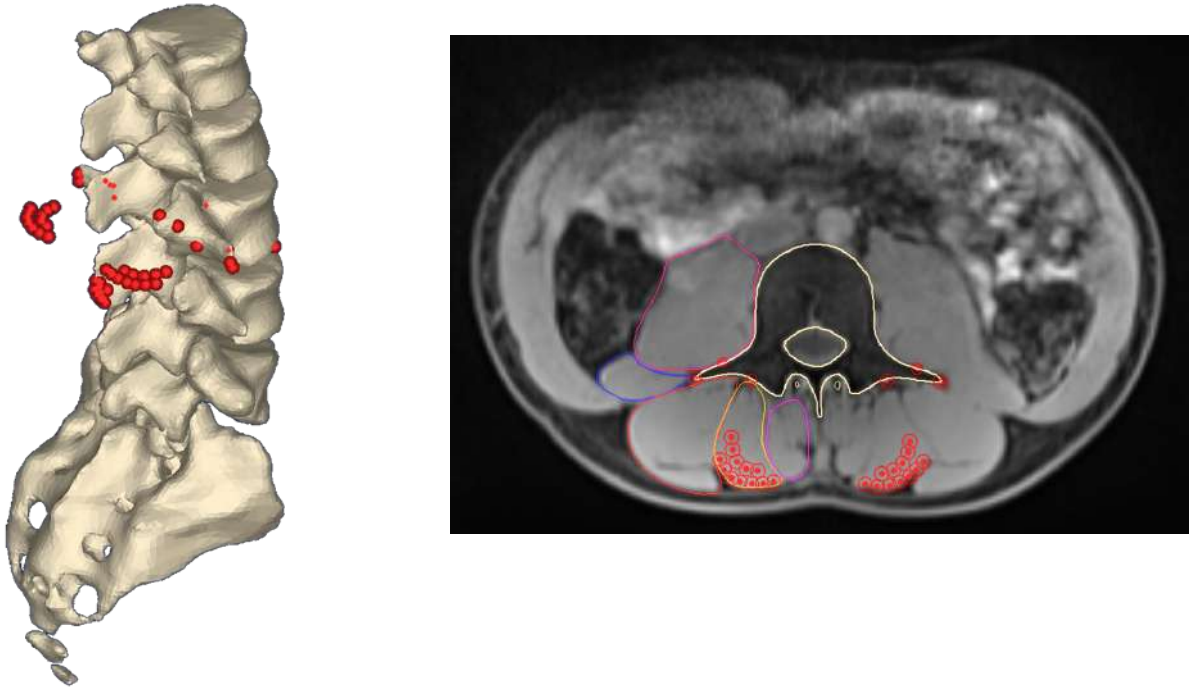

Figure 5.12: Muscle insertions and longissimus path points (red dots) on L3 determined on MRI axial slices (right) and visualized on the 3D geometry (left).

5.1.2.1 Muscles of the lower limbs

Musculotendon actuators of the lower limbs are adapted from the London Lower Limb Model (LLLM) developed by Modenese et al. (2011). The LLLM model is a generic unilateral musculoskeletal model of the lower limb, based on the anatomical dataset published by Horsman et al. (2007). It is composed of 163 actuators representing 38 muscles divided into 57 muscle parts composed of up to six bundles. This model was first mirrored to create the actuators of the contralateral limb. The insertion and attachment points of these actuators were updated to match the subject-specific geometry using the method described previously.

New path points were added to increase the accuracy of the line of action of the muscles. A cylindrical wrapping surface is used at the knee to guide the rectus femoris and vastii muscles along the femoral anterior surface (Figure 5.13). A spherical wrapping surface is used at the hip to prevent hip muscles from penetrating the femoral head (Figure 5.14). A cylindrical wrapping surface is used on the superior pubic ramus to guide

the iliopsoas (Figure 5.15). A combination of ellipsoidal and cylindrical wrapping surfaces are used at the hip to guide the gluteus muscle during hip flexion (Figure 5.16). Existing wrapping surfaces guiding the vastii muscles around the femur shaft were replaced by path points to simplify the model and increase computational efficiency in future simulations (Figure 5.17).

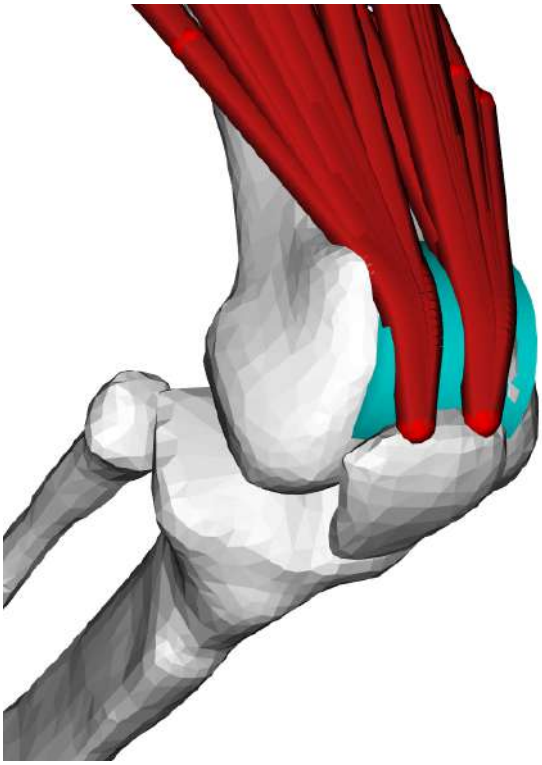

Figure 5.13: Rectus femoris and vastii musculotendon fibers of the right leg wrapping around the cylindrical surface of the anterior femur.

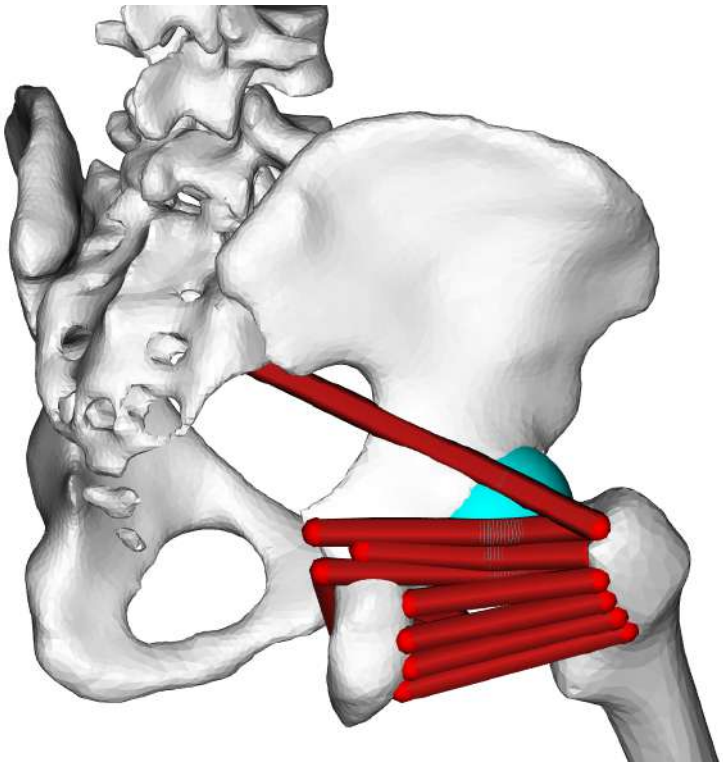

Figure 5.14: Spherical wrapping surface around the right femoral head.

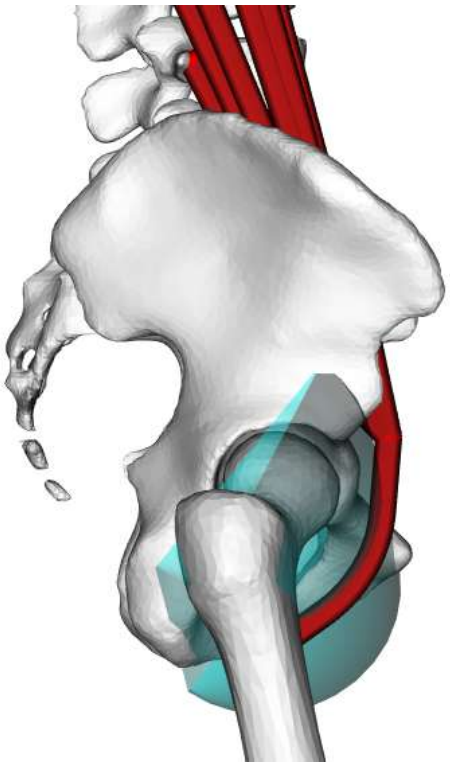

Figure 5.15: Iliopsoas musculotendon fibers wrapping around the cylindrical surface of the right superior pubic ramus.

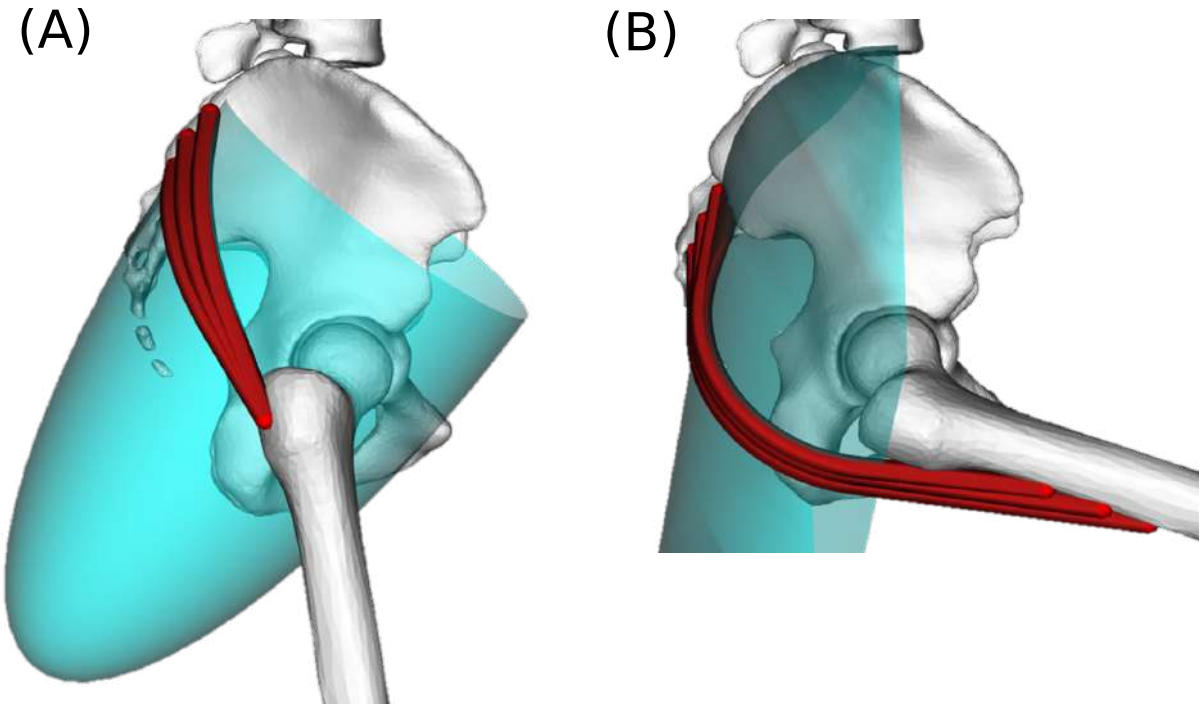

Figure 5.16: Wrapping surface of the gluteus muscle. (A) Cylindrical wrapping surface of the inferior fibers of the gluteus maximus. (B) Ellipsoidal wrapping surface of the superior fibers of the gluteus maximus.

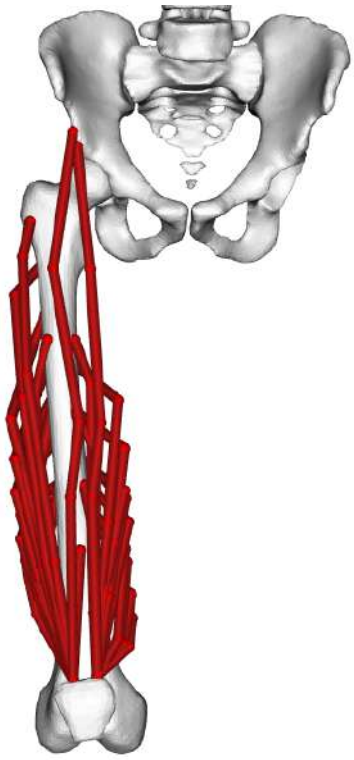

Figure 5.17: Rectus femoris and vastii musculotendon fibers with via points.

5.1.2.2 Muscles of the lumbar spine

Musculotendon actuators of the lumbar spine are adapted from the model developed by Christophy et al. (2012). The Christophy model is a generic musculoskeletal model of the lumbar spine based on anatomical data published by Bogduk, Macintosh & Pearcy (1992), Bogduk, Pearcy & Hadfield (1992), Bogduk et al. (1998), Bogduk & Endres (2005), Macintosh & Bogduk (1986), Macintosh & Bogduk (1987), Macintosh & Bogduk (1991), Stokes & Gardner-Morse (1999), Wilkenfeld et al. (2006), Santaguida & McGill (1995) and Phillips et al. (2008). It is composed of 238 actuators representing 8 muscle groups of the lumbar region: erector spinae, rectus abdominis, internal obliques, external obliques, psoas major, quadratus lumborum, lumbar multifidus and latissimus dorsi. Transversus abdominis were also implemented from the model developed by Bruno et al. (2015). In the Christophy model, the latissimus dorsi bundles attach to the humerus and wrap around the ribcage using an ellipsoidal wrapping surface. In the current model, the ribcage is articulated which increases the complexity of the wrapping surfaces to be used in order to prevent the muscle from penetrating the ribs. The humerii are also articulated and the latissimus dorsi is the only muscle spanning the shoulder. This configuration would generate erroneous muscle forces for this muscle. Previous studies also reported that the latissimus dorsi contribution to the lumbar spine extensor moment during lifting tasks is less than 5% (McGill & Norman 1988, Bogduk et al. 1998). It was therefore decided to remove the latissimus dorsi from the model.

Using the method described previously, muscle insertions, attachments, path points and via points were adapted to match the subject-specific geometry. Cylindrical wrapping surfaces are used to guide the transversus abdominis (Figure 5.18). The lumbar cylindrical wrapping surface originally used to curve the lumbar muscle bundles was replaced by path points at several lumbar levels to simplify the model (Figure 5.19).

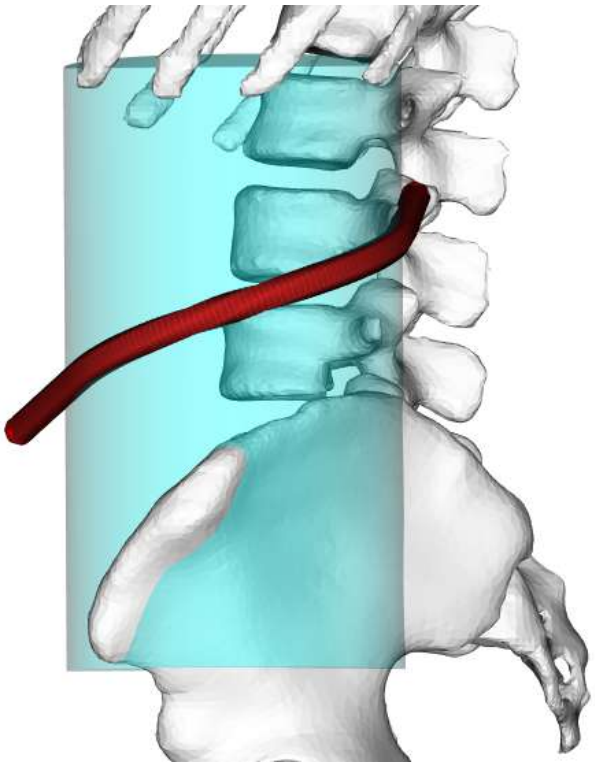

Figure 5.18: Transverse abdominis fiber originating from L3 and wrapping around a cylindrical surface.

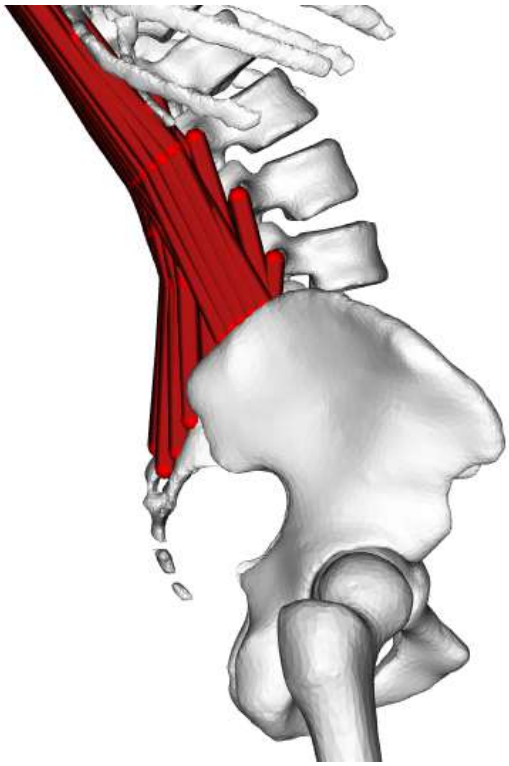

Figure 5.19: Musculotendon fibres of the erector spinae with via points.

5.1.2.3 Other actuators

The current study focuses on the lumbar spine and the lower limbs, with extensive representation of the muscles in these areas. Other areas of the full body model such as the head and upper limbs are only modelled to take into account the inertial effects during large movements. Musculotendon actuators are not modelled for these segments, which still need to be actuated. At elbows, shoulders, and C7-T1 intervertebral joint, coordinate actuators are used to produce the moments necessary to move the attached segments. At T7-T8 and T12-L1 intervertebral joints, only a few muscles from the lumbar back cross these joints. Reserve actuators are therefore used to account for the back muscles that are not modelled in the thoracic back region. Although the mass and inertial properties of each segment are derived from the MRI scans, this is still an approximation, especially in the lumbar region where it is difficult to assign inertial properties to the abdominal soft tissues during large movements of the spine. This approximation can create residual forces in the model. Residual actuators are used at the ground-pelvis joint to account for these forces which remain small for the full body model. Residual actuators also account for any potential miscalibration of the forceplates.

5.1.3 Modelling the spine

Intervertebral joints are complex. They are composed of the intervertebral disc and are surrounded by ligaments, which limit the range of motion and stiffen the joint. This stiffness was implemented in the model with linear bushing elements adapted from a model developed by Senteler et al. (2015) and located between each lumbar vertebra. These bushing elements are available in OpenSim. They have six degrees of freedom and linearly apply reaction forces and moments in response to the translation and rotation between the segments they are attached to. In the present model, all translations are locked at the intervertebral joints so only reaction moments can be applied (Table 5.1). Following a similar method as Senteler et al. (2015), the bushings were positioned so that no reaction moment was produced in the lying supine position, considered as a neutral position. Bushing reference frames are therefore coincident with the joint reference frames.

Table 5.1: Rotational stiffness of the lumbar bushing elements from Senteler et al. (2015).

	Rotational stiffness (Nm/rad)		
	Lateral bending	**Axial rotation**	**Flexion-Extension**
	(X axis)	**(Y axis)**	**(Z axis)**
L1-L2	70	233	23
L2-L3	64	268	37
L3-L4	69	291	51
L4-L5	94	293	65
L5-S1	131	281	79

Skin artifacts are particularly large in the back making tracking the movement of individual vertebrae very difficult with standard motion capture where markers are taped directly on the skin. White et al. (1978) demonstrated that individual lumbar vertebrae can be assumed to move as a linear function of the overall movement of the spine which can be tracked more accurately. Based on this assumption, it is common practice to use linear kinematic constraints at each lumbar level for all degrees of freedom (Han et al. 2012, Christophy et al. 2012, Raabe & Chaudhari 2016, Actis et al. 2018, Beaucage-Gauvreau et al. 2019). These constraints allow to track the pelvis and the thoracic spine, and distribute the overall angle between the lumbar segments. Coefficients for the kinematic constraints are usually derived from in-vivo experiments. It is therefore crucial to ensure the modelling approach is compatible with the experimental methods used to measure these coefficients. However it appears that most of the existing models of the lumbar spine tend to neglect the limitations related to the use of the lumbar kinematic constraints.

The model from Han et al. (2012) is developed on a platform commercialised by AnyBody Technology (Aalborg, Denmark). This model uses kinematic constraint coefficients adapted from an experimental study by Wong et al. (2006). This study only provides values for flexion and extension of the spine. It is unclear if they used the same values for the other rotations. The models from Raabe & Chaudhari (2016), Actis et al. (2018) and Beaucage-Gauvreau et al. (2019) are OpenSim models based on the model from Christophy et al. (2012). In their model, Christophy et al. (2012) adapted the kinematic constraint coefficients from experimental measurements by Wong et al. (2006) for flexion

and extension of the spine, Rozumalski et al. (2008) for lateral bending, and Fujii et al. (2007) for axial rotation.

Wong et al. (2006) used videofluoroscopy to investigate the lumbar spine kinematics. They were able to quantify the range of motion of each lumbar segment for different angles of flexion and extension of the spine for 30 healthy subjects. Based on their publication, it is possible to express the flexion angle for each lumbar vertebra as a function of the angle between the inferior endplate of L1 and the superior endplate of S1. Rozumalski et al. (2008) inserted wires in each lumbar spinous process in 10 healthy young-adults. Reflective markers were attached to these wires to track the movement of the lumbar vertebrae with motion capture. They were then able to quantify the range of motion of lumbar vertebrae for various movements of the spine, including pure flexion extension, lateral bending, and axial rotation. In the same manner as Wong et al. (2006), it is then possible to express the angle between consecutive lumbar vertebrae as a function of the angle between the inferior endplate of L1 and the superior endplate of S1, assuming this relationship is linear. Fujii et al. (2007) used MRI and a custom built device to estimate the axial rotation of each lumbar vertebra as a function of the axial rotation between the shoulders and the pelvis in 10 healthy volunteers. Wong et al. (2006) and Rozumalski et al. (2008) describe the lumbar vertebrae movements as a function of the angle between S1 and L1, while Fujii et al. (2007) describes the same lumbar vertebrae movements as a function of the angle between S1 and the shoulders. In their model, Christophy et al. (2012) use constraint coefficients from these three different sets which are not consistent with each other, and the thoracic spine, cervical spine, and head are modelled as one rigid body. To remain consistent with the different definitions of the lumbar constraint coefficients by Wong et al. (2006), Rozumalski et al. (2008) and Fujii et al. (2007), this model can therefore only be used for small movements of the spine where the relative movements of thoracic vertebrae can be neglected.

In their study, Raabe & Chaudhari (2016) investigated jogging biomechanics. The assumption of limited relative movement between thoracic vertebrae seems acceptable in this case. However, they used markers on the head and shoulders to track the thoracic and cervical spine, considered as a single rigid body in the model. This could be a limitation for the investigation of jogging activities where relative movements between the head

and the shoulders are to be expected. The assumption of limited relative movement between thoracic vertebrae becomes less adequate when tracking larger movements of the spine. The study by Actis et al. (2018) focuses on spine movements in all directions. The thoracic spine is tracked using markers at T10, C7 and xiphoid processes, sternal notch, and bilaterally at the acromion and T8. Depending on how the virtual markers are weighted for inverse kinematics, three possibilities emerge. If T8 and T10 virual markers are more heavily weighted, lumbar spine movements are tracked from the lower thoracic spine. This configuration is in agreement with the kinematic constraint coefficient used for flexion extension and lateral bending (Wong et al. 2006, Rozumalski et al. 2008), but is inconsistent with the coefficients used for axial rotation (Fujii et al. 2007). In the opposite configuration where the virual markers on C7 and the sternum are more heavily weighted, the lumbar spine is tracked from the upper thoracic spine resulting in flexion extension and lateral bending movements being inaccurately tracked. If the virtual thoracic markers are equally weighted, none of the lumbar spine movement can be considered as accurately tracked. To address this limitation, it is important to choose coefficients for the lumbar kinematic constraints that are consistent with the modelling approach and the marker set used. Beaucage-Gauvreau et al. (2019) have changed these coefficients when adapting the model of Raabe & Chaudhari (2016) to simulate lifting tasks. They used ratios reported by Arjmand & Shirazi-Adl (2006) for flexion extension, Dvorak et al. (1991) for lateral bending and adapted the coefficients from Fujii et al. (2007) to track the lumbar spine from T12. However, the marker set they used only permitted the upper thoracic spine to be tracked. The thoracic and cervical spine and the head were modelled as a single rigid body in their study. Whilst this allows the position of the shoulders to be tracked accurately, the lumbar vertebra angles will be overestimated when tracking large movement of the spine occurring during lifting tasks.

The current study addresses the potential limitations of existing models. Kinematic constraint coefficients for flexion extension, lateral bending and axial rotation are taken from the study by Rozumalski et al. (2008) (Table 5.2). The modelling choices made for the spine are consistent with this data set. The three-segment thoracic and cervical spine makes it possible to track separately the lower thoracic spine, upper thoracic spine, and head which ensures anatomically correct lumbar spine movements and accurate positioning of the shoulders and head. The marker set used to track these segments is described

in the next Section. Greater consistency between the three vertebral rotations is also ensured as all coefficients come from the same data set.

Table 5.2: Kinematic constraint coefficients adapted from Rozumalski et al. (2008).

	Lateral bending (X axis)	**Axial rotation (Y axis)**	**Flexion-Extension (Z axis)**
L1-L2	0.187939	0.213982	0.179705
L2-L3	0.250128	0.209729	0.208948
L3-L4	0.245332	0.183679	0.221445
L4-L5	0.181086	0.200691	0.210822
L5-S1	0.135515	0.191919	0.179080

It is important to note that these constraints are only used during inverse kinematics. Once the body kinematics are known, the constraints are removed for the rest of the simulations, and especially for static optimisation. If kinematic constraints are used during static optimisation, OpenSim considers that muscles are not needed to move the constrained vertebrae and therefore underestimates muscle activations.

5.1.4 Virtual marker set

The experimental markerset described in Chapter 3 was implemented on the model for inverse kinematic (IK) simulations (Figures 5.20 and 5.21). Virtual marker coordinates in the OpenSim model were derived from the MRI images. Cod liver oil capsules placed using the method described in Chapter 4 were located in Mimics. In a similar manner to the muscle attachments, their positions were then exported in 3-Matic and transformation matrices applied to obtain their coordinates in the desired body segment coordinate system.

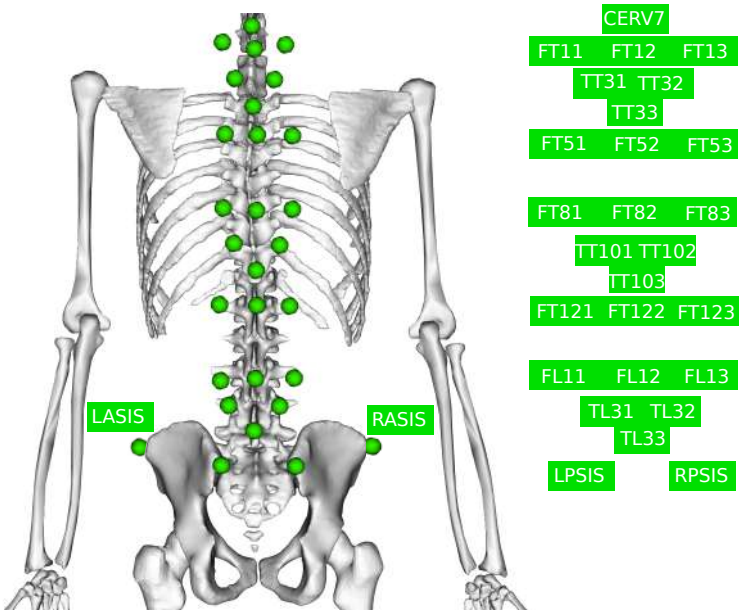

Figure 5.20: Virtual markers of the back implemented on the model.

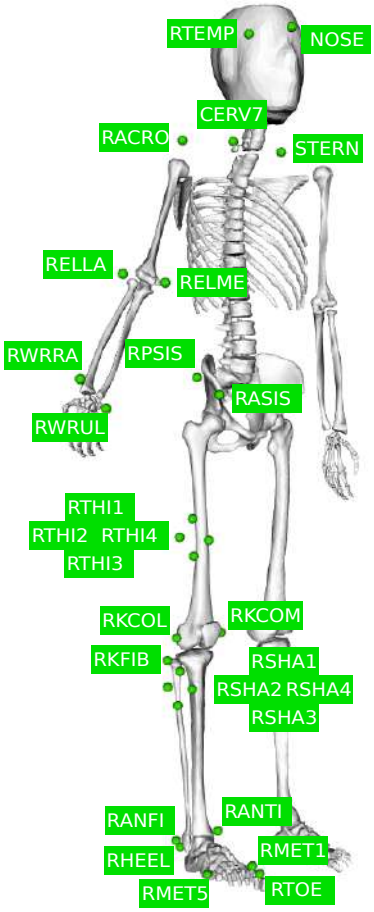

Figure 5.21: Virtual markers of the right side implemented on the model.

The numerous markers used on the spine allow spinal regions to be tracked despite skin artifacts. By weighting equally the virtual markers of a single rigid body during IK (Appendix B), OpenSim will average the position of this segment to match all the experimental markers attached to it with the same accuracy. For instance, three clusters of three markers each are attached to the lower thoracic spine segment. One cluster is located at T12 level, one at T10 and one at T8. During spine movement the experimental markers will move relative to each other. Because of skin artifacts, it is impossible to track T12, T10 and T8 individually. In the model, these vertebrae are modelled as one single rigid body and the virtual markers at T12, T10 and T8 cannot move relative to each other. During IK, the algorithm will try to match the position of the virtual markers with the position of the experimental markers, and eventually choose an average position. This method is believed to reduce the impact of skin artefacts in most cases. However this method has limitations, especially if the artefact displacements and directions are similar for each marker of the body segment. In this particular case, the resulting position of the segment will be offset.

5.2 Assessing the musculoskeletal model

5.2.1 Model verification

5.2.1.1 Muscle moment arms

The musculoskeletal model was built based on images of a volunteer lying in a supine position. Muscle paths were then adjusted in this neutral position. It is therefore necessary to check that muscle moment arms are reasonable for the full range of motion the model will be used for. Moment arms (MA) of all musculotendon actuators were checked to ensure that they are physiologically feasible. This means that at each joint, the sign of the moment arm is in agreement with the role of the muscle and there is no discontinuity of the moment arm during a prescribed movement. Beaucage-Gauvreau et al. (2019) reported physically inaccurate moment arms for the hips and knees for the lifting tasks they investigated and had to remove lower limb muscles from their model. It was therefore considered important to validate moment arms of the lower limbs against experimental measurements from the literature (Blemker & Delp 2005, Buford et al. 1997, Spoor & van Leeuwen 1992, Grood et al. 1984, Maganaris 2004, Fath et al. 2010, Németh & Ohlsén 1985, Dostal et al. 1986, Delp et al. 1999, Arnold et al. 2000). Moment arms were computed over the full range of motion for every joint and degree of freedom of interest with the OpenSim Analyse tool. The moment arm of a muscle was calculated as the average of all its muscle actuators' moment arms. Overall, moment arms were in agreement with reported values. At the hip joint, moment arms of the gluteus muscles are within the range reported by Blemker & Delp (2005) and Delp et al. (1999), and follow the trends reported by Németh & Ohlsén (1985) and Dostal et al. (1986). Only the gluteus medius is slightly outside the reported range for hip adduction (Figure 5.22). Moment arms of psoas, semitendinous and semimembranous also follow the trends reported by Arnold et al. (2000) (Figure 5.23). Moment arms of the main knee flexors and extensors are in agreement with experimental data reported by Grood et al. (1984), Spoor & van Leeuwen (1992) and Buford et al. (1997), apart from the biceps femoris and gracilis (Figure 5.24). At the ankle joint, model moment arms for tibialis anterior, gastrocnemius and soleus are

smaller than the experimental data from Maganaris (2004), Fath et al. (2010) and Spoor & van Leeuwen (1992) (Figure 5.25).

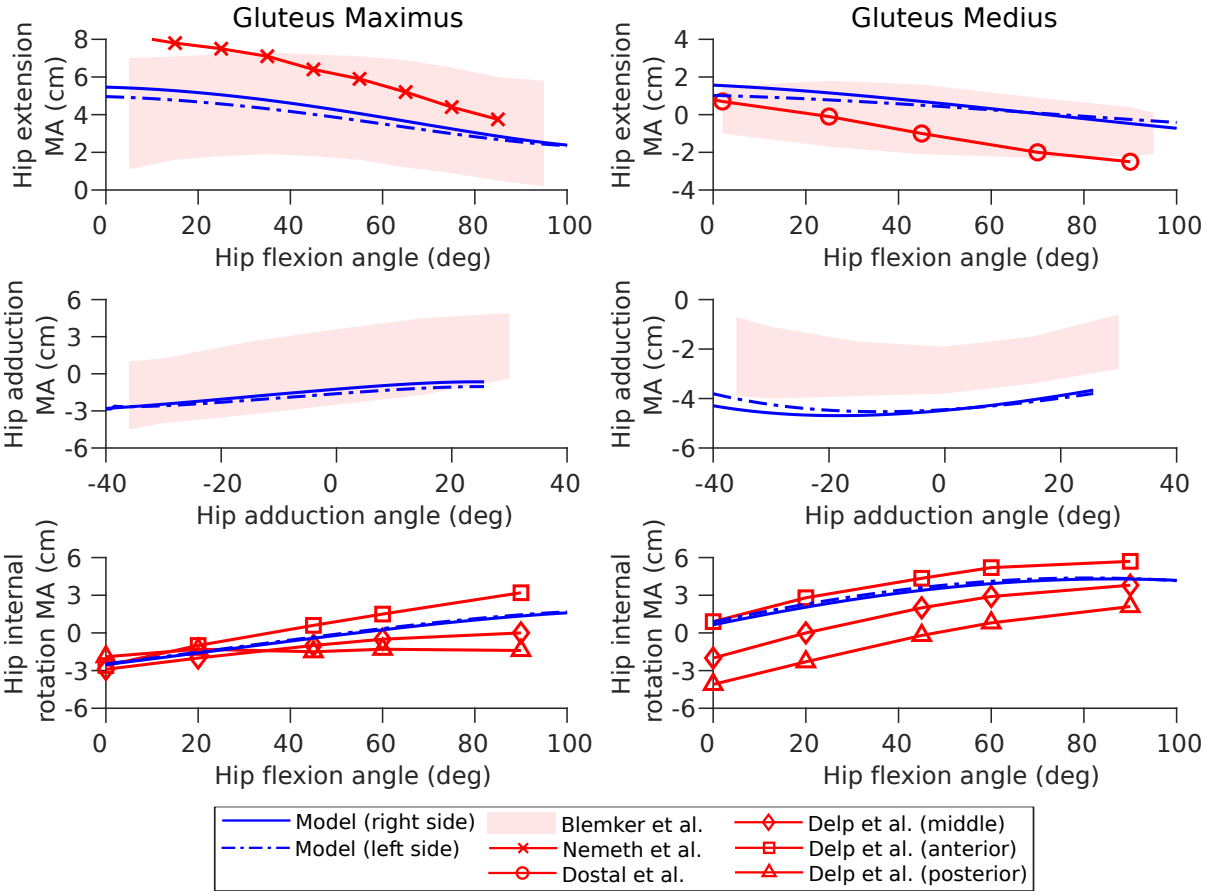

Figure 5.22: Model moment arms at the hip joint for the gluteus maximus and gluteus medius compared to experimental data reported by Blemker & Delp (2005), Németh & Ohlsén (1985), Dostal et al. (1986) and Delp et al. (1999). The first row shows the hip extension moment arm as a function of hip flexion. The second row shows the hip adduction moment arm as a function of hip adduction. The third row shows the hip internal rotation moment arm as a function of hip flexion.

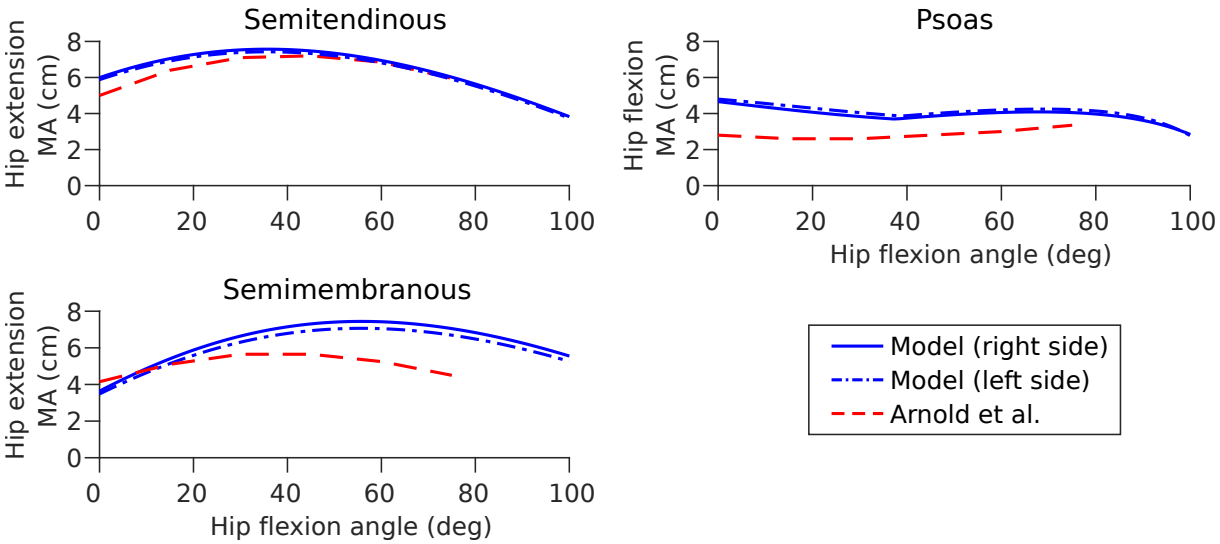

Figure 5.23: Model moment arms at the hip joint for the psoas, semitendinous and semimembranous compared to experimental data reported by Arnold et al. (2000). The first row shows the hip flexion moment arm of the psoas as a function of hip flexion. The second and third rows show the hip extension moment arms of the semitendinous and semimembranous as function of hip flexion respectively.

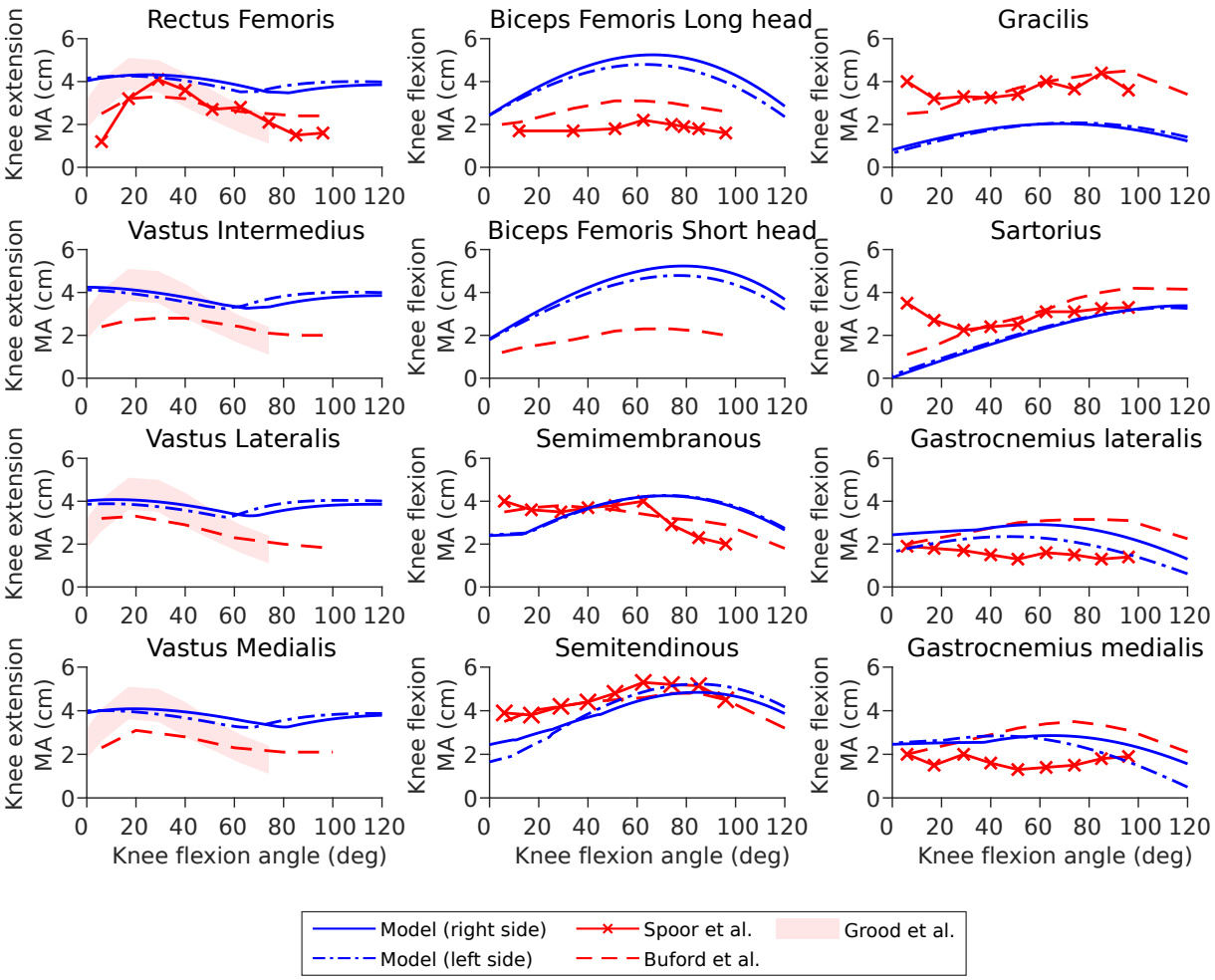

Figure 5.24: Model moment arms at the knee joint for the main flexors and extensors compared to experimental data reported by Grood et al. (1984), Spoor & van Leeuwen (1992) and Buford et al. (1997). The first column shows the knee extension moment arm of the rectus femoris and vastii as a function of knee flexion. The second and third columns show the knee flexion moment arms of the biceps femoris, semimembranous, semitendinous, gracilis, sartorius and gastrocnemius as a function of knee flexion.

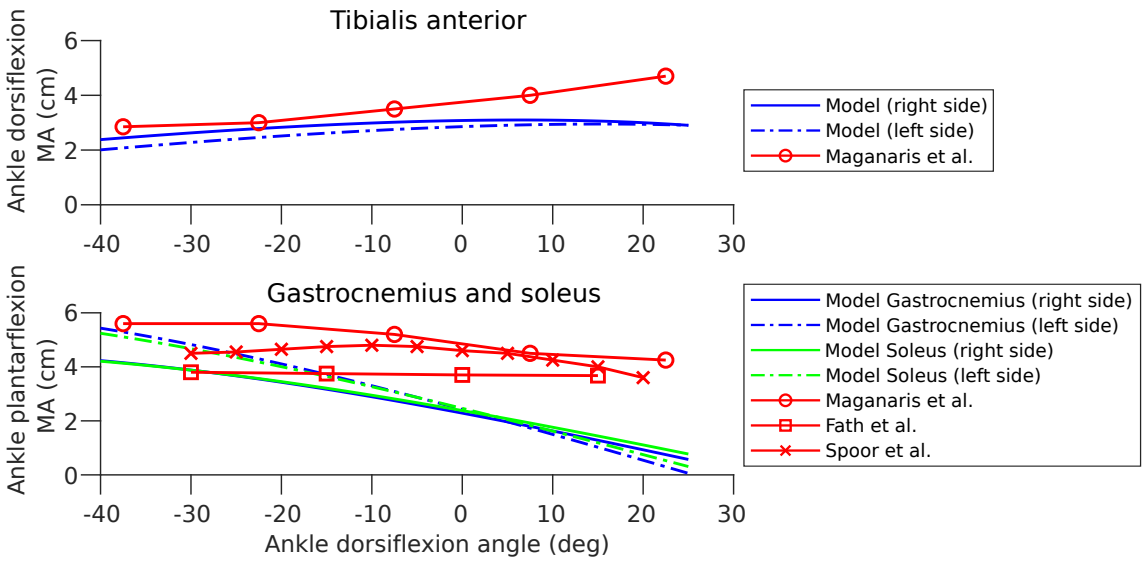

Figure 5.25: Model moment arms at the ankle joint for the main flexors and extensors compared to experimental data reported by Maganaris (2004), Spoor & van Leeuwen (1992) and Fath et al. (2010). The first row shows the ankle dorsiflexion moment arm of the tibialis anterior as function of ankle dorsiflexion. The second row shows the ankle plantarflexion moment arm of the gastrocnemius and the soleus as a function of ankle dorsiflexion.

Few studies have investigated the lumbar muscle moment arms in other positions of the spine than upright standing. Jorgensen et al. (2003) reported moment arms of the erector spinae muscle group at all lumbar levels from MRI images taken in flexed positions of the spine. The musculoskeletal model is in agreement at L1-L2 and L2-L3 joints, but differs from the reported value at the other three lumbar levels (Figure 5.26). Jorgensen et al. (2003) measured the flexion moment arms as the shortest distance between the centroid of the erector spinae and the centroid of the intervertebral disc in a plane through and parallel to the disc. In the model, moment arms are calculated as the distance between the musculotendon actuator line of action and the joint center. This difference in measurement techniques explains the discrepancy in moment arms at the three lower lumbar joints (Figure 5.27).

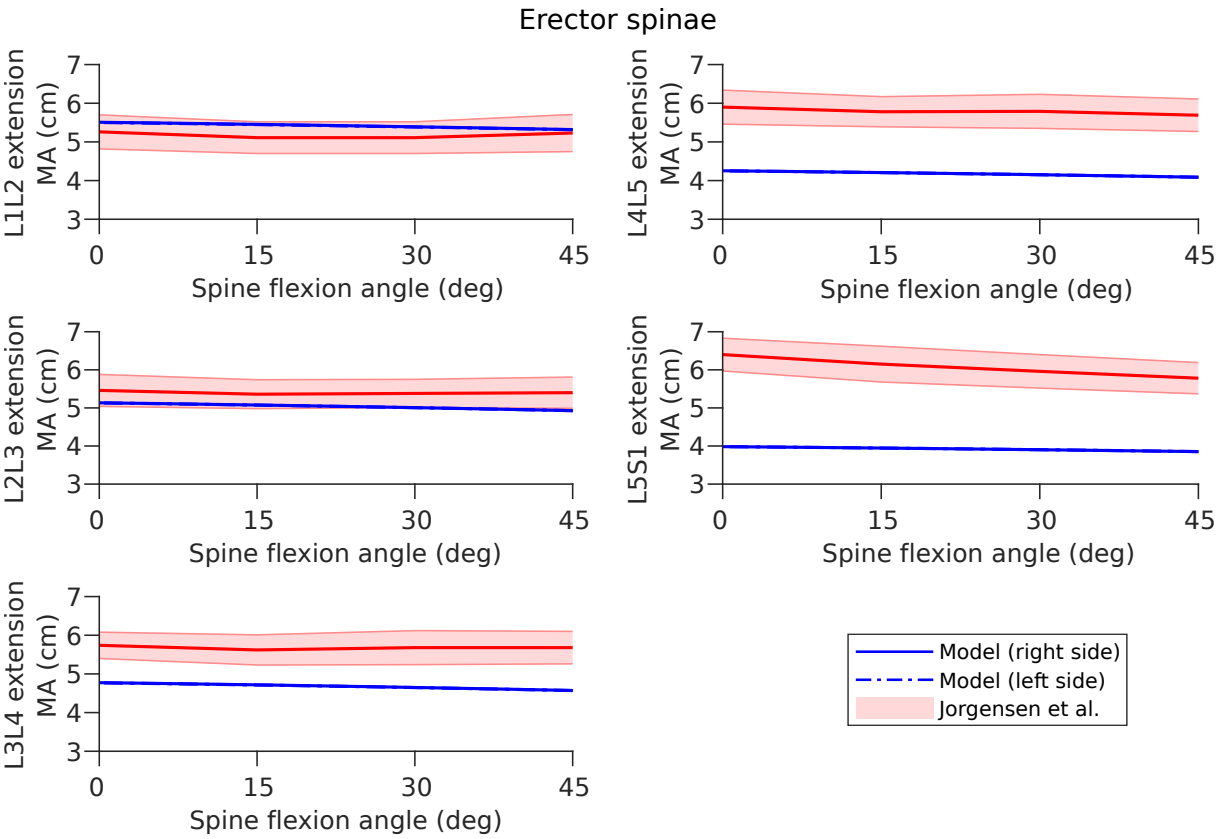

Figure 5.26: Model moment arms at the lumbar joints for the erector spinae compared to experimental data reported by Jorgensen et al. (2003). The shaded area is one standard deviation. At each lumbar level, the extension moment arms are shown as a function of spine flexion.

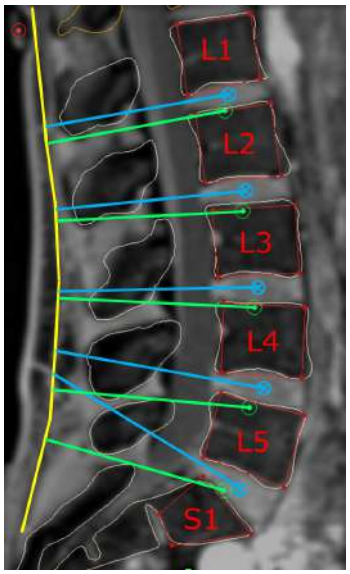

Figure 5.27: Different measurement techniques for the erector spinae moment arms. The erector spinae line of action is in yellow and the vertebrae are in red. The green lines and circled dots are the model moment arms and joint centers respectively. The blue lines and circled crosses are the moment arms and joint centres as they would be measured with the technique from Jorgensen et al. (2003) respectively.

5.2.1.2 Maximum isometric moments

Maximum isometric moments in the lumbar spine region were checked after the increase of maximum muscle stress to ensure they are physiologically possible. They were calculated using the OpenSim analysis tool for a forward flexion of the spine. Maximum isometric moments of the model vary between 175 Nm and 310 Nm (Figure 5.28) for an overall spine flexion of 0° to 65°, which is within the range of 171-480 Nm reported by Hansen et al. (2006).

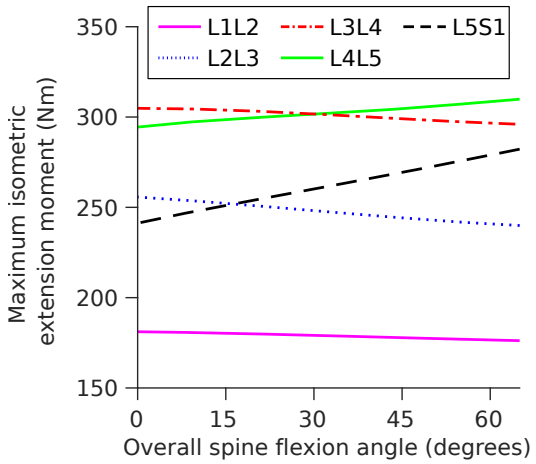

Figure 5.28: Maximum isometric extension moments at each lumbar level as a function of overall spine flexion.

5.2.2 Assessment against literature

Using the simulation pipeline described in Chapter 2, Section 2.4.2, joint reaction forces were estimated at all lumbar levels for various activities. Static positions involving simple movements of the spine are shown here: upright standing, forward flexion at 30°, maximal flexion with finger tips to toes, extension at 15°, lateral bending on both sides at 20°, axial rotation on both sides at 15°, sitting upright and sitting flexed forward. The subject moved very slowly at a constant pace in flexion, extension, lateral bending and axial rotation on both sides. Based on angles obtained after the inverse kinematics step, the frames corresponding as close as possible to the static positions of interest were selected. Joint reaction forces calculated for these specific frames are presented in this Section.

Figure 5.29 shows the total joint reaction force at each lumbar level for these static positions. As expected, the total reaction force is higher in the lower lumbar levels. The joint reaction force estimated with the model follows the same trend for all lumbar levels. Compared to upright standing, the joint reaction force largely increases for flexed and extended positions, while it only increases slightly for lateral bending positions. Axial rotation positions do not influence significantly the joint reaction force compared to upright standing. Upright sitting appears to increase slightly the joint reaction force compared to upright standing, potentially due to a different pelvic tilt angle when seating.

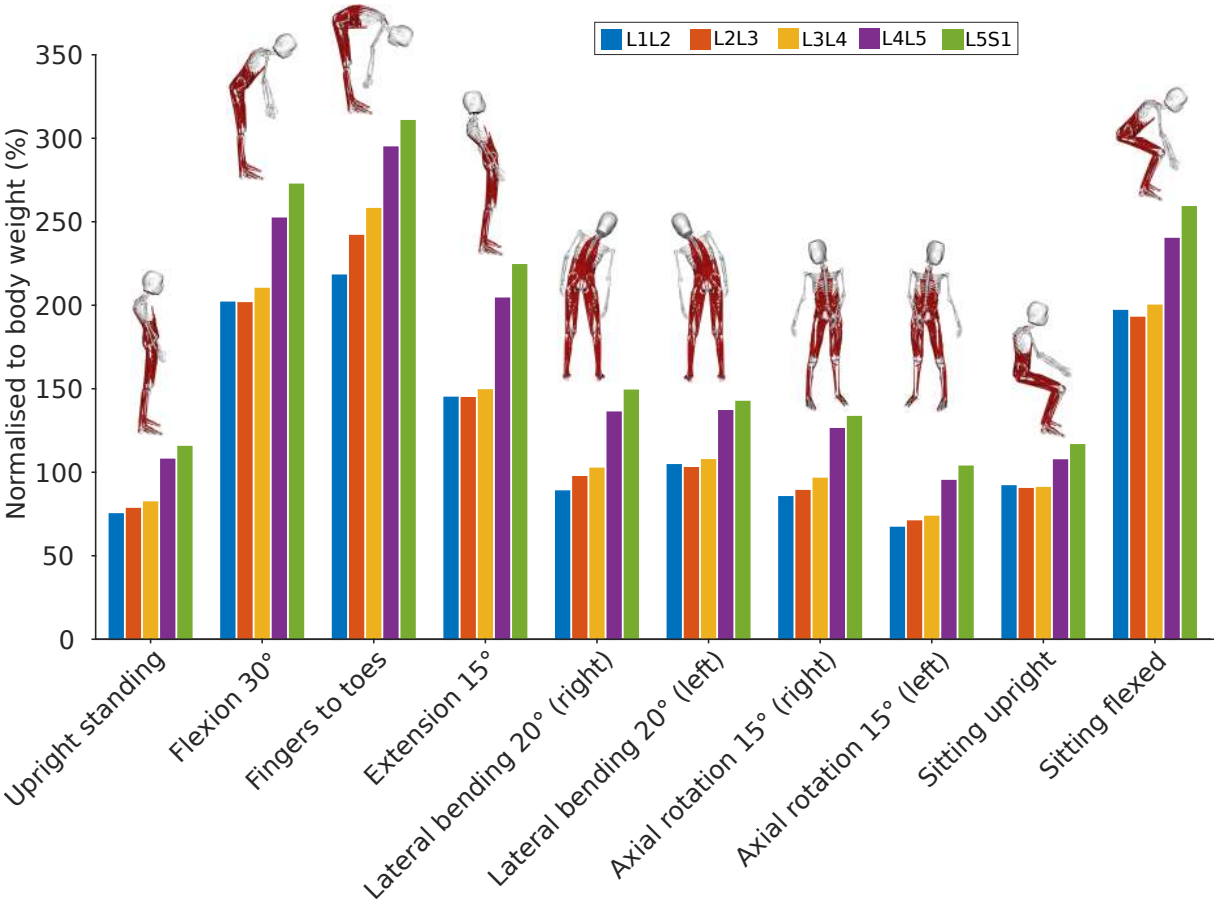

Figure 5.29: Total joint reaction force normalised to body weight at each lumbar level for static positions of the spine.

Figure 5.30 shows the decomposition of the total reaction force on the X, Y and Z axes of the vertebra coordinate systems defined on Figure 5.8. The Y component of the reaction force shows a trend similar to the total reaction force for most positions at all lumbar levels except L5-S1. At this level, the contribution of the X component

is significant for all positions due to the orientation of L5 (Figure 5.8). For positions involving little movement of the spine in the sagittal plane, the X component of the reaction force is positive at L1-L2 and L2-L3 levels and negative for the three other lumbar levels. This is due to the orientation of the vertebrae following the lumbar curvature in an upright position (Figure 5.8). For larger movements in the sagittal plane, especially spine flexion, the orientation of the vertebrae changes, and the X component of the reaction force changes sign at L1-L2 and L2-L3 levels. The contribution of the Z component in sagittally symmetric positions is minimal but not zero. For lateral bending positions, the Z component of the reaction force is higher on the right than on the left side. This potentially indicate a minor asymmetry in the subject's spine, but could also be related to a side preference from the subject, or a discrepancy in the calibration of the forceplates.

The model was assessed by comparing these estimated joint reaction forces to experimental measurements from the literature at different lumbar levels (Nachemson 1965, Schultz et al. 1982, Sato et al. 1999, Wilke et al. 1999, Wilke et al. 2001, Takahashi et al. 2006, Rohlmann et al. 2008). These experimental measurements come from different subjects of varying age, size, and mass. Absolute comparison is not possible and a relative comparison approach was chosen. For each activity, the Y component of the reaction force corresponding to the axial compression force and the data from the literature were normalised to the corresponding values in the upright standing position.

5.2.2.1 L4-L5 level

At L4-L5 level, the comparison was made with disc pressure measured in-vivo in healthy volunteers by Nachemson (1965), Wilke et al. (1999, 2001), Sato et al. (1999) and Takahashi et al. (2006). Since few in-vivo measurements are available for comparison, size, body weight and age were not considered as an exclusion criteria and all healthy male subjects from these studies were included in the comparison. Nachemson (1965) studied eight male subjects. A pressure transducer embedded in a needle was inserted dorsolaterally into the nucleus pulposus of the L4-L5 intervertebral disc and localised with a roentgen image intensifier apparatus. The needle had to be held perpendicularly to the back of the subject during the movement. The subject was instructed to flex forward from the hips, keeping the back straight. A forward flexion of 10° was measured with a protractor.

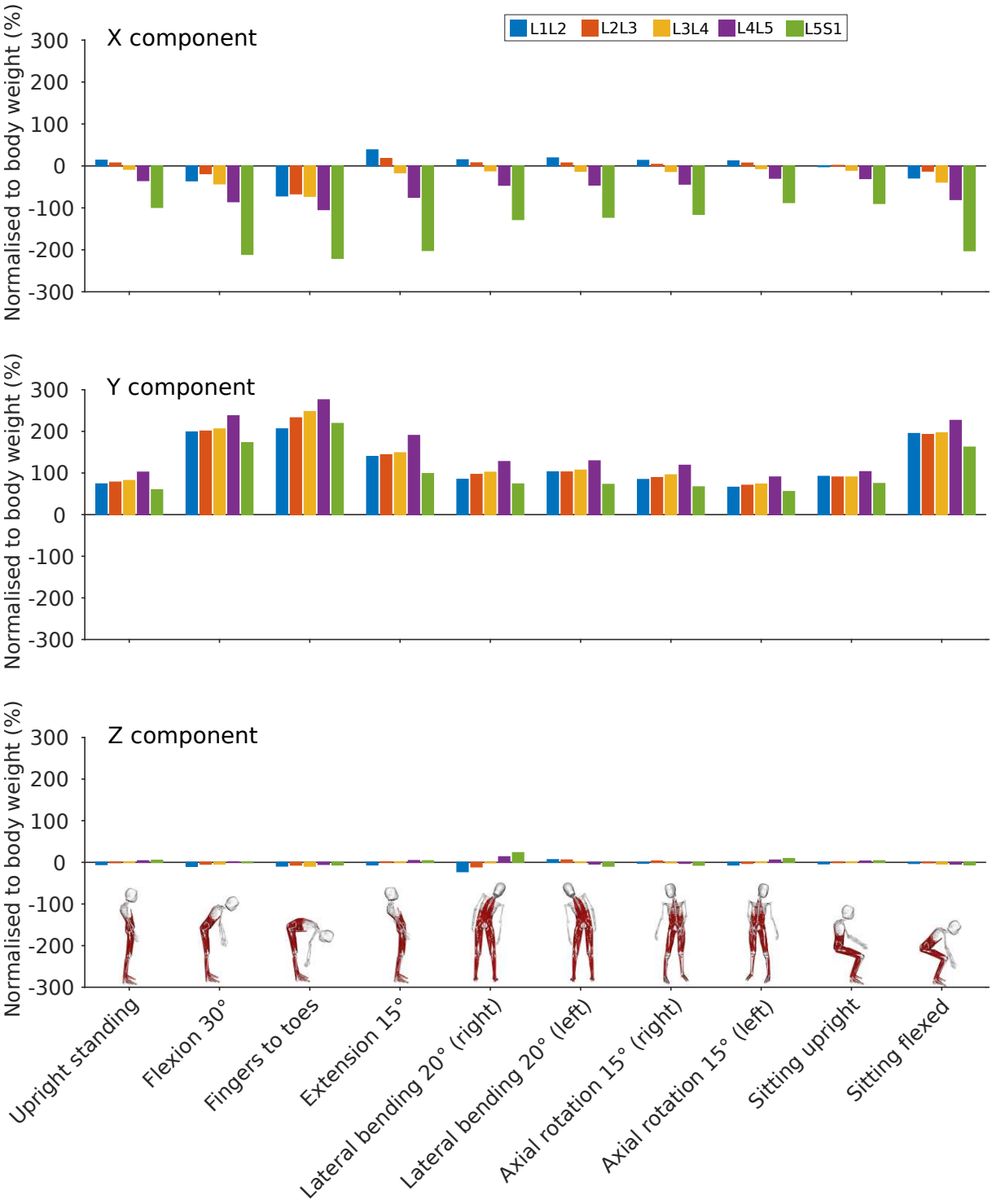

Figure 5.30: X, Y and Z components of the joint reaction force normalised to body weight at each lumbar level for static positions of the spine. Forces are expressed in the vertebra coordinate systems.

Disc pressures were recorded in the upright and flexed positions. Although this method is not the most accurate and does not involve movements of the spine, it is one of the first in-vivo disc pressure measurements available in the literature and is worth including in the comparison. Among the eight subjects, only patient number 8 (male, 43 yo, 74 kg, 176 cm) was relevant for the comparison. Wilke et al. (1999, 2001) measured the pressure in the L4-L5 intervertebral disc of one healthy volunteer (male, 45 yo, 70kg, 168 cm) for a large range of activities including the basic spine movements of interest for this comparison. They inserted a pressure transducer with a dorsolateral transforaminal approach into the nucleus pulposus and checked the location of the needle with radiographs. The needle was held in position with a special belt. Spine movements where quantified with a motion analysis system measuring the angle between S1 and T12 vertebrae. Sato et al. (1999) investigated the L4-L5 intradiscal pressure during flexion and extension of the spine from standing and sitting postitions in 8 healthy volunteers and 28 patients with low back pain and sciatica. Only the healthy volunteers (average 25 yo, 73 kg, 174 cm) were included for the comparison here. Sato et al. (1999) used a pressure sensor in a percutaneous needle guided with fluoroscopy to the center of the nucleus pulposus. They also used the radiograms during spine movement to measure the angle between adjacent vertebrae. Takahashi et al. (2006) also inserted a needle with a pressure sensor in the nucleus pulposus of the L4-L5 disc of three healthy male volunteers (average 25 yo, 72 kg, 176 cm), guided with fluoroscopy. They investigated forward flexion of the spine with and without external weight in the volunteers hands, and measured the angle between S1 and L5 vertebrae with a magnetic 3D motion analysis system.

Dreischarf et al. (2013) showed that intradiscal pressure and lumbar compressive force follow a linear relationship. Normalised intervertebral joint reaction forces estimated with the model at L4-L5 level can therefore be compared directly to the reported normalised in-vivo disc pressures measured by Nachemson (1965), Wilke et al. (1999, 2001), Sato et al. (1999) and Takahashi et al. (2006) (Figure 5.31). It is important to note that in-vivo measurements were recorded with a needle between 1.2 mm and 1.5 mm in diameter inserted in the nucleus pulposus of the L4-L5 intervertebral disc in these studies. Although they reported special care was taken when inserting the needle and throughout the experiment, it can still induce discomfort to the subject when performing spine movements and alter the kinematics.

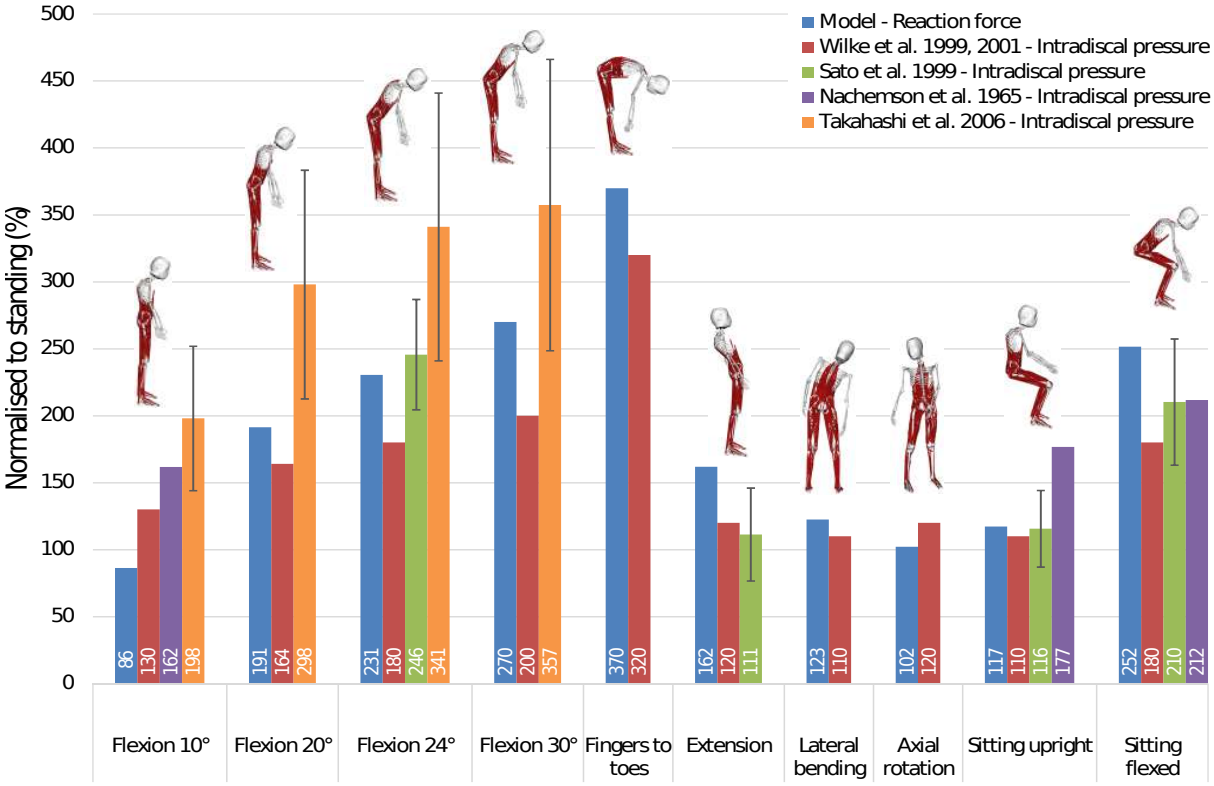

Figure 5.31: Comparison between in-vivo intradiscal pressure (Wilke et al. 1999, Wilke et al. 2001, Sato et al. 1999, Nachemson 1965, Takahashi et al. 2006) and the Y component of the joint reaction force in the model at L4-L5 level, all normalised to upright standing. Error bars are one standard deviation for studies with more than one subject. Extension is at 15°, lateral bending at 20° and axial rotation at 15°. Normalised value (%) is indicated in white in each bar.

The model shows agreement with the pressures reported by Sato et al. (1999) and Wilke et al. (1999, 2001), with average differences of 18.2% and 23.6% respectively across all the positions considered here. Differences with values reported by Takahashi et al. (2006) are higher, with the model predicting a lower joint reaction force by 37.2% on average for the four poses with the spine flexed forward.

5.2.2.2 L3-L4 level

Schultz et al. (1982) validated a biomechanical analysis to predict loads in the L3 vertebra using intradiscal pressures and myoelectric signals. Their study includes four volunteers (average 21.8 yo, 62.8 kg, 174 cm). Intradiscal pressure was measured with a pressure transducer built into the tip of a needle inserted in the nucleus pulposus of the L3-L4

intervertebral disc. With the recorded muscle activations, they predicted the compressive load acting on L3 vertebra for different activities in a standing and a sitting position. These activities consisted mainly of resisting horizontal forces applied to the chest via a harness and a set of pulleys, without any movement of the spine. Despite previous spine models (Han et al. 2012) having used these results for validation in different positions of the spine, it was considered inappropriate to compare compression loads obtained with a straight spine resisting external forces with reaction forces estimated for a curved spine only resisting its own weight. Still, the study of Schultz et al. (1982) provides three measurements that can be used for the comparison. Disc pressure was measured for standing upright and sitting upright without external forces applied. It was also measured for a 30° forward flexion at the hips with a straight back, with arms slightly stretched out. To an extent, this position is comparable to a 30° flexion of the spine, and is included in the comparison.

Comparison is made between intervertebral joint reaction forces estimated with the model at L3-L4 level normalised to upright standing and the reported in-vivo disc pressures also normalised to upright standing, based on the same assumption used for the L4-L5 level comparison (Dreischarf et al. 2013) (Figure 5.32).

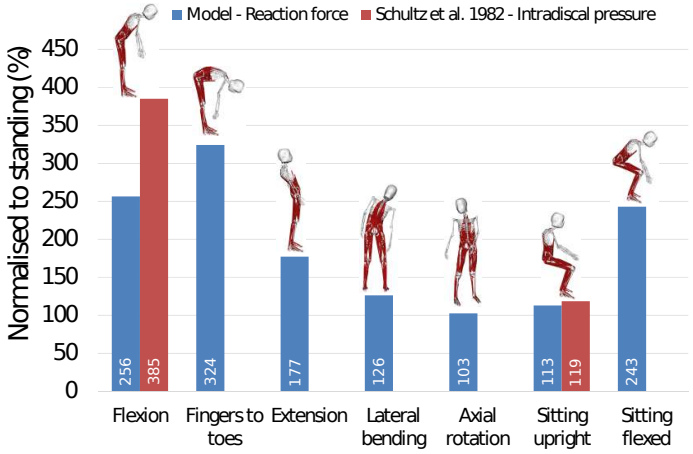

Figure 5.32: Comparison between predicted compression force from Schultz et al. (1982) and the Y component of the joint reaction force in the model at L2-L3 level, all normalised to upright standing. Flexion is at 30°, extension at 15°, lateral bending at 20° and axial rotation at 15°. Normalised value (%) is indicated in white in each bar.

The model predicts a lower joint reaction force by 33% for forward flexion at 30°. This was expected as the positions of the spine are not completely identical. In the model, the spine is flexed forward by 30° while in the in-vivo study by Schultz et al. (1982), the subject flexes the hips by 30° maintaining a straight back which implies a higher contraction of the erector spinae and therefore a higher intervertebral reaction force. Lumbar muscle will also contract more due to the outstretched arms, producing higher compression forces in the spine. For the sitting upright position, there is less than 5% difference between the model estimate and the in-vivo measurement. Other spine positions were not reported by Schultz et al. However, reaction force estimations from the model for these activities follow a pattern similar to the other lumbar levels.

5.2.2.3 L1-L2 level

At L1-L2 level, the comparison was made with forces in an instrumented vertebral body replacement (VBR) implant inserted by Rohlmann et al. (2008). These implants were used in two male patients with a fractured L1 vertebral body (average 66.5 yo, 70 kg, 168.5 cm). The vertebral body of L1 was removed, along with the adjacent discs and parts of the cranial endplate of L2. The VBR was then connected the caudal endplate of T12 with the vertebral body of L2. Interspinal fixators were used to stabilise the spine between T12 and L2. The instrumented implant was able to measure forces and moments acting on the VBR for any movement of the spine. Recorded movements include all basic positions of the spine considered for the evalution of the model (Figure 5.33). For each activity, they recorded a video which allowed an estimation of the overall spine angle needed for the comparison.

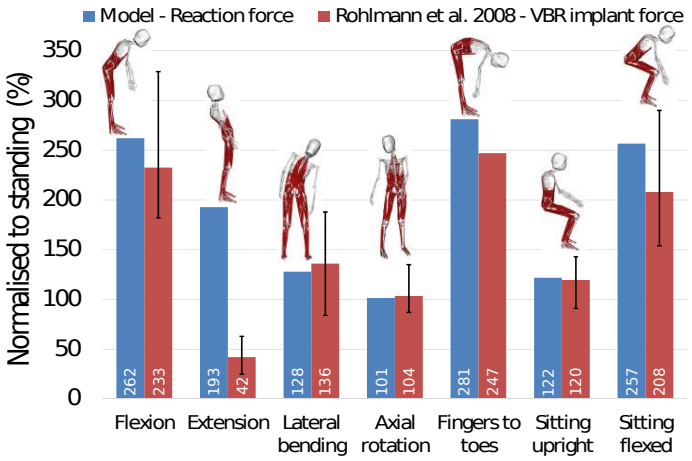

Figure 5.33: Comparison between in-vivo measured forces using the VBR implant (Rohlmann et al. 2008) and the Y component of the joint reaction force in the model at L1-L2 level, all normalised to upright standing. Errors bars represent the range. Flexion is at 30°, extension at 15°, lateral bending at 20° and axial rotation at 15°. Normalised value (%) is indicated in white in each bar.

Reaction forces estimated with the model are within 6% of forces measured by the VBR for lateral bending, axial rotation and sitting upright poses. For positions involving forward flexion of the spine, the difference between the model estimates and the measured forces is below 23%. For spine extension, the force obtained with the model is higher by 359% compared to the measured force. The forces measured by the implant are much smaller than the forces estimated by the model for this position. This is potentially due to the center of rotation of the above vertebrae being shifted posteriorly by the implant (Rohlmann et al. 2000), reducing the load on the vertebral body for this type of movement.

5.2.3 Comparison with recorded sEMG

Results from musculoskeletal simulations were assessed by comparing estimated muscle activations against recorded sEMG for the lumbar muscles. This comparison was done for basic movements of the spine at normal speed: maximum forward flexion from standing upright, forward flexion to reach a box from sitting upright, lifting a 5 kg box from the floor to the chest while standing, lifting a 5 kg box at an angle from the floor to a table while sitting. Using the same method applied for virtual marker placement and described

in Chapter 3, cod liver oil capsules of 1000 mg were used during MRI scanning to locate sEMG electrodes in the model. For each electrode, musculotendon actuators located directly below the 30 mm by 44 mm electrode area were selected, and the average of their activations used for the comparison. Model activations were low-pass filtered at 10 Hz. Raw sEMG signals were demeaned, high-pass filtered at 30 Hz with a zero-phase fourth order Butterworth filter and rectified. Rectified signals were low-pass filtered at 10 Hz (Arnold et al. 2013, Klemt et al. 2019). Both model activations and sEMG signals were normalised to the peak filtered value for each trial. Agreement between the model predictions and the in-vivo measurements was quantified by the percentage of the trial where both normalised signals are either below or above a 50% threshold at the same time, following the same method than Actis et al. (2018).

On average, model activations and sEMG measurements of the erector spinae muscles are in agreement during 84.6% of the trial for forward flexion from a standing upright position (Figure 5.34). For forward flexion from a sitting upright position, the agreement reaches 82.9% on average (Figure 5.35). For lifting tasks, the model compares well with the EMG recordings for the standing lifting task where the spine doesn't twist (Figure 5.36) with an average agreement of 80.7%. The agreement is lower for lifting tasks combining lateral bending and axial rotation of the spine. There is an average agreement of 74.4% and 53.9% for the 90° floor to table sitting lifting task (Figure 5.37) and the 180° floor to floor standing lifting task (Figure 5.38) respectively. In this last lifting task, the left and right longissimus are below 50% agreement. This is potentially due to the skin-mounted EMG electrodes moving away from the selected muscle bundles for extreme positions of the spine, allowing a high level of crosstalk.

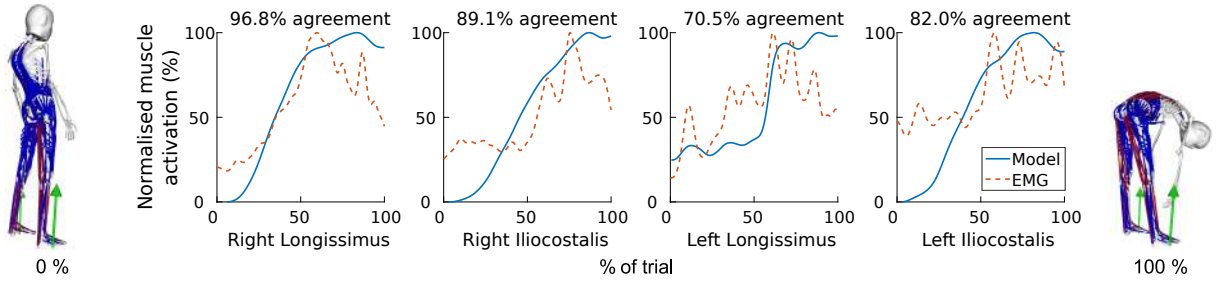

Figure 5.34: Model activation and sEMG activation for the right and left longissimus and iliocostalis during a forward flexion of the spine from a standing upward position. Activations are normalised to the maximum activation over the trial. Agreement between model activations and sEMG measurements is the percentage of the trial where both signals are either above or below a 50% activation threshold at the same time. It is shown above each plot.

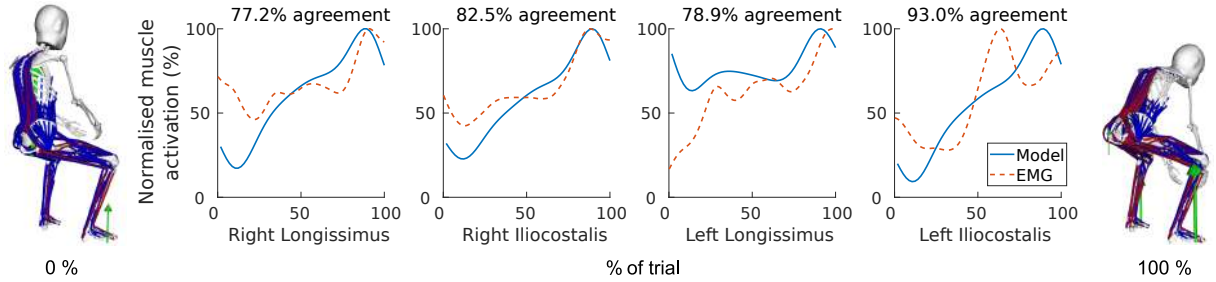

Figure 5.35: Model activation and sEMG activation for the right and left longissimus and iliocostalis during a forward flexion of the spine from a sitting upward position. Activations are normalised to the maximum activation over the trial. Agreement between model activations and sEMG measurements is the percentage of the trial where both signals are either above or below a 50% activation threshold at the same time. It is shown above each plot.

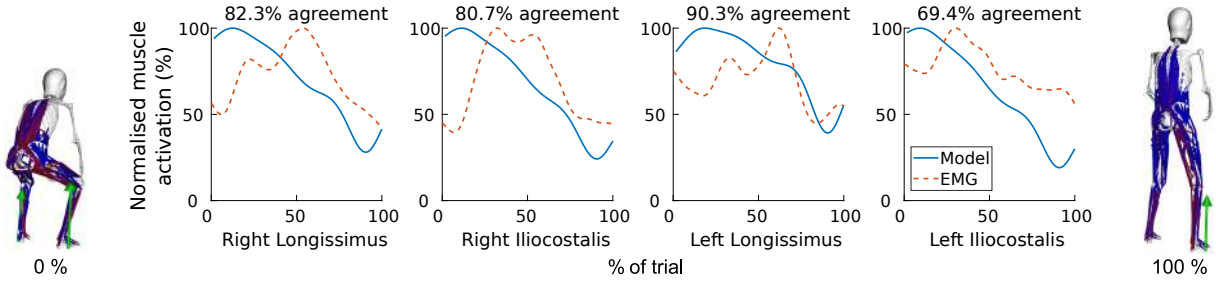

Figure 5.36: Model activation and sEMG activation for the right and left longissimus and iliocostalis during a lifting task while standing. The task consists in lifting from the floor a 5 kg box located in front of the subject's feet and bringing it to the chest. Activations are normalised to the maximum activation over the trial. Agreement between model activations and sEMG measurements is the percentage of the trial where both signals are either above or below a 50% activation threshold at the same time. It is shown above each plot.

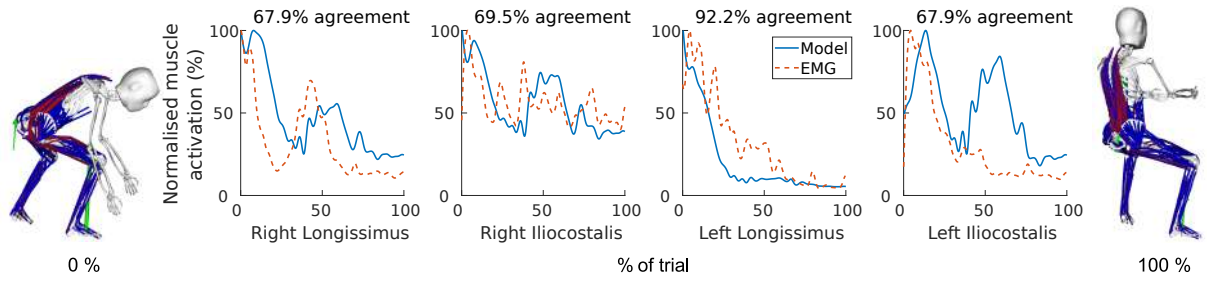

Figure 5.37: Model activation and sEMG activation for the right and left longissimus and iliocostalis during a lifting task while sitting. The task consists in lifting from the floor a 5 kg box located to the right of the subject and putting it on a table located directly in front. Activations are normalised to the maximum activation over the trial. Agreement between model activations and sEMG measurements is the percentage of the trial where both signals are either above or below a 50% activation threshold at the same time. It is shown above each plot.

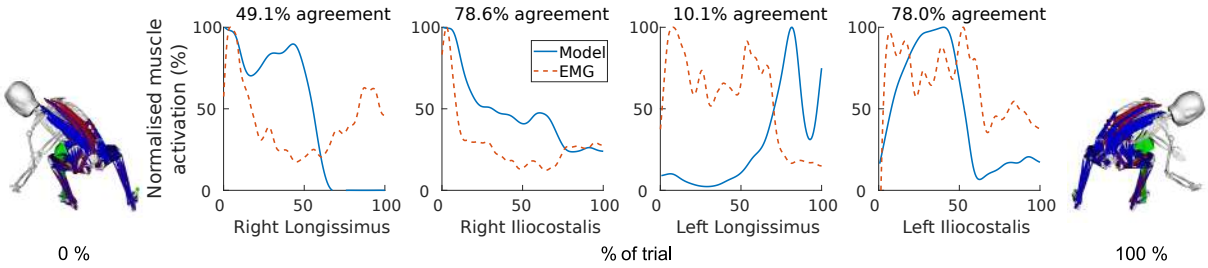

Figure 5.38: Model activation and sEMG activation for the right and left longissimus and iliocostalis during a lifting task while standing. The task consists in displacing a 5 kg box from the left to the right of the subject. Activations are normalised to the maximum activation over the trial. Agreement between model activations and sEMG measurements is the percentage of the trial where both signals are either above or below a 50% activation threshold at the same time. It is shown above each plot.

Reserve actuators are used at every joint to account for muscles not represented in the model. In the lumbar region where the musculature is very detailed in the model, the moments provided by these reserve actuators remain close to zero for all the aforementioned activities (Table 5.3). For the first four activities, reserve actuator moments remain below 1 Nm. When displacing a 5 kg box from the left to the right while standing, some reserve actuators for lateral bending and axial rotation are between 1 and 2.3 Nm at lumbar levels L1-L2, L2-L3 and L4-L5. Higher reserve actuator moments are observed for this last activity due to its larger range of motion involving core muscles such as the obliques and the quadratus lumborum. Implementation of intra abdominal pressure in the model could help reducing the activation of reserve actuators for such activities.

Table 5.3: Maximum absolute moment of the flexion extension (F-E), lateral bending (LB) and axial rotation (AR) reserve actuators at the lumbar joints for the activities shown previously. Task 1: forward flexion of the spine from a standing upward position. Task 2: forward flexion of the spine from a sitting upward position. Task 3: lifting from the floor a 5 kg box located in front of the subject's feet and bringing it to the chest while standing. Task 4: lifting from the floor a 5 kg box located to the right of the subject and putting it on a table located directly in front while sitting. Task 5: displacing a 5 kg box from the left to the right of the subject while standing.

Maximum reserve actuator absolute moment (Nm)

	Task 1			**Task 2**			**Task 3**			**Task 4**			**Task 5**		
	F-E	**LB**	**AR**	**F-E**	**LB**	**AR**	**F-E**	**LB**	**AR**	**F-E**	**LB**	**AR**	**F-E**	**LB**	**AR**
L1-L2	0.104	0.064	0.102	0.130	0.052	0.131	0.187	0.074	0.094	0.242	0.230	0.180	0.292	0.804	2.209
L2-L3	0.080	0.046	0.039	0.049	0.042	0.019	0.079	0.072	0.101	0.085	0.153	0.101	0.176	1.480	0.267
L3-L4	0.066	0.030	0.074	0.054	0.020	0.080	0.055	0.016	0.051	0.108	0.061	0.112	0.147	0.799	0.978
L4-L5	0.065	0.033	0.048	0.117	0.020	0.058	0.099	0.037	0.058	0.091	0.105	0.148	0.327	1.314	1.514
L5-S1	0.128	0.010	0.064	0.204	0.006	0.066	0.161	0.012	0.031	0.218	0.034	0.109	0.197	0.036	0.125

5.3 Discussion

The musculoskeletal model presented in this Chapter was developed to provide physiological loading conditions for finite element models of the lumbar vertebrae. It is based on full body MRI scans of a healthy volunteer and includes a detailed representation of the muscles of the lumbar spine and the lower limbs. Geometrical and inertial musculoskeletal parameters were derived from the MRI scans while muscle physiological parameters were scaled from generic models. Consistency between modelling choices and parameters adapted from in-vivo studies was ensured. The model was assessed for static positions and dynamic movements involving spine flexion, extension, lateral bending and axial rotation, and gives satisfying results regarding lumbar joint reaction forces and muscle activations.

The assessment of the model against in-vivo data reported in the literature was conclusive for the static positions of the spine of interest. However, the data reported in the literature can be influenced by numerous factors and can only be used to assess a general trend in the results. An important factor which cannot be neglected when using in-vivo data from other studies for validation is inter-subject variability. This variability seems to be present in the lumbar spine, particularly for spine kinematics and lumbar lordosis. Focusing on some of the available data for L4-L5 intradiscal pressure (Sato et al. 1999, Wilke et al. 1999, Wilke et al. 2001, Takahashi et al. 2006), a few observations can be made. All these studies measured intradiscal pressure for upright standing and forward flexion of the spine at 24° and data is available for a total of twelve subjects. Characteristics of these subjects are summarised in Table 5.4.

Among the subjects, the reported disc pressures vary between 215 and 747 kPa in an upright standing position, and between 684 and 1502 kPa whilst flexed at 24°. However, the variation in intradiscal pressure between upright standing and forward flexion is different for each subject. Percentage of muscle mass and level of fitness could influence intradiscal pressure during dynamics activities. For the static positions reported here, it could be hypothesised that the pressure variability among the subjects is related to their body mass or to the area of their intervertebral disc since pressure is a measure of a force per area unit. Figure 5.39 (A) shows the intradiscal pressure measured in standing and flexed positions as a function of the disc area for the twelve subjects from the three

Table 5.4: Age, height, body mass and disc area of the twelve subjects selected from the studies by Sato et al. (1999), Wilke et al. (1999, 2001), Takahashi et al. (2006).

	Subject number	**Age**	**Height** (cm)	**Body mass** (kg)	**Disc area** (cm^2)
Sato et al. 1999	1	26	168	72	16.9
	2	24	168	74	14.2
	3	22	181	65	14.6
	4	24	181	94	13.4
	5	23	177	66	15.4
	6	24	166	60	16.0
	7	24	172	66	17.4
	8	29	174	85	18.9
Wilke et al. 1999,2001	9	45	170	70	18.0
Takahashi et al. 2006	10	24	178	77	17.3
	11	26	170	70	18.8
	12	26	180	70	21.2

studies (Sato et al. 1999, Wilke et al. 1999, Wilke et al. 2001, Takahashi et al. 2006). A correlation between the disc area and the disc pressure can be seen for both positions. However, there is no obvious correlation between the disc area and the relative pressure increase from upright standing to flexed position. This observation is confirmed in Figure 5.39 (C) which shows the intradiscal pressure in the flexed position normalised to the pressure value in upright standing as a function of the disc area. In a similar way, Figure 5.39 (D) shows that there is no correlation between the relative pressure increase from the upright to the flexed position and the body mass. No correlation was found between body mass and disc area among the twelve subjects studied by Sato et al. (1999), Wilke et al. (1999, 2001), Takahashi et al. (2006) (Figure 5.39 (B)).

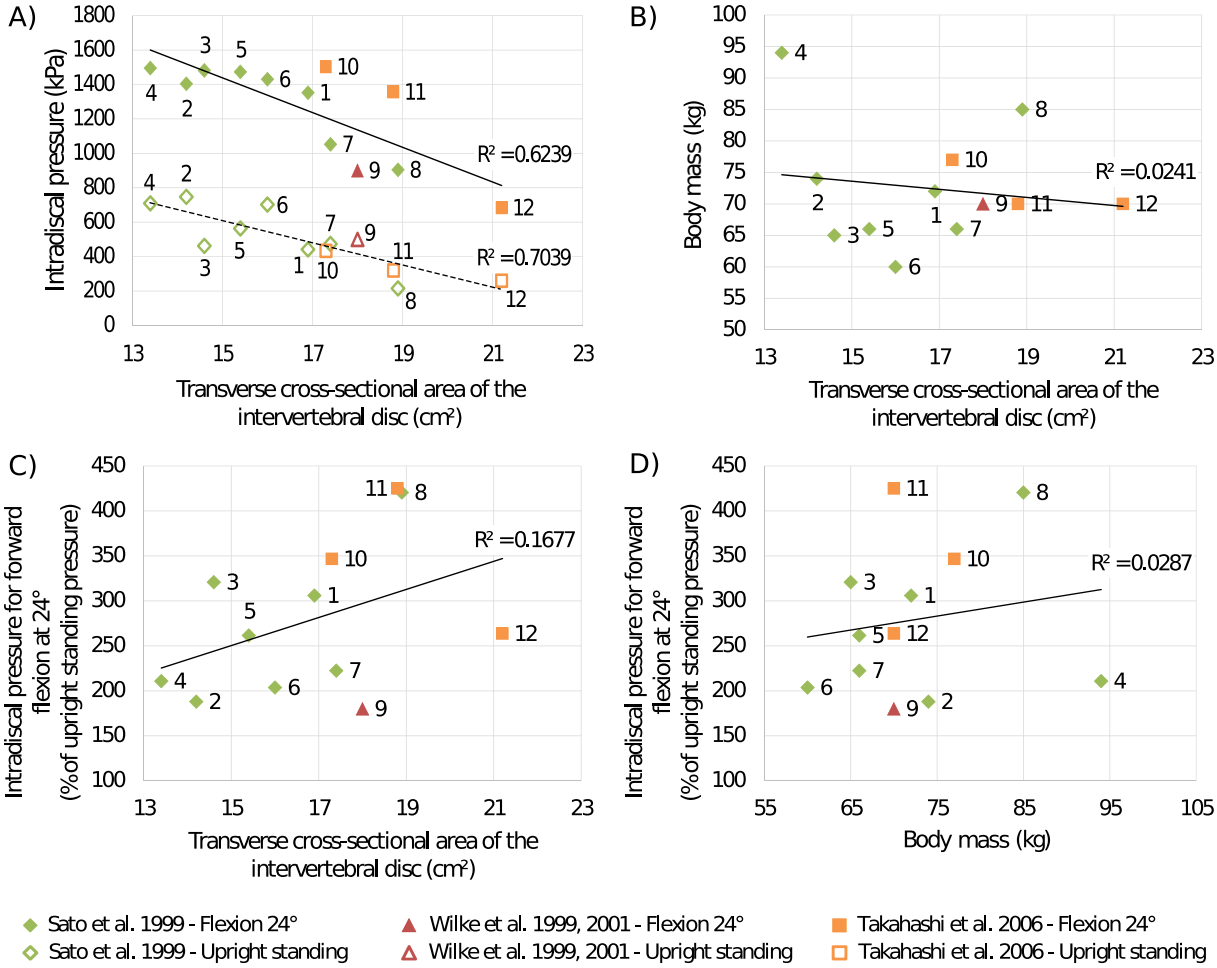

Figure 5.39: Correlation between intradiscal pressure, body mass and transverse cross-sectional area of the intervertebral disc at the L4-L5 level based on the in-vivo measurements from Sato et al. (1999), Wilke et al. (1999, 2001) and Takahashi et al. (2006). Subjects from these three studies are numbered form 1 to 12. The black lines are the linear trendlines with their coefficient of determination. On Figure (A), the filled markers with the plain trendline are for the flexed position and the empty markers with the dashed trendline are for the upright standing.

Since the variability in relative intradiscal pressure increase between subjects is not related to disc size or body mass, it is likely to be correlated with the kinematics of the spine, and more specifically the angle between adjacent vertebrae. This hypothesis is supported by the current model. Focusing on the reaction force calculated during forward flexion of the spine, it appears that a higher reaction force is obtained for upright standing than for the spine flexed at 10°. Looking at the full movement from upright standing to maximum spine flexion, it appears that the smallest reaction force is not obtained for upright standing but for a forward flexion of 9° (Figure 5.40). The subject selected to build the current model has a slight pelvic retroversion which was noted after the study. This

could influence the reaction force in the upright position. It also supports the hypothesis that lumbar curvature and anteroposterior pelvic tilt can influence intervertebral reaction loads. Six heatlhy volunteers were recruited under the current ethics approval, and future work will focus on developing other subject-specific models to look at the variability in the lumbar spine curvature and its influence on spinal loads.

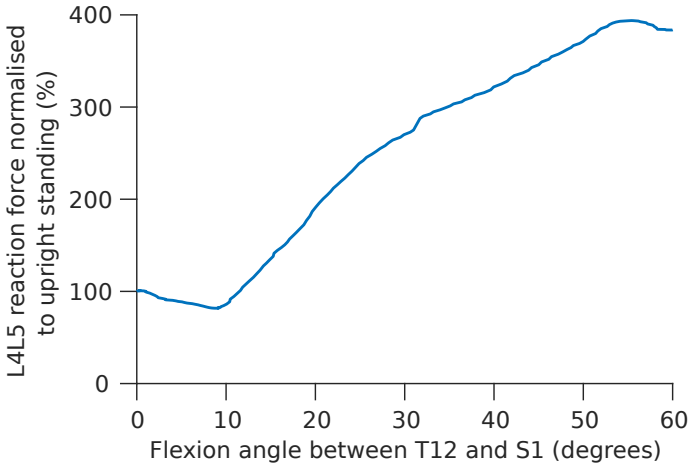

Figure 5.40: Reaction force estimated with the model at the L4-L5 level for a forward flexion of the spine.

The musculoskeletal model was also assessed by comparing calculated muscle activations with EMG measurements recorded in-vivo. General agreement was found between the two signals for the erector spinae muscles. However, some discrepancies can be observed, especially for positions where the spine is upright. In these positions, the model activations drop close to 0% while sEMG measurements never do. This is because the spine is at an equilibrium that can be considered unstable. The center of mass is vertically aligned with the pelvis, and lumbar joint moments calculated with inverse dynamics are close to zero so almost no muscle force is needed to balance the model. In real life, maintaining balance in an upright position requires constant postural adjustment. These small adjustments are controlled by the central nervous system which uses muscle synergies to co-activate agonist and antagonist muscles. Previous work in the Structural Biomechanics group has shown that muscle synergies can be deduced from inverse dynamics simulations (Gopalakrishnan et al. 2014). Muscle synergies can also be deduced from EMG signals (Pizzolato et al. 2015). Implementing these muscle synergies in the model would result in a more realistic muscle activation for movements involving balan-

cing of the spine. The objective function of the static optimisation algorithm currently minimises the sum of muscle activations squared. This objective function is well suited for movements such as walking where effort must be minimised to maximise endurance. However, some movements such as the lifting tasks the central nervous system may choose to maximise accuracy or power. In these cases, the objective function should be adapted to optimise the estimation of muscle activations. Future model developments should aim at implementing synergy methods and new objective functions in the simulation pipeline to improve muscle activation predictions for unstable equilibrium positions of the spine and lifting tasks respectively.

Despite the mentioned limitations, this model estimates muscle and joint reaction forces in the lumbar spine region with sufficient physiological feasibility for the purpose of this project. The forces estimated for the different activities presented in this Chapter, along with other activities of daily living involving the lower limbs mentioned in Chapter 3, will be used as loading conditions for the structural finite element model in the following Chapter.

Chapter 6

Structural finite element modelling of the lumbar vertebrae

This Chapter presents the development of mesoscale structural finite element models of the lumbar vertebrae from the same healthy volunteer (26 yo, 175 cm, 67.8 kg) as the musculoskeletal model described in Chapter 5. The modelling pipeline introduced in Chapter 2 is used to produce models adapted to a 18 activity loading regime representative of daily living.

6.1 Introduction

As mentioned in Chapter 2, Section 2.3, very few finite element models have been developed to study the structure of lumbar vertebrae and their adaptation to the mechanical environment they are subjected to. Macroscale continuum models developed by Homminga et al. (2012) and van Rijsbergen et al. (2018) both predict bone remodelling of the lumbar spine in an altered mechanical environment using a strain energy density driven optimisation of bone material properties. Although this approach allows for the study of bone stiffness adaptation, it does not capture the directionality of trabeculae and the thickness variations in the cortex. Microscale continuum models developed by Tsubota et al. (2003) and Badilatti et al. (2015) are able to capture the remodelling of individual trabeculae in an entire vertebra under a particular loading envelope. However, these detailed models come with limitations in the context of this study. The model developed by Badilatti et al. (2015) is based on high resolution μCT images which cannot be ethically obtained on healthy volunteers. Tsubota et al. (2003) created an axisymmetric model based on a cross-sectional photograph of a vertebral body available in the literature (L 1990). Both studies applied simplified loading on the vertebral bodies of their models, which are still computationally demanding. In this Chapter, the modelling framework presented in Chapter 2, Section 2.3 is applied to the five lumbar vertebrae in a loading scenario representative of daily living. The converged models obtained with the adaptation algorithm are expected to show trabecular and cortical architecture comparable to in-vivo observations made on healthy vertebrae.

6.2 Methods

Structural finite element models were created for each lumbar vertebra following a method developed in the Structural Biomechanics Group at Imperial College London (Phillips 2012, Phillips et al. 2015, Zaharie & Phillips 2018, Zaharie & Phillips 2019). In this Chapter, the method used to create these models is presented for L4 only. While results are only discussed for some lumbar levels in this Chapter, converged models of the five lumbar vertebrae are shown in Appendix C.

6.2.1 Initial structural mesh

The initial structural model of the vertebra was created from the MRI scans of the volunteer. The bone geometry was segmented in Mimics (Mimics Research 19.0, Materialise NV, Leuven, Belgium), reconstructed and exported as an STL file following the method described in Chapter 4. The STL file was then imported in 3-matic (3-matic Research 11.0, Materialise NV, Leuven, Belgium) where the coordinate system of the vertebra was adjusted to match the joint definition of the musculoskeletal model (Chapter 5, Section 5.1). The 3-matic meshing tools were used to create a volumetric mesh of the vertebra composed of 68232 four-noded tetrahedral elements with a 3 mm average edge length. This volumetric mesh was adapted to create a structural mesh using MATLAB (The MathWorks, Inc., USA). Cortical bone was modelled with three-noded linear triangular shell elements defined by the nodes and element faces of the tetrahedral elements located on the external surface of the volumetric mesh. These shell elements were arbitrarily assigned an initial thickness of 0.1 mm. The internal nodes were used to create a network of two-noded truss elements representative of trabecular bone. Each node was linked to its closest sixteen neighbours. These truss elements were arbitrarily assigned an initial radius of 0.1 mm. This minimum nodal connectivity of 16 provides a range of element directionalities sufficient to enable specific trabecular trajectories to develop during bone adaptation (Villette 2016). For L4, the average nodal connectivity was 21.30 (SD 3.69, min 16, max 57). The initial model was composed of 3600 cortical shell elements and 115988 trabecular truss elements. Figure 6.1 shows a 2.5 mm slice of the initial model in

the sagittal plane. All elements were assigned linear isotropic material properties representative of bone material with a Young's modulus of 18.0 GPa and a Poisson's ratio of 0.3 (Turner et al. 1999).

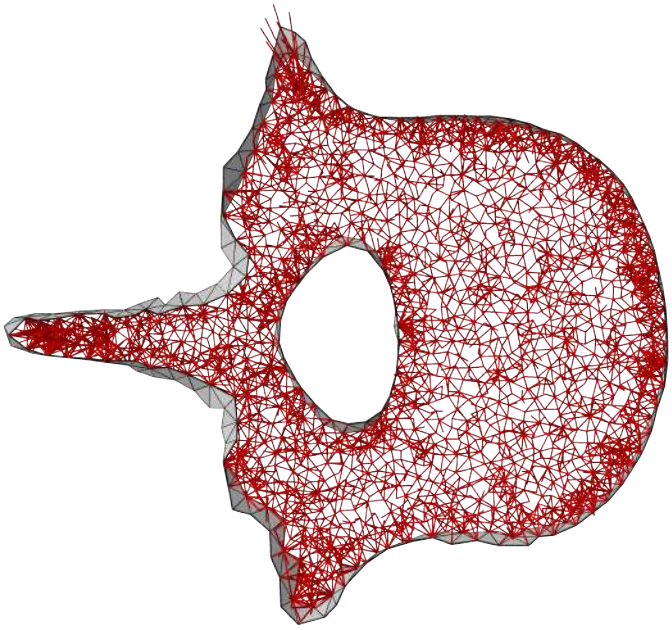

Figure 6.1: 2.5 mm slice of the initial structural finite element model of L4 in the transverse plane. Cortical bone is modelled with shell elements in grey and trabecular bone with truss elements in red.

6.2.2 Loading

Loading conditions include muscle and joint reaction forces estimated with the musculoskeletal model, as well as inertial loads.

6.2.2.1 Loading scenario

In this Chapter, the loading scenario is representative of daily living activities of a healthy subject. It includes six static positions of the spine (Figure 6.2) (flexion at 20°, extension at 15°, lateral bending at 20° on both sides and axial rotation at 15° on both sides), five activities related to locomotion (Figure 6.3) (level walking, stair ascent, stair descent,

sit-to-stand and stand-to-sit) and seven more demanding activities involving spine movements while sitting (maximum flexion, lifting a box from floor to table (from both sides)) and standing (maximum flexion, lifting a box from floor to chest, lifting a box from floor to floor (on both sides) (Figure 6.4). These activities, which are described in more detail in Chapter 3, Section 3.2, Table 3.1, constitute the 'healthy scenario'. To ensure computational efficiency, subsets of load cases were selected from these activities based on the reaction force calculated at the inferior idealised joint in the musculoskeletal model (L4-L5 joint in the case of L4). For each activity, the full set of frames was first subsampled at 10 Hz (every 10 frames) to reduce the number of frames for the simulations. Any peak value was also added to the subset. This initial subset was then optimised by removing frames until a 1% difference between the integrated load for the initial subset of frames and the integrated load for the final subset of frames was reached. At each selected frame, the corresponding muscle forces, joint reaction forces and inertia forces were applied in consecutive steps in the finite element model. For the healthy scenario presented in this Chapter, 116 load cases were applied to the L4 model.

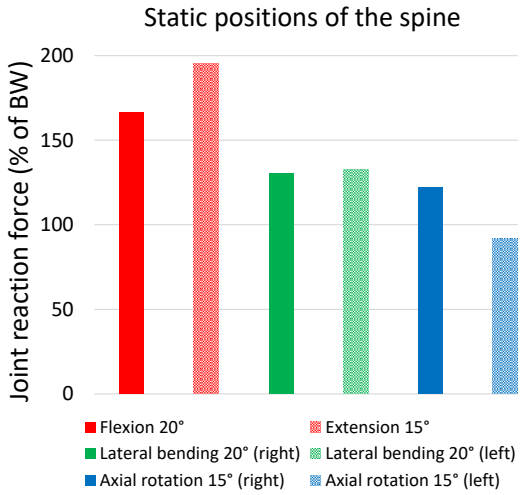

Figure 6.2: Reaction force at L4-L5 joint derived from the musculoskeletal model and used for the finite element analysis for six static positions of the spine. Forces are normalised to body weight (BW).

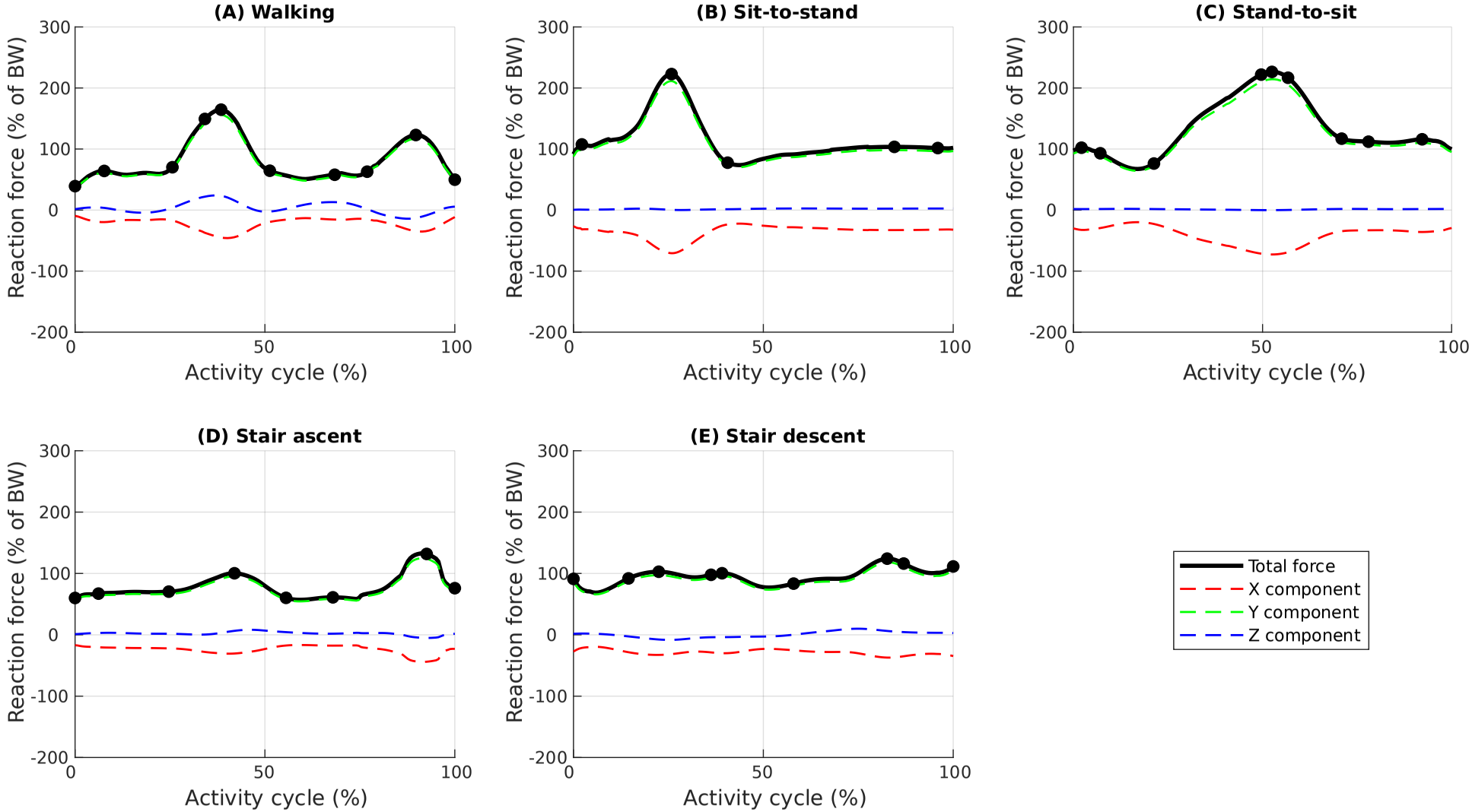

Figure 6.3: Total reaction force at L4-L5 joint derived from the musculoskeletal model and normalised to body weight (BW) for five activities related to locomotion ((A) level walking, (B) standing up from a chair, (C) sitting down on a chair, (D) walking up the stairs, and (E) walking down the stairs) are shown as black lines. Dots indicate the frames selected for the finite element analysis. Red, green and blue dashed lines show X, Y and Z components of the reaction force expressed in the vertebra coordinate system.

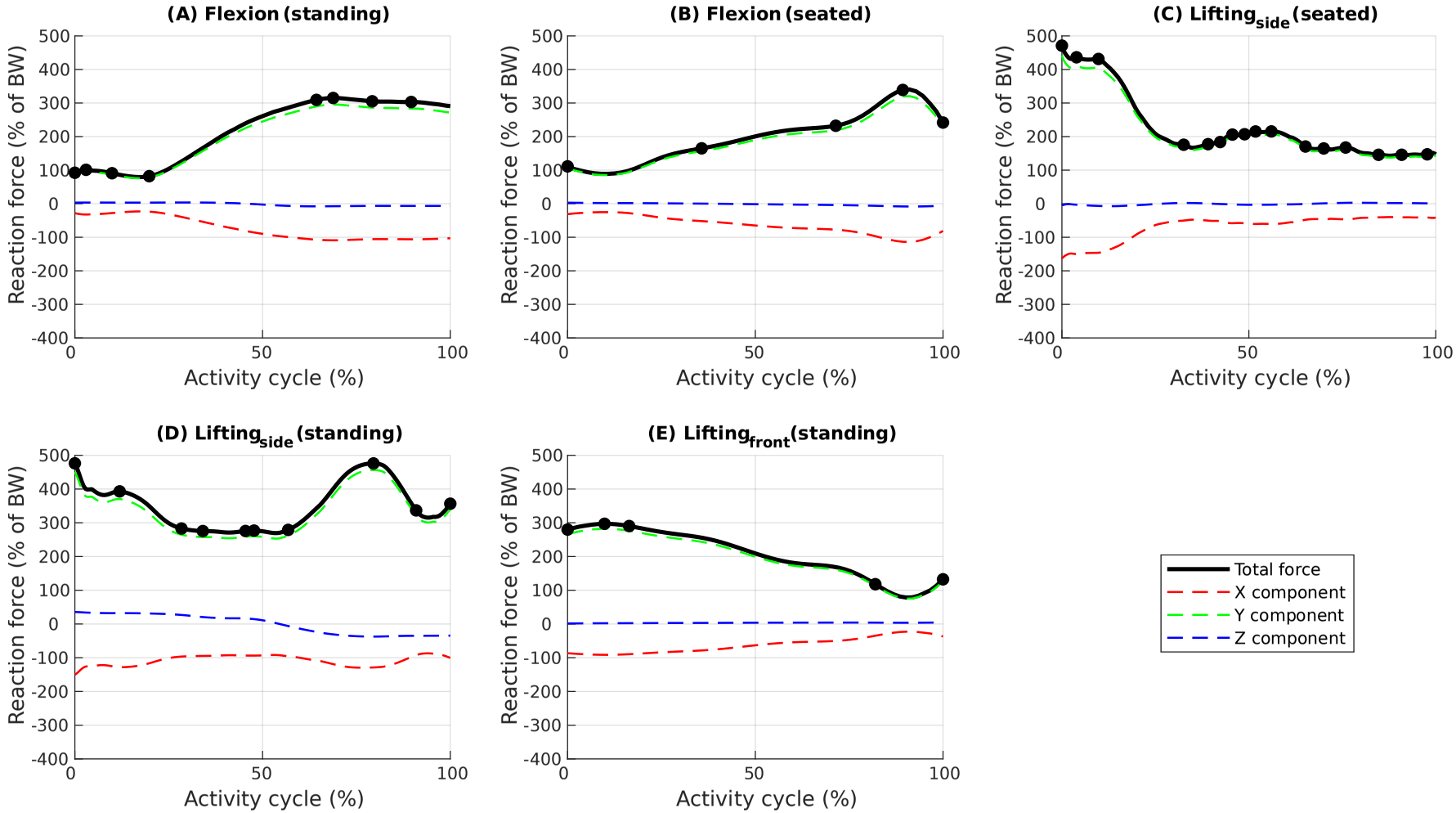

Figure 6.4: Reaction force at L4-L5 joint derived from the musculoskeletal model and normalised to body weight (BW) for seven activities involving spine movements ((A) forward flexion from upright standing to maximum flexion, (B) forward flexion from upright sitting, (C) in a seated position, lifting a box from the floor, from one side to a table in front, (D) in a standing position, lifting a box from the floor, from one side to the other, and (E) in a standing position, lifting a box from the floor and hold it in front of the chest) are shown as black lines. Dots indicate the frames selected for the finite element analysis. Activities (C) and (D) were recorded on one side and mirrored for the other side. Red, green and blue dashed lines show X, Y and Z components of the reaction force expressed in the vertebra coordinate system.

6.2.2.2 Joint reaction forces

Joint reaction forces at L4-L5 and L3-L4 joints calculated at the joint centres in OpenSim were applied on the vertebra with specific constructs called 'load applicators'. As opposed to modelling contact at each joint, these applicators spread the load over the corresponding bone surface reducing significantly the CPU time during the finite element analysis. The load applicators were composed of four layers of six-noded linear continuum wedge elements. To build each layer, surface nodes corresponding to the vertebral endplates were projected four times with a distance of 2 mm outward and orthogonally to the average endplate plane. Material properties of these applicators were adopted from the work of Villette (2016). The two layers closest to the bone were assigned linear elastic material properties representative of cartilage (E = 10 MPa; ν = 0.3). The two external layers were assigned linear elastic material properties of the same stiffness as bone (E = 18 GPa; ν = 0.3). In the musculoskeletal model, intervertebral joints are modelled with three rotational degrees of freedom which only allow the transfer of forces. Since no moments are transferred through these idealised joints, truss elements were used to connect the joint centers as defined in the musculoskeletal model with the external nodes of the load applicators. These trusses were assigned a 2.5 mm^2 circular cross sectional area and linear elastic material properties similar to bone (E = 18 GPa; ν = 0.3). The joint reaction forces obtained with the musculoskeletal model were applied at the joint centres and spread over the vertebral endplates by the load applicators, replicating the behaviour of the intervertebral discs (Figure 6.5).

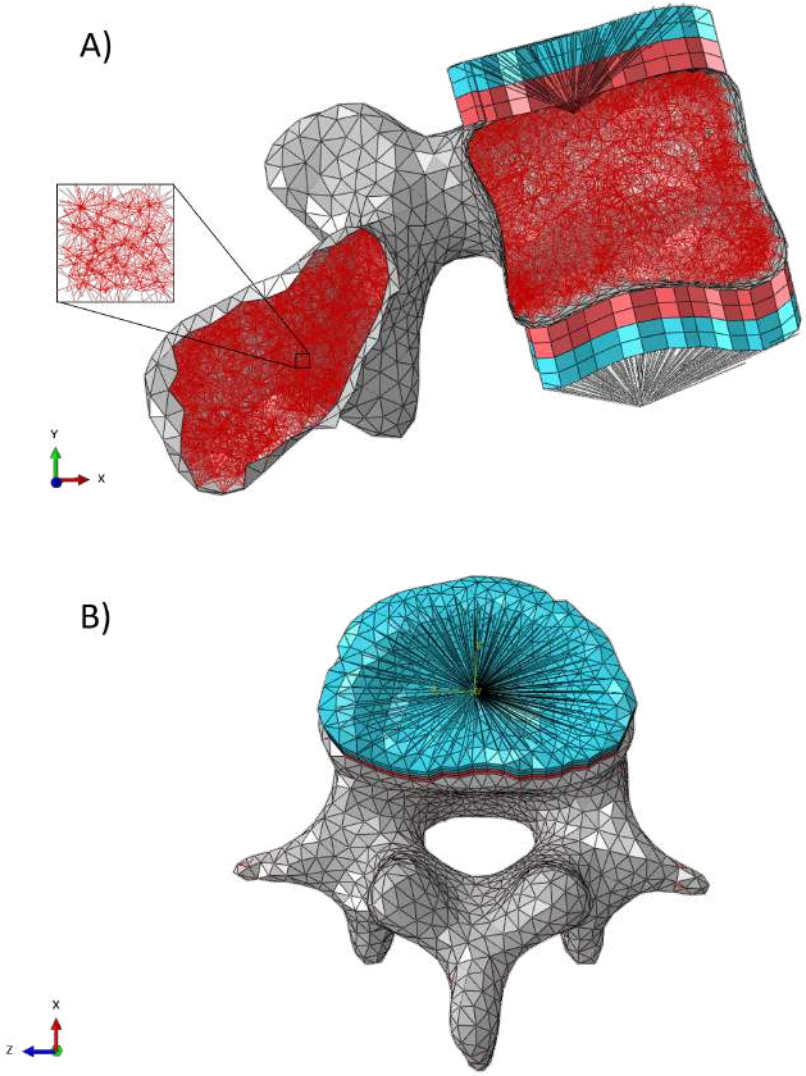

Figure 6.5: Load applicators at the superior and inferior endplates of L4. A) Side cut. B) Bottom view. Cortical shell elements are shown in grey and trabecular truss elements in dark red. Wedge elements of the softer layers of the applicators are shown in light red while the stiffer layers elements are in light blue. Truss elements connecting the nodes on the external layers of the applicators to the joint centres where the load is applied are shown in black.

6.2.2.3 Bushing rotational stiffness

At each intervertebral lumbar joint, the contribution of the intervertebral disc, the ligaments, and the facet joint's capsules in resisting the movements is modelled with linear bushing elements in the musculoskeletal model (Chaper 5, Section 5.1.3). These bushings create moments proportional to the lumbar joint angles along the three orthogonal axes of the vertebra's coordinate frame, providing rotational stiffness at each lumbar level

(Figures 6.6 and 6.7). To ensure equilibrium of the vertebra in the finite element model, these moments should be applied along with the joint reaction forces, muscle forces and inertial loads. Applying these moments representative of the net passive stiffness of the spine at the lumbar joint centres where they are calculated using the load applicators would be inappropriate in the current finite element approach. It would result in applying the contributions of ligaments and facet joint's capsules on the vertebral endplate. If the intervertebral disc spreads the compressive load across the surface of the vertebral endplate, it is also unclear how a moment would be shared between the annulus fibrosus and the nucleus pulposus, and transferred to the bone. The moments produced by the OpenSim bushing elements were therefore not included in the finite element loading for the current study.

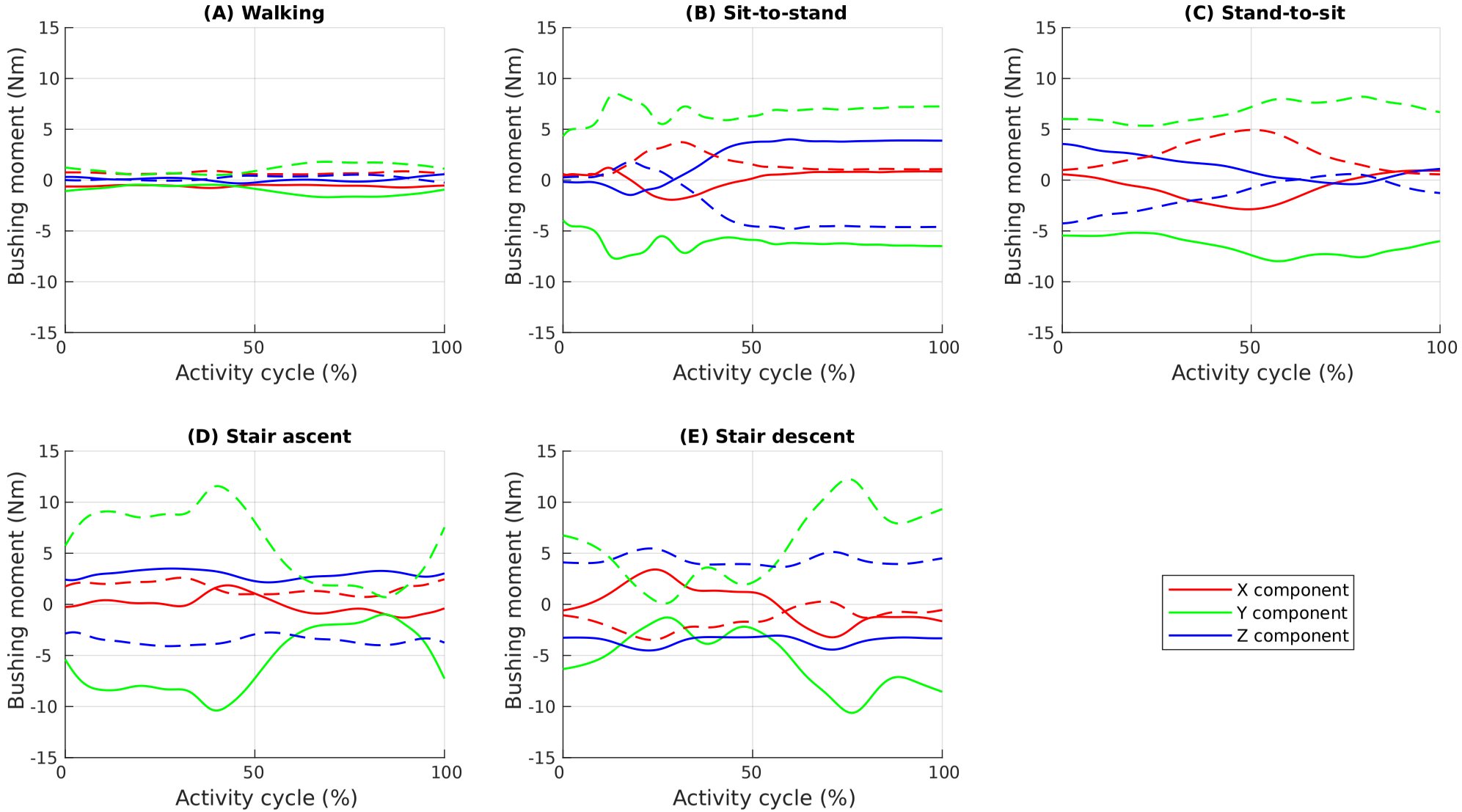

Figure 6.6: Rotational stiffness produced by the bushing elements for five activities related to locomotion ((A) level walking, (B) standing up from a chair, (C) sitting down on a chair, (D) walking up the stairs, and (E) walking down the stairs). Solid lines represent moments produced at the L3-L4 joint. Dashed lines represent moments produced at the L4-L5 joint. Moments are expressed in the vertebra coordinate system.

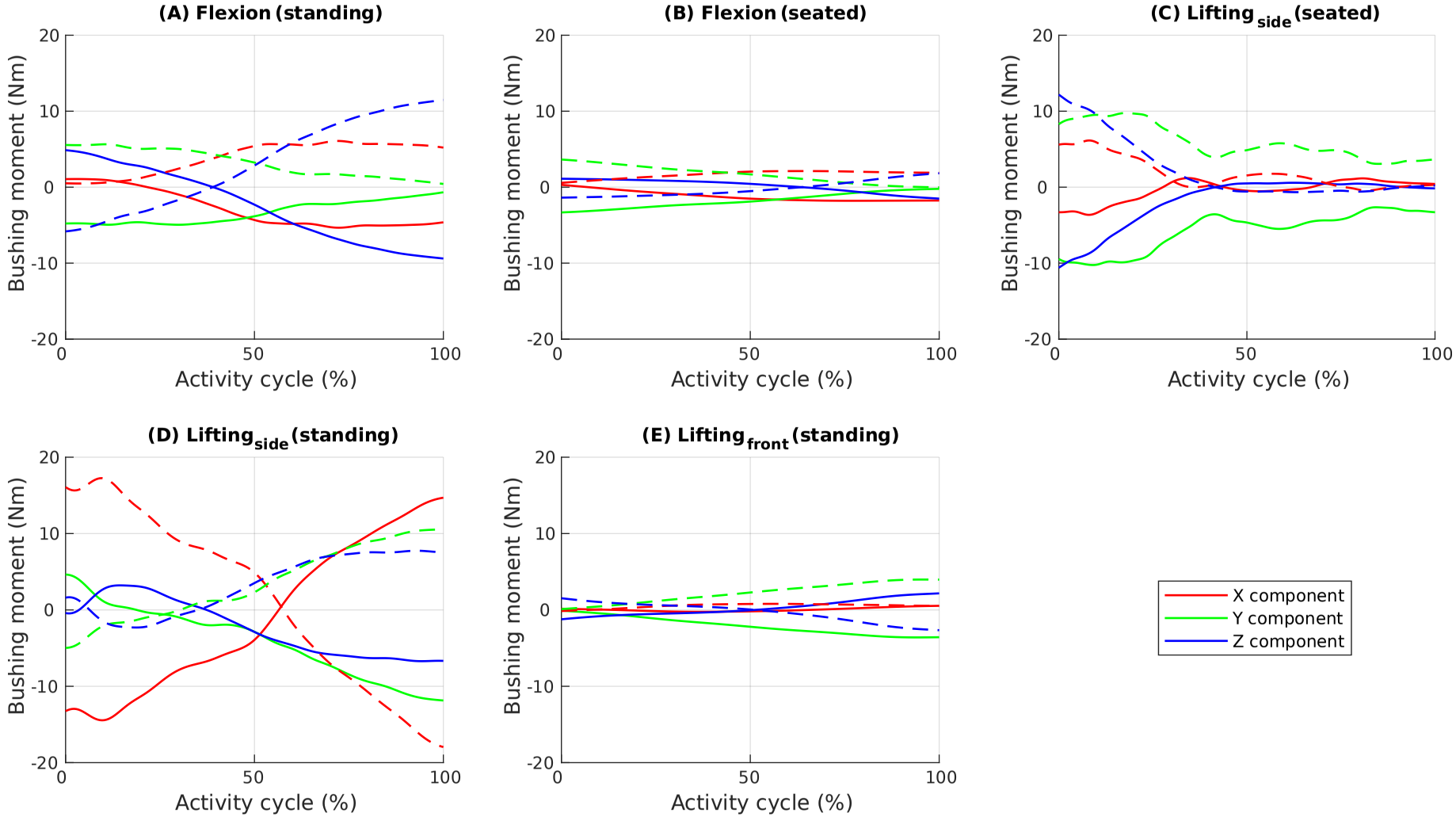

Figure 6.7: Rotational stiffness produced by the bushing elements for five activities involving spine movements ((A) forward flexion from upright standing to maximum flexion, (B) forward flexion from upright sitting, (C) in a seated position, lifting a box from the floor, from the right side to a table in front, (D) in a standing position, lifting a box from the floor, from the left to the right, and (E) in a standing position, lifting a box from the floor and hold it in front of the chest). Solid lines represent moments produced at the L3-L4 joint. Dashed lines represent moments produced at the L4-L5 joint. Moments are expressed in the vertebra coordinate system.

6.2.2.4 Muscle forces

The attachment site coordinates and fiber direction of the OpenSim (Delp et al. 2007) musculotendon actuators acting on L4 were extracted from the musculoskeletal model at each timeframe with a dedicated plugin developed by Modenese (van Arkel et al. 2013). A MATLAB script was then used to locate the surface nodes closest to the attachment sites in the finite element model. Muscle forces were applied as point loads, with the magnitude and direction of the force vector corresponding to the muscle force estimated from the musculoskeletal simulations.

6.2.2.5 Inertia

To apply the inertial load of the lumbar segment to the vertebra, a construct called an 'inertia applicator' based on the same concept as the load applicator was used. Spreading the inertial load over the whole volume of the vertebra is computationally demanding ((Villette 2016)). Every cortical node of the vertebra was therefore connected to a node located at the centre of mass of the lumbar segment with soft truss elements (Figure 6.8). These trusses have a circular cross sectional area of 2.5 mm^2 and were assigned linear elastic material properties with a low stiffness (E = 5 MPa; $\nu = 0.3$) to avoid stiffening of the model. The 'body kinematics' tool available in OpenSim 3.3 was used to determine the position and velocity of the vertebra in the global coordinate system at each timeframe. The direction and magnitude of the inertial load was calculated based on these positions and velocities, and the mass of the lumbar segment. The inertial load was applied at the node located at the centre of mass of the lumbar segment.

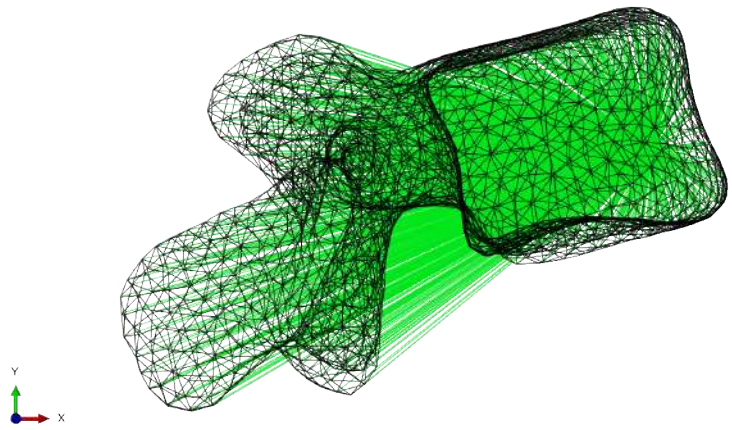

Figure 6.8: Side view of the inertia applicator of L4. Cortical shell elements are shown as a wireframe. Trabecular truss elements are not shown for clarity. Truss elements connecting cortical nodes to the node located at the centre of mass of the lumbar segment are shown in green.

6.2.2.6 Boundary conditions

The loading applied to the finite element model of the vertebra is obtained with the musculoskeletal model. At each time step, musculoskeletal simulations are solved for equilibrium of each segment. If all loads are applied, the vertebra should be at equilibrium in the finite element analysis, and no boundary condition should be needed. As explained previously, bushing rotational stiffness implemented at each lumbar joint in the musculoskeletal model is not considered in the finite element approach. To ensure numerical stability of the finite element model, soft boundary conditions were applied using a similar approach as the load applicators. At the inferior joint, beam elements connecting the external nodes of the inferior endplate applicator with a duplicate node at the joint centre were added (Figure 6.9). This duplicate node was constrained in all six degrees of freedom. The beam elements were assigned a circular cross section of 2.5 mm^2, a Young's modulus of 1 GPa and a Poisson's ratio of 0.3. These relatively soft material properties compared to the load applicator properties prevent stiffening of the vertebra's structure induced by the boundary condition.

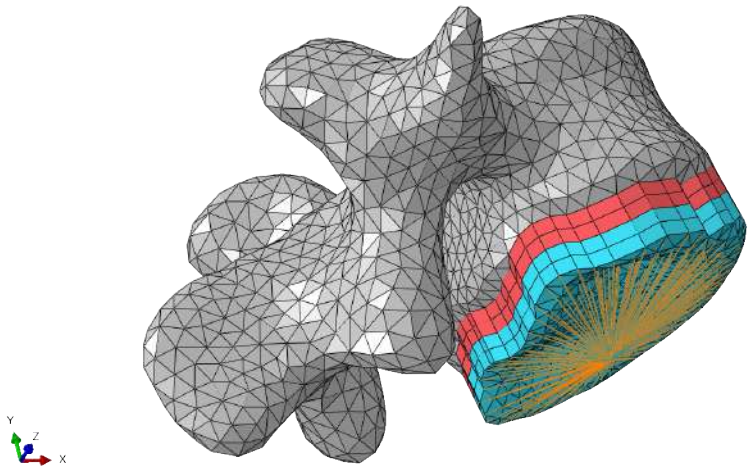

Figure 6.9: Boundary condition applicator of L4. Cortical shell elements are shown in grey. Load applicator wedge elements are shown in light red an blue. Beam elements connecting the nodes on the external layer of the load applicator to the duplicate node at the inferior joint centre are shown in orange.

6.2.3 Adaptation

As mentioned before, truss elements representing trabecular bone were assigned a 0.1 mm radius and shell elements representing the cortex a 0.1 mm thickness in the initial model. These section properties were optimised towards a target strain of 1250 $\mu\epsilon$ for all the load cases of the loading scenario using the algorithm introduced in Chapter 2, Section 2.5.2, which simulates the adaptation behaviour of bone described by Frost (1987, 2003). To increase computational efficiency, shell thicknesses were discretised linearly into 256 categories. The thickness of cortical bone varies between 0.2 and 0.9 mm in the vertebral body (Ritzel et al. 1997, Edwards et al. 2001). The thickness range of the shell elements was set between 0.1 and 2.0 mm to account for potential inter-subject variability. The same approach was used for the truss cross-sectional areas which were linearly discretised in 255 categories. The radius range of the truss elements was set between 0.1 and 2.0 mm, which characterises trabecular bone at a mesoscale level (Nagele et al. 2004, Phillips et al. 2015). An extra category with a radius of 1 μm was added and allocated to elements in the dead zone. With such a small radius, the contribution of these elements is negligible while the numerical stability of the model is maintained. Elements in the

dead zone were also allowed to grow back and be reassigned to one of the 255 categories if appropriate at a later iteration.

6.3 Results

The structural finite element model of L4 converged in 20 iterations. 6.3% of the initial truss elements ended in the dead zone after adaptation to 116 load cases representative of daily activities. The remaining truss elements have an average connectivity of 17.21 (SD 3.95) and a total volume of 9010.4 mm^3. Cortical shell elements were also adapted and reached a final volume of 4877.3 mm^3. The relative density of the vertebra was 19.8%, calculated as the ratio between the volume of all the bone elements and the total volume of the vertebra. This value is within the range reported for by Eriksen et al. (2002) (19.0%, SD 8.5%) and Muller (2004) (17.9%, SD 6.7%).

Focusing on the cortex adaptation, it is clear that shell elements thicken towards the posterior part of the vertebral body, the pedicles, and the transverse processes (Figure 6.10). In the pedicles and the transverse processes, the cortex is thicker in the superior and inferior parts, while the sides remain thinner. This is consistent with the pedicles and transverse processes bending respectively about the medio-lateral axis during flexion extension activities and the antero-posterior axis during lateral bending activities.

The trabecular architecture shows clear trajectories comparable to observations made in the literature. Figure 6.11 shows a selection of slices and cut views of the model alongside a description of the vertebra's internal architecture by Gallois & Japiot (1925). A difference is made between the trusses with a radius of 0.1 mm representing what will be called the 'ground matrix' and the thicker ones. The trabecular ground matrix is believed to give a base stiffness to the bone, while the thicker trusses resist the loads which are not resisted by the ground matrix. Some of the trabecular trajectories can be seen among these thicker trusses, particularly the group running perpendicular to the endplates and resisting vertical compression in the vertebral body. A second group of trabecular trajectories resisting mediolateral tension can also be highlighted in the transverse processes. A final group can be identified running diagonally across the vertebral body and the pedicles, finishing in the transverse and superior articular processes. A more detailed view of the structure of the vertebra is shown in Figures 6.12, 6.13, 6.14 and 6.15.

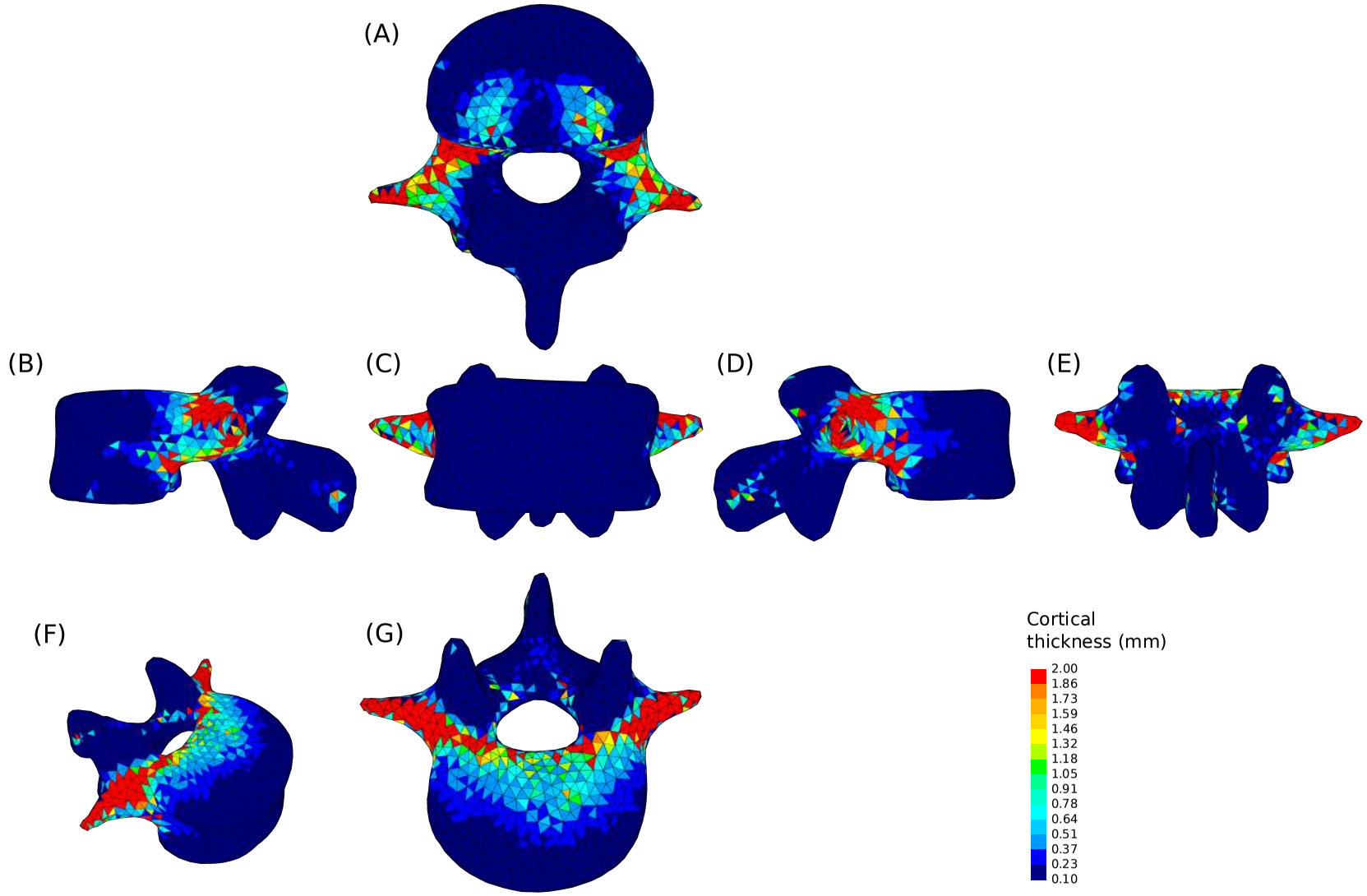

Figure 6.10: Cortical thickness of the converged mesoscale structural model of L4 ranging from 0.1 to 2 *mm*. (A) caudal view, (B) left lateral view, (C) frontal view, (D) right lateral view, (E) dorsal view, (F) isometric view, (G) cranial view.

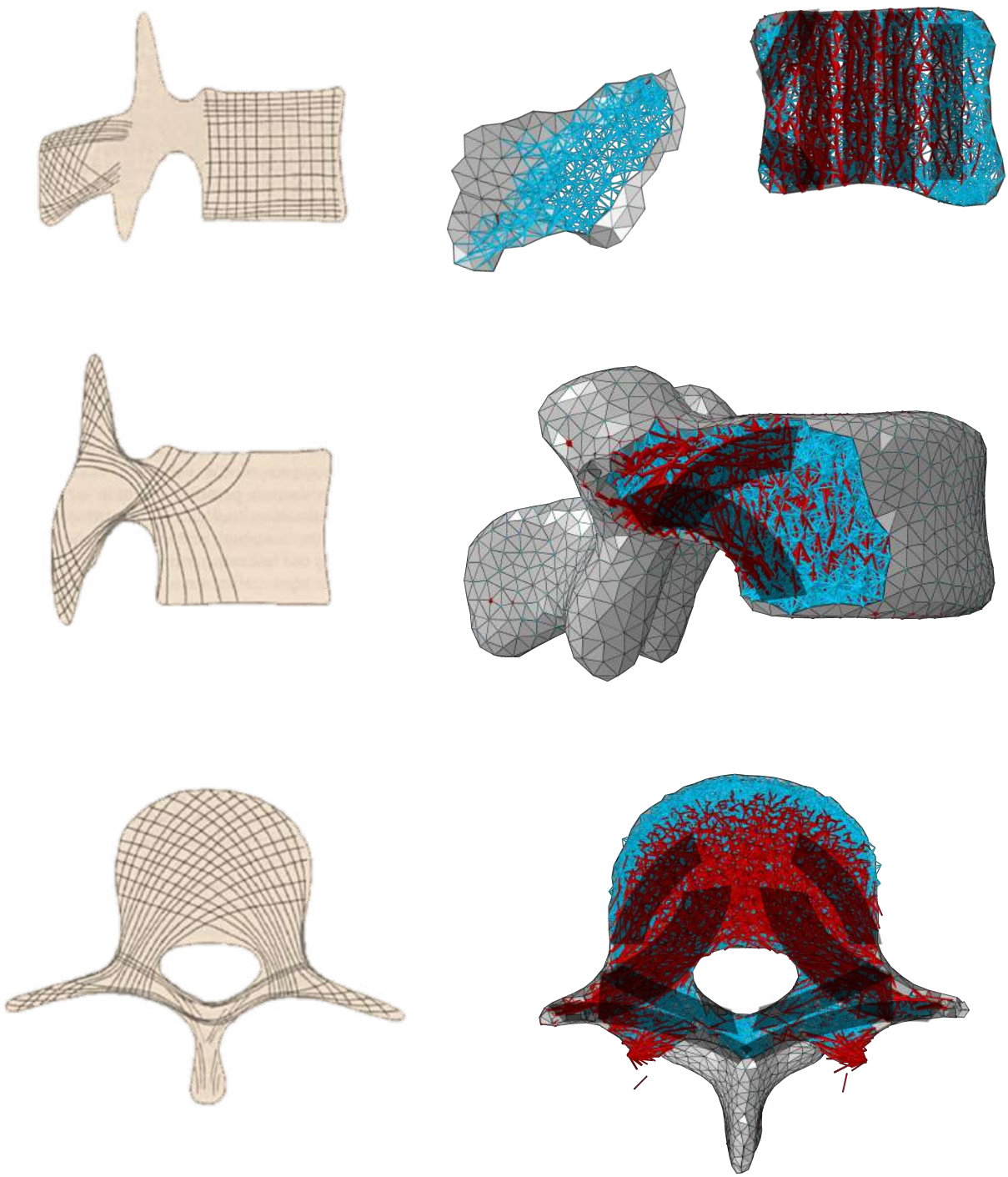

Figure 6.11: Structural architecture of the lumbar vertebra. On the left, observations made by Gallois & Japiot (1925). On the right, the converged L4 model adapted to 116 load cases representative of 18 daily living activities. Cortical shell elements are shown in grey. Trabecular truss elements with a radius of 0.1 mm representing the ground matrix are shown in blue. Thicker truss elements are shown in red. Truss elements in the dead zone (with a radius of 1 μm) are not shown for clarity.

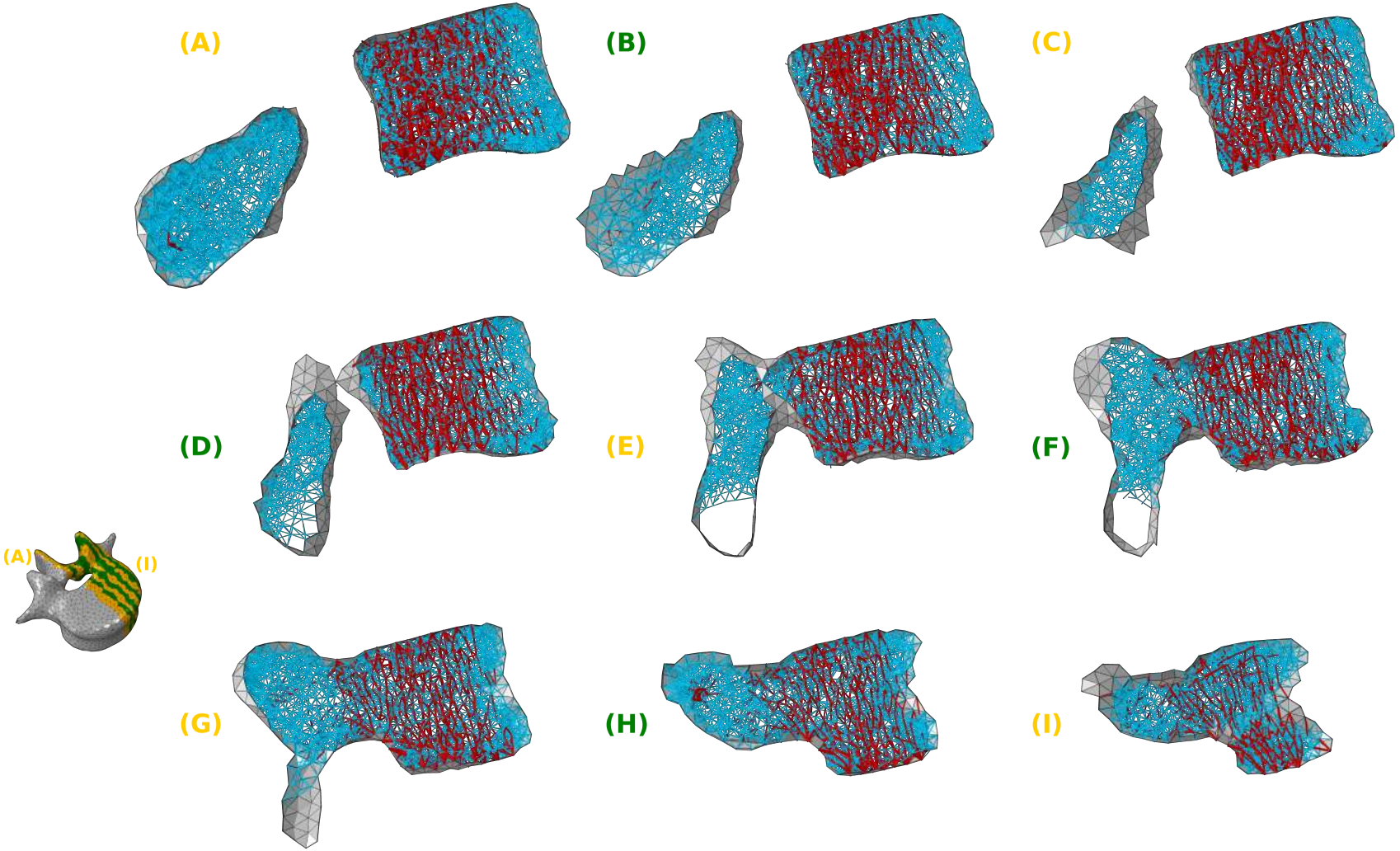

Figure 6.12: Selected sagittal 3 *mm* slices for the converged L4 model adapted to the 116 load cases representative of 18 daily living activities. Cortical shell elements are shown in grey. Trabecular truss elements representing the ground matrix (with a radius of 0.1 *mm*) are shown in blue. Thicker truss elements are shown in red. Truss elements in the dead zone (with a radius of 1 μm) are not shown for clarity.

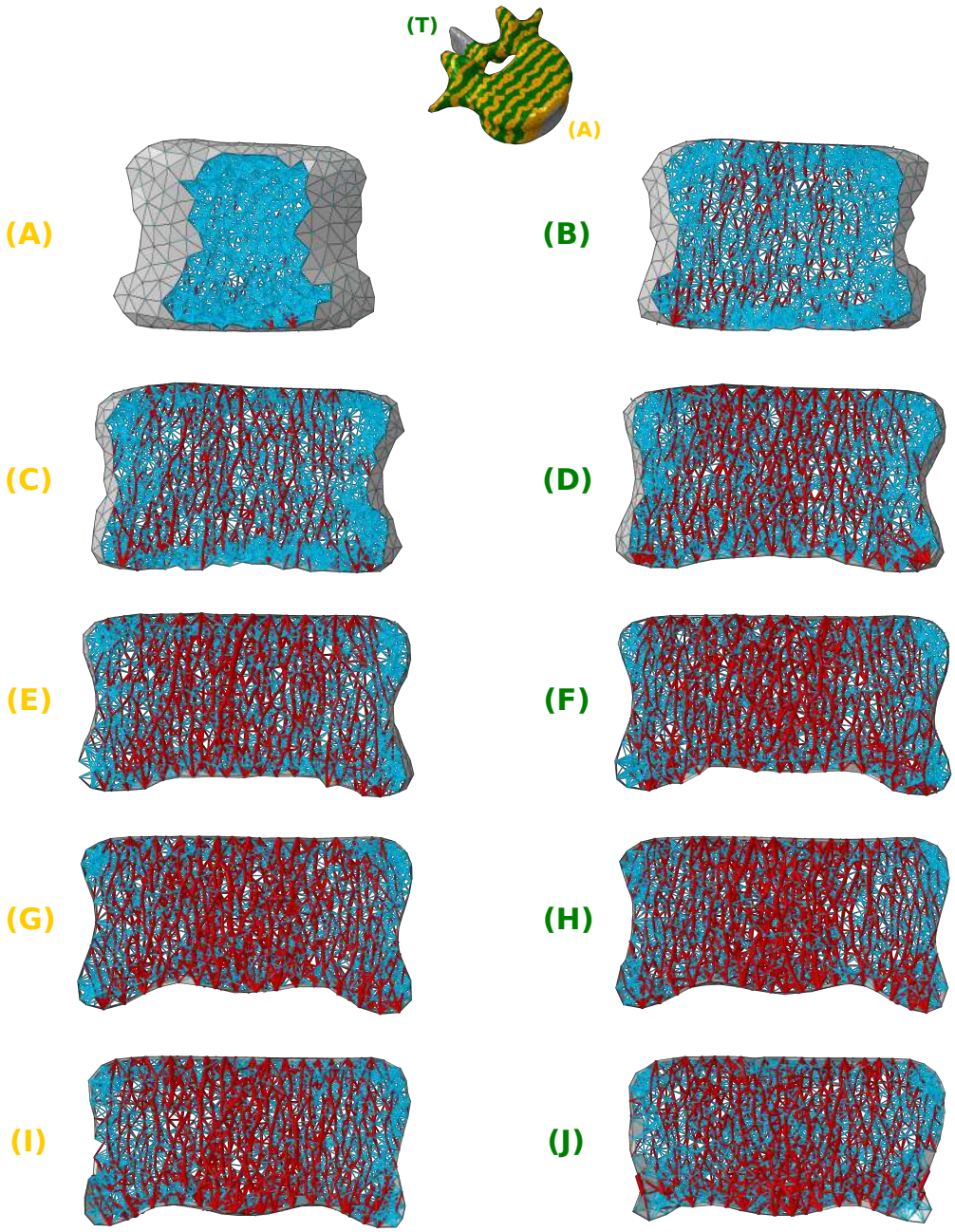

Figure 6.13: Selected coronal 3 *mm* slices in the vertebral body of the converged L4 model adapted to the 116 load cases representative of 18 daily living activities. Cortical shell elements are shown in grey. Trabecular truss elements representing the ground matrix (with a radius of 0.1 *mm*) are shown in blue. Thicker truss elements are shown in red. Truss elements in the dead zone (with a radius of 1 µm) are not shown for clarity.

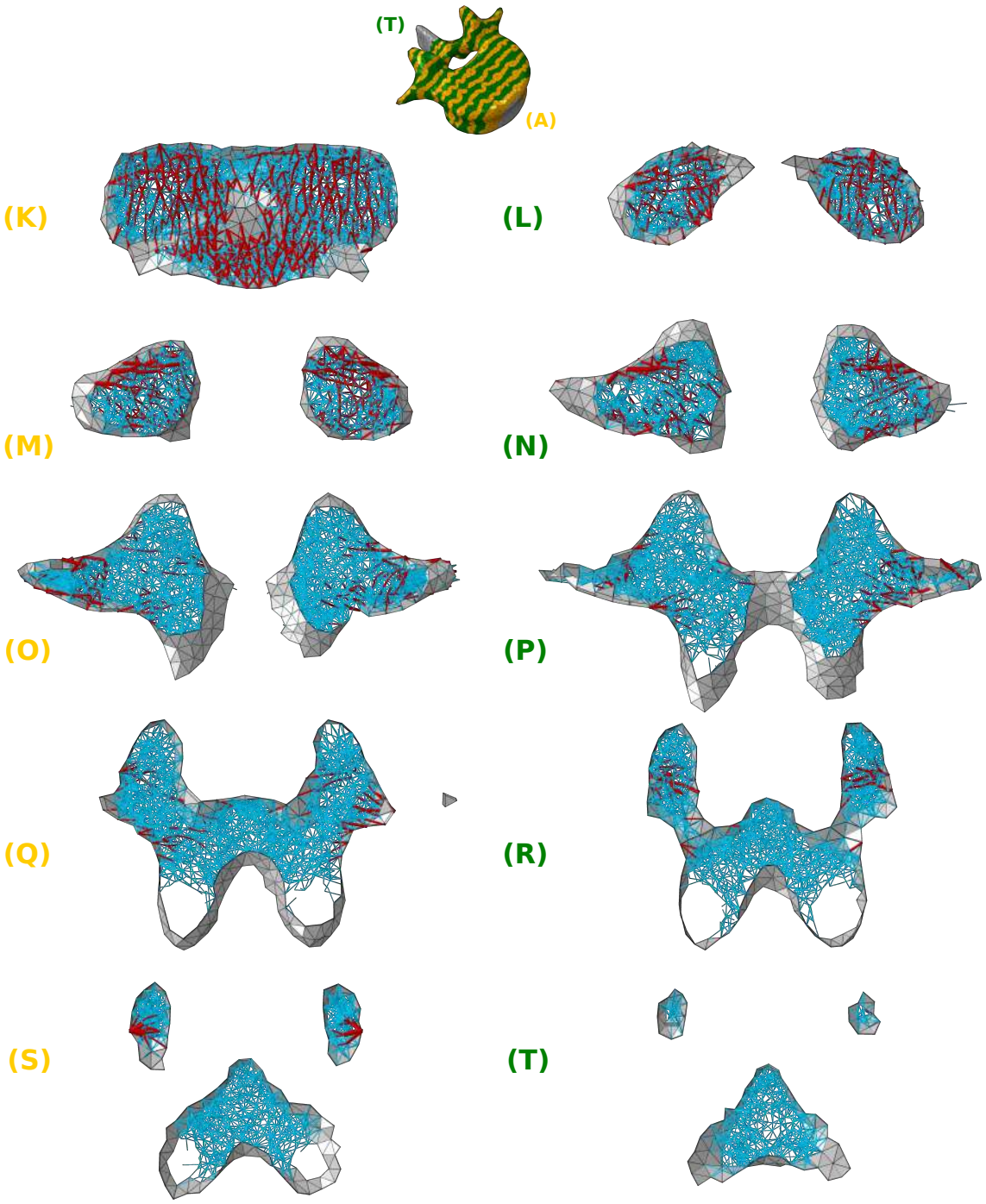

Figure 6.14: Selected coronal 3 *mm* slices in the posterior elements of the converged L4 model adapted to the 116 load cases representative of 18 daily living activities. Cortical shell elements are shown in grey. Trabecular truss elements representing the ground matrix (with a radius of 0.1 *mm*) are shown in blue. Thicker truss elements are shown in red. Truss elements in the dead zone (with a radius of 1 μm) are not shown for clarity.

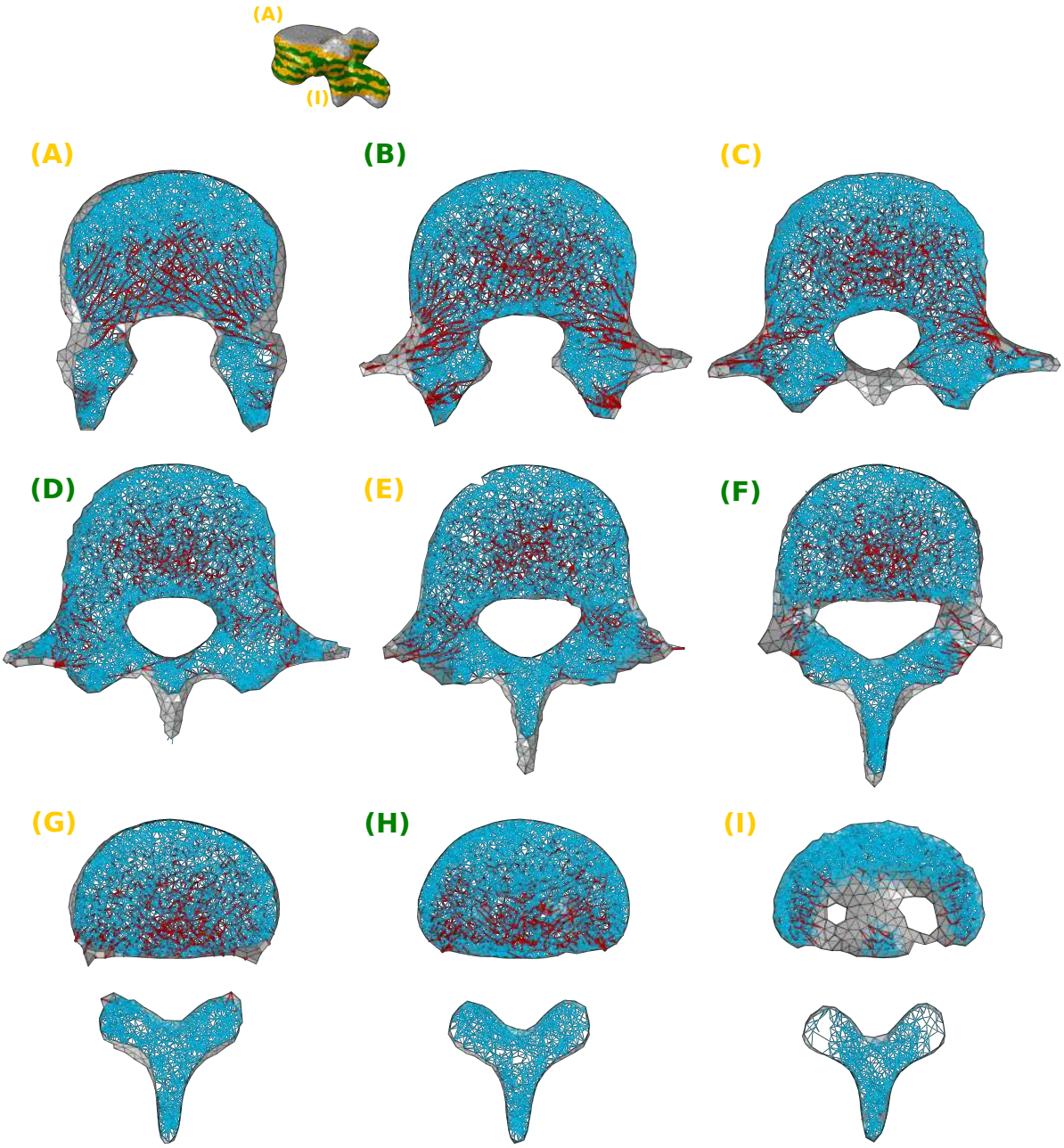

Figure 6.15: Selected transverse 3 mm slices for the converged L4 model adapted to the 116 load cases representative of 18 daily living activities. Cortical shell elements are shown in grey. Trabecular truss elements representing the ground matrix (with a radius of 0.1 mm) are shown in blue. Thicker truss elements are shown in red. Truss elements in the dead zone (with a radius of 1 μm) are not shown for clarity.

To investigate more quantitatively the orientation of the trabecular trajectories, bone anisotropy in the lumbar vertebrae was characterised using coloured spheres at each node. Every truss element was expressed as a normalised vector of X, Y and Z components in the vertebra's coordinate system. These element vectors were then weighted based on the cross-sectional area of the elements. For each node, connected weighted element vectors were summed to create a node vector. The norm of this node vector was used to scale the sphere radius at each node. Components of the normalised node vector were used as RGB values for the sphere's color, with X, Y and Z components corresponding to red, green and blue respectively. Figure 6.16 shows how the color scale should be interpreted. With this method, if a node links truss elements oriented along the X axis (respectively Y or Z) only, a red (respectively green or blue) sphere will be produced. Similarly, if a node links truss elements oriented at +/- 45° in the XY plane (respectively XZ plane or YZ plane) only, a yellow (respectively magenta or cyan) sphere will be produced. A grey sphere corresponds to no clear orientation of the truss elements attached to that particular node.

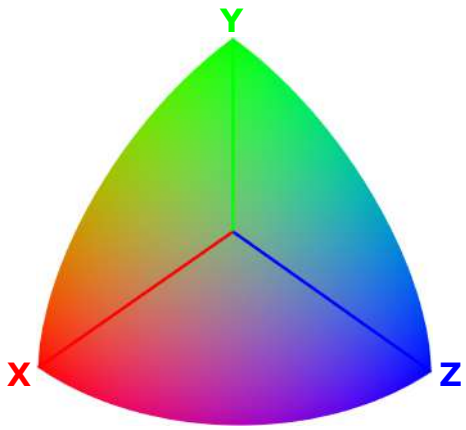

Figure 6.16: Color scale for Figures 6.17 and 6.18. Trajectories aligned with X, Y or Z axes will show in red, green or blue respectively. Trajectories that are a combination of three axis components will show in a combination of red, green and blue.

Figure 6.17 shows the sphere plots for trabecular truss elements with a radius of 0.1 *mm* forming the ground matrix for all lumbar vertebrae, while Figure 6.18 focuses only on thicker elements with a radius superior to 0.1 *mm*. Focusing on the ground matrix plots (Figure 6.17), the nodes in the vertebral body are oscillating between pink and purple, indicating a principal orientation of the truss elements in the XZ plane, at +/- 45°. For the thicker elements (Figure 6.18) there is a clear orientation along the Y axis for the

trabeculae in the vertebral body as green is the dominant color. Blue is the dominant color in the transverse processes and the vertebral arch, indicating that most trabeculae run mediolaterally in these parts of the vertebrae. It can also be noted that due to the orientation of its axis system, the main color in the L5 vertebral body is oscillating between green and orange, which is consistent with trabecular elements aligned vertically. These results confirm the visual assessment done in Figures 6.11 to 6.15.

While clear trabecular trajectories and cortical thickness patterns can be observed in the vertebral body, pedicles and transverse processes, the structure of the most posterior elements of the vertebra such as the spinous process and the articular processes is less defined. No clear trajectories are observed in the spinous process, which is almost only filled with trabecular ground matrix. This suggests the musculotendon actuators included in the musculoskeletal model are only partially influencing the structure of the spinous process. Looking at the lumbar anatomy discussed in Chapter 2, Section 2.2, a lot of ligaments and fascia are also attached to this process (Figure 2.7). For large movements of the spine, they would apply tension on the spinous process and increase the strains in the trabeculae, creating more defined trajectories. A similar observation can be made for the inferior articular processes, where no trabecular bone was left after adaptation. This is due to the absence of contact forces at the facet joints. Ligament forces and contact forces on the facets' articular surfaces could be determined with a more complex musculoskeletal model. However, maintaining a subject-specific approach would become challenging as ligaments are difficult to segment on the MRI scans. This is discussed further in Section 6.4.

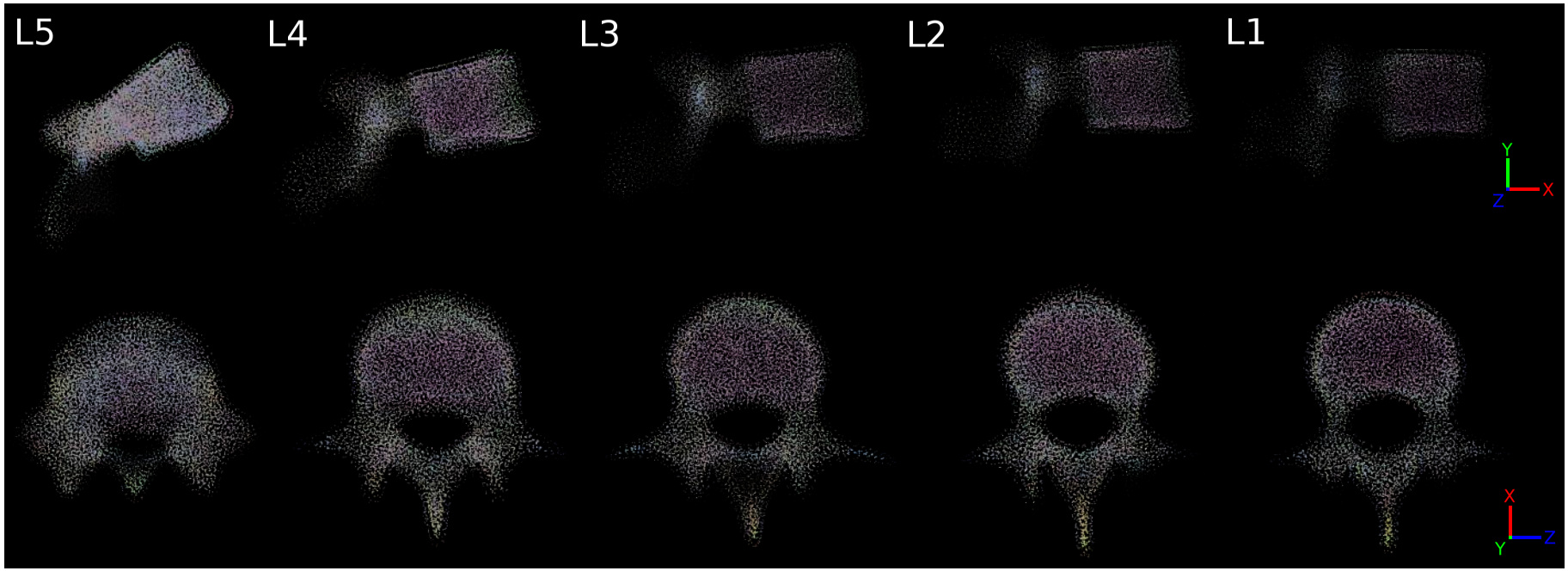

Figure 6.17: Side view (top row) and top view (bottom row) of the lumbar vertebrae showing the orientation of the trabecular trusses of the ground matrix (with a radius of 0.1 mm). Spheres are attached to each node, with colour and size varying with the orientations and radii of the truss elements connected to that particular node respectively. Orientation along the X, Y or Z axes are in red, green or blue respectively. Any orientation that is not colinear with these axes will show as a combination of red, green and blue (Figure 6.16).

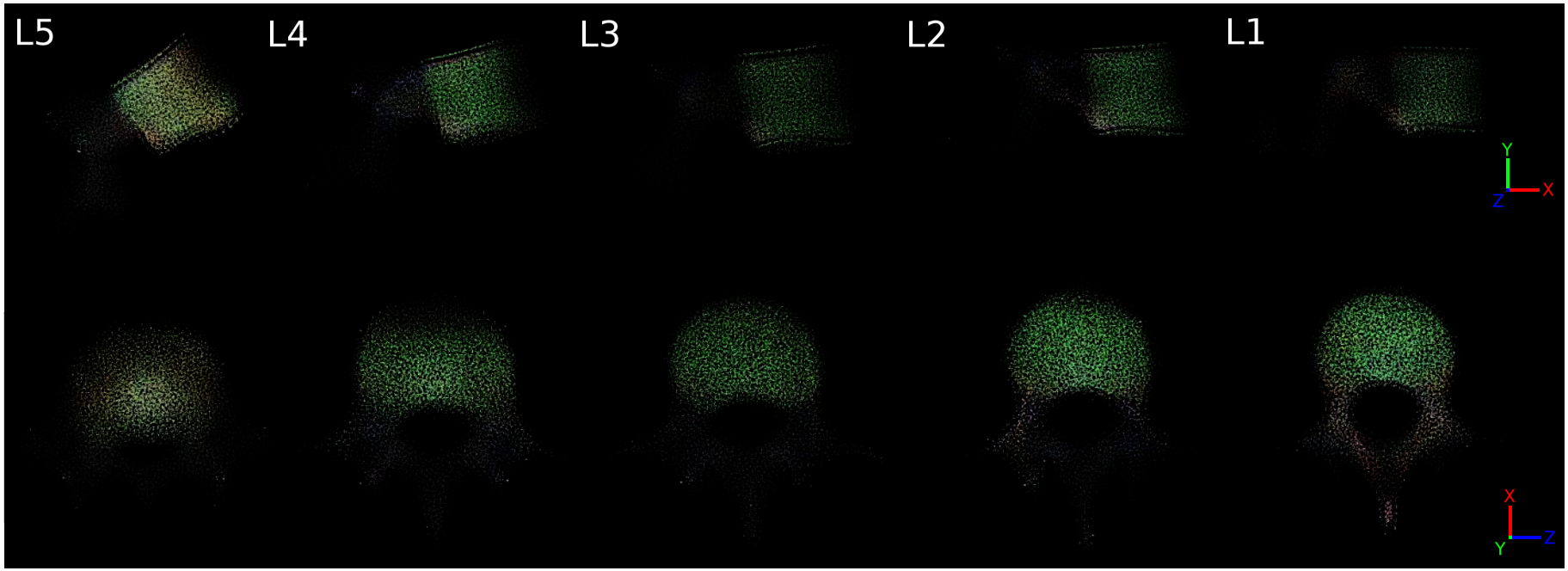

Figure 6.18: Side view (top row) and top view (bottom row) of the lumbar vertebrae showing the orientation of the thicker trabecular trusses (with a radius superior to 0.1 mm). Spheres are attached to each node, with colour and size varying with the orientations and radii of the truss elements connected to that particular node respectively. Orientation along the X, Y or Z axes are in red, green or blue respectively. Any orientation that is not colinear with these axes will show as a combination of red, green and blue (Figure 6.16).

6.3.1 Comparison to in-vivo architecture

In-vivo observations of the vertebral architecture are not abundant in the literature for healthy young subjects, as most studies focus on elderly and pathological populations. This Section presents comparisons at different lumbar levels between converged models and in-vivo observations. Detailed results for all five lumbar vertebrae can be found in Appendix C.

The structural architecture of L4 obtained after adaptation was compared to photographs of human fourth lumbar vertebral body slices made by Jayasinghe et al. (1994). Figure 6.19 shows a mid-sagittal slice of L4 from a 31 year old male subject. The corresponding slice from the model shows the same trend of a higher density of thin trabeculae close to the endplates and larger trabeculae when moving towards the center. The vertical orientation of the large trabeculae can be seen both on the model slices and the photographs. This trabecular orientation is also apparent on Figure 6.20 which presents three slices in the coronal plane from a 30 year old female subject. On the most posterior slice (Figure 6.20 (C)), the photograph shows a low density of trabecular bone in the center of the slice. This is where the basivertebral vein emerges from the foramina. Although its boundaries were not clearly defined, this cavity was partially visible on the MRI scans (Figure 6.21) and could potentially be modelled. However, a different approach has to be considered to build the model as the cavity is not bounded by cortical bone and elements would have to be removed manually. Comparison in the transverse plane is made in Figure 6.22. On these slices, thickening of the cortex towards the posterior part of the vertebral body and the pedicles can be seen.

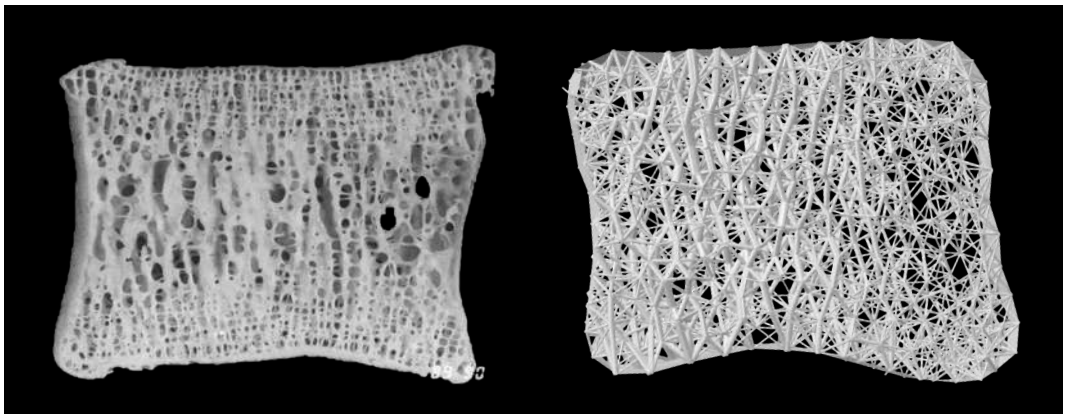

Figure 6.19: Mid-sagittal 4 *mm* slice of the L4 vertebral body. On the left, photograph taken from a 31 years old male specimen by Jayasinghe et al. (1994). On the right, the corresponding slice in the converged model with truss elements in the dead zone removed. Photograph is adapted by permission from Springer Nature Customer Service Centre GmbH: Springer Nature, Anatomy and Embryology, *Three-dimensional photographic study of cancellous bone in human fourth lumbar vertebral bodies*, Jayasinghe et al., © 2014).

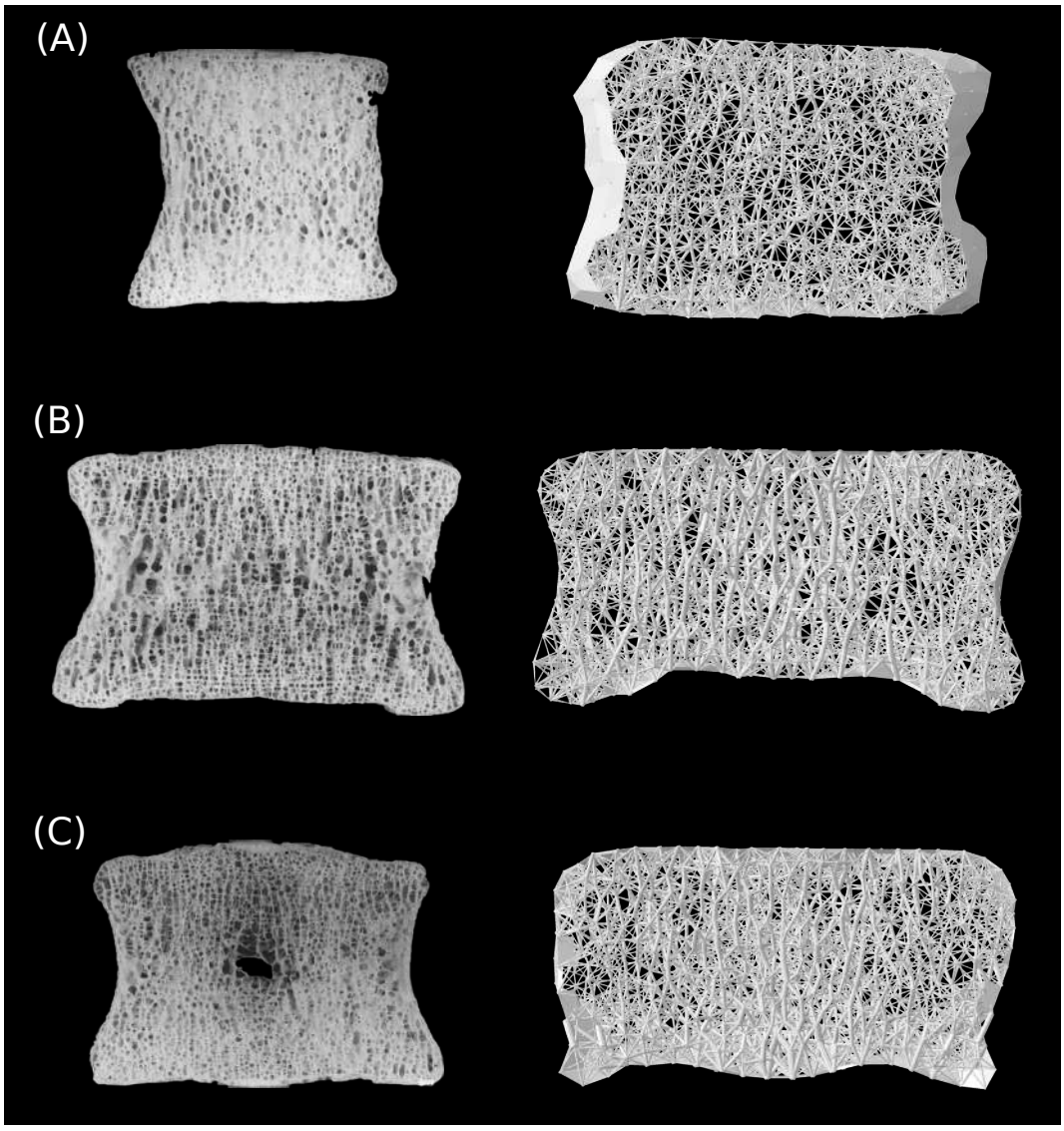

Figure 6.20: (A) anterior, (B) midpoint and (C) posterior coronal 4 *mm* slices of the L4 vertebral body. On the left, photographs taken from a 30 years old female specimen by Jayasinghe et al. (1994). On the right, the corresponding slices in the converged model with truss elements in the dead zone removed. Photograph are adapted by permission from Springer Nature Customer Service Centre GmbH: Springer Nature, Anatomy and Embryology, *Three-dimensional photographic study of cancellous bone in human fourth lumbar vertebral bodies*, Jayasinghe et al., © 2014).

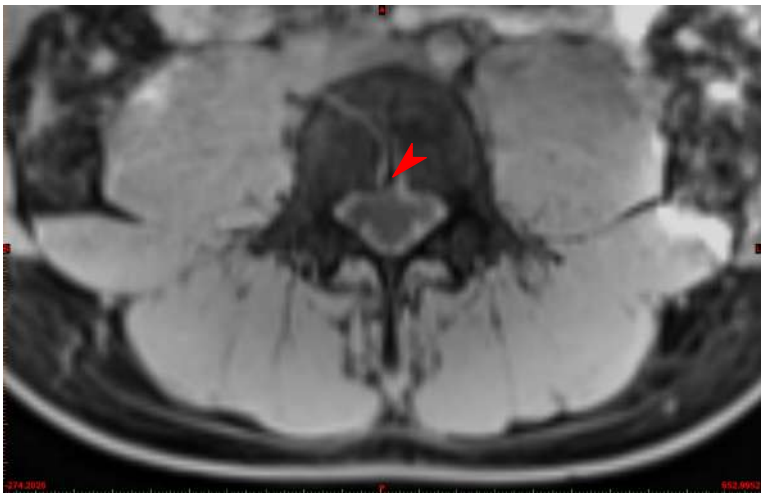

Figure 6.21: Transverse MRI slice of the L4 showing the basivertebral vein cavity with a red arrow. Boundaries of the cavity are not clearly defined at this resolution.

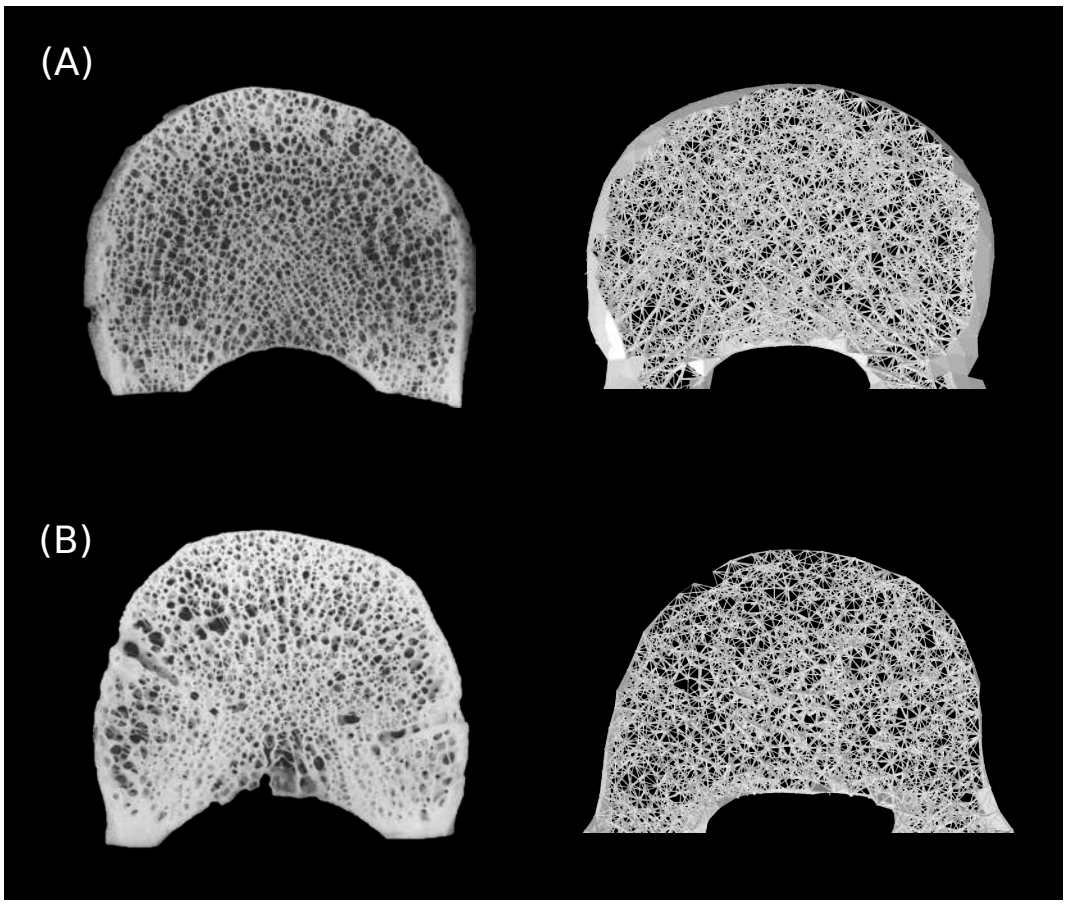

Figure 6.22: (A) superior and (B) inferior transverse 4 *mm* slices of the L4 vertebral body. On the left, photographs taken from a 30 years old female specimen by Jayasinghe et al. (1994). On the right, the corresponding slices in the converged model with truss elements in the dead zone removed. Photographs are adapted by permission from Springer Nature Customer Service Centre GmbH: Springer Nature, Anatomy and Embryology, *Three-dimensional photographic study of cancellous bone in human fourth lumbar vertebral bodies*, Jayasinghe et al., © 2014).

L3 was compared to a photomicrograph of a midsagittal section taken by Keller et al. (1989). Similar to the observations made on L4, the trabecular architecture presents thin trabeculae close to the endplates and thicker vertical ones towards the midaxial plane. The orientation of the trabeculae is visible in the L3 converged model (Figure 6.23). Density of trabeculae is difficult to compare as the slice thickness of the photomicrograph is unknown. The 3 *mm* thick model slice shows higher density close to the endplates.

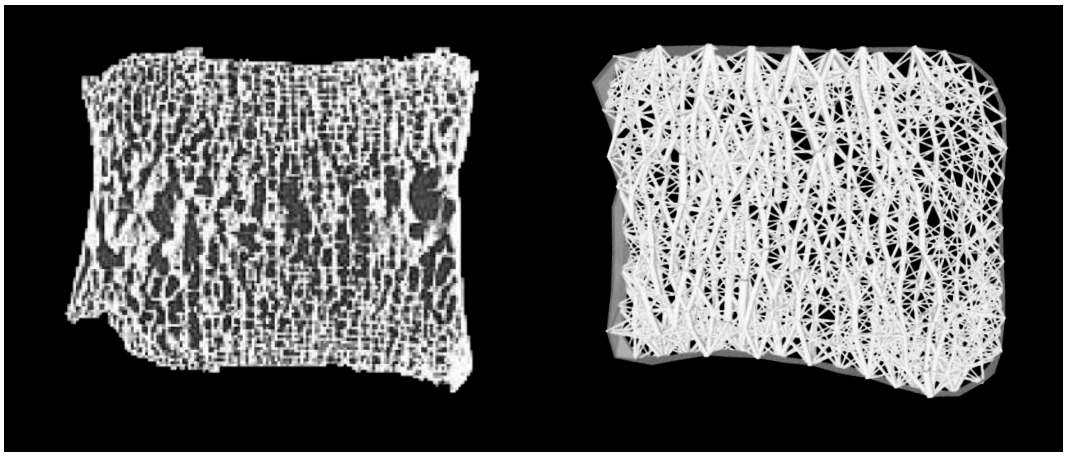

Figure 6.23: Mid-sagittal slice of the L3 vertebral body. On the left, photomicrograph taken by Keller et al. (1989). On the right, the corresponding slice (3 *mm*) in the converged L3 model with truss elements in the dead zone removed. Photomicrograph is reproduced by permission from Wolters Kluwer Health, Inc., Spine, *Regional Variations in the Compressive Properties of Lumbar Vertebral Trabeculae: Effects of Disc Degeneration*, Keller et al., © 1989).

Keller et al. (1989) also provide photomicrographs of L2 in the transverse plane at three different levels. Figure 6.24 shows the corresponding slices from the converged L2 model. Thickening of the cortex towards the pedicles can be observed both on the photomicrograph and the model slices, while the cortical bone in the frontal part of the vertebral body remains thin. The inferior and superior slices also show similarities in trabecular bone density.

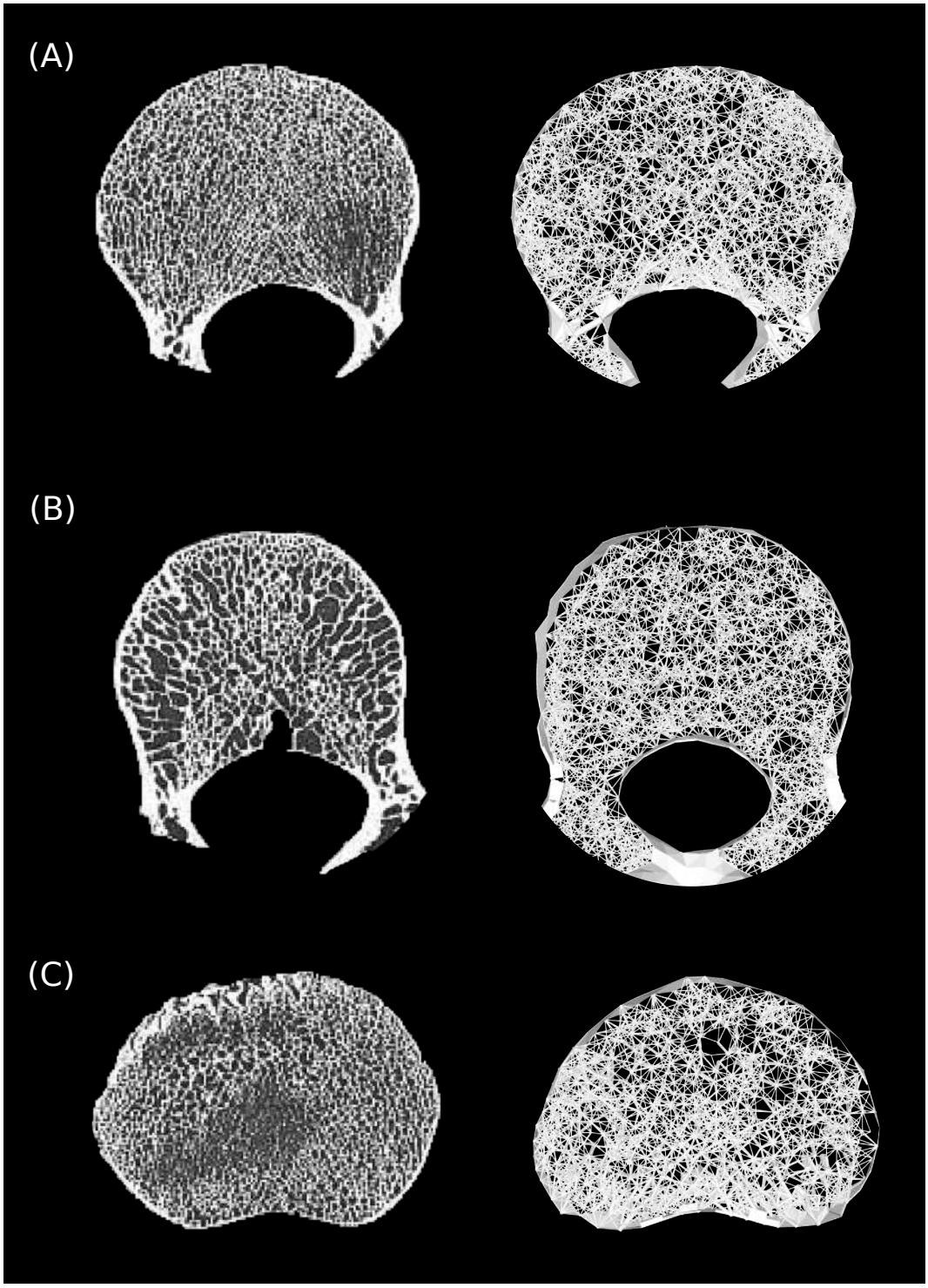

Figure 6.24: (A) superior (B) midpoint and (C) inferior transverse slices of the L2 vertebral body. On the left, photomicrographs taken by Keller et al. (1989). On the right, the corresponding slices (3 *mm*) in the converged L2 model with truss elements in the dead zone removed. Photomicrographs are reproduced by permission from Wolters Kluwer Health, Inc., Spine, *Regional Variations in the Compressive Properties of Lumbar Vertebral Trabeculae: Effects of Disc Degeneration*, Keller et al., © 1989).

Cortical bone thickness in the pedicles are also compared to a photograph of a L2 section taken by Maillot & Wolfram-Gabel (1993). Figure 6.25 clearly shows thickening of the trabecular bone in the superior and inferior parts of the pedicles while the medial and lateral parts remain thin. This observation is made both in the converged model and the photograph despite the shape variations between the two subjects.

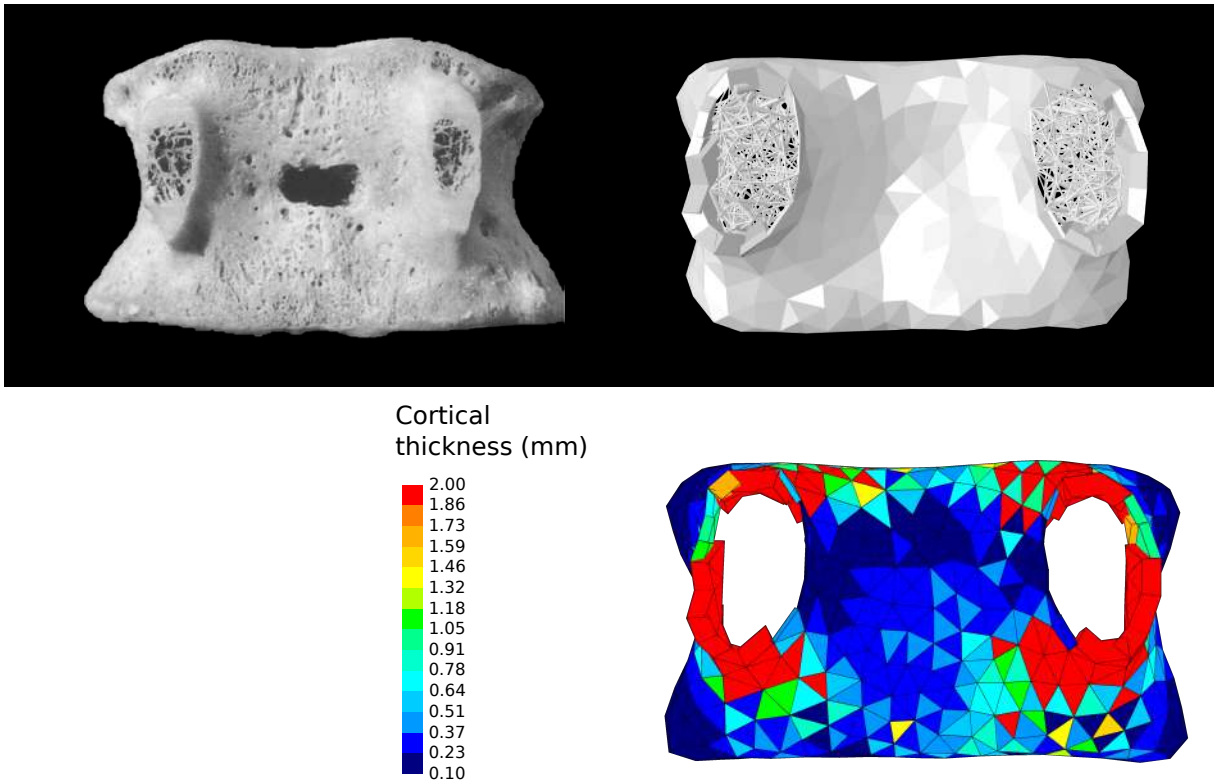

Figure 6.25: Coronal section through the pedicles of L2. On the left, photograph taken by Maillot & Wolfram-Gabel (1993). On the right, the corresponding section in the converged L2 model with truss elements in the dead zone removed. The color mapped version shows the variations in shell thickness in the model. Photograph is reproduced by permission from Springer Nature Customer Service Centre GmbH: Springer Nature, Surgical and Radiologic Anatomy, *Pedicles of lumbar vertebrae*, Maillot et al., © 1993).

Despite the limited number of in-vivo studies investigating the lumbar vertebra architecture in young healthy populations, this visual comparison at three lumbar levels is promising. It confirms that the adaptation approach used in the current study produces structural architectures similar to those observed in-vivo when load cases representative of daily living activities are applied. The next Section takes advantage of the numerical approach to investigate the influence of the different activities on the vertebral structure.

6.3.2 Contribution of each activity

The influence of each activity on the structural architecture of L4 is shown in Figures 6.26, 6.27, 6.28 and 6.29, where each element is assigned a colour corresponding to the activity producing the highest absolute maximum strain value. Most of the vertebra's architecture results from the lifting tasks with a large range of motion. The lifting while sitting activities directly influence the trabecular architecture in the posterior part of the vertebral body, the pedicles and the superior articular processes. The lifting while standing tasks cause the trabecular structure to develop in the anterior part of the vertebral body. It is also clear that lifting tasks performed from the right side influence the structure of the left transverse process due to the left lumbar muscle activating to extend and rotate the spine at the same time. The same phenomenon is observed on the opposite side.

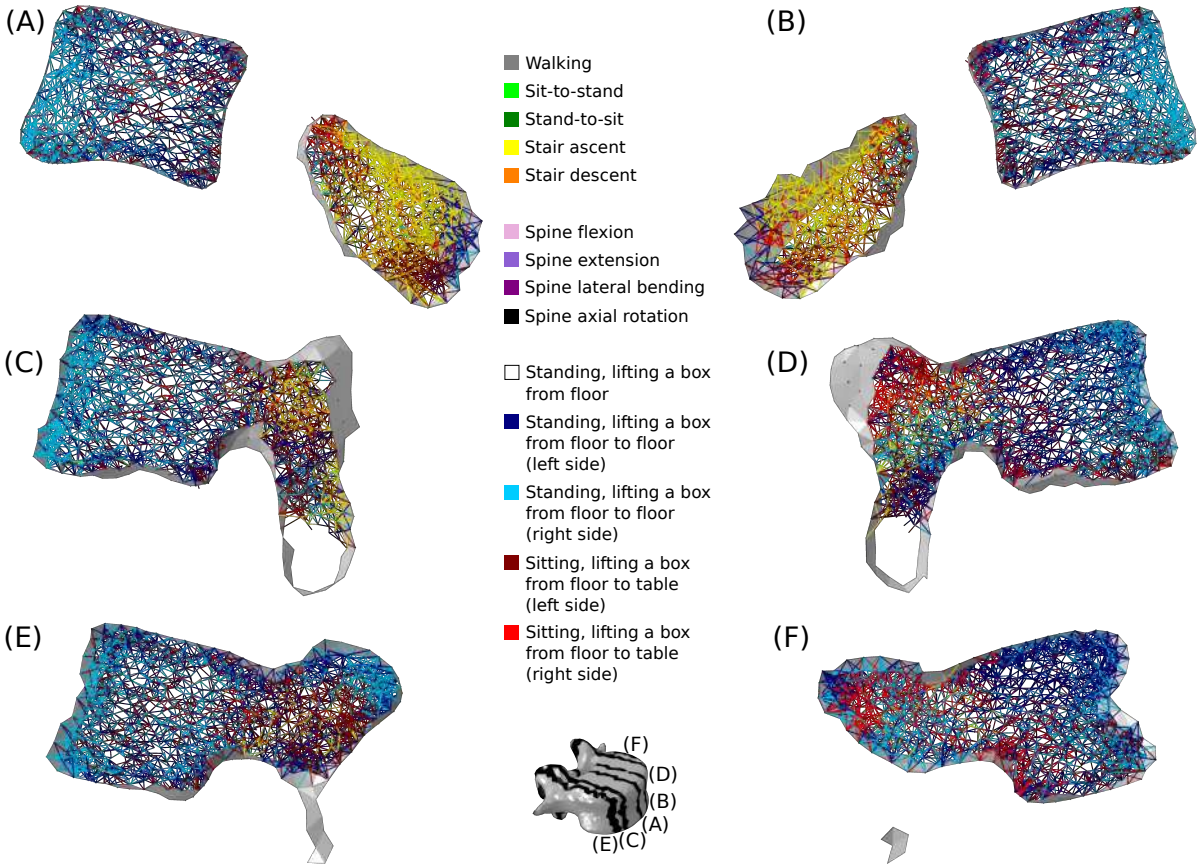

Figure 6.26: Selected sagittal 3 *mm* slices for the converged L4 model adapted to the 116 load cases representative of daily living. Cortical shells and trabecular truss elements are colour mapped based on the activity most influential to their final geometry. Only trabecular truss elements representing the ground matrix (with a radius of 0.1 *mm*) are shown.

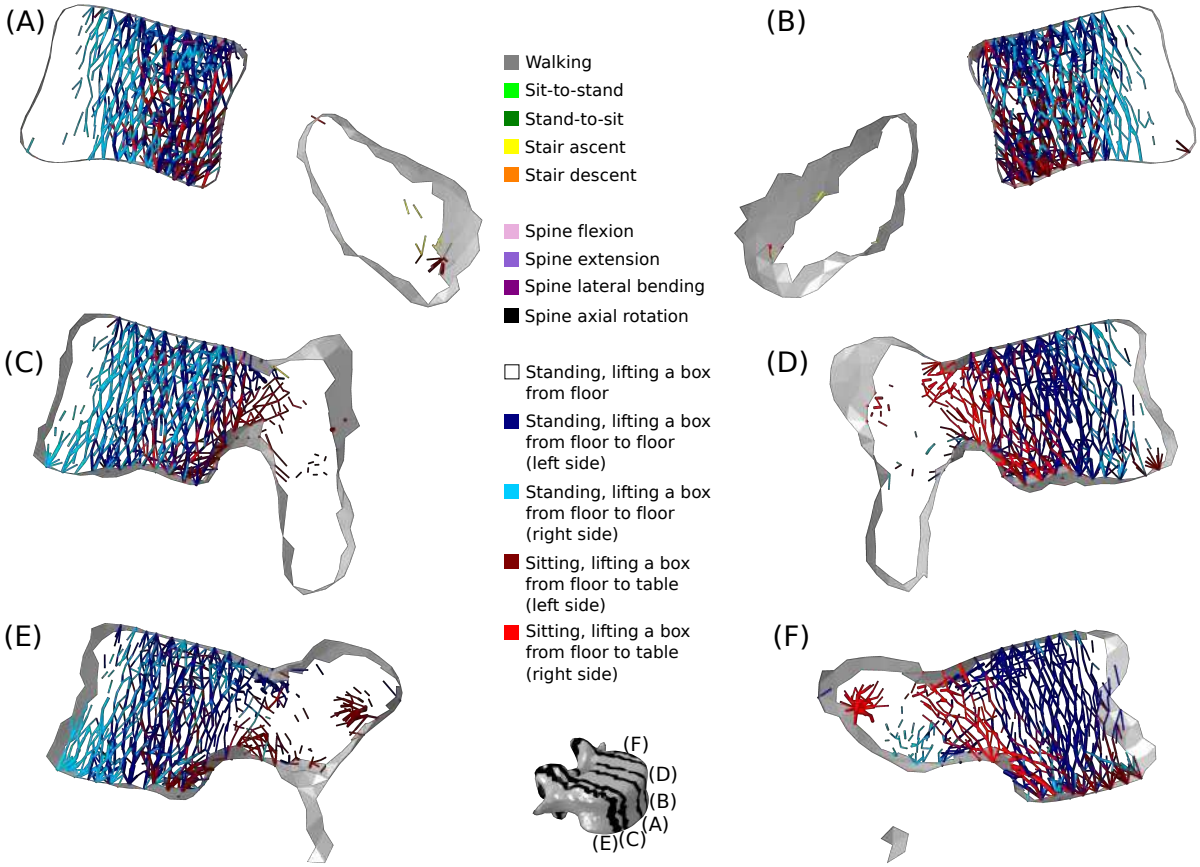

Figure 6.27: Selected sagittal 3 *mm* slices for the converged L4 model adapted to the 116 load cases representative of daily living. Cortical shells and trabecular truss elements are colour mapped based on the activity most influential to their final geometry. Only trabecular truss elements with a radius superior to 0.1 *mm* are shown.

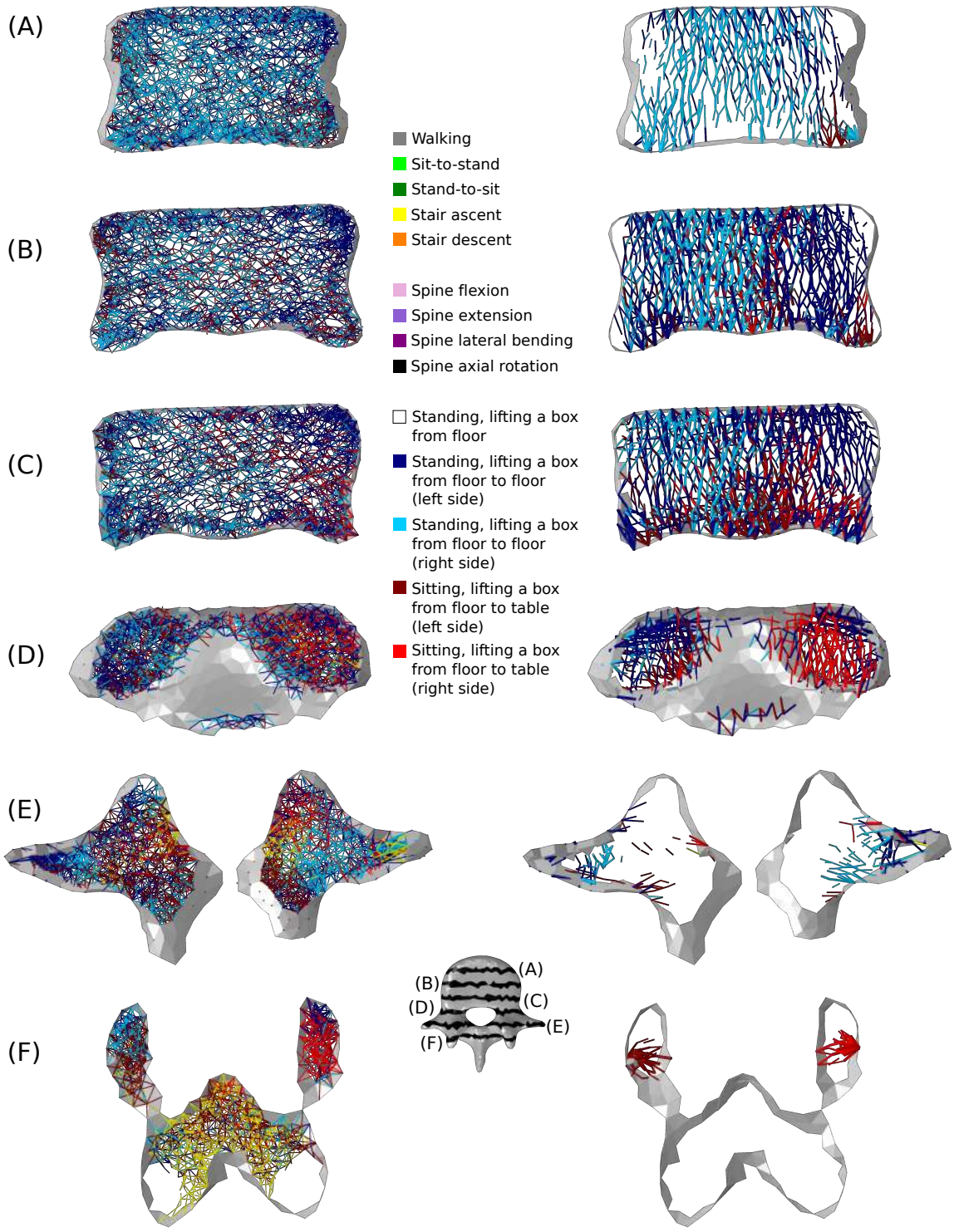

Figure 6.28: Selected transverse 3 mm slices for the converged L4 model adapted to the 116 load cases representative of daily living. Cortical shells and trabecular truss elements are colour mapped based on the activity most influential to their final geometry. On the left, trabecular truss elements with a radius inferior to 0.1 mm are omitted. On the right, only trabecular truss elements representing the ground matrix (with a radius of 0.1 mm) are shown.

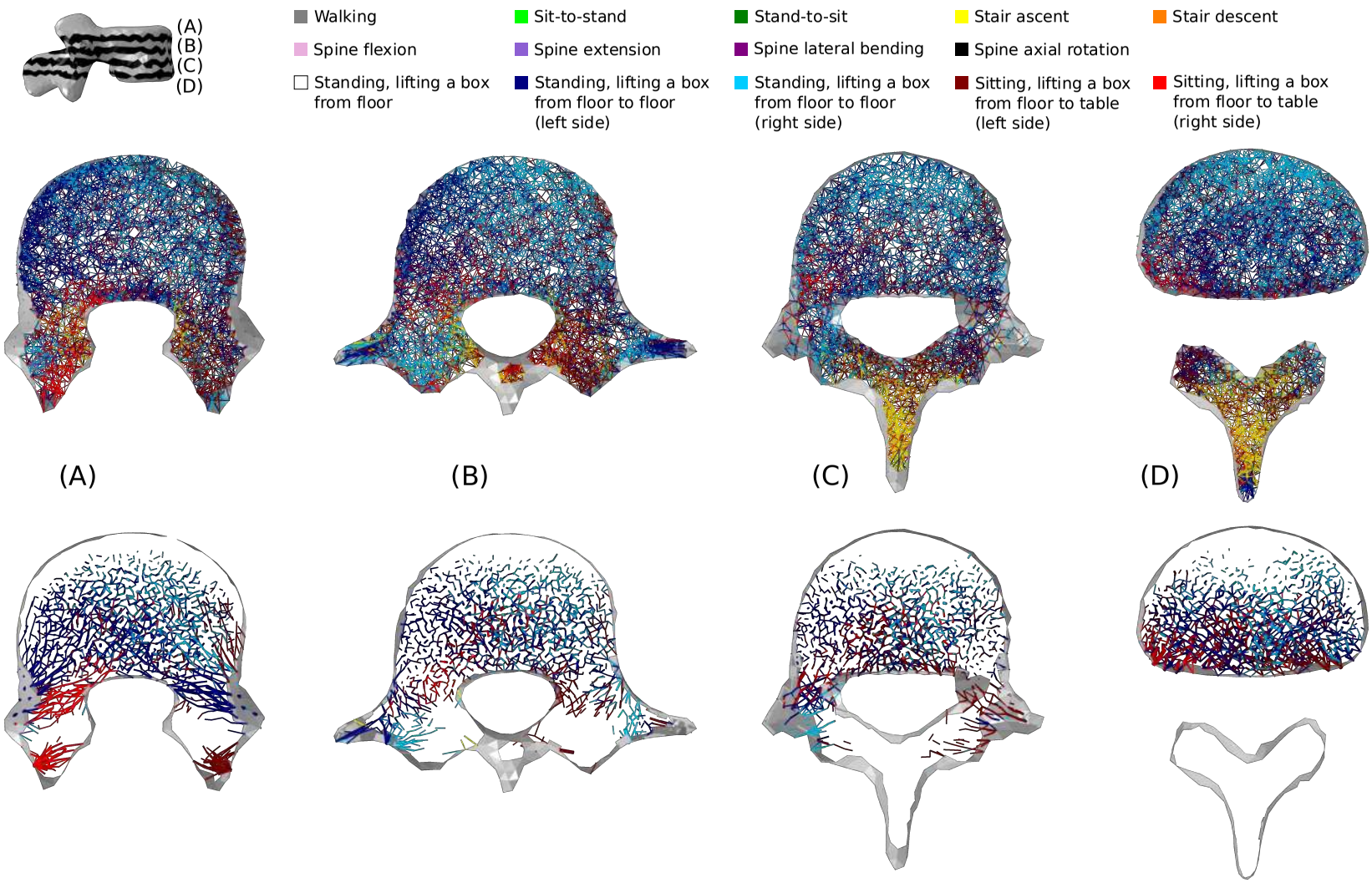

Figure 6.29: Selected transverse 3 mm slices for the converged L4 model adapted to the 116 load cases representative of daily living. Cortical shells and trabecular truss elements are colour mapped based on the activity most influential to their final geometry. Only trabecular truss elements with a radius superior to 0.1 mm are shown in the top row. Trabecular truss elements representing the ground matrix only (with a radius of 0.1 mm) are shown in the bottom row.

The majority of the vertebra's architecture appears to be primarily optimised for large movements of the spine involving lifting tasks. This was expected as such activities produce larger intervertebral loads (Figures 6.3 and 6.4) and potentially higher spine muscle activations than locomotion activities where the spine only requires to be stabilised in an upright position. It is interesting to note that the truss elements in the spinous process are mainly influenced by the stair ascent activity. In the musculoskeletal model, the musculotendons attached to the spinous process run along the direction of the spine (Figure 6.30). Their contribution in activities involving twisting and lateral bending of the spine is therefore very limited due to their small moment arms in these directions. In the sagittal plane however, they have a much bigger moment arm and can contribute to the extension of the spine. It is therefore reasonable to assume that lifting tasks in the sagittal plane would be the most demanding activities for these muscles. However, participants were allowed to bend their knees to lift the box and the spine extensor muscle activations were never very high as the spine flexion angle remained small. During stair ascent, the subjects bent slightly forward to look at the steps and extensors of the spine had to be activated to maintain a straight spine, producing a force similar to that required for the lifting tasks. However, when the subjects pushed on their legs to climb a step, the upward movement of the pelvis caused the spine to bend forward and spine extensors had to activate even more to prevent this, making stair ascent the most influencing activity for the trabecular architecture in the spinous process. Figure 6.31 illustrates this phenomenon by comparing activation of the multifidus musculotendons attached to the spinous process of L4 in stair ascent and standing lifting task.

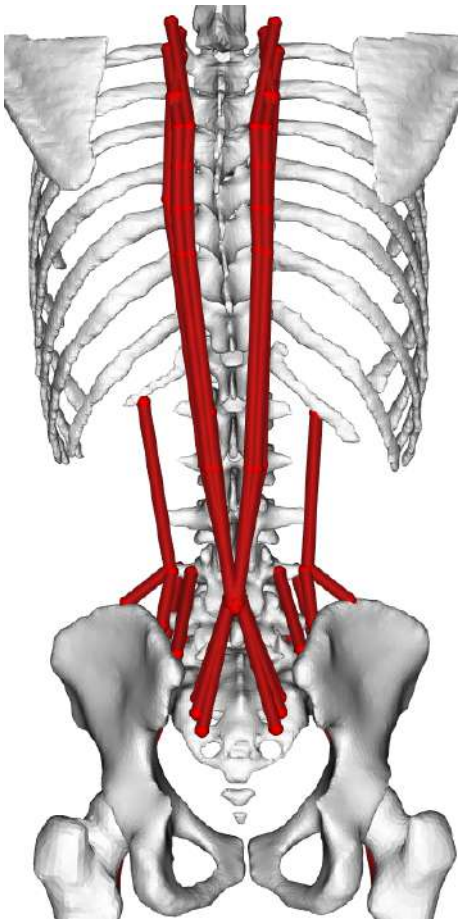

Figure 6.30: Posterior view of the musculotendon attaching to the L4 in the musculoskeletal model. The fibers attaching to the spinous process of L4 run along the direction of the spine making them particularly useful to extend the spine in the sagittal plane.

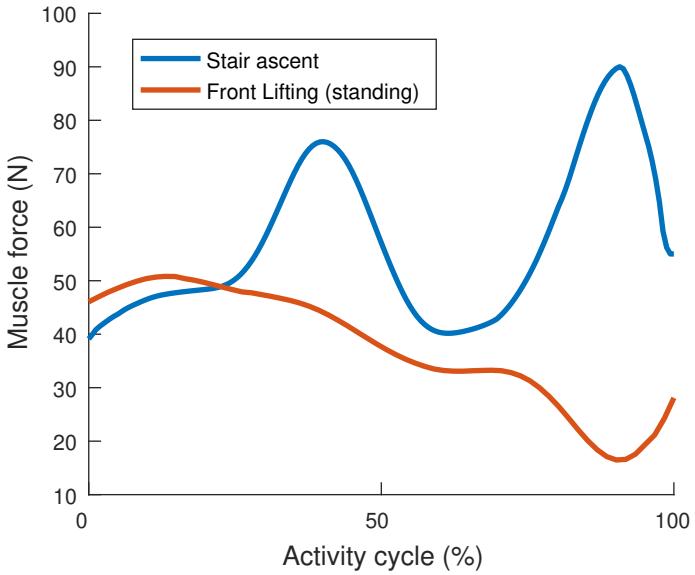

Figure 6.31: Force developed by the eight bundles of the left and right multifidus attached to the L4 spinous process for stair ascent and standing lifting task in the sagittal plane.

6.4 Discussion

Combining physiological loading representative of daily living activities with the bone structural adaptation algorithm in the modelling pipeline described in Chapter 2 produces cortical and trabecular vertebral structures which compare favorably with in-vivo observations. The assessement of the orientation of trabecular trajectories in the lumbar vertebrae with the sphere plots (Figures 6.17 and 6.18) confirmed the visual observations and gives a first assessment of bone anisotropy. Should a μCT scan of a full healthy lumbar vertebra become available, a similar method could be used to further validate the model. The computational cost of these converged mesoscale structural models of the lumbar vertebrae remains reasonable. With a total of 119588 elements, the L4 model converged in 20 iterations for the 116 loadcases, with each iteration taking 15 minutes (finite element analysis and structural adaptation) on a personal workstation (Intel Xeon E5-2630 v2 2.60 GHz, 12 CPUs, RAM 64 GB). This is extremely computationally efficient compared to microscale continuum models. In their microscale finite element approach, Tsubota et al. (2003) developed a model to investigate bone remodelling in the vertebra under vertical compression after insertion of a spinal fixation screw. They only modelled half of the vertebral body of L3, but at a resolution of 250 μm, they had to use 0.79 million voxel-based continuum elements. They did not report run times. Another microscale finite element study by Badilatti et al. (2015) investigated bone remodelling under a combination of three 1000 N loads in axial compression, antero-posterior shear, and medio-lateral shear. They developed a μCT derived model of the complete L2 at a resolution of 43.5 μm using 365 million elements. They reported a run time of 8 hours per iteration on a supercomputer with 1024 CPUs. Combined with the musculoskeletal model in the modelling pipeline, the mesoscale structural finite element adaptation has the potential to produce models of vertebrae adapted to a complex mechanical environment at a low computational cost. Some limitations inherent to the combined modelling approach and to the structural adaptation modelling choices remain and should be acknowledged.

Physiological loading and boundary conditions are essential to provide a realistic mechanical environment for finite element simulations (Bitsakos et al. 2005, Speirs et al. 2007, Phillips et al. 2007, Phillips 2009). The combined multiscale modelling approach relies

on a detailed musculoskeletal model with identical geometry to provide this mechanical environment. However, assumptions made for the musculoskeletal model will impact the finite element results (Wagner et al. 2010, Cronskaer et al. 2013, Zhu et al. 2013). The idealised representation of intervertebral joints in the musculoskeletal model requires the development of load applicators in the finite element model to spread the reaction force calculated at the fixed centre of rotation. In particular, the three degree of freedom joint neglects any possible translation normally limited by the intervertebral disc, ligaments and facet joints. These vertebral components also generate rotational stiffness which is accounted for with bushing elements in the musculoskeletal model. However, these bushings are located at the musculoskeletal joint centre. As discussed previously, this representation of intervertebral stiffness is not physiological and was not implemented in the finite element model. Figure 6.32 shows the converged mesoscale structural L4 model with the bushing moments applied with the current load applicators, using beam elements instead of trusses to transfer moments. For this particular model, the relative density of the vertebra was 143.15 %. The shell thickness in the vertebral body exceeds the range reported in the literature (0.2 to 0.9 mm (Ritzel et al. 1997, Edwards et al. 2001)) in most parts. With this example, it can be seen that applying a non-physiological loading in the finite element simulations results in overestimating the structural architecture of the vertebra. Future work will focus on implementing ligaments and discs in a finite element model of multiple spinal units. This is expected to reduce the impact of idealised musculoskeletal joints on the vertebra of interest. Because the bushing moments were not applied in the current finite element model, soft boundary conditions were used in the current finite element model to ensure numerical stability. The musculoskeletal model represents bones as rigid bodies while the finite element model allows bones to deform, which compromises the equilibrium condition found in the musculoskeletal simulations. Should all the musculoskeletal loads be included, such as in the example shown in Figure 6.32, soft boundary conditions would still be needed to maintain numerical stability.

The converged mesoscale structural model shows discontinuities in the cortex, with shell thickness varying significantly from one element to the next in some locations. This phenomenon should be addressed in future work to provide a smoother and more realistic thickness variation across the vertebral cortex, potentially constraining thickness adaptation of each element with the thickness of its neighbours. Another limitation of the

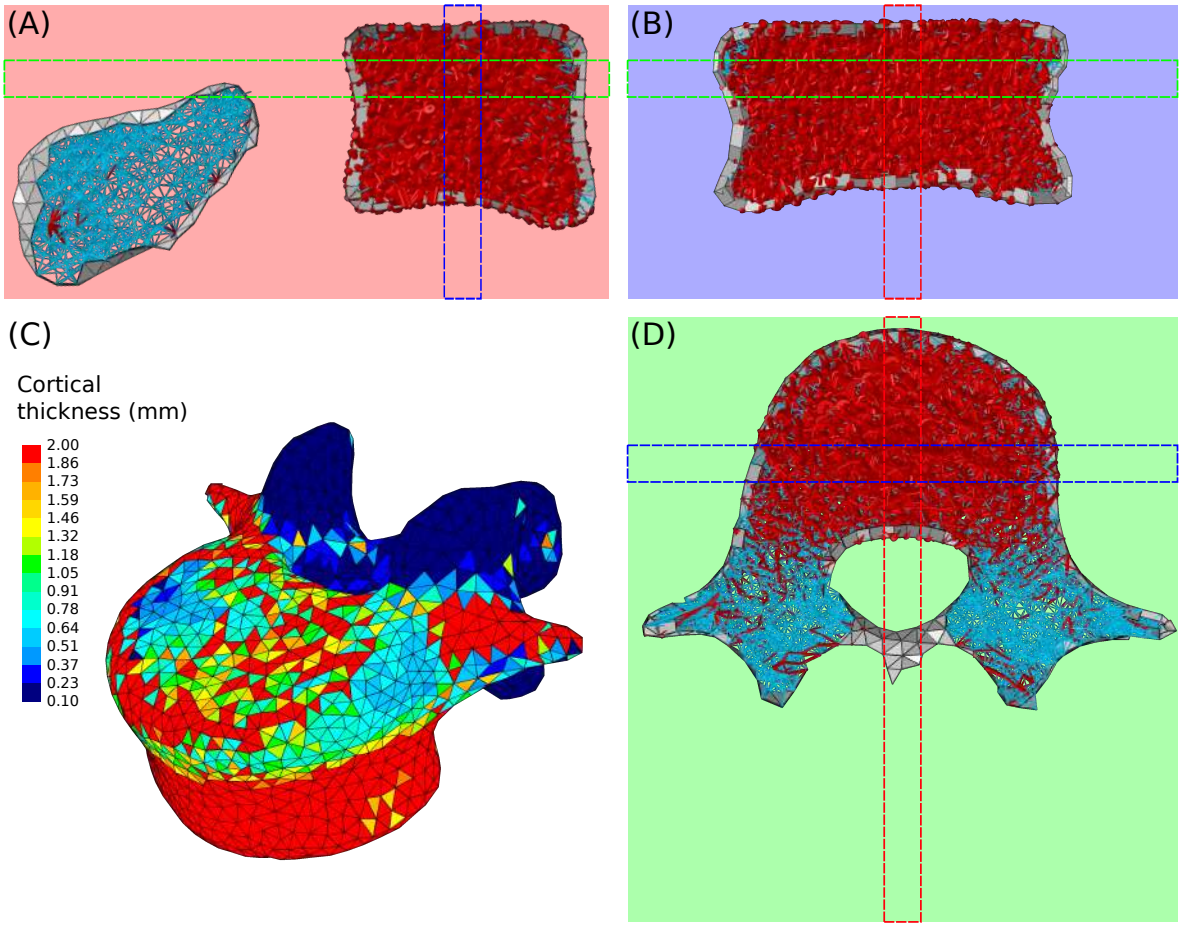

Figure 6.32: Structural architecture of L4 adapted to 116 load cases representative of 18 activities of daily living, with inclusion of bushing moments. 4 *mm* (A) midsagittal, (B) midcoronal and (D) through processes transverse slices showing the internal architecture. Cortical shell elements are shown in grey. Trabecular truss elements with a radius of 0.1 *mm* representing the ground matrix are shown in blue. Thicker truss elements are shown in red. Truss elements in the dead zone (with a radius of 1 µm) are not shown for clarity. (C) Cortical thickness ranging from 0.1 to 2 *mm*.

structural approach is the geometry of the truss elements representing trabecular bone. In-vivo observations show a combination of rod-like and plate-like trabeculae in the vertebral body. Many studies have investigated the role of these two types of trabeculae. Although transverse trabecular rods have been shown to contribute largely to the mechanical stiffness in the transverse plane of the vertebral body (Liu et al. 2009), trabecular plates appear to have a dominant role in defining the elastic properties of trabecular bone (Liu et al. 2006, Liu et al. 2007, Wang et al. 2013). The circular section truss elements used in the structural model are suitable to model the rod-like trabeculae, but may be insufficient to capture the mechanical behaviour of plate-like trabeculae, resulting in a higher trabecular density in the converged model. The trabecular density in the mod-

el is also impacted by the choice of element for the trabeculae. If it has been shown that truss elements ensure a physiological macroscale behaviour of bone (Villette & Phillips 2015, Villette & Phillips 2018), local architecture may be improved through using a beam element based bone adaptation with an alternative approach to generating the initial network (Phillips 2019a, Phillips 2019b, Phillips 2019c). It is also important to note that the range of truss element diameters in the converged models exceed the range reported by Rho et al. (1998) and Keaveny et al. (2002) (100 to 300 μm), with maximum diameters of 736 μm found in L5. However, very few elements are outside the reported physiological range, although radii of up to 2 *mm* are allowed during adaptation (Figure 6.33). In all cases, ground matrix elements represent more than 80% of the total number of trabecular elements. Refining the trabecular size categories in the adaptation algorithm may improve the match between converged models and in-vivo observations. An additional limitation characteristic of the strain-driven adaptation approach is the choice of values for the target strain, lazy zone and dead zone in the optimisation algorithm. These values are in agreement with previous studies (Aamodt et al. 1997, Phillips 2012, Zaharie & Phillips 2018) and provide reasonable results, but are likely to change depending on age, sex, pathological conditions, and even regions of the skeletal system.

Despite the aforementioned limitations, the structural adaptation finite element approach presented in this Chapter as part of the combined musculoskeletal and finite element modelling pipeline shows promising results when predicting healthy bone architecture. This computational approach can easily be used to investigate different loading scenarios representative of altered living conditions. Chapter 7 uses the approach to investigate the influence of spine movements and lifting tasks on the structural architecture of the lumbar vertebrae.

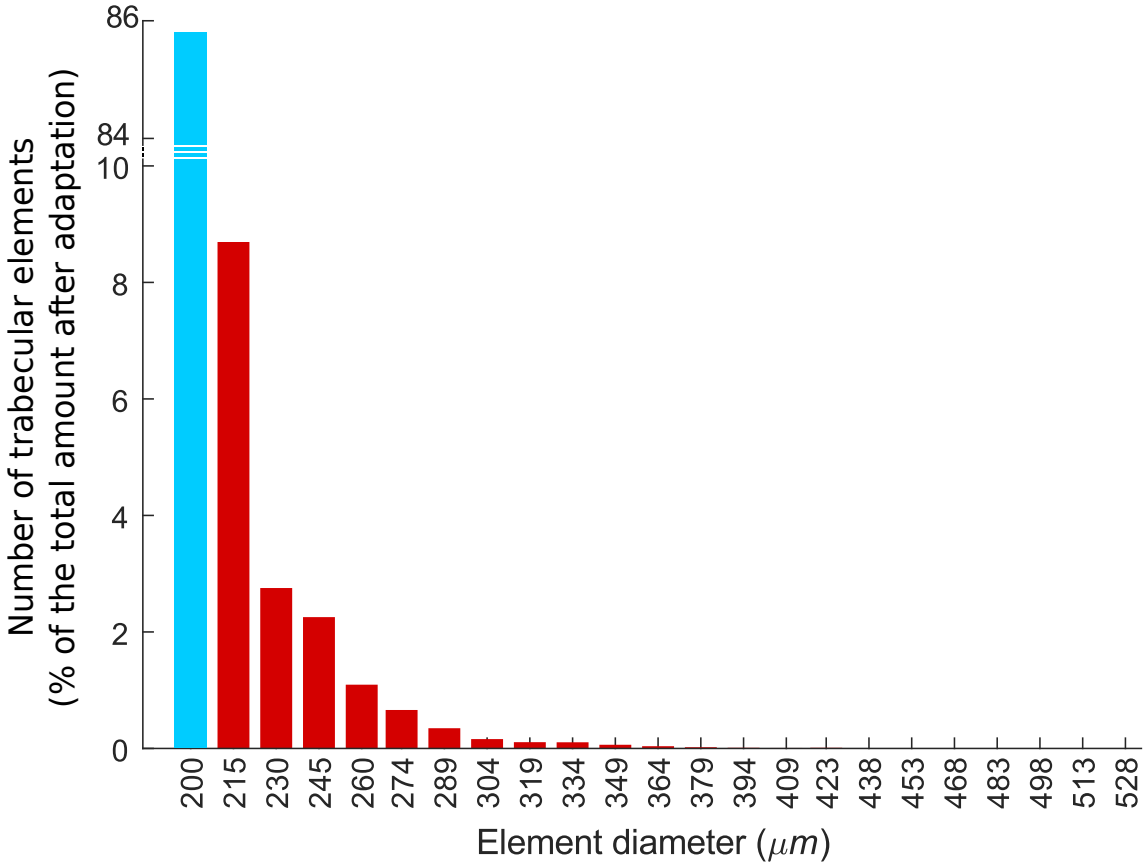

Figure 6.33: Number of trabecular elements in each diameter category for the converged L4 model. The blue bar corresponds to ground matrix elements. The red bars correspond to thicker trabecular truss elements.

Chapter 7

Adaptation of lumbar vertebrae to different loading scenarios

This Chapter uses the modelling pipeline described in the previous Chapters to investigate the effect of different activities on the structure of the lumbar vertebrae. Exemplar results are shown in this Chapter, while the complete results for each lumbar vertebra are included in Appendix C. The study is based on the same healthy volunteer (26 yo, 175 cm, 67.8 kg) as Chapter 5 and 6.

7.1 Introduction

Chapter 6 presented mesoscale finite element models of the lumbar vertebrae adapted to 18 activities of daily living. These activities are assumed to be representative of a healthy lifestyle. The converged models showed a structure similar to that observed in-vivo. Using the same modelling pipeline, it is possible to investigate the influence of different sets of activities on the structural adaptation of the vertebrae. The contribution of each activity was highlighted in Chapter 6, Section 6.3.2, and it was found that most of the lumbar vertebrae's structure is influenced by large spine movements rather than lower limb dominant activities. In this Chapter, two sets of activities are tested to investigate the importance of lower limb dominant activities for the adaptation of the lumbar vertebrae. One of the set involves only lower limb dominant activities while the other only focuses on spine dominant activities. Models of the five lumbar vertebrae adapted to these sets of activities are shown in Section 7.2. The in-silico approach developed in this thesis allows for time-dependent hypothesis to be tested in a time efficient way without putting a patient at risk. Section 7.3 takes advantage of this feature to investigate the effect of a simplified low back pain scenario where a subject may opt not to perform lifting tasks or reach their feet. For practical reasons, the spine dominant activities will be called spine activities, while lower limb dominant activities will be called locomotion activities in this Chapter. The set of 18 activities of daily living representative of a healthy lifestyle is referred to as the healthy scenario, while the back pain scenario refers to the altered loading conditions without any lifting tasks or large spine movement tasks.

7.2 Spine dominant versus lower limb dominant activities

The mobility of the lumbar spine is paramount for balance strategies. This is particularly relevant during locomotion activities where the position of the body's center of mass has to be adjusted continuously. One would think the lumbar vertebrae should therefore be adapted to these important activities. However, the healthy scenario investigated in Chapter 6 showed that locomotion activities have a limited influence on the structure of the lumbar vertebrae. Using the modelling pipeline, the influence of such activities were investigated for all lumbar vertebrae.

7.2.1 Loading scenario

Two loading scenarios were investigated for the five lumbar vertebrae. The first scenario was based on spine activities, while the second scenario implemented locomotion activities. The spine activities include the six static positions of the spine and the seven more demanding activities involving spine movements while sitting and standing described in Chapter 6, Section 6.2.2.1. The locomotion activities include level walking, stair ascent, stair descent, sit-to-stand and stand-to-sit. For each vertebra in each loading scenario, a mesoscale structural finite element model was developed and adapted to the corresponding set of load cases determined using the method described in Chapter 6, Section 6.2. The number of load cases for each vertebra in each scenario is indicated in Table 7.1.

Table 7.1: Characteristics of the converged mesoscale structural finite element models after adaptation to healthy, spine activities and locomotion activities scenarios.

		L1	L2	L3	L4	L5	Average
	Trabecular elements (initial mesh)	89042	101805	115063	115988	130460	110471.6
	Total vertebra volume (mm^3)	54400	59320	69630	70094	78820	66453
Healthy scenario	Load cases	114	115	118	116	113	115.2
	Iterations	25	23	30	20	27	25
	Trabecular elements (converged model)	79826	86905	93452	98558	96483	91044.8
	Trabecular connectivity						
	Mean (SD)	18.20 (3.96)	17.45 (4.23)	16.77 (4.30)	17.21 (3.96)	16.38 (4.36)	17.20 (4.16)
	Minimum	1	1	1	1	1	1
	Maximum	49	45	53	46	31	44.8
	Trabecular volume (mm^3)	9185	7948	7828	9010	10050	8804
	Cortical volume (mm^3)	6026	4608	3875	4877	2249	4327
	Relative density (% of bone volume over total volume)	27.96	21.17	16.81	19.81	15.60	20.27
	Dead elements (% of initial trabecular elements)	10.35	14.64	18.78	15.03	26.04	16.97
Spine activities	Load cases	73	77	77	75	71	74.6
	Iterations	28	22	27	22	27	25.2
	Trabecular elements (converged model)	79546	86856	93513	97278	96531	90744.8
	Trabecular connectivity						
	Mean (SD)	18.15 (3.95)	17.44 (4.23)	16.76 (4.32)	17.09 (4.00)	16.35 (4.36)	17.16 (4.17)
	Minimum	1	1	1	1	1	1
	Maximum	49	45	53	46	31	44.8
	Trabecular volume (mm^3)	9139	7947	7831	8942	10044	8780
	Cortical volume (mm^3)	5978	4607	3873	4783	2243	4297
	Relative density (% of bone volume over total volume)	27.79	21.16	16.81	19.58	15.59	20.19
	Dead elements (% of initial trabecular elements)	10.66	14.68	18.73	16.13	26.01	17.24
Locomotion activities	Load cases	41	38	41	41	42	40.6
	Iterations	27	25	91	35	35	42.6
	Trabecular elements (converged model)	50251	60741	43923	66537	61834	56657.2
	Trabecular connectivity						
	Mean (SD)	14.32 (4.56)	13.77 (4.50)	11.63 (4.61)	13.19 (4.45)	13.74 (4.73)	13.33 (4.57)
	Minimum	1	1	1	1	1	1
	Maximum	28	30	37	41	28	32.8
	Trabecular volume (mm^3)	2943	3301	2616	3865	4269	3399
	Cortical volume (mm^3)	1373	1433	1486	2434	1560	1657
	Relative density (% of bone volume over total volume)	7.93	7.98	5.89	8.99	7.40	7.64
	Dead elements (% of initial trabecular elements)	43.56	40.34	61.83	42.63	52.60	48.19

7.2.2 Results

The average number of load cases over the five lumbar vertebrae was 74.6 for the thirteen spine activities scenario and 40.6 for the five locomotion activities scenario. The structural finite element models converged in fewer iterations for the spine activities, with an average of 25.2 iterations against 42.6 for the locomotion activities. On average, vertebrae produced with the spine activities scenario contained a relative density of 20.19%, with a mean connectivity of 17.16 (SD 4.17) and 17.24% of the trabecular elements in the dead zone. In the locomotion activities scenario, relative density was only 7.64%, with a mean connectivity of 13.33 (SD 4.57) and 48.19% of the trabecular elements in the dead zone. The spine activities results show a high similarity with the converged models subjected to the healthy scenario, with a difference of 0.4% in bone volume on average. The difference in bone volume between the locomotion activities scenario and the healthy scenario was 61.5% on average for the five lumbar vertebrae. Table 7.1 shows detailed results for the three scenarios mentioned here.

7.2.2.1 Cortical thickness

Figure 7.1 shows the cortical shell thickness for the converged lumbar vertebrae models in the healthy, spine activities and locomotion activities scenarios. In the healthy scenario, the cortex thickens in the transverse processes for L1, L2, L3 and L4. The cortical shells of the spinous process of L1 also thicken. L5 has a thinner cortex overall. A similar pattern can be observed at all lumbar levels in the spine activities scenario. The locomotion activities minimally influence cortical thickness in the transverse and spinous processes of all lumbar vertebrae. Figure 7.2 focuses on coronal sections through the pedicles for the five lumbar vertebrae in the three scenarios mentioned before. In both the healthy and spine activities scenarios, L1, L2, L3 and L4 have a typical thickness pattern, with the inferior and superior parts of the pedicles being thicker than the medial and lateral parts. This is potentially due to the pedicles having to resist bending along the medio-lateral axis during flexion-extension movements. L5 does not show this pattern for reasons potentially related to its shape, function, and muscular environment. In the spine activities scenario, the pedicle cortex is thin for all lumbar vertebrae, as muscles are balancing the spine

in an upright position, creating smaller bending moments along the medio-lateral axis. The pedicles of L5 are shorter and larger than the pedicles of the other lumbar vertebrae as they merge with the transverse processes closer to the vertebral body, resulting in an improved load spreading across the surface of the pedicle. The load acting on the posterior parts of L5 is thought to be smaller as a result of the limited range of motion of this vertebra and the smaller number of muscles attached to it. This results in a thinner cortex across the three scenarios.

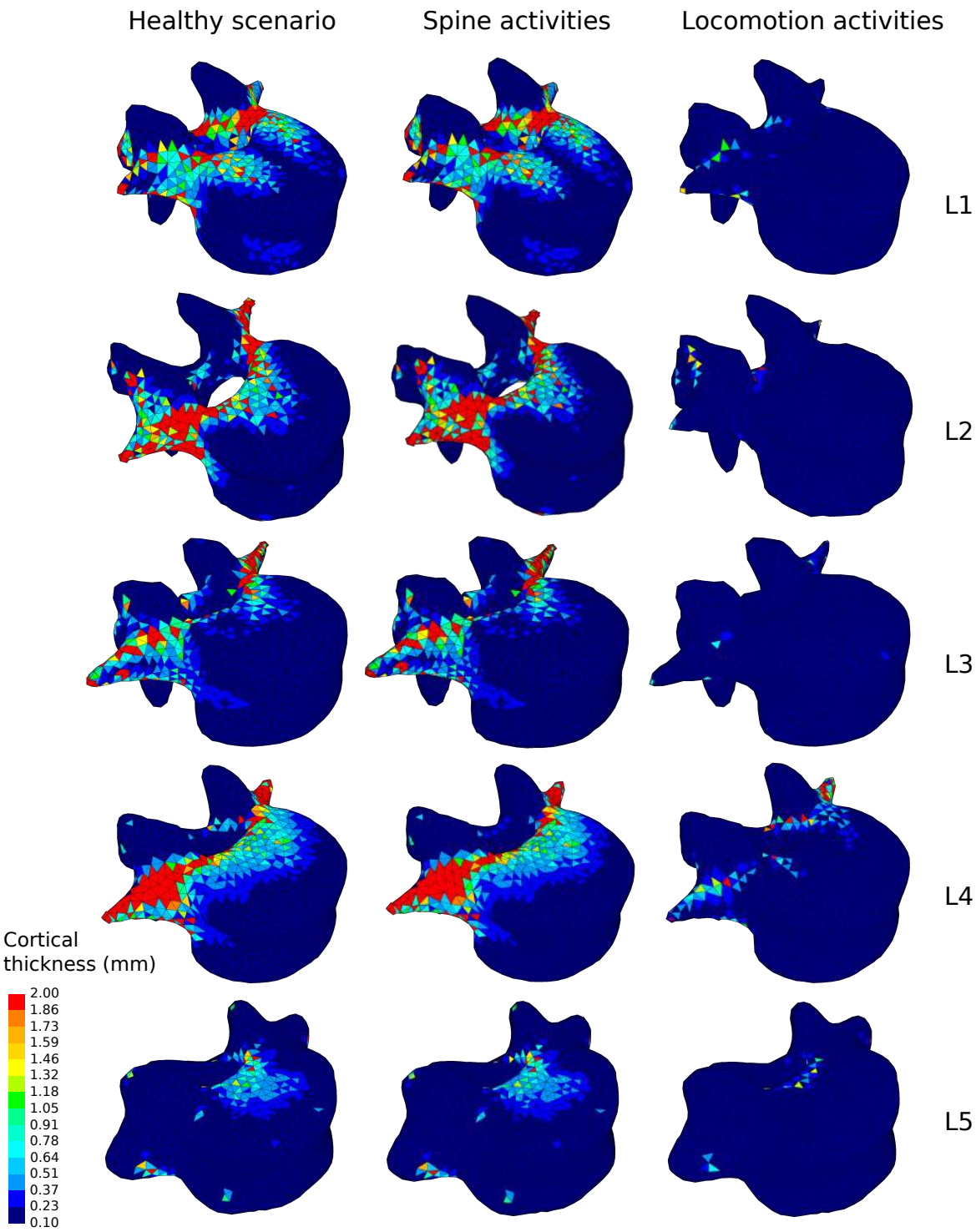

Figure 7.1: Cortical thickness of the converged mesoscale structural models of the lumbar vertebrae ranging from 0.1 to 2.0 mm adapted to the healthy, spine activities and locomotion activities scenarios.

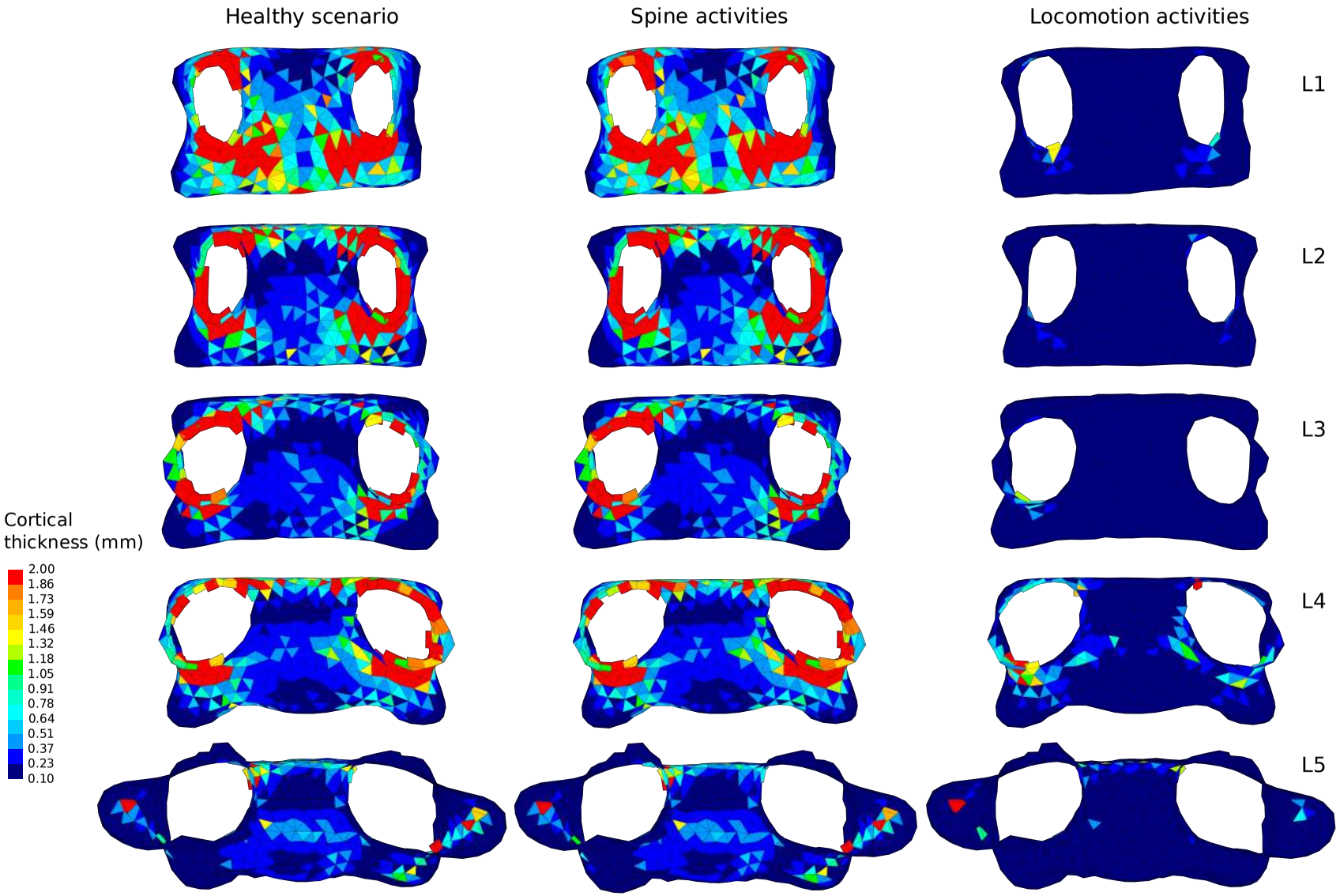

Figure 7.2: Coronal section through the pedicles of the converged mesoscale structural models of the lumbar vertebrae adapted to the healthy, spine activities and locomotion activities scenarios, showing cortical thickness ranging from 0.1 to 2.0 mm.

7.2.2.2 Trabecular architecture

Figures 7.3, 7.4 and 7.5 show the trabecular architecture of the five converged lumbar vertebrae models for the three scenarios. In these Figures, the ground matrix made of the thinnest trabeculae and primary architecture made of thicker trabeculae are highlighted in the three anatomical planes. For the healthy scenario, trabecular ground matrix fills most of the vertebra volume at all lumbar levels, apart from some areas in the spinous processes of L2, L3 and L5, and in the transverse processes of L5. The same observation can be made for the thicker trabecular trusses which are almost nonexistent in the spinous processes at all levels and in the transverse processes of L5. This is potentially due to the absence of ligaments in the finite element models, especially the supraspinous and interspinous ligaments normally attached to the spinous process (Figure 2.7) and the iliolumbar ligaments linking the transverse processes of L5 to the pelvis (Figure 2.4). In the spine activities scenario, a similar trabecular architecture is observed at all lumbar levels. The structure differs largely in the locomotion activities scenario. In this case, the thicker truss elements are sparser and mainly located in the center of the vertebral body of each vertebra. The ground matrix has almost disappeared from the spinous processes of all lumbar vertebrae. Transverse processes of L1, L3 and L5 also have ground matrix elements missing. L3, L4 and L5 are missing trabecular elements in the frontal part of the vertebral body. As seen for L4 in Chapter 6, Section 6.2.2.1, Figures 6.3 and 6.4, intervertebral reaction loads for locomotion activities are smaller and mainly acting in vertical compression compared to spine activities. Reaction loads at the other lumbar joints are shown in Appendix C. For locomotion activities, the lumbar muscle activations are also limited to balancing the spine. The reduced muscle and joint reaction forces explain the scarce trabecular architecture.

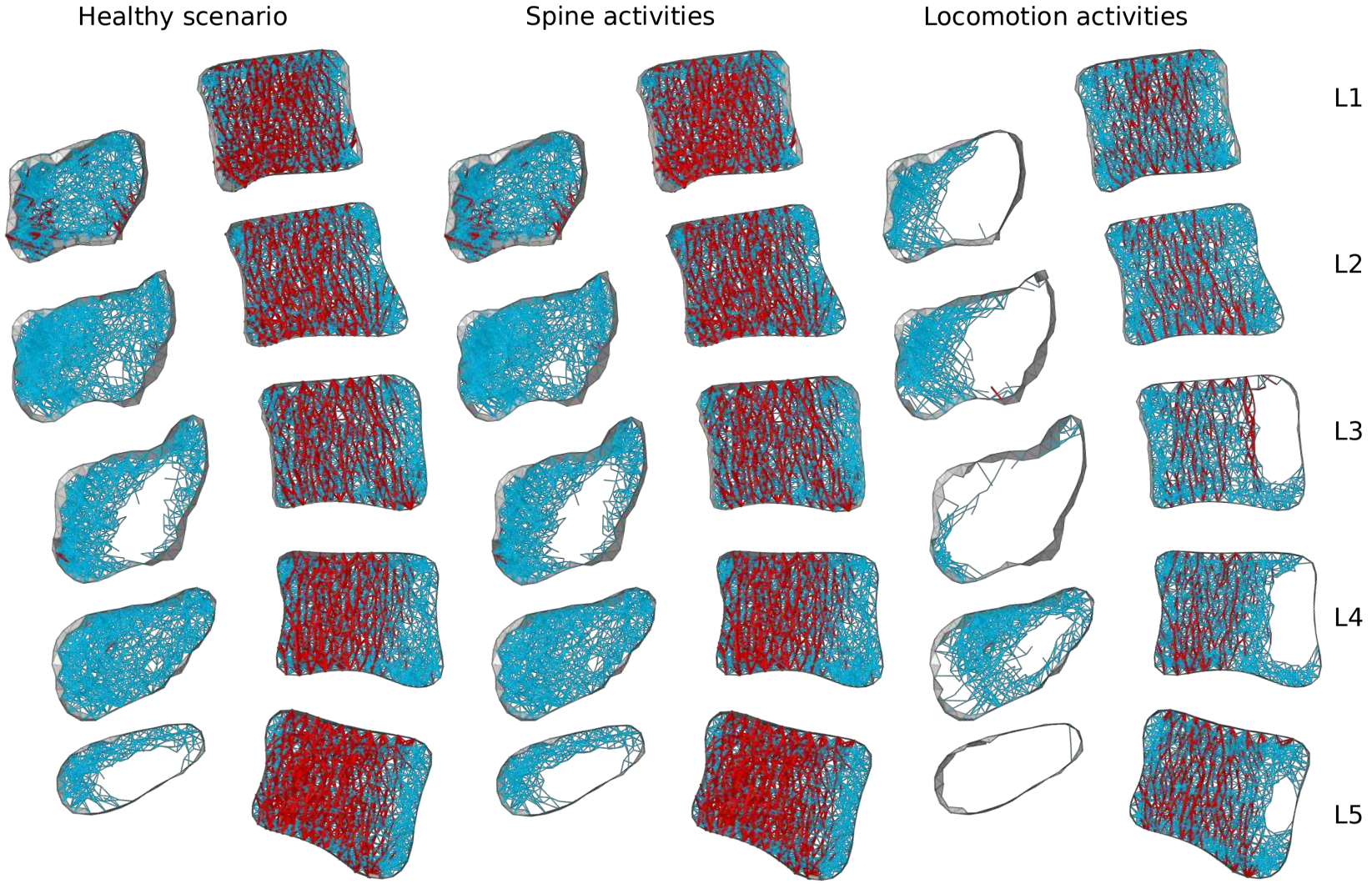

Figure 7.3: 3 mm mid-sagittal slices for the converged models adapted to the three scenarios. Cortical shell elements are shown in grey. Trabecular truss elements representing the ground matrix (with a radius of 0.1 mm) are shown in blue. Thicker truss elements are shown in red. Truss elements in the dead zone (with a radius of 1 μm) are not shown for clarity.

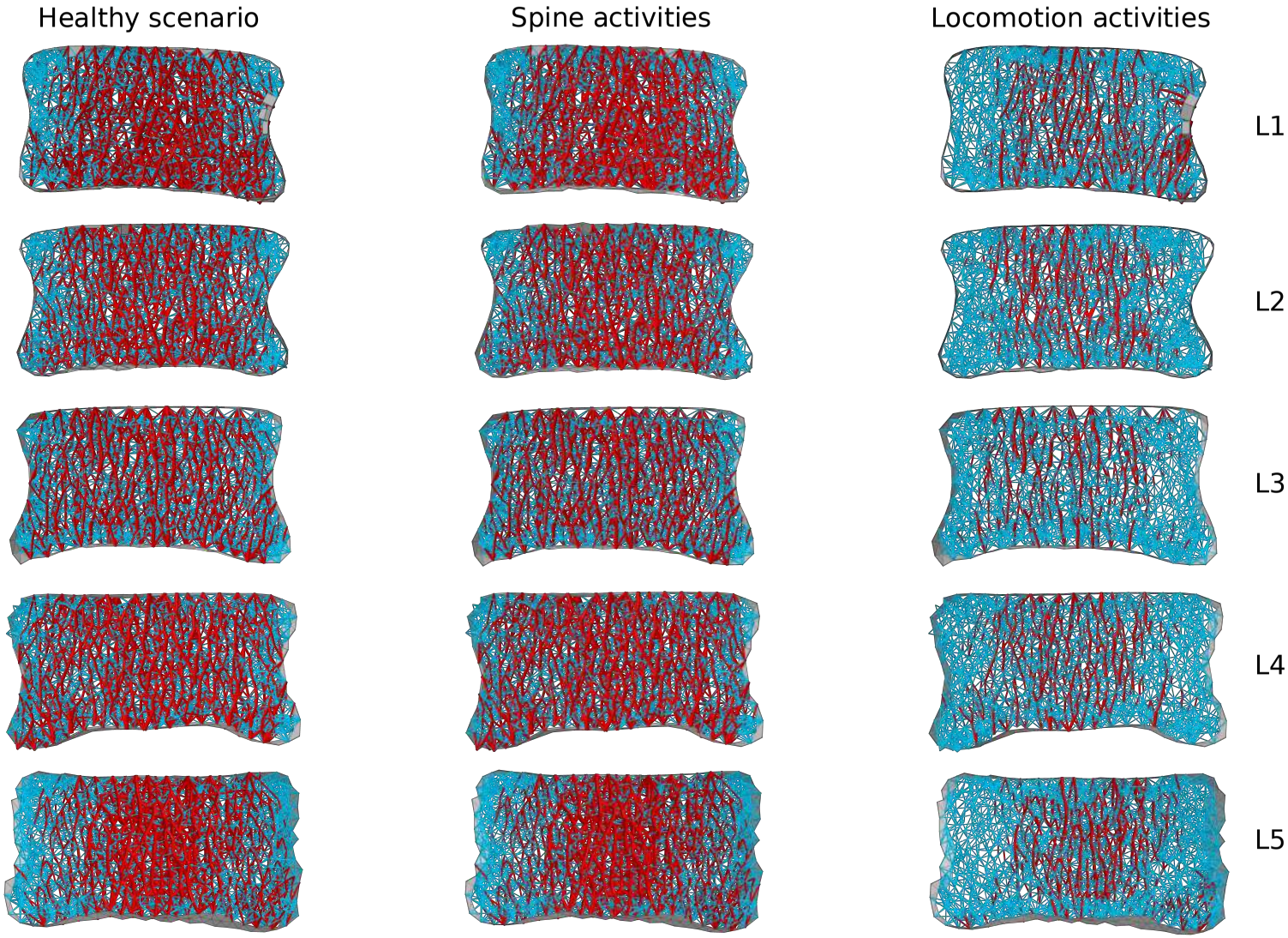

Figure 7.4: 3 *mm* coronal slices through the mid-point of the vertebral body for the converged models adapted to the three scenarios. Cortical shell elements are shown in grey. Trabecular truss elements representing the ground matrix (with a radius of 0.1 *mm*) are shown in blue. Thicker truss elements are shown in red. Truss elements in the dead zone (with a radius of 1 μm) are not shown for clarity.

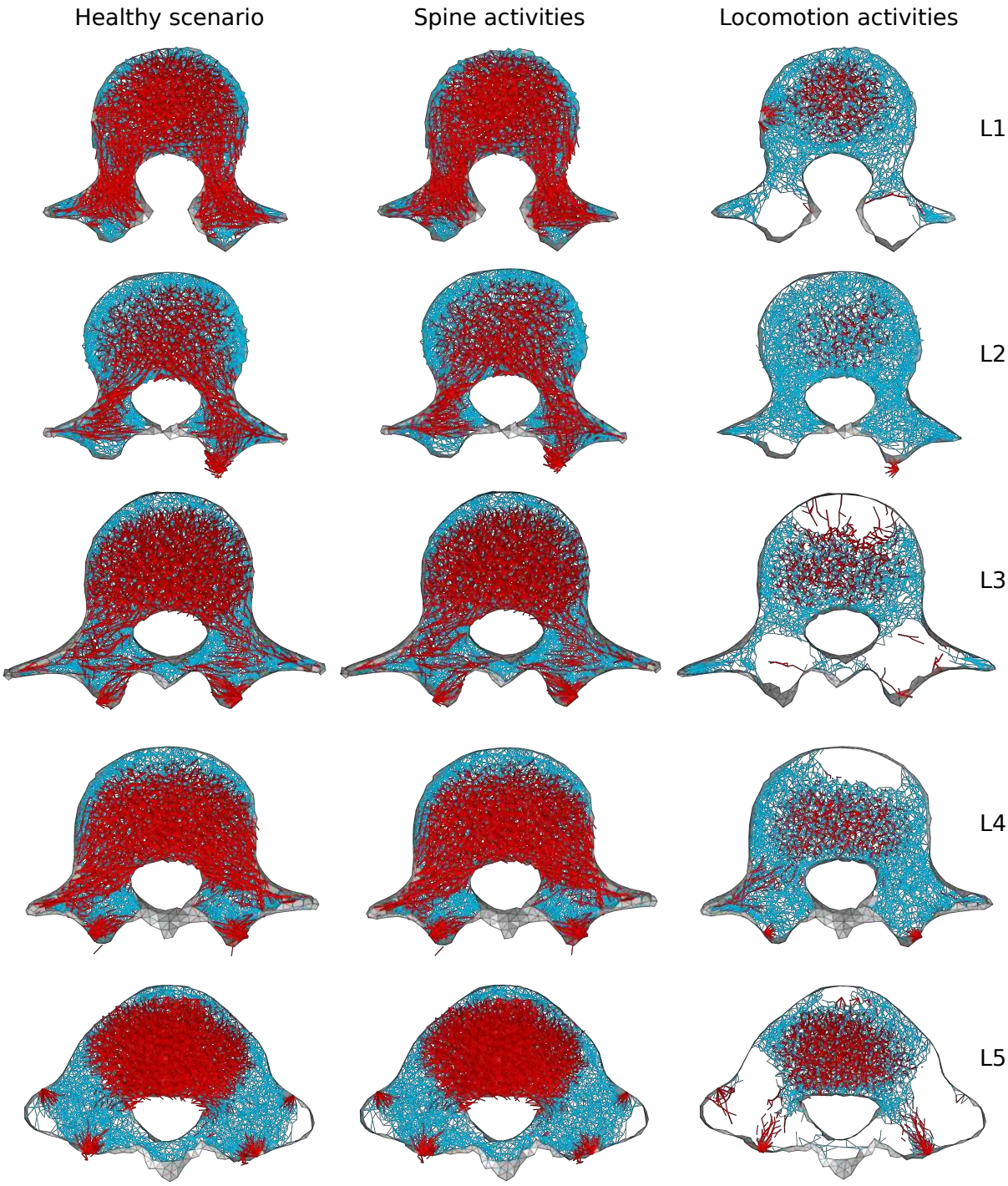

Figure 7.5: Through-processes transverse slices for the converged models adapted to the three scenarios. In the background, cortical shell elements are shown in grey and trabecular truss elements representing the ground matrix (with a radius of 0.1 mm) are shown in blue for a 3 mm slice. Thicker truss elements located between the superior endplate and the through-processes transverse slice are shown in red. Truss elements in the dead zone (with a radius of 1 µm) are not shown for clarity.

7.2.2.3 Contribution of each activity

The contribution of each activity used in the three scenarios to the adaptation of the cortex is highlighted in Figure 7.6. In the healthy scenario, spine activities were the most influential, especially the lifting activities involving bending and twisting of the spine. In particular, the tasks consisting of moving a box from left to right and from right to left were primarily responsible for cortical adaptation in the transverse processes. The lifting while sitting tasks were more limited to the adaptation of the vertebral bodies. A few shell elements of L3 are most influenced by the sagittal plane lifting task. Spine flexion and extension also influenced parts of L5. For L4, stair ascent influences parts of the spinous cortex, as explained in Chapter 6, Section 6.3.2. The activity mapping pattern of the healthy scenario is similar to the pattern produced by the spine activities scenario for the five lumbar vertebrae. In the locomotion activities scenario, stair ascent and sit-to-stand are the most influential activities. Walking and stand-to-sit contribute to the cortex adaptation in the transverse processes and the endplates of L2, L3 and L4. Stair descent did not influence significantly cortical adaptation at any lumbar level.

Focusing on the contribution of activities to the adaptation of the trabecular structure, a difference between ground matrix (Figures 7.7, 7.9 and 7.11) and thicker trabeculae (Figures 7.8, 7.10 and 7.12) can be made. In the spine activities scenario, thicker trabeculae resisting vertical compression are only influenced by lifting tasks. These tasks also contribute to the adaptation of the ground matrix, but spine flexion and extension activity contributions can be observed in the vertebral bodies of L1, L2 and L5, and in the spinous process of L2 and L5. The trabecular architecture in the healthy scenario is influenced by the same spine activities, although some trabecular elements influenced by the stair ascent activity can be observed in L1, L4 and L5. In the locomotion activities scenario, stair ascent and sit-to-stand activities are most influential for most of the trabecular structure. Walking also contributes to the adaptation of the ground matrix in most vertebrae.

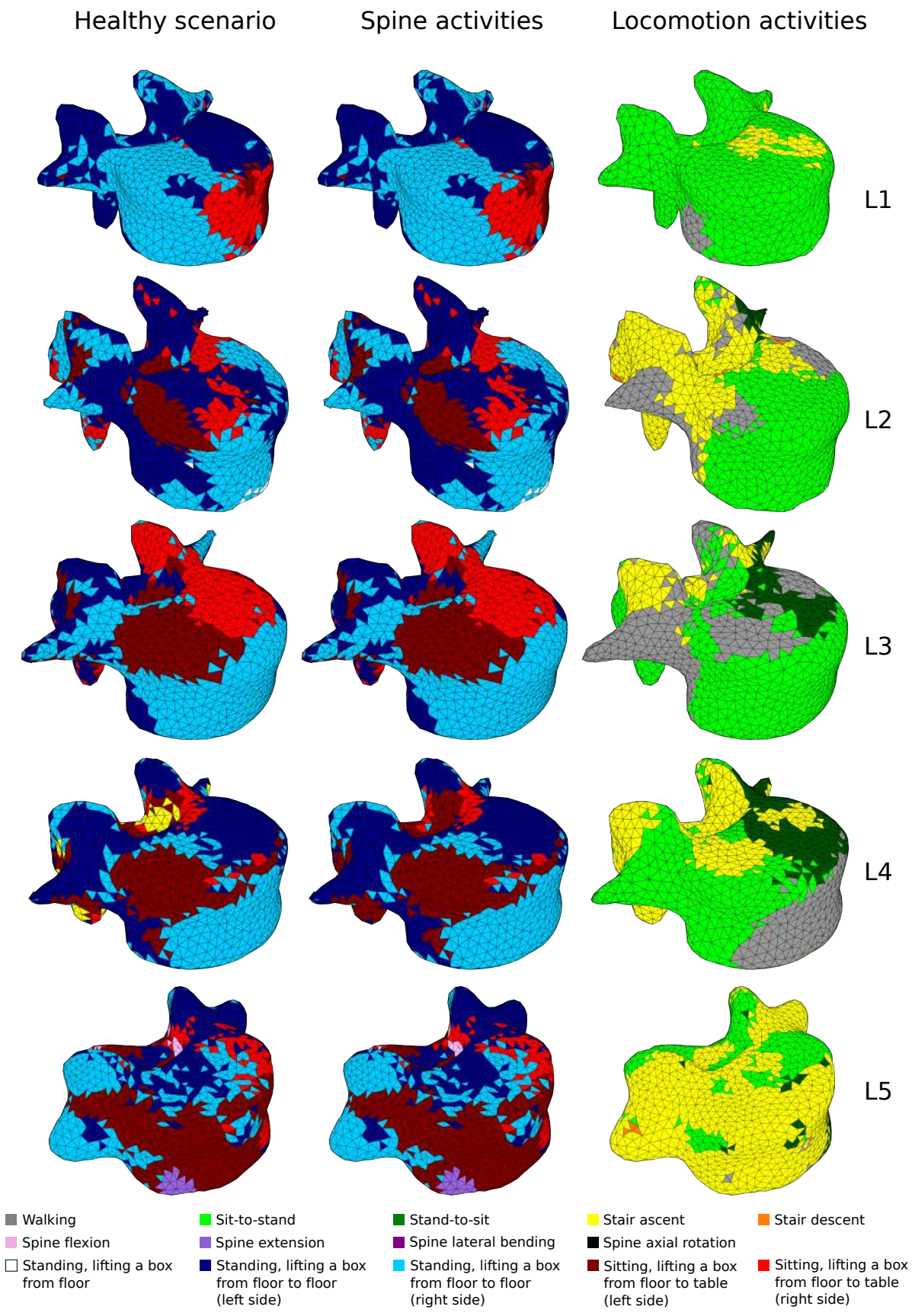

Figure 7.6: Contribution of each activity to the adaptation of the cortical shells for the healthy, spine activities and locomotion activities scenarios.

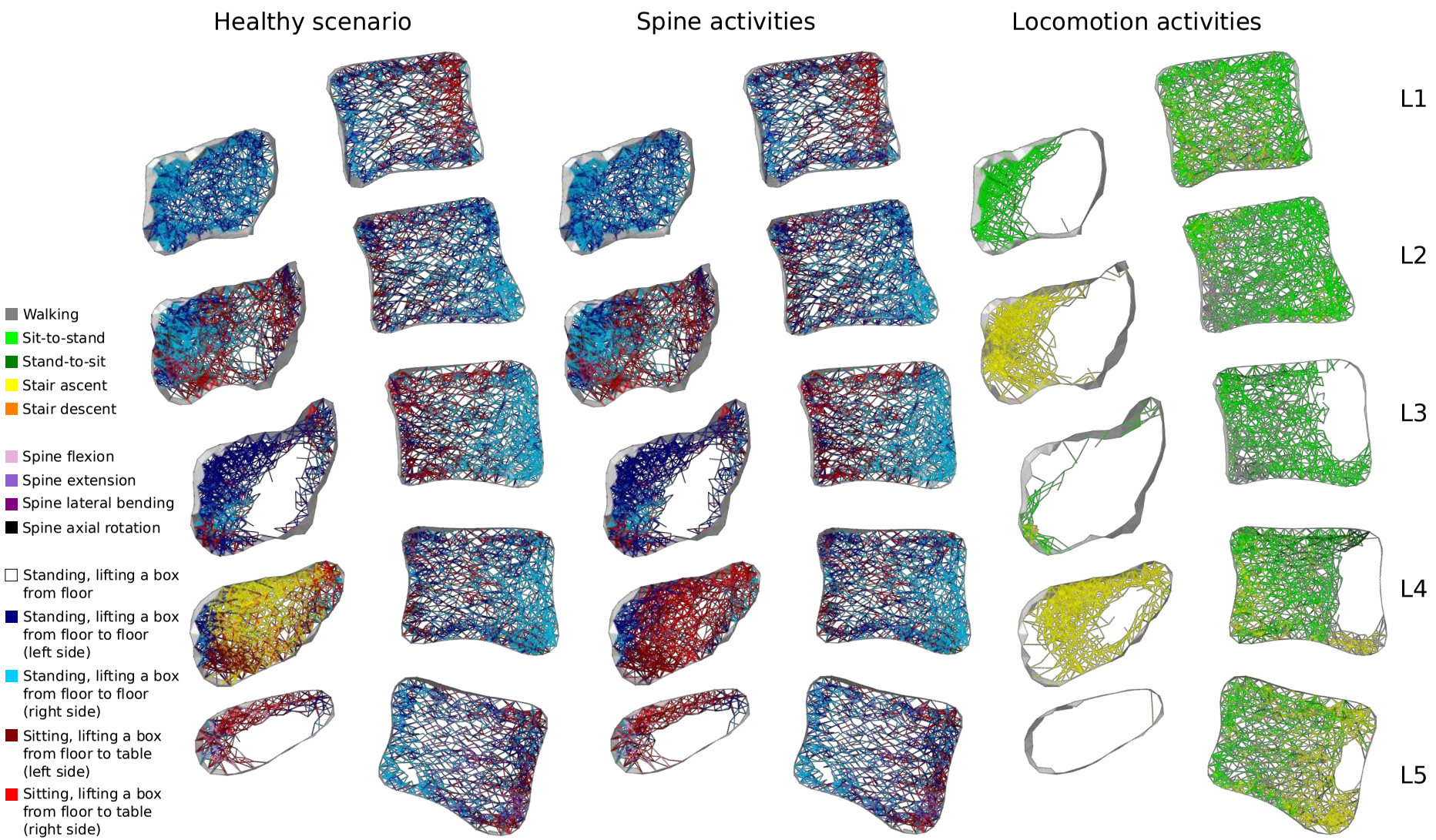

Figure 7.7: 3 mm mid-sagittal slices of the converged models adapted to healthy, spine activities and locomotion activities scenarios. Only trabecular truss elements representing the ground matrix (with a radius of 0.1 mm) are shown. Trabecular truss elements are colour mapped based on the activity most influential to their final geometry. Cortical shell elements are sown in light grey.

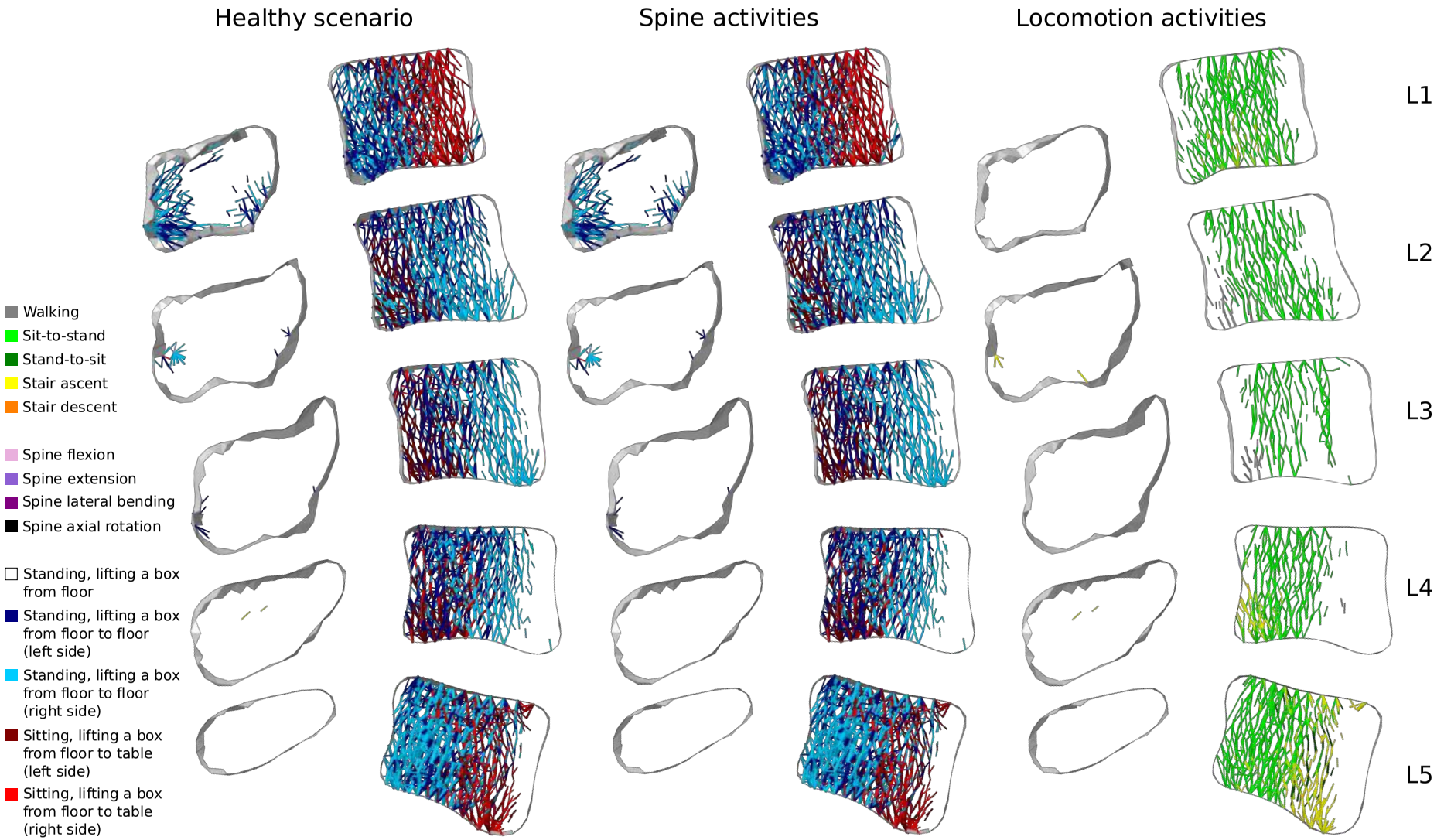

Figure 7.8: 3 *mm* mid-sagittal slices of the converged models adapted to healthy, spine activities and locomotion activities scenarios. Only trabecular truss elements with a radius superior to 0.1 *mm* are shown. Trabecular truss elements are colour mapped based on the activity most influential to their final geometry. Cortical shell elements are sown in light grey.

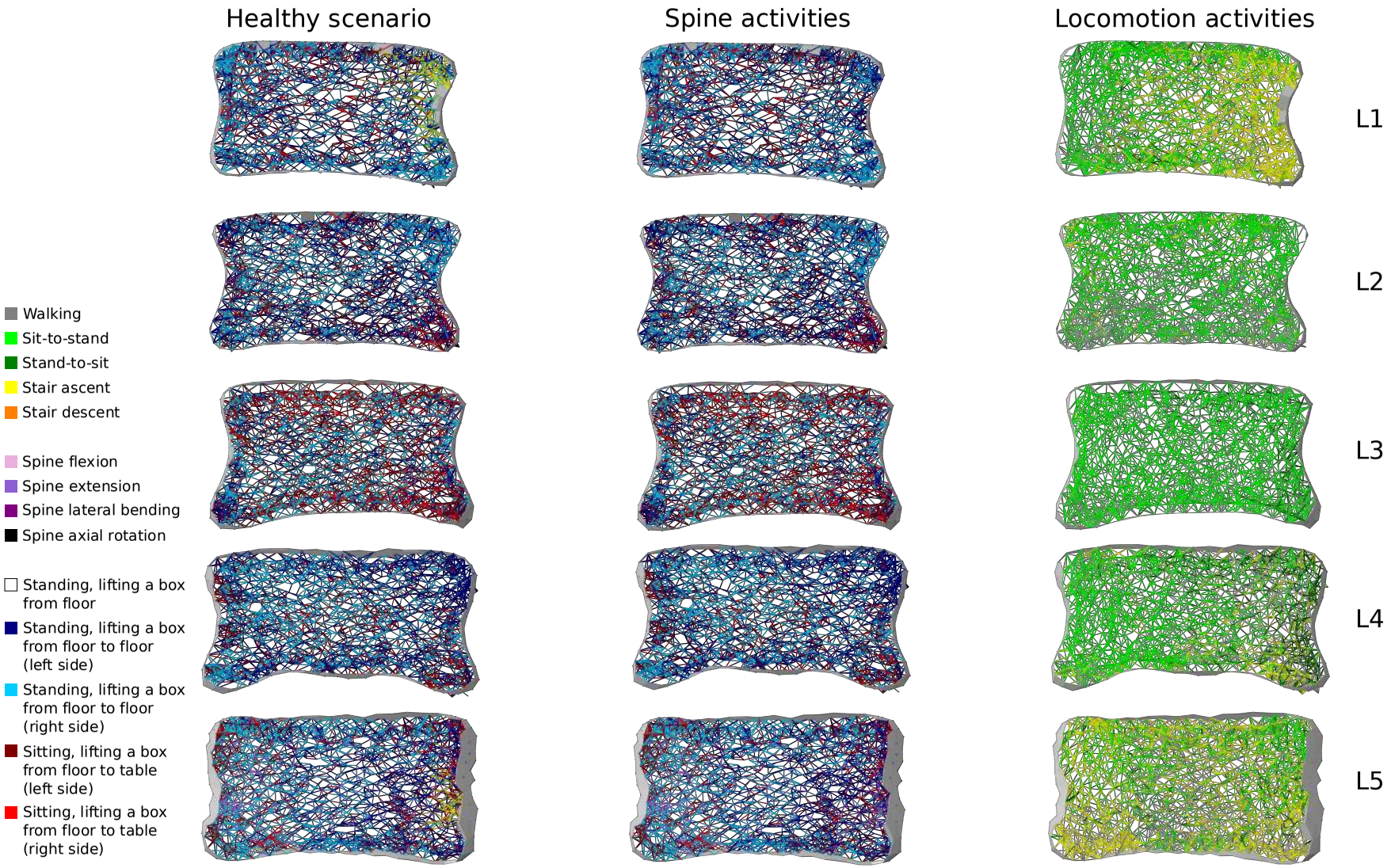

Figure 7.9: 3 mm coronal slices at the midpoint of the vertebral bodies of the converged models adapted to healthy, spine activities and locomotion activities scenarios. Only trabecular truss elements representing the ground matrix (with a radius of 0.1 mm) are shown. Trabecular truss elements are colour mapped based on the activity most influential to their final geometry. Cortical shell elements are sown in light grey.

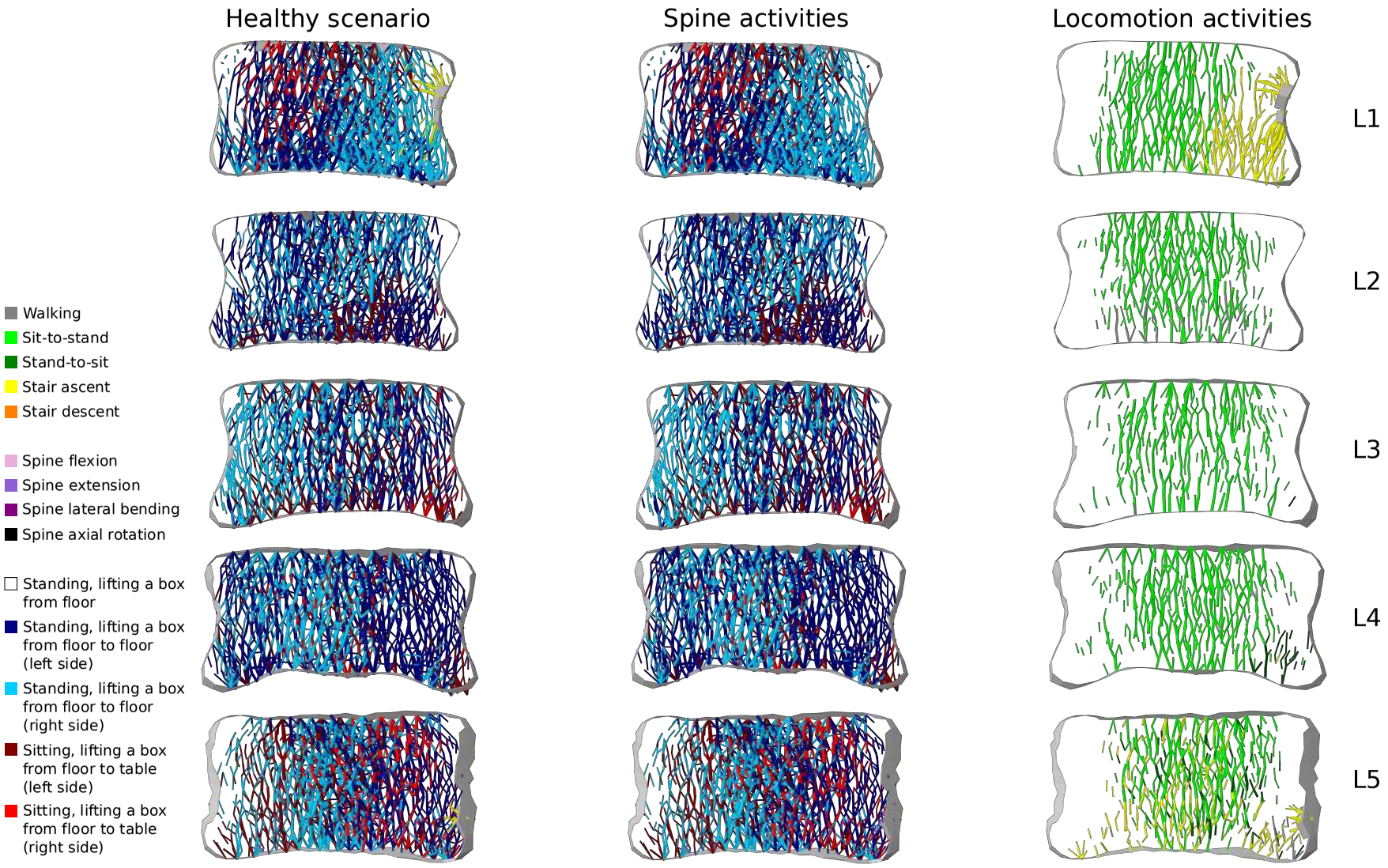

Figure 7.10: 3 *mm* coronal slices at the midpoint of the vertebral bodies of the converged models adapted to healthy, spine activities and locomotion activities scenarios. Only trabecular truss elements with a radius superior to 0.1 *mm* are shown. Trabecular truss elements are colour mapped based on the activity most influential to their final geometry. Cortical shell elements are sown in light grey.

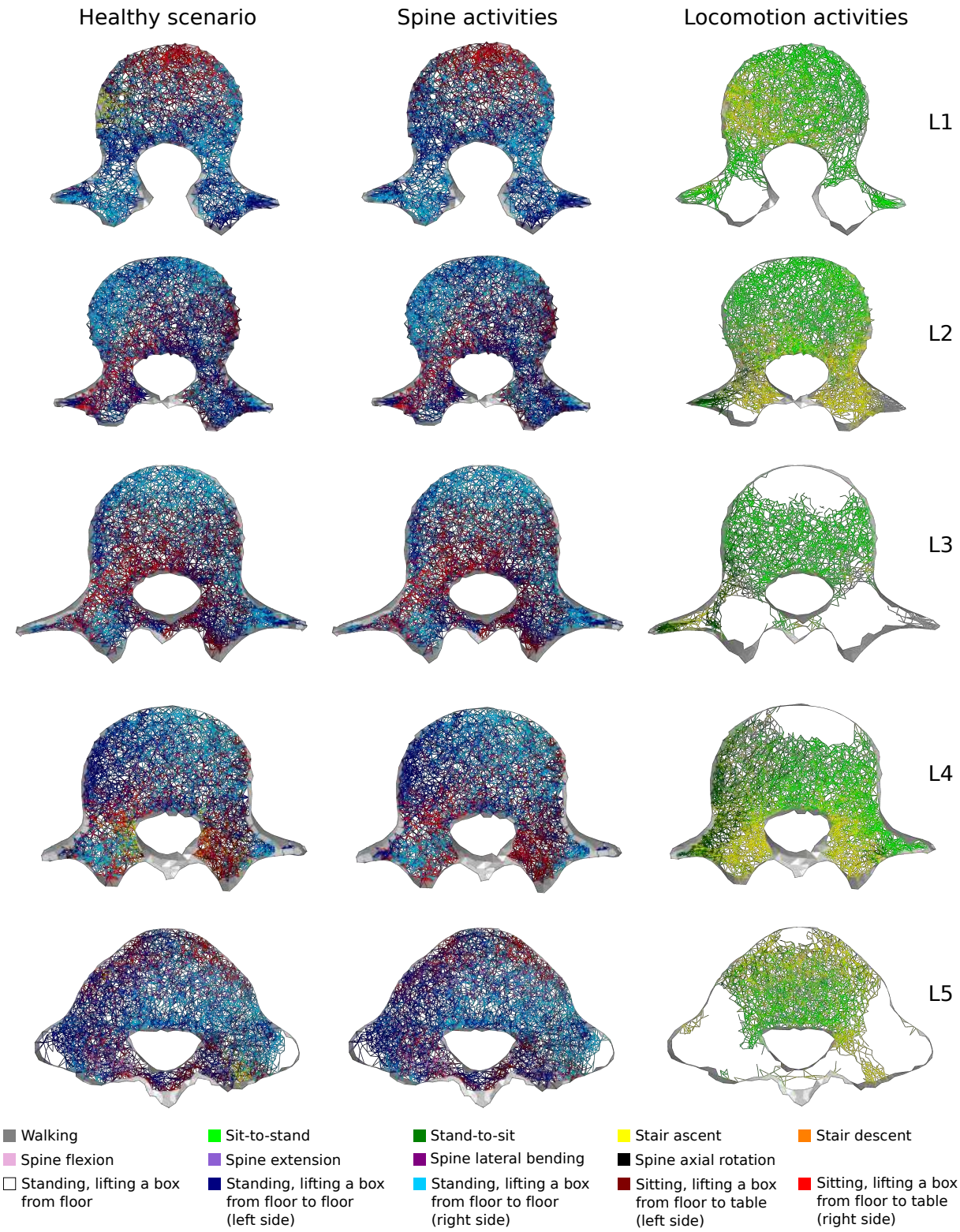

Figure 7.11: 3 mm through-processes transverse slices of the converged models adapted to healthy, spine activities and locomotion activities scenarios. Only trabecular truss elements representing the ground matrix (with a radius of 0.1 mm) are shown. Trabecular truss elements are colour mapped based on the activity most influential to their final geometry. Cortical shell elements are sown in light grey.

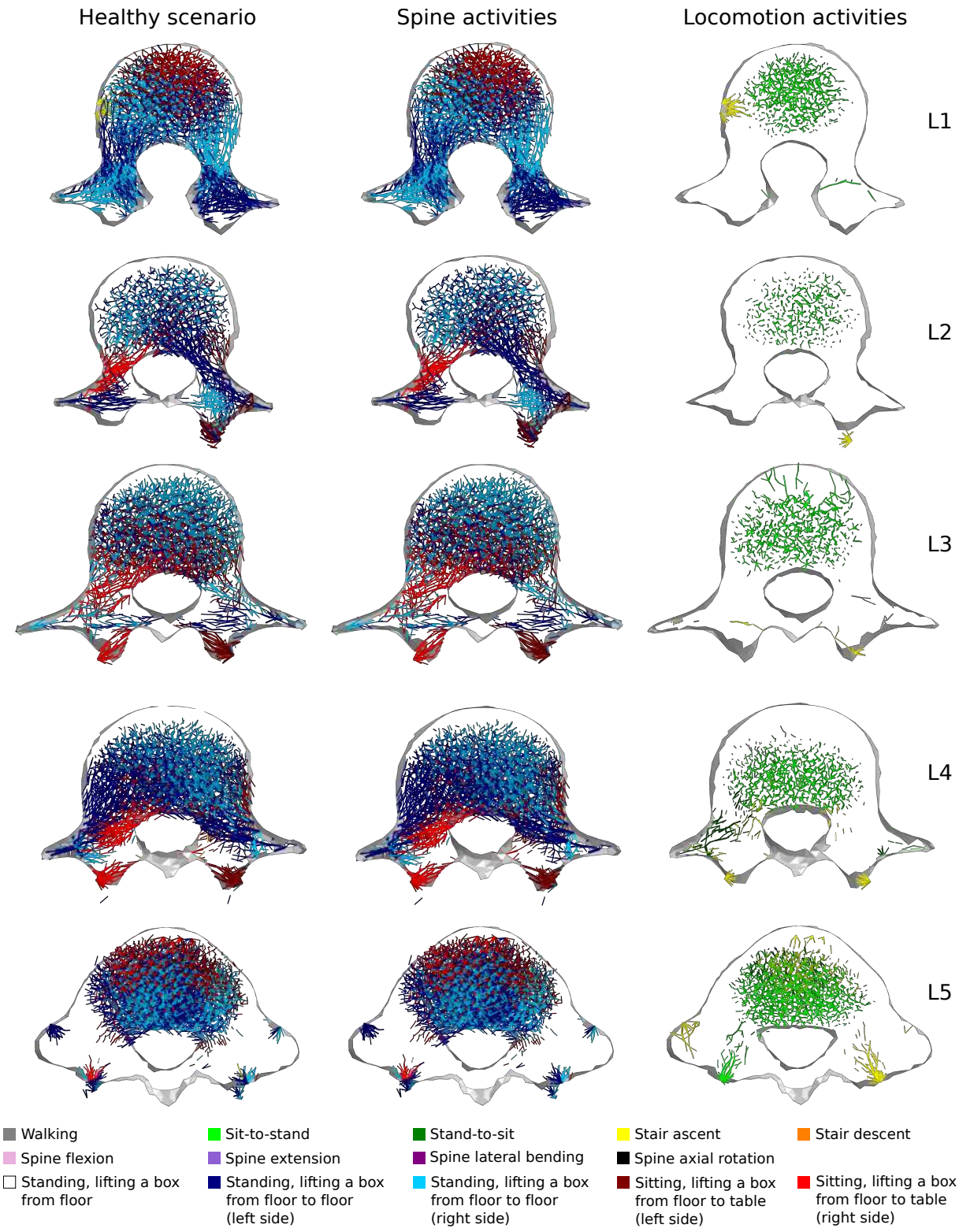

Figure 7.12: 3 *mm* through-processes transverse slices of the converged models adapted to healthy, spine activities and locomotion activities scenarios. Only trabecular truss elements located between the transverse slice and the superior endplate with a radius superior to 0.1 *mm* are shown. Trabecular truss elements are colour mapped based on the activity most influential to their final geometry. Cortical shell elements are sown in light grey.

7.2.3 Conclusion

The trabecular and cortical structures of all lumbar vertebrae in the healthy scenario are similar to the structures obtained with spine activities only. Relative densities obtained with the healthy and the spine activities scenarios are also very close with a maximum difference of 1.16% for L4. Looking at the most influential activities in the structural adaptation, it appeared that vertebrae in the healthy and in the spine activities scenarios adapt to the same activities, and particularly the lifting tasks. The locomotion activities only contribute to part of the vertebrae's structure. This suggests the lumbar vertebrae are primarily optimised for resiting loads induced by large movements of the spine and lifting tasks involving twisting and bending.

7.3 Altered loading scenario: Back pain

Based on the conclusion of the previous Section, the majority of the structural architecture of the lumbar vertebrae is driven by lifting tasks involving large bending and twisting movements. Such tasks can be demanding for pathological populations. For example, Ordway et al. (2008) reported that patients with intervertebral disc replacement have a reduced lateral bending range of motion 12 months after surgery. Spinal mobility has also been shown to decrease with age, mainly in the coronal and sagittal planes (Einkauf et al. 1987, Intolo et al. 2009, Saidu et al. 2011). Low back pain also affects coronal (Jayaraman et al. 1994) and sagittal (Laird et al. 2019) range of motion of the lumbar spine. A limited spinal range of motion can alter the functionality of the spine and reduce the level of activity of the patient. Back pain itself has been shown to impact physical activities such as lifting and stooping (Weiner et al. 2003, Kothe et al. 2007, Bjoernsdottir et al. 2012).

Using the modelling pipeline, it was of interest to investigate how the bone structure might change in the lumbar spine of a patient with back pain. Based on the findings of Bjoernsdottir et al. (2012), the simple assumption that back pain patients would stop performing lifting tasks was made.

7.3.1 Loading scenario

To simulate the effect of back pain preventing a patient from performing lifting tasks, a specific loading scenario was implemented. For the current study, it was assumed that a patient with low back pain would remain able to walk and sit, and maintain a minimal degree of spinal mobility. The mesoscale structural models of the lumbar vertebrae adapted to the healthy scenario were used as the initial models. Eleven activities including the five locomotion activities and the six static positions of the spine described previously were applied in this new adaptation. The number of load cases for this back pain scenario is indicated in Table 7.2.

Table 7.2: Characteristics of the converged mesoscale structural finite element models after adaptation to the healthy scenario and the back pain scenario.

			L1	L2	L3	L4	L5	Average
	Trabecular elements (initial mesh)		89042	101805	115063	115988	130460	110471.6
	Vertebra volume (mm^3)		54400	59320	69630	70094	78820	66453
Healthy scenario	Load cases		114	115	118	116	113	115.2
	Iterations		25	23	30	20	27	25
	Trabecular elements (converged model)		79826	86905	93452	98558	96483	91044.8
	Trabecular connectivity							
		Mean (SD)	18.20 (3.96)	17.45 (4.23)	16.77 (4.30)	17.21 (3.96)	16.38 (4.36)	17.20 (4.16)
		Minimum	1	1	1	1	1	1
		Maximum	49	45	53	46	31	44.8
	Trabecular volume (mm^3)		9185	7948	7828	9010	10050	8804
	Cortical volume (mm^3)		6026	4608	3875	4877	2249	4327
	Relative density (% of bone volume over total volume)		27.96	21.17	16.81	19.81	15.60	20.27
	Dead elements (% of initial trabecular elements)		10.35	14.64	18.78	15.03	26.04	16.97
Back pain scenario	Load cases		51	48	51	51	52	50.6
	Iterations		24	38	56	39	44	40.2
	Trabecular elements (converged model)		49535	57404	38233	63703	61477	54070.4
	Trabecular connectivity							
		Mean (SD)	14.70 (4.64)	13.36 (4.53)	10.75 (4.39)	12.78 (4.36)	13.88 (4.67)	13.10 (4.52)
		Minimum	1	1	1	1	1	1
		Maximum	28	37	26	36	28	31
	Trabecular volume (mm^3)		3074	3246	2468	3765	4729	3456
	Cortical volume (mm^3)		1549	1628	1666	3476	1719	2008
	Relative density (% of bone volume over total volume)		8.50	8.22	5.94	10.33	8.18	8.23
	Dead elements (% of initial trabecular elements)		37.95	33.95	59.09	35.36	36.28	40.53

7.3.2 Results

The average number of load cases over the five lumbar vertebrae was 50.6 for the eleven spine activities scenario. The structural finite element models converged in 40.2 iterations on average and contained 8.23% of bone, with a mean connectivity of 13.10 (SD 4.52) and 40.53% of the trabecular elements in the dead zone. On average over the five lumbar vertebrae, relative density was 58.39% lower than in the healthy scenario, showing that a diminution of the activity level leads to a decrease of bone volume in the lumbar spine. Table 7.2 shows detailed results for the healthy and the back pain scenarios.

7.3.2.1 Cortical thickness

Looking at the cortical thickness in the converged models adapted to the healthy and the back pain scenarios, a reduced level of activity produces a thinner cortex (Figure 7.13). In the healthy scenario the thicker shell elements are found in the transverse processes and the pedicles, as these structures have to resist bending moments induced by the lumbar muscles attached to them during large movements of the spine. In the back pain scenario, the thickness of the cortex in these parts of the vertebrae reduces considerably, especially in L1, L2 and L3 (Figure 7.14).

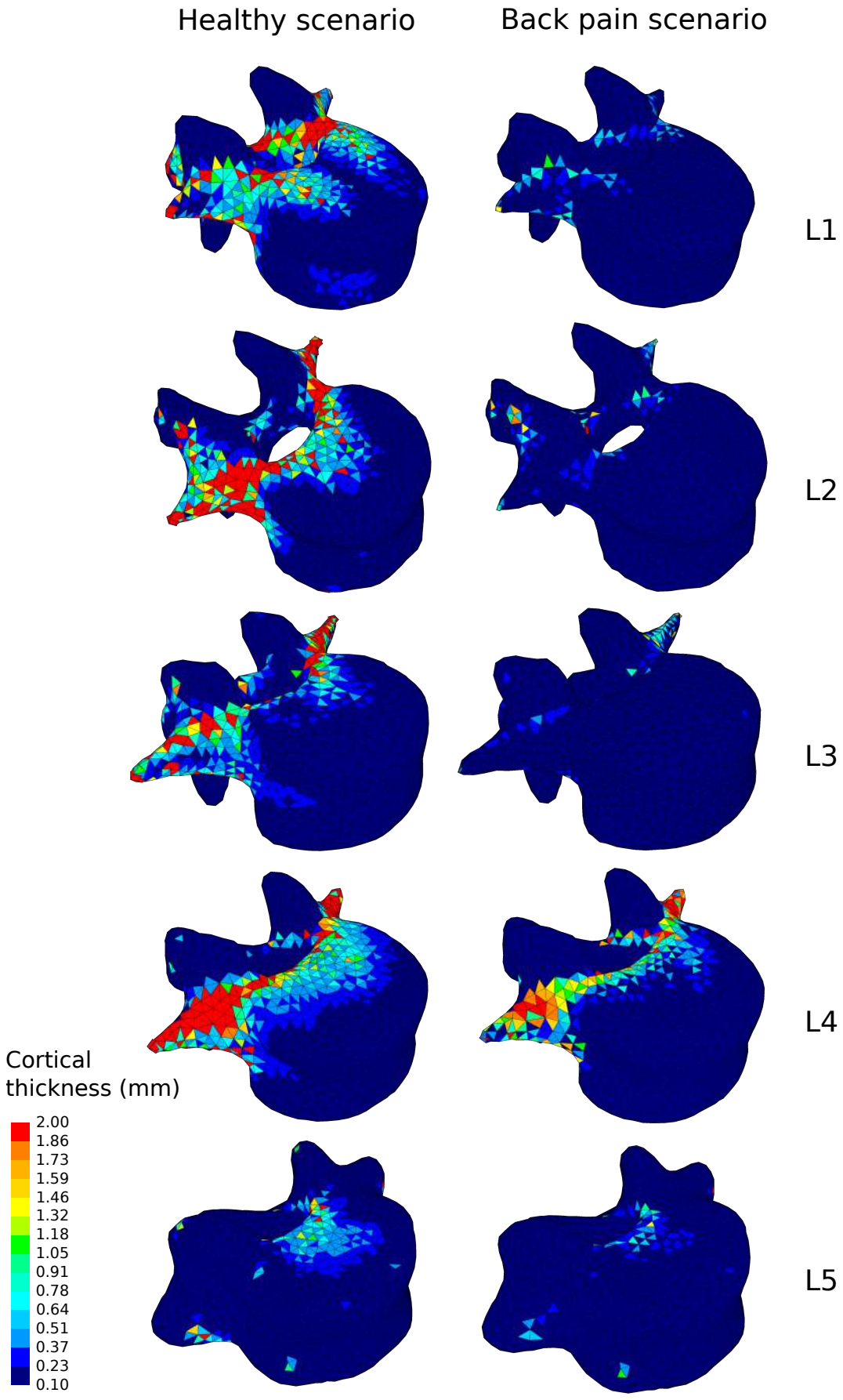

Figure 7.13: Cortical thickness of the converged mesoscale structural models of the lumbar vertebrae ranging from 0.1 to 2.0 mm adapted to the healthy and the back pain scenarios.

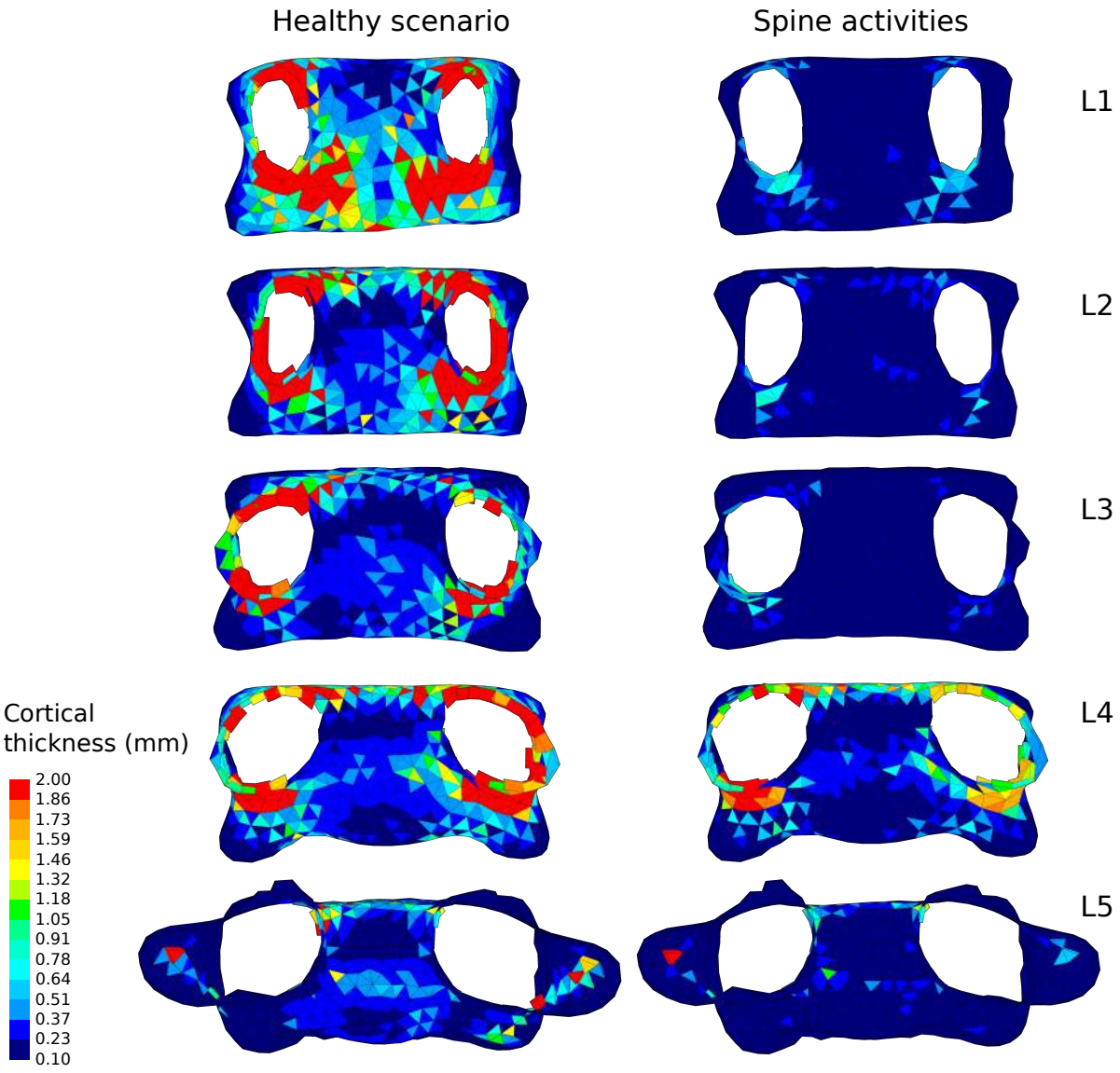

Figure 7.14: Coronal section through the pedicles of the converged mesoscale structural models of the lumbar vertebrae adapted to the healthy and the back pain scenarios, showing cortical thickness ranging from 0.1 to 2.0 mm.

7.3.2.2 Trabecular architecture

Figures 7.15, 7.16 and 7.17 compare the adapted trabecular structure of the five lumbar vertebrae between the healthy and the back pain scenario. The trabecular bone matrix present in the spinous and transverse processes tends to disappear when the vertebrae are subjected to a reduced level of activity. L3, L4 and L5 also show this trend in the frontal part of the vertebral body. For all lumbar vertebrae, the larger trabeculae resisting

vertical compression are clustered in the center of the vertebral body. Apart for L2 and L4 where some of the broader structure remains, the larger trabecular structure is completely missing in the transverse processes.

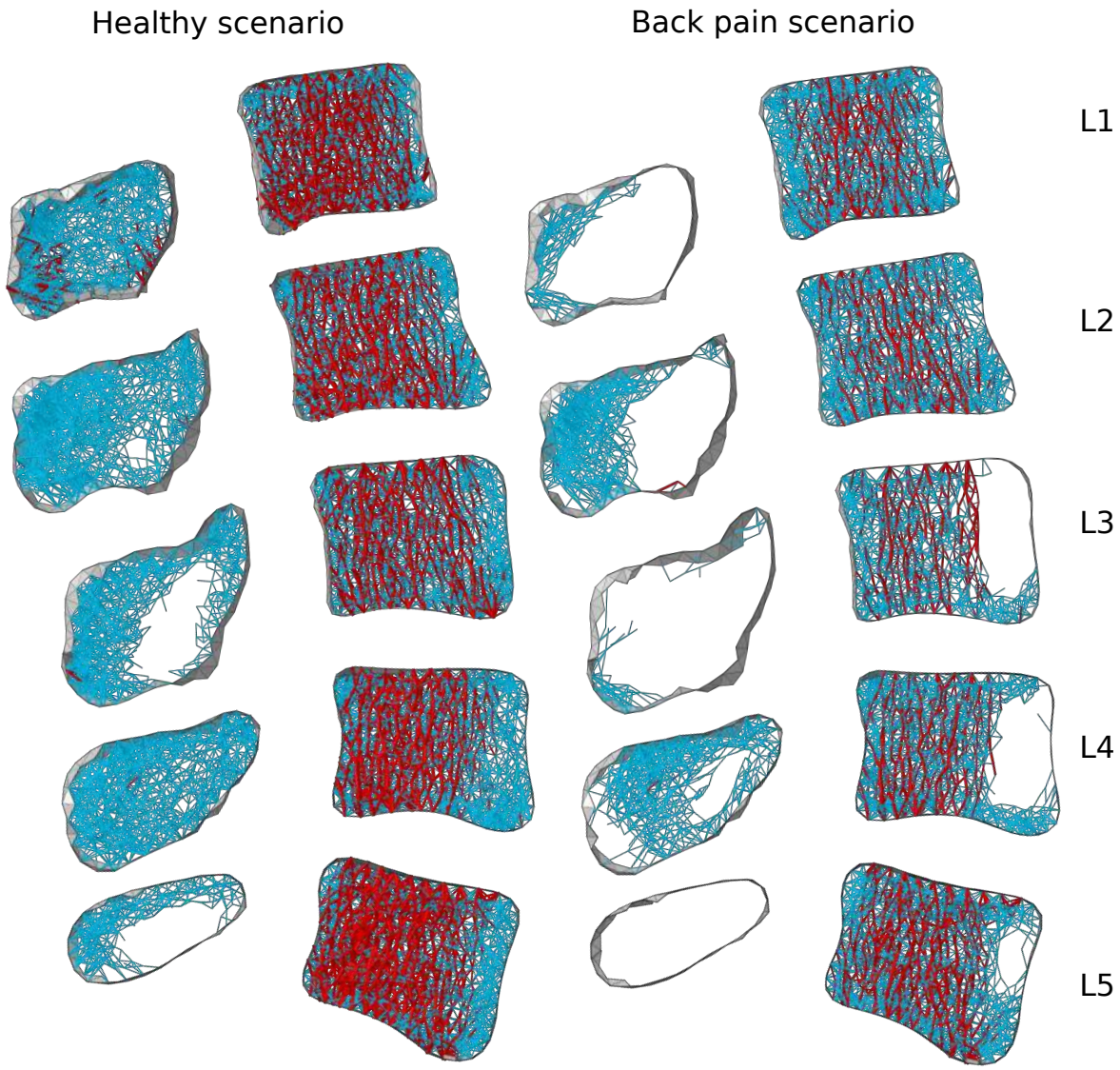

Figure 7.15: 3 *mm* mid-sagittal slices for the converged models adapted to the healthy and the back pain scenarios. Cortical shell elements are shown in grey. Trabecular truss elements representing the ground matrix (with a radius of 0.1 *mm*) are shown in blue. Thicker truss elements are shown in red. Truss elements in the dead zone (with a radius of 1 μm) are not shown for clarity.

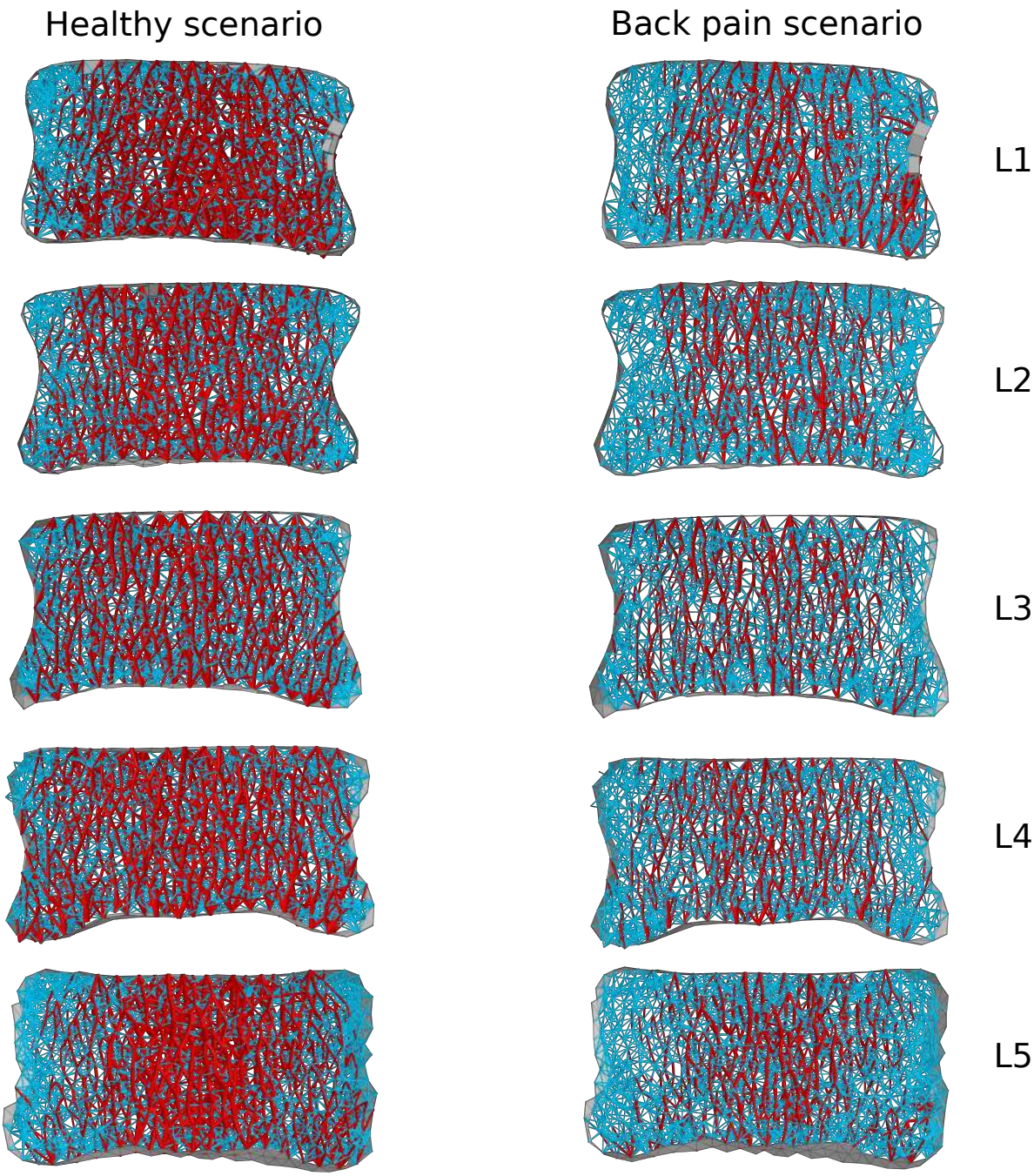

Figure 7.16: 3 mm coronal slices through the mid-point of the vertebral body for the converged models adapted to the healthy and the back pain scenarios. Cortical shell elements are shown in grey. Trabecular truss elements representing the ground matrix (with a radius of 0.1 mm) are shown in blue. Thicker truss elements are shown in red. Truss elements in the dead zone (with a radius of 1 μm) are not shown for clarity.

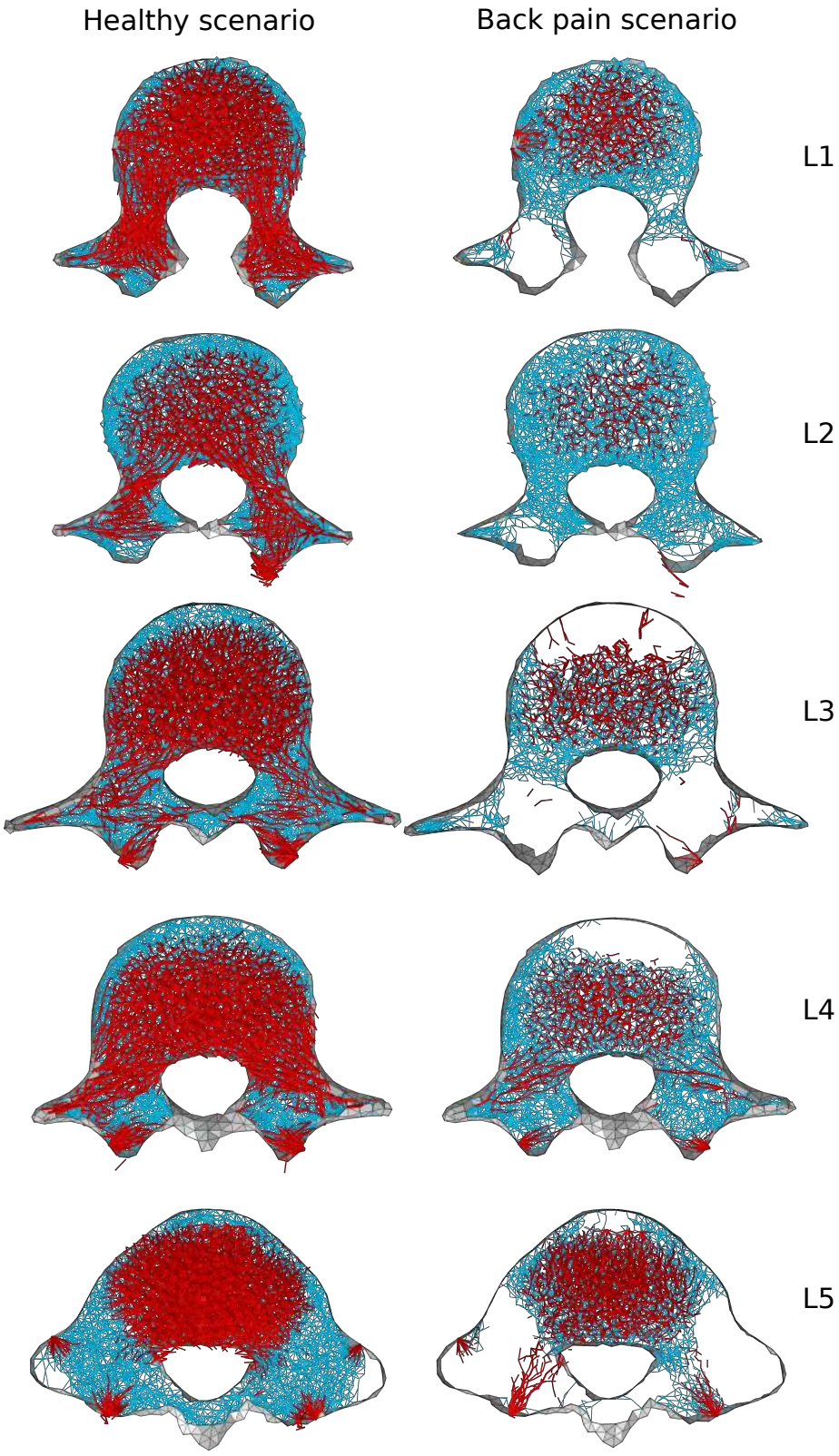

Figure 7.17: Through-processes transverse slices for the converged models adapted to the healthy and the back pain scenarios. In the background, cortical shell elements are shown in grey and trabecular truss elements representing the ground matrix (with a radius of 0.1 mm) are shown in blue for a 3 mm slice. Thicker truss elements located between the superior endplate and the through-processes transverse slice are shown in red. Truss elements in the dead zone (with a radius of 1 µm) are not shown for clarity.

7.3.2.3 Comparison to in-vivo architecture

When pain arises, it is usually more important to find treatments to relieve pain in the short term. As a result, long term bone health deterioration under low back pain conditions is rarely investigated in-vivo. Tracking the evolution of bone health in-vivo over time also implies repeated exposure to radiations, which cannot be justified for back pain symptoms only. Most of the in-vivo studies investigating bone architecture are focused on osteoporosis. Although many intricate biological variables are implicated in osteoporosis, the changes in the bone architecture are believed, in part, to be related to the loading regime (Daly et al. 2019). Figure 7.18 compares cadaveric mid-sagittal slices of L4 obtained from osteoporotic subjects (Jayasinghe et al. 1994) with five lumbar models adapted to the back pain loading scenario. The models and cadaveric material show similar patterns of architectural degradation. While the structural architecture of L1 and L2 resembles specimen (A), the total disparition of trabeculae in some parts of the vertebral bodies of L3, L4 and L5 is similar to that observed in specimens (B) and (C).

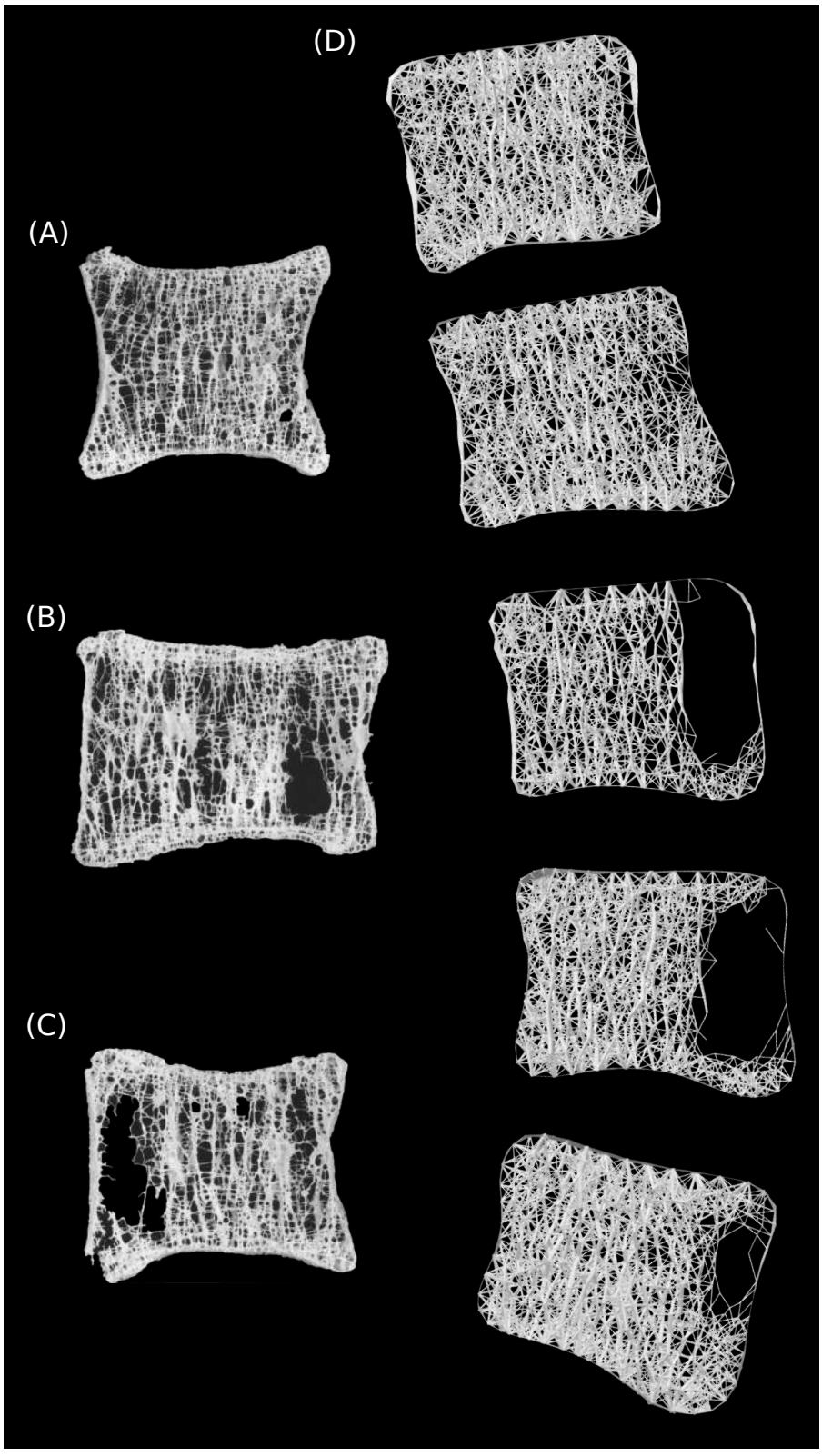

Figure 7.18: Mid-sagittal 4 *mm* slices of the vertebral bodies. (A), (B) and (C) are osteoporotic vertebrae photographs taken from a 88 female, 89 male and 89 female by Jayasinghe et al. (1994) respectively. (D) shows the corresponding slices in the five lumbar vertebra models adapted to the back pain loading scenario, with truss elements in the dead zone removed. (A), (B) and (C) are adapted by permission from Springer Nature Customer Service Centre GmbH: Springer Nature, Anatomy and Embryology, *Three-dimensional photographic study of cancellous bone in human fourth lumbar vertebral bodies*, Jayasinghe et al., © 2014).

7.3.2.4 Contribution of each activity

The structure obtained in the back pain scenario resembles the structure adapted to locomotion activities only. However, some spine activities are still considered in the back pain scenario. Figures 7.19, 7.20, 7.21 and 7.22 show the contribution of each activity to the adaptation of the vertebral architecture. The cortex adaptation is mainly driven by locomotion activities (Figure 7.19). Spine extension also influences significantly the shell thickness adaptation in L1, L2, L4 and L5. In L4, spine lateral bending also contributes to the adaptation of a few cortical elements in the articular superior processes.

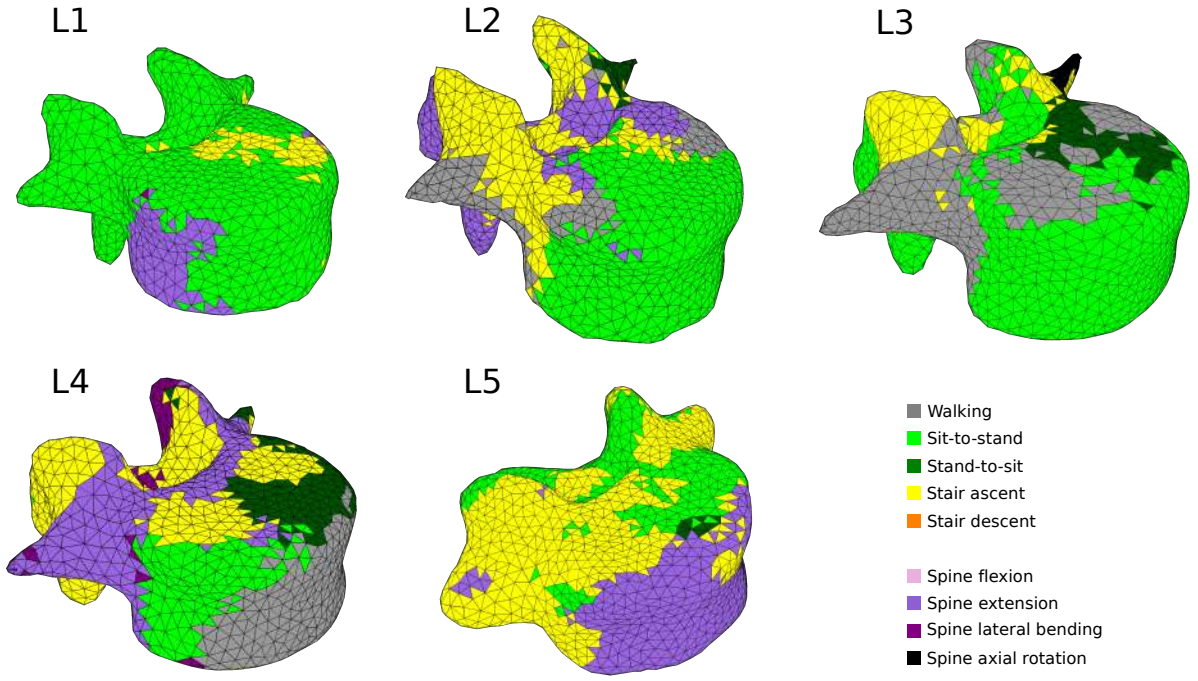

Figure 7.19: Contribution of each activity to the adaptation of the cortical shells for the back pain scenario.

A similar observation can be made in the trabecular structure where most of the structure reflects adaptation to locomotion activities (Figures 7.20, 7.21 and 7.22). Spine extension influences the trabecular structure in the vertebral bodies of L1, L2 and L5, the transverse processes of L4, the pedicles and the spinous process of L2 at both the ground matrix and the thicker trabeculae levels. Minor contributions are also made by spine lateral bending in the transverse processes of L4 and by spine axial rotation in the transverse processes of L3 at the ground matrix level.

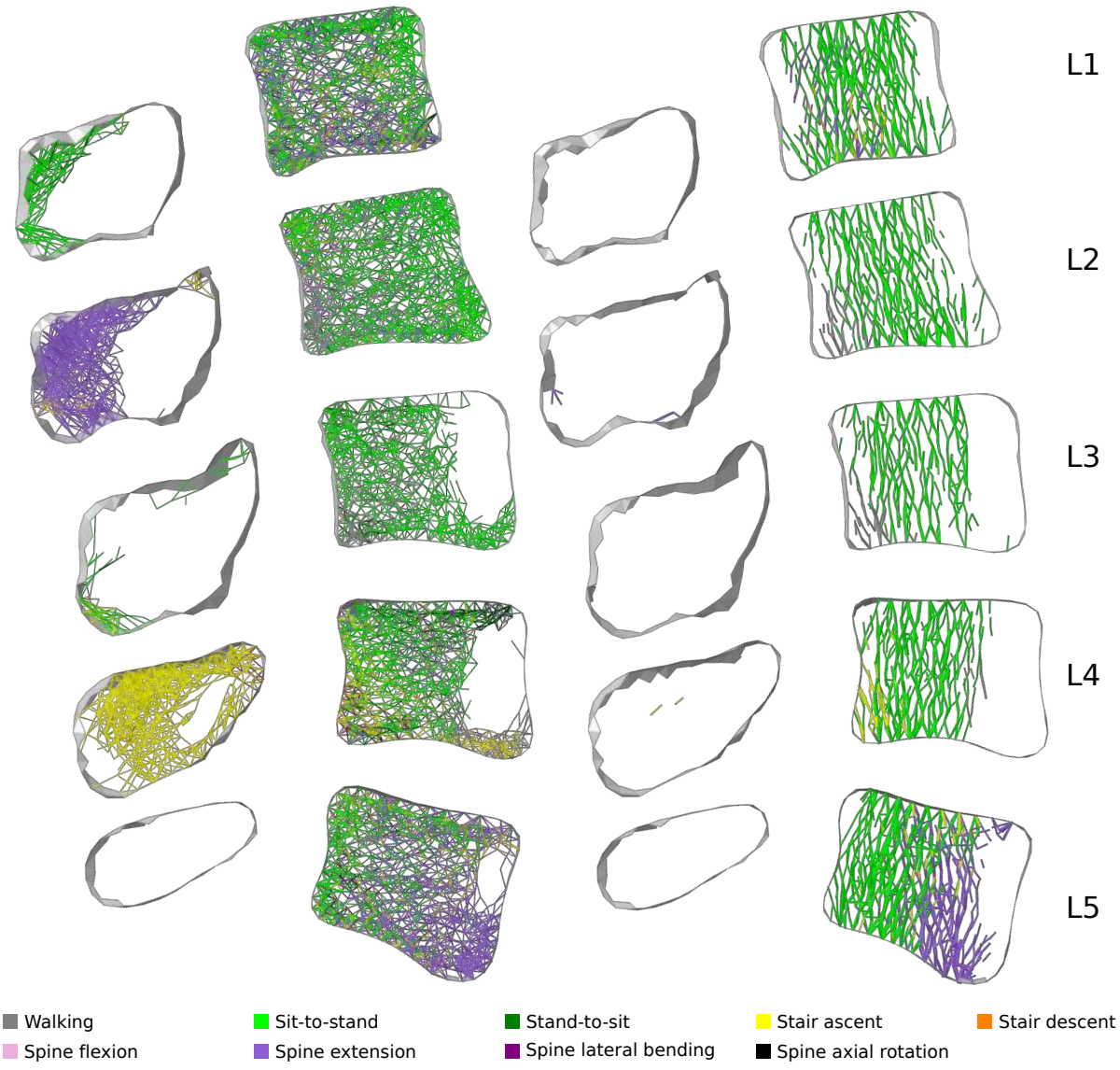

Figure 7.20: 3 *mm* mid-sagittal slices of the converged models adapted to the back pain scenario. Trabecular truss elements are colour mapped based on the activity most influential to their final geometry. On the left, only trabecular truss elements representing the ground matrix (with a radius of 0.1 *mm*) are shown. On the right, only trabecular truss elements with a radius superior to 0.1 *mm* are shown. Cortical shell elements are sown in light grey.

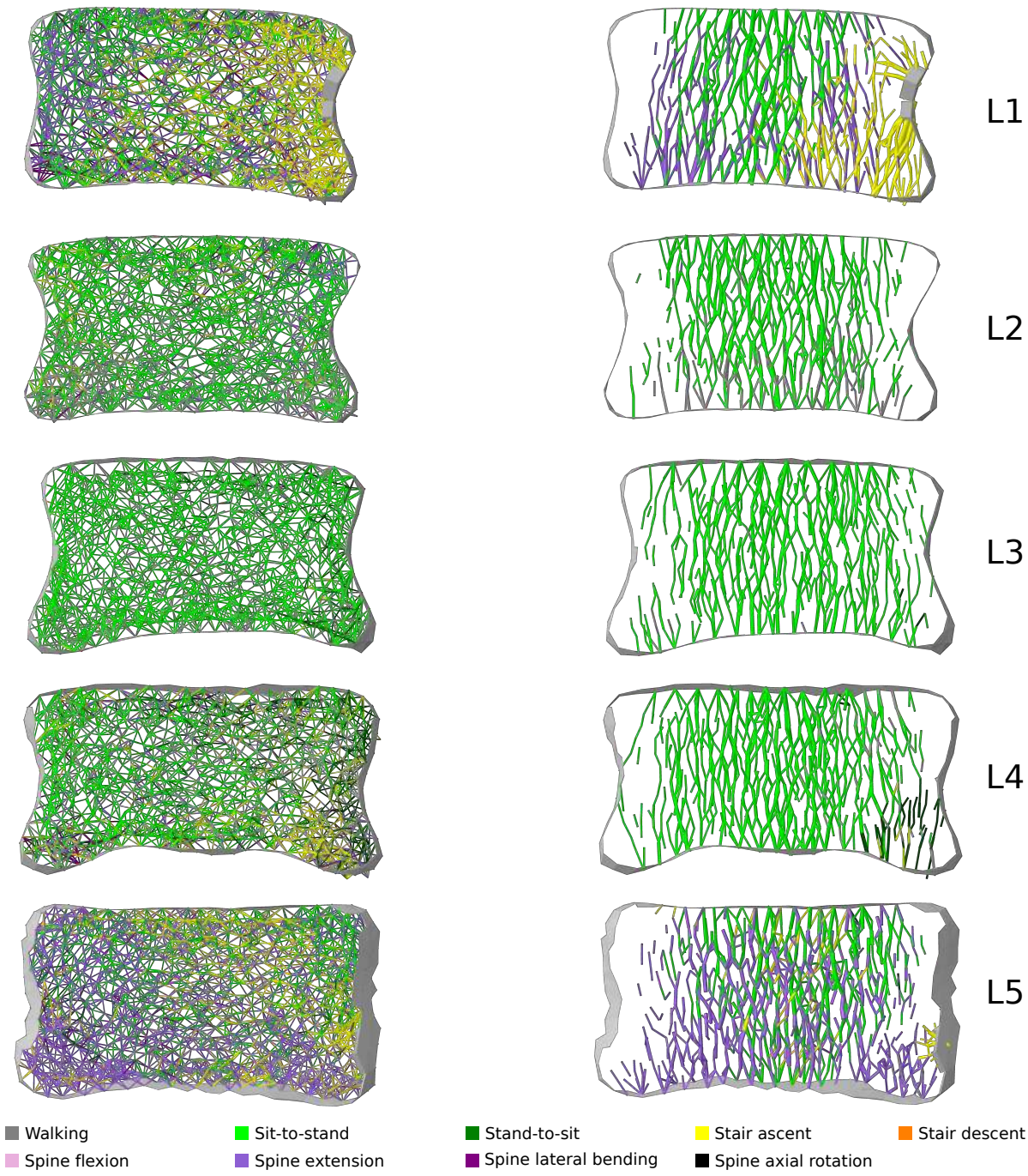

Figure 7.21: 3 *mm* coronal slices at the midpoint of the vertebral bodies of the converged models adapted to the back pain scenario. Trabecular truss elements are colour mapped based on the activity most influential to their final geometry. On the left, only trabecular truss elements representing the ground matrix (with a radius of 0.1 *mm*) are shown. On the right, only trabecular truss elements with a radius superior to 0.1 *mm* are shown. Cortical shell elements are sown in light grey.

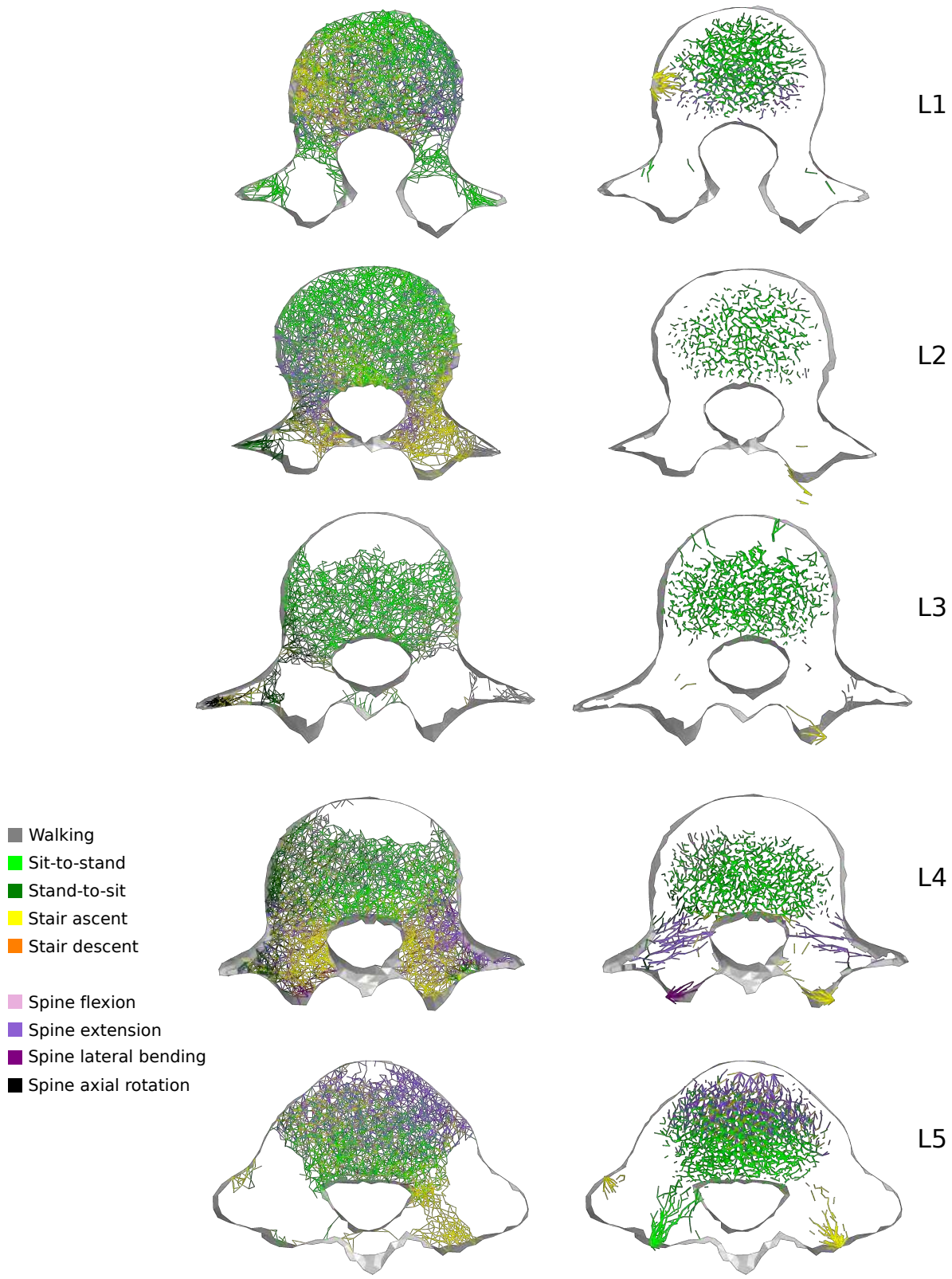

Figure 7.22: 3 mm through-processes transverse slices of the converged models adapted to the back pain scenario. Trabecular truss elements are colour mapped based on the activity most influential to their final geometry. On the left, only trabecular truss elements representing the ground matrix (with a radius of 0.1 mm) are shown. On the right, only trabecular truss elements located between the transverse slice and the superior endplate with a radius superior to 0.1 mm are shown. Cortical shell elements are sown in light grey.

7.3.3 Conclusion

The mesoscale structural finite elements models of the lumbar vertebrae adapted to the back pain scenario show a reduced cortical thickness and less dense trabecular architecture compared to the healthy scenario. This structure lacks most of the trabecular trajectories and the thicker cortex in the posterior elements of the spine characteristic of healthy vertebrae. The vertebral body is also less dense than in a healthy vertebra. This sparse trabecular structure is similar to that observed in osteoporotic specimens. In the back pain scenario, adaptation of the vertebrae is mainly influenced by the locomotion activities and spine extension which are less intense than lifting activities. These observations support the statement made in the previous Section that healthy lumbar vertebrae are adapted to resist the loading of the spine for large movements and lifting tasks.

7.4 Discussion

The modelling pipeline allows the investigation of the influence of different activities on the structure of the lumbar vertebrae. Results from this Chapter suggest that lumbar vertebrae are adapted for heavy loads occurring during large spine movements and complex lifting tasks. A back pain scenario was simulated by removing such activities from the loading envelope, altering the mechanical environment of the lumbar vertebrae and therefore the structure of the vertebrae.

Limitations of the finite element modelling choices have been discussed in Chapter 6. The current approach to simulate an altered loading envelope representative of a low back pain condition also has limitations. While it is relevant to remove demanding lifting activities to simulate a back pain scenario, other aspects of the pathology should be considered in future work. Muscle or ligament damage, disc degeneration, spine shape and fear-avoidance (Vlaeyen & Linton 2000) are potential back pain-related factors that influence balance strategies even in simple locomotion and spine activities. To ensure an accurate simulation of the condition, the modelling pipeline could be modified to represent these musculoskeletal alterations. Impaired balance control in a patient with back pain should also be considered, as it would lead to different kinematics in the musculoskeletal model which in turn would alter the loading conditions in the finite element model. It should also be noted that the current study only predicts a final adapted state. A large amount of trabecular elements fall in the dead zone in the back pain scenario (Table 7.2). This is due to the adaptation approach which does not include physiological bone remodelling rate. Future developments should consider implementing the remodelling rate between 1000 and 250 $\mu\epsilon$ to obtain a more gradual bone resorption.

Despite these limitations, the current approach to modelling the impact of back pain shows that changes to the loading conditions of the lumbar spine will lead to adaptations in the vertebral architecture. Some of these adaptations reflect those observed in-vivo in healthy and pathological spines. This supports recommendations from the clinical field that an active lifestyle is essential to maintain bone health in the lumbar spine, especially for populations at risk such as the elderly (Guadalupe-Grau et al. 2009, Gomez-Cabello et al. 2012) or postmenopausal women (Kelley et al. 2002, Daly et al. 2019). For

reasons involving muscle strengthening and core stability, chronic back pain patients are also recommended to maintain a moderate level of activity such as walking (Pillastrini et al. 2012, Vanti et al. 2017). However, the current study has shown that locomotion activities are not sufficient to maintain bone health in the lumbar vertebrae. This supports the idea of an interconnection loop between lumbar spine bone health, low back pain and actvity levels introduced in Chapter 1. In future work, the modelling pipeline could be used as a platform to investigate various scenarios and determine specific exercises likely to help maintaining bone health in the lumbar spine while taking in consideration patient's abilities and level of pain.

Chapter 8

Conclusion

8.1 Summary of achievements

The aim of this research was to develop a computationally efficient predictive modelling framework for the investigation of bone structural adaptation in the lumbar vertebrae under various loading scenarios representative of healthy and pathological conditions. Models were developed based on a healthy population and simulations predicted bone architecture in healthy and back pain conditions.

The first part of this thesis described the data acquisition on healthy participants necessary for the development of the modelling framework. This database is unique as it contains full body high resolution MRI scans, kinematic, kinetic and electromyography (EMG) data collected on six male volunteers representative of a young healthy population for a range of activities of daily living. These activities include locomotion activities involving the lower limbs (walking, stair ascent and descent, sit-to-stand and stand-to-sit), isolated spine movements in the three anatomical planes and lifting tasks of varying complexity.

In the second part of the thesis, the imaging data was used to create a novel full body musculoskeletal model with a detailed representation of the lower limbs and the lumbar spine. Unlike existing generic models, joint locations and musculotendon actuator paths were adjusted to match bone and muscle geometries segmented from MRI scans, resulting in a subject-specific model consistent across the whole body. Modelling choices were made to ensure physiological feasibility. Collected kinematic and kinetic data was used for musculoskeletal simulations. The joint reaction forces estimated with the model at the lumbar joints compared favourably with measured in-vivo data reported in the literature. Comparison of muscle activations estimated with the model and EMG recordings were also satisfactory. The musculoskeletal model is considered suitable to be integrated in the predictive modelling framework.

The third part of the thesis focused on the development of mesoscale structural finite element models of the lumbar vertebrae which would allow the prediction of bone architecture in different scenarios. In these models, shell elements were used to represent cortical bone while truss elements represented trabecular bone. Bone remodelling was simulated

with a strain driven adaptation algorithm which optimises shell thicknesses and truss radii to the loading applied. Physiological loading conditions including muscle, joint reaction and inertial forces were obtained with the musculoskeletal model for a range of daily living activities. The architecture of finite element models adapted for this loading regime representative of a healthy lifestyle compared favourably with the in-vivo observations reported in the literature. In the vertebral bodies, the predicted trabecular architecture exhibited main trajectories resisting vertical compression. A ground matrix composed of thin trabecular trusses aligned with the two other orthogonal directions was observed. This ground matrix resists any forces in the transverse plane and stabilises the main vertical trajectories, preventing them from displacing in that plane. In the posterior part of the vertebrae, trabeculae resisting tension in the transverse processes and the vertebral arch were identified, merging into the ground matrix of the vertebral bodies. The cortical shell elements also thicken in the posterior part of the vertebrae, and similarities with cadaveric material were observed in the pedicles. The modelling approach is computationally efficient compared to microscale continuum finite element models considered as the gold standard for predictive simulation of bone architecture, saving substantial amounts of simulation time and CPUs.

In the last part of the thesis, the modelling framework was used to investigate the influence of different activities on the structural adaptation of the lumbar vertebrae. Lifting tasks proved to be the most influential activities, while locomotion activities only influence parts of the vertebral body trabeculae resisting vertical compression. A simplified back pain scenario was investigated, where converged models representative of healthy vertebrae were further adapted to altered loading conditions. Although these loading conditions can be considered as a worst case scenario, it appears that deconditioning related to back pain leads to weak vertebral structures in the long term, potentially increasing the risk of vertebral compression fractures.

8.2 Current limitations and future work

The limitations of the modelling approach developed in this thesis have been discussed in the previous Chapters. This Section presents general comments related to these current limitations.

The musculoskeletal model estimates joint reaction and muscle forces necessary in the modelling pipeline based on the kinematic and kinetic data recorded on the volunteers for various activities. The bone geometry and muscle paths and insertions in the model are derived from MRI scans and are specific to the volunteer. Although a specific protocol with cod liver oil capsules was used during data collection to ensure consistency between experimental and virtual tracking markers, it is still not feasible to track individual lumbar vertebrae due to skin artefacts, especially for complex large movements of the spine. Kinematic constraints were used to obtain the position of the lumbar vertebrae as a function of the thoracic spine movements. The marker set developed for the study was consistent with the definition of these kinematic constraints. However, the coefficients for these constraints are adapted from other studies and are not specific to the physiology of the volunteer. Muscle physiology and rotational stiffness in the bushing elements used at the lumbar joints were also scaled from existing generic models and may not represent the physical capacities of the subject. Further personalisation of the musculoskeletal model could be achieved in the future. Bushing stiffness could be estimated for the current model based on the method developed by Senteler et al. (2015). Maximum isometric forces of the musculotendon actuators could also be adjusted using segmented volumes from the MRI scans. These improvements coupled with the implementation of lumbar ligaments and intra abdominal pressure would enhance the joint reaction force estimations and provide more physiological loading conditions for the finite element simulations. Some current limitations are also associated with the static optimisation method used to estimate muscle activations. As discussed in Chapter 5, this technique cannot predict co-activation of muscles needed for stability strategies. Muscle synergies could be implemented in future developments of the model (Gopalakrishnan et al. 2014). Since EMG signals have been collected for all activities, EMG-driven simulations could also be investigated to account for muscle synergies (Pizzolato et al. 2015).

The limitation associated with the combination of different modelling techniques has been acknowledged in Chapter 6. Musculoskeletal modelling is a multibody dynamics approach based on the assumption of rigid bodies and idealised joints while finite element modelling considers deformations of the bones. Muscle and joint reaction forces calculated to equilibrate the musculoskeletal model may not satisfy equilibrium of the finite element model. As explained in Chapter 6, this is addressed with the use of soft boundary conditions in the finite element models which maintain numerical stability. However this technique can influence the response of the model during adaptation as it may stiffen the structure. Idealised joints in the musculoskeletal model also implies joint reactions are calculated at a single point. Specific load applicators are used in the finite element models to spread the load on the articular surfaces but this representation may still lack biofidelity. Rotational stiffness calculated with the bushing elements in the musculoskeletal model were not implemented in the finite element simulations as they account for overall joint passive stiffness from the intervertebral disc, ligaments and facet joints, and would create non-physiological loading conditions. A finite element model of multiple spinal units including intervertebral discs, lumbar ligaments and facet joint contacts would address the mentioned limitations, as the simplified loading conditions obtained with the musculoskeletal model would be applied further away from the vertebra of interest, with the implemented lumbar passive structures ensuring physiological loading. Alternatively, a more integrated musculoskeletal and finite element approach could be considered using dedicated softwares such as the ArtiSynth Simulation framework (http://www.artisynth.org), although structural elements have not yet been fully implemented in these.

The modelling framework developed in this thesis allows the prediction of bone structural adaptation to its mechanical environment. The adaptation algorithm implemented in the pipeline does not consider the physiological time needed for bone remodelling and only predicts the final remodelled state. The approach also neglects the frequency at which activities are performed as well as any resting time. This approximation is acceptable given that bone remodelling occurs over longer periods. However resting time (Robling et al. 2001) and loading frequency (Turner et al. 1994) have been shown to influence bone remodelling, and future work should aim at implementing loading time profiles and remodelling rate to improve simulation of bone adaptation in pathological

scenarios. Another limitation related to the algorithm resides in the strain driven optimisation chosen for to simulate bone adaptation. Considering the scale the current model operates at, strain is an acceptable surrogate for the physiological phenomenon that takes place at the cellular level. However, modelling the cellular response to fluid motion which has been proposed as a mechanistic driver for bone remodelling could be a significant advancement for the model as it would allow the investigation of lumbar pathologies such as osteoporosis at different scales. This could be achieved with the use of metamodels described in the work of Villette & Phillips (2017).

Compared to microscale continuum finite element models, the mesoscale structural approach ensures computational efficiency while capturing the internal architecture of the vertebrae. While the resolution of the model is sufficient to represent trabecular trajectories and cortical thickness, it is not representative of individual trabeculae as the truss lengths and radii are above the size of rod-like trabeculae and are not representative of plate-like trabeculae that can be observed in-vivo. Truss elements can only resist axial force. This is an acceptable modelling choice considering that axial deformation would be preferred to bending in an optimised structure. However this representation does not capture the low connectivity of the trabecular matrix and the thinning observed in the middle of rod-like trabeculae. The use of beam elements arranged in a Voronoi network (Phillips 2019a, Phillips 2019b, Phillips 2019c) could offer a structural modelling alternative to the current approach, maintaining computational efficiency while improving trabecular representation.

The adapted bone architecture obtained with the current modelling pipeline for different loading scenarios is in agreement with observations made on cadaveric material reported in the literature. Further assessment of the results against in-vivo data obtained with high resolution CT images would provide more confidence in the modelling pipeline. Finally, the modelling framework was only used on one of the six datasets recorded on the cohort of healthy volunteers. Future work should focus on processing the other datasets with the developed modelling framework to investigate variability between individuals at the musculoskeletal and bone structure levels.

8.3 Applications to the clinical field

The modelling framework developed in this thesis is a computationally efficient tool for the prediction of bone structural architecture in the lumbar vertebrae. It offers an alternative to microscale continuum modelling approaches which are generally based on high-dose radiation imaging techniques like CT scans. This risk free modelling approach can be used to investigate various pathologies associated to bone health in the lumbar spine.

Chapter 7 highlighted the consequences of deconditioning on bone structure in a worst case scenario of low back pain and showed that reducing the range of activities to avoid pain is likely to cause a cascade of effects leading to degradation of the structures of the lumbar spine. It is therefore proposed to include a broad range of activities with a large range of motion in prevention and rehabilitation programs for populations at risk of osteoporosis.

The approach could be refined further to model sedentary behaviours and low physical activity levels representative of many of the elderly populations. The method could also be extended to investigate the effect of prolonged space flight and life on the Moon or Mars by implementing time dependency in the bone adaptation algorithm. This would also allow the simulation of different bone remodelling rates and broaden the potential applications to the clinical field. Osteoporosis and ageing could be investigated further. Knowing how a particular activity can influence bone remodelling in the lumbar spine, specific exercises taking the reduced capabilities and pain thresholds of individual patients into account can be developed to limit osteoporosis and its associated fracture risk, or offer rehabilitation training plans after surgical interventions.

The risk of vertebral fracture in the elderly population is commonly assessed based on bone mineral density in the lumbar spine measured with imaging techniques involving varying doses of radiations. However, it has been shown that bone mineral density is only one of the many factors influencing bone strength (Feltrin et al. 2001, Epstein 2005, Friedman 2006, Fonseca et al. 2013). The structural modelling approach is particularly suited for the simulation of fracture (Villette & Phillips 2018), and could be used to

predict fracture risk and assess bone strength in the elderly population, providing a safer and more robust measure of bone structural health.

The computational efficiency of the modelling framework also allows applications in the prediction of the outcome of surgical procedures in the short and long term, particularly interventions such as vertebroplasty and the use of instrumentation to fuse the spine. Long term effect of disc implants on the adjacent vertebrae could also be simulated, and the modelling framework could be used to inform the development of new implant designs.

Other spinal pathologies involving bone remodelling can be investigated with the modelling framework. In patient with adolescent idiopathic scoliosis, the irregular spine curvature is associated with changes in the internal architecture and the external shape of the vertebrae (Stilwell 1962, Smith et al. 1991). Implementing shape adaptation in the algorithm would allow predictions of the evolution of the entire structure of the vertebrae for different treatments, helping surgeons and clinicians in the decision-making process.

The modelling approach presented in this thesis contributes to a deeper understanding of bone architecture in the lumbar vertebrae and encourage future collaborations with the clinical field providing efficient numerical tools that can simulate bone behaviour under physiological conditions to inform clinical decisions.

References

Aamodt, A., Lund-Larsen, J., Eine, J., Andersen, E., Benum, P. & Husby, O. S. (1997). In vivo measurements show tensile axial strain in the proximal lateral aspect of the human femur, *Journal of Orthopaedic Research* **15**(6): 927–931.

Actis, J. A., Honegger, J. D., Gates, D. H., Petrella, A. J., Nolasco, L. A. & Silverman, A. K. (2018). Validation of lumbar spine loading from a musculoskeletal model including the lower limbs and lumbar spine, *Journal of Biomechanics* **68**: 107–114.

Al-Saeed, O., Mohammed, A., Azizieh, F. & Gupta, R. (2013). Evaluation of bone mineral density in patients with chronic low back pain, *Asian Spine Journal* **7**(2): 104.

Allaire, B. T., Lu, D., Johannesdottir, F., Kopperdahl, D., Keaveny, T. M., Jarraya, M., Guermazi, A., Bredella, M. A., Samelson, E. J., Kiel, D. P., Anderson, D. E., Demissie, S. & Bouxsein, M. L. (2018). Prediction of incident vertebral fracture using CT-based finite element analysis, *Osteoporosis International* **30**(2): 323–331.

Alyas, F., Connell, D. & Saifuddin, A. (2008). Upright positional MRI of the lumbar spine, *Clinical Radiology* **63**(9): 1035–1048.

Andreasen, M. L., Langhoff, L., Jensen, T. S. & Albert, H. B. (2007). Reproduction of the lumbar lordosis: A comparison of standing radiographs versus supine magnetic resonance imaging obtained with straightened lower extremities, *Journal of Manipulative and Physiological Therapeutics* **30**(1): 26–30.

Andreoli, A., Monteleone, M., Van Loan, M., Promenzio, L., Tarantino, U. & De Lorenzo, A. (2001). Effects of different sports on bone density and muscle mass in highly trained athletes., *Medicine and science in sports and exercise* **33**: 507–511.

Arbanas, J., Klasan, G. S., Nikolic, M., Jerkovic, R., Miljanovic, I. & Malnar, D. (2009). Fibre type composition of the human psoas major muscle with regard to the level of its origin, *Journal of Anatomy* **215**(6): 636–641.

Arjmand, N. & Shirazi-Adl, A. (2006). Model and in vivo studies on human trunk load partitioning and stability in isometric forward flexions., *Journal of biomechanics* **39**: 510–521.

Arnold, A. S., Salinas, S., Hakawa, D. J. & Delp, S. L. (2000). Accuracy of muscle moment arms estimated from MRI-based musculoskeletal models of the lower extremity, *Computer Aided Surgery* **5**(2): 108–119.

Arnold, E. M., Hamner, S. R., Seth, A., Millard, M. & Delp, S. L. (2013). How muscle fiber lengths and velocities affect muscle force generation as humans walk and run at different speeds, *Journal of Experimental Biology* **216**(11): 2150–2160.

Arnold, E. M., Ward, S. R., Lieber, R. L. & Delp, S. L. (2009). A model of the lower limb for analysis of human movement, *Annals of Biomedical Engineering* **38**(2): 269–279.

Ayturk, U. M. & Puttlitz, C. M. (2011). Parametric convergence sensitivity and validation of a finite element model of the human lumbar spine, *Computer Methods in Biomechanics and Biomedical Engineering* **14**(8): 695–705.

Badilatti, S. D., Christen, P., Ferguson, S. J. & Muller, R. (2017). Computational modeling of long-term effects of prophylactic vertebroplasty on bone adaptation, *Proceedings of the Institution of Mechanical Engineers, Part H: Journal of Engineering in Medicine* **231**(5): 423–431.

Badilatti, S. D., Christen, P., Levchuk, A., Marangalou, J. H., van Rietbergen, B., Parkinson, I. & Muller, R. (2015). Large-scale microstructural simulation of load-adaptive bone remodeling in whole human vertebrae, *Biomechanics and Modeling in Mechanobiology* **15**(1): 83–95.

Badilatti, S. D., Christen, P., Parkinson, I. & Muller, R. (2016). Load-adaptive bone remodeling simulations reveal osteoporotic microstructural and mechanical changes in whole human vertebrae, *Journal of Biomechanics* **49**(16): 3770–3779.

Barre, A. & Armand, S. (2014). Biomechanical ToolKit: Open-source framework to visualize and process biomechanical data, *Computer Methods and Programs in Biomedicine* **114**(1): 80–87.

Beaucage-Gauvreau, E., Robertson, W. S. P., Brandon, S. C. E., Fraser, R., Freeman, B. J. C., Graham, R. B., Thewlis, D. & Jones, C. F. (2019). Validation of an OpenSim full-body model with detailed lumbar spine for estimating lower lumbar spine loads during symmetric and asymmetric lifting tasks, *Computer Methods in Biomechanics and Biomedical Engineering* pp. 1–14.

Benedetti, M. G., Furlini, G., Zati, A. & Mauro, G. L. (2018). The effectiveness of physical exercise on bone density in osteoporotic patients, *BioMed Research International* **2018**: 1–10.

Bennell, K., Malcolm, S., Khan, K., Thomas, S., Reid, S., Brukner, P., Ebeling, P. & Wark, J. (1997). Bone mass and bone turnover in power athletes, endurance athletes, and controls: A 12-month longitudinal study, *Bone* **20**(5): 477–484.

Bergmark, A. (1989). Stability of the lumbar spine, *Acta Orthopaedica Scandinavica* **60**(sup230): 1–54.

Bitsakos, C., Kerner, J., Fisher, I. & Amis, A. A. (2005). The effect of muscle loading on the simulation of bone remodelling in the proximal femur, *Journal of Biomechanics* **38**(1): 133–139.

Bjoernsdottir, S., Jonsson, S. & Valdimarsdottir, U. (2012). Functional limitations and physical symptoms of individuals with chronic pain, *Scandinavian Journal of Rheumatology* **42**(1): 59–70.

Blemker, S. S. & Delp, S. L. (2005). Three-dimensional representation of complex muscle architectures and geometries, *Annals of Biomedical Engineering* **33**(5): 661–673.

Bogduk, N. & Endres, S. (2005). *Clinical anatomy of the lumbar spine and sacrum*, 4 edn, Edinburgh ; New York : Elsevier Churchill Livingstone.

Bogduk, N., Johnson, G. & Spalding, D. (1998). The morphology and biomechanics of latissimus dorsi., *Clinical biomechanics (Bristol, Avon)* **13**: 377–385.

Bogduk, N., Macintosh, J. E. & Pearcy, M. J. (1992). A universal model of the lumbar back muscles in the upright position., *Spine* **17**: 897–913.

Bogduk, N., Pearcy, M. & Hadfield, G. (1992). Anatomy and biomechanics of psoas major, *Clinical Biomechanics* **7**(2): 109–119.

Breen, A. C., Teyhen, D. S., Mellor, F. E., Breen, A. C., Wong, K. W. N. & Deitz, A. (2012). Measurement of intervertebral motion using quantitative fluoroscopy: Report of an international forum and proposal for use in the assessment of degenerative disc disease in the lumbar spine, *Advances in Orthopedics* **2012**: 1–10.

Brink, R., Schlosser, T., Colo, D., Vinken, K., van Stralen, M., Hui, S., Chu, W., Cheng, J. & Castelein, R. (2016). Upright, prone and supine spinal morphology in adolescent idiopathic scoliosis, *The Spine Journal* **16**(4): S81.

Bruno, A. G., Bouxsein, M. L. & Anderson, D. E. (2015). Development and validation of a musculoskeletal model of the fully articulated thoracolumbar spine and rib cage, *Journal of Biomechanical Engineering* **137**(8): 081003.

Buchanan, T. (1995). Evidence that maximum muscle stress is not a constant: differences in specific tension in elbow flexors and extensors, *Medical Engineering & Physics* **17**(7): 529–536.

Buford, W. L., Ivey, F. M., Malone, J. D., Patterson, R. M., Peare, G. L., Nguyen, D. K. & Stewart, A. A. (1997). Muscle balance at the knee–moment arms for the normal knee and the acl-minus knee., *IEEE transactions on rehabilitation engineering : a publication of the IEEE Engineering in Medicine and Biology Society* **5**: 367–379.

Center, J. R., Nguyen, T. V., Schneider, D., Sambrook, P. N. & Eisman, J. A. (1999). Mortality after all major types of osteoporotic fracture in men and women: an observational study, *The Lancet* **353**(9156): 878–882.

Chou, Y., Shih, C., Lin, J., Chen, T. & Liao, C. (2013). Low back pain associated with sociodemographic factors, lifestyle and osteoporosis: A population-based study, *Journal of Rehabilitation Medicine* **45**(1): 76–80.

Christophy, M., Senan, N. A. F., Lotz, J. C. & O'Reilly, O. M. (2012). A musculoskeletal model for the lumbar spine, *Biomechanics and Modeling in Mechanobiology* **11**(1): 19–34.

Clough, R. (1960). *The Finite Element Method in Plane Stress Analysis*, American Society of Civil Engineers.

Cooper, C., Atkinson, E. J., Jacobsen, S. J., O'Fallon, W. M. & Melton, L. J. (1993). Population-based study of survival after osteoporotic fractures, *American Journal of Epidemiology* **137**(9): 1001–1005.

Cronskaer, M., Rasmussen, J. & Tinnsten, M. (2013). Combined finite element and multibody musculoskeletal investigation of a fractured clavicle with reconstruction plate, *Computer Methods in Biomechanics and Biomedical Engineering* **18**(7): 740–748.

Daly, R. M., Via, J. D., Duckham, R. L., Fraser, S. F. & Helge, E. W. (2019). Exercise for the prevention of osteoporosis in postmenopausal women: an evidence-based guide to the optimal prescription, *Brazilian Journal of Physical Therapy* **23**(2): 170–180.

Damadian, R. (1971). Tumor detection by nuclear magnetic resonance, *Science* **171**(3976): 1151–1153.

Dao, T. T., Pouletaut, P., Charleux, F., Lazáry, Á., Eltes, P., Varga, P. P. & Tho, M. C. H. B. (2014). Estimation of patient specific lumbar spine muscle forces using multiphysical musculoskeletal model and dynamic MRI, *Advances in Intelligent Systems and Computing*, Springer International Publishing, pp. 411–422.

de-las Peñas, C. F., Hernández-Barrera, V., Alonso-Blanco, C., Palacios-Ceña, D., Carrasco-Garrido, P., Jiménez-Sánchez, S. & Jiménez-García, R. (2011). Prevalence of neck and low back pain in community-dwelling adults in spain, *Spine* **36**(3): E213–E219.

de Zee, M., Hansen, L., Wong, C., Rasmussen, J. & Simonsen, E. B. (2007). A generic detailed rigid-body lumbar spine model, *Journal of Biomechanics* **40**(6): 1219 – 1227.

Delp, S. L., Anderson, F. C., Arnold, A. S., Loan, P., Habib, A., John, C. T., Guendelman, E. & Thelen, D. G. (2007). Opensim: open-source software to create and analyze dynamic simulations of movement, *IEEE transactions on biomedical engineering* **54**(11): 1940–1950.

Delp, S. L., Hess, W. E., Hungerford, D. S. & Jones, L. C. (1999). Variation of rotation moment arms with hip flexion, *Journal of Biomechanics* **32**(5): 493–501.

Delp, S. L., Loan, J. P., Hoy, M. G., Zajac, F. E., Topp, E. L. & Rosen, J. M. (1990). An interactive graphics-based model of the lower extremity to study orthopaedic surgical procedures, *IEEE Transactions on Biomedical engineering* **37**(8): 757–767.

Dostal, W. F., Soderberg, G. L. & Andrews, J. G. (1986). Actions of hip muscles, *Physical Therapy* **66**(3): 351–359.

Dreischarf, M., Rohlmann, A., Zhu, R., Schmidt, H. & Zander, T. (2013). Is it possible to estimate the compressive force in the lumbar spine from intradiscal pressure measurements? a finite element evaluation, *Medical Engineering & Physics* **35**(9): 1385–1390.

Dvorak, J., Panjabi, M. M., Chang, D. G., Theiler, R. & Grob, D. (1991). Functional radiographic diagnosis of the lumbar spine. flexion-extension and lateral bending., *Spine* **16**: 562–571.

Edwards, W. T., Zheng, Y., Ferrara, L. A. & Yuan, H. A. (2001). Structural features and thickness of the vertebral cortex in the thoracolumbar spine, *Spine* **26**(2): 218–225.

Einkauf, D. K., Gohdes, M. L., Jensen, G. M. & Jewell, M. J. (1987). Changes in spinal mobility with increasing age in women, *Physical Therapy* **67**(3): 370–375.

Eng, J. J. & Winter, D. A. (1995). Kinetic analysis of the lower limbs during walking: What information can be gained from a three-dimensional model?, *Journal of Biomechanics* **28**(6): 753–758.

Epstein, S. (2005). The roles of bone mineral density, bone turnover, and other properties in reducing fracture risk during antiresorptive therapy, *Mayo Clinic Proceedings* **80**(3): 379–388.

Eriksen, E., Melsen, F., Sod, E., Barton, I. & Chines, A. (2002). Effects of long-term risedronate on bone quality and bone turnover in women with postmenopausal osteoporosis, *Bone* **31**(5): 620–625.

Eswaran, S. K., Bayraktar, H. H., Adams, M. F., Gupta, A., Hoffmann, P. F., Lee, D. C., Papadopoulos, P. & Keaveny, T. M. (2007). The micro-mechanics of cortical shell removal in the human vertebral body, *Computer Methods in Applied Mechanics and Engineering* **196**(31-32): 3025–3032.

Fallon, J. F. & Simandl, B. K. (1978). Evidence of a role for cell death in the disappearance of the embryonic human tail, *American Journal of Anatomy* **152**(1): 111–129.

Fath, F., Blazevich, A. J., Waugh, C. M., Miller, S. C. & Korff, T. (2010). Direct comparison of in vivo achilles tendon moment arms obtained from ultrasound and MR scans, *Journal of Applied Physiology* **109**(6): 1644–1652.

Feltrin, G., Macchi, V., Saccavini, C., Tosi, E., Dus, C., Fassina, A., Parenti, A. & Caro, R. D. (2001). Fractal analysis of lumbar vertebral cancellous bone architecture, *Clinical Anatomy* **14**(6): 414–417.

Fleckenstein, J. L., Crues, J. V. & Reimers, C. D. (eds) (1996). *Muscle Imaging in Health and Disease*, Springer New York.

Fonseca, H., Moreira-Gonçalves, D., Coriolano, H.-J. A. & Duarte, J. A. (2013). Bone quality: The determinants of bone strength and fragility, *Sports Medicine* **44**(1): 37–53.

Francis, R. M., Aspray, T. J., Hide, G., Sutcliffe, A. M. & Wilkinson, P. (2007). Back pain in osteoporotic vertebral fractures, *Osteoporosis International* **19**(7): 895–903.

Friedman, A. W. (2006). Important determinants of bone strength, *Journal of Clinical Rheumatology* **12**(2): 70–77.

Frost, H. M. (1987). Bone mass and the mechanostat: A proposal, *The Anatomical Record* **219**(1): 1–9.

Frost, H. M. (2003). Bone's mechanostat: A 2003 update, *The Anatomical Record* **275A**(2): 1081–1101.

Fujii, R., Sakaura, H., Mukai, Y., Hosono, N., Ishii, T., Iwasaki, M., Yoshikawa, H. & Sugamoto, K. (2007). Kinematics of the lumbar spine in trunk rotation: in vivo three-dimensional analysis using magnetic resonance imaging, *European Spine Journal* **16**(11): 1867–1874.

Gallois, M. & Japiot, M. (1925). Architecture interieure des vertebres, *Revue de Chirurgie* **63**: 687–708.

Gatchel, R. J., Neblett, R., Kishino, N. & Ray, C. T. (2016). Fear-avoidance beliefs and chronic pain, *Journal of Orthopaedic & Sports Physical Therapy* **46**(2): 38–43.

Ghezelbash, F., Schmidt, H., Shirazi-Adl, A. & El-Rich, M. (2019). Internal load-sharing in the human passive lumbar spine: Review of in vitro and finite element model studies, *Journal of Biomechanics* p. 109441.

Gibbons, S. G. & Comerford, M. J. (2001). Strength versus stability part i; concept and terms, *Orthopaedic Division Review* pp. 21–27.

Gilbertson, L. G., Doehring, T. C. & Kang, J. D. (2000). New methods to study lumbar spine biomechanics: Delineation of in vitro load-displacement characteristics by using a robotic/UFS testing system with hybrid control, *Operative Techniques in Orthopaedics* **10**(4): 246–253.

Goda, I. & Ganghoffer, J.-F. (2015). Identification of couple-stress moduli of vertebral trabecular bone based on the 3d internal architectures, *Journal of the Mechanical Behavior of Biomedical Materials* **51**: 99–118.

Goff, B. (1972). The application of recent advances in neurophysiology to miss m. rood's concept of neuromuscular facilitation., *Physiotherapy* **58**: 409–415.

Gokaslan, Z. L. & Hsu, W. (2012). Surgical resection of sacral tumors, *Schmidek and Sweet Operative Neurosurgical Techniques*, Elsevier, chapter 193, pp. 2201–2216.

Gold, D. T. (2003). Osteoporosis and quality of life, *Clinics in Geriatric Medicine* **19**(2): 271–280.

Gold, D. T., Bales, C. W., Lyles, K. W. & Drezner, M. K. (1989). Treatment of osteoporosis, *Journal of the American Geriatrics Society* **37**(5): 417–422.

Gold, D. T., Smith, S. D., Bales, C. W., Lyles, K. W., Westlund, R. E. & Drezner, M. K. (1991). Osteoporosis in late life: Does health locus of control affect psychosocial adaptation?, *Journal of the American Geriatrics Society* **39**(7): 670–675.

Gomez-Cabello, A., Ara, I., Gonzalez-Aguero, A., Casajus, J. & Vicente-Rodriguez, G. (2012). Effects of training on bone mass in older adults, *Sports Medicine* **42**(4): 301–325.

Gopalakrishnan, A., Modenese, L. & Phillips, A. T. M. (2014). A novel computational framework for deducing muscle synergies from experimental joint moments, *Frontiers in Computational Neuroscience* **8**.

Gray, H. (1862). *Anatomy: descriptive and surgical*, Blanchard and Lea.

Grood, E. S., Suntay, W. J., Noyes, F. R. & Butler, D. L. (1984). Biomechanics of the knee-extension exercise. effect of cutting the anterior cruciate ligament., *The Journal of Bone & Joint Surgery* **66**(5): 725–734.

Guadalupe-Grau, A., Fuentes, T., Guerra, B. & Calbet, J. A. (2009). Exercise and bone mass in adults, *Sports Medicine* **39**(6): 439–468.

Hamner, S. R., Seth, A. & Delp, S. L. (2010). Muscle contributions to propulsion and support during running, *Journal of Biomechanics* **43**(14): 2709–2716.

Han, K.-S., Zander, T., Taylor, W. R. & Rohlmann, A. (2012). An enhanced and validated generic thoraco-lumbar spine model for prediction of muscle forces, *Medical Engineering & Physics* **34**(6): 709 – 716.

Hansen, L., de Zee, M., Rasmussen, J., Andersen, T. B., Wong, C. & Simonsen, E. B. (2006). Anatomy and biomechanics of the back muscles in the lumbar spine with reference to biomechanical modeling, *Spine* **31**(17): 1888–1899.

Haskell, W. L., Lee, I.-M., Pate, R. R., Powell, K. E., Blair, S. N., Franklin, B. A., Macera, C. A., Heath, G. W., Thompson, P. D. & Bauman, A. (2007). Physical activity and public health: updated recommendation for adults from the american college of sports medicine and the american heart association., *Medicine and science in sports and exercise* **39**: 1423–1434.

Haxton, H. A. (1944). Absolute muscle force in the ankle flexors of man, *The Journal of Physiology* **103**(3): 267–273.

Hermens, H. J., Freriks, B., Merletti, R., Stegeman, D., Blok, J., Rau, G., Disselhorst-Klug, C. & Hägg, G. (1999). European recommendations for surface electromyography, *Roessingh research and development* **8**(2): 13–54.

Hicks, J. L., Uchida, T. K., Seth, A., Rajagopal, A. & Delp, S. L. (2015). Is my model good enough? best practices for verification and validation of musculoskeletal models and simulations of movement, *Journal of Biomechanical Engineering* **137**(2): 020905.

Hill, P. A. (1998). Bone remodelling., *British Journal of Orthodontics* **25**(2): 101–107.

Hodges, P. W. & Richardson, C. A. (1996). Inefficient muscular stabilization of the lumbar spine associated with low back pain, *Spine* **21**(22): 2640–2650.

Hodges, P. W. & Richardson, C. A. (1997). Contraction of the abdominal muscles associated with movement of the lower limb, *Physical Therapy* **77**(2): 132–142.

Hodges, P. W. & Richardson, C. A. (1998). Delayed postural contraction of transversus abdominis in low back pain associated with movement of the lower limb., *Journal of spinal disorders* **11**: 46–56.

Hoffman, S. L., Harris-Hayes, M. & Dillen, L. R. V. (2010). Differences in activity limitation between 2 low back pain subgroups based on the movement system impairment model, *Physical Medicine and Rehabilitation* **2**(12): 1113–1118.

Holzbaur, K. R. S., Murray, W. M. & Delp, S. L. (2005). A model of the upper extremity for simulating musculoskeletal surgery and analyzing neuromuscular control, *Annals of Biomedical Engineering* **33**(6): 829–840.

Homminga, J., Aquarius, R., Bulsink, V. E., Jansen, C. T. & Verdonschot, N. (2012). Can vertebral density changes be explained by intervertebral disc degeneration?, *Medical Engineering & Physics* **34**(4): 453–458.

Homminga, J., Van-Rietbergen, B., Lochmuller, E., Weinans, H., Eckstein, F. & Huiskes, R. (2004). The osteoporotic vertebral structure is well adapted to the loads of daily life, but not to infrequent "error" loads, *Bone* **34**(3): 510–516.

Homminga, J., Weinans, H., Gowin, W., Felsenberg, D. & Huiskes, R. (2001). Osteoporosis changes the amount of vertebral trabecular bone at risk of fracture but not the vertebral load distribution, *Spine* **26**(14): 1555–1560.

Horsman, M. K., Koopman, H., van der Helm, F., Prosé, L. P. & Veeger, H. (2007). Morphological muscle and joint parameters for musculoskeletal modelling of the lower extremity, *Clinical Biomechanics* **22**(2): 239–247.

Intolo, P., Milosavljevic, S., Baxter, D. G., Carman, A. B., Pal, P. & Munn, J. (2009). The effect of age on lumbar range of motion: A systematic review, *Manual Therapy* **14**(6): 596–604.

Jayaraman, G., Nazre, A. A., McCann, V. & Redford, J. B. (1994). A computerized technique for analyzing lateral bending behavior of subjects with normal and impaired lumbar spine. a pilot study., *Spine* **19**: 824–832.

Jayasinghe, J., Jones, S. & Boyde, A. (1994). Three-dimensional photographic study of cancellous bone in human fourth lumbar vertebral bodies, *Anatomy and Embryology* **189**(3).

Jorgensen, M. J., Marras, W. S., Gupta, P. & Waters, T. R. (2003). Effect of torso flexion on the lumbar torso extensor muscle sagittal plane moment arms., *The spine journal : official journal of the North American Spine Society* **3**: 363–369.

Kanis, J. A. & Johnell, O. (2004). Requirements for dxa for the management of osteoporosis in europe, *Osteoporosis International* **16**(3): 229–238.

Kannus, P. (1995). Effect of starting age of physical activity on bone mass in the dominant arm of tennis and squash players, *Annals of Internal Medicine* **123**(1): 27.

Keaveny, T. M., Morgan, E. F. & Yeh, O. C. (2002). *Standard handbook of biomedical engineering and design*, McGraw-Hill Professional, chapter 8. Bone mechanics, pp. 1–24.

Keller, T. S., Hansson, T. H., Abram, A. C., Spengler, D. M. & Panjabi, M. M. (1989). Regional variations in the compressive properties of lumbar vertebral trabeculae, *Spine* **14**(9): 1012–1019.

Kelley, G. A., Kelley, K. S. & Tran, Z. V. (2002). Exercise and lumbar spine bone mineral density in postmenopausal women: A meta-analysis of individual patient data, *The Journals of Gerontology Series A: Biological Sciences and Medical Sciences* **57**(9): M599–M604.

Kiapour, A., Ambati, D., Hoy, R. W. & Goel, V. K. (2012). Effect of graded facetectomy on biomechanics of dynesys dynamic stabilization system, *Spine* **37**(10): E581–E589.

Klemt, C., Nolte, D., Ding, Z., Rane, L., Quest, R. A., Finnegan, M. E., Walker, M., Reilly, P. & Bull, A. M. J. (2019). Anthropometric scaling of anatomical datasets for subject-specific musculoskeletal modelling of the shoulder, *Annals of Biomedical Engineering* **47**(4): 924–936.

Koenig, A. & Vitzthum, H.-E. (2001). Functional MRI of the spine: different patterns of positions of the forward flexed lumbar spine in healthy subjects, *European Spine Journal* **10**(5): 437–442.

Konrad, P. (2006). *The ABC of EMG: a practical introduction to kinesiological electromyography*, 1.4 edn, Noraxon USA, Inc.

Kothe, R., Kohlmann, T., Klink, T., Ruther, W. & Klinger, R. (2007). Impact of low back pain on functional limitations, depressed mood and quality of life in patients with rheumatoid arthritis, *Pain* **127**(1): 103–108.

Krahl, H., Michaelis, U., Pieper, H.-G., Quack, G. & Montag, M. (1994). Stimulation of bone growth through sports, *The American Journal of Sports Medicine* **22**(6): 751–757.

Kuiken, T. A., Lowery, M. M. & Stoykov, N. S. (2003). The effect of subcutaneous fat on myoelectric signal amplitude and cross-talk., *Prosthetics and orthotics international* **27**: 48–54.

Kular, J., Tickner, J., Chim, S. M. & Xu, J. (2012). An overview of the regulation of bone remodelling at the cellular level, *Clinical Biochemistry* **45**(12): 863–873.

L, M. (1990). Age-related loss of vertebral trabecular bone mass and structure-biomechanical consequences, *in* W. S. Mow VC, Ratcliffe A (ed.), *Biomechanics of diarthrodial joints*, Springer-Verlag, New York, pp. 83–96.

Laird, R. A., Keating, J. L., Ussing, K., Li, P. & Kent, P. (2019). Does movement matter in people with back pain? investigating 'atypical' lumbo-pelvic kinematics in people with and without back pain using wireless movement sensors, *BMC Musculoskeletal Disorders* **20**(1).

Lang, T., LeBlanc, A., Evans, H., Lu, Y., Genant, H. & Yu, A. (2004). Cortical and trabecular bone mineral loss from the spine and hip in long-duration spaceflight., *Journal of bone and mineral research : the official journal of the American Society for Bone and Mineral Research* **19**: 1006–1012.

Lau, R. Y. & Guo, X. (2011). A review on current osteoporosis research: With special focus on disuse bone loss, *Journal of Osteoporosis* **2011**: 1–6.

Lauterbur, P. C. (1973). Image formation by induced local interactions: Examples employing nuclear magnetic resonance, *Nature* **242**(5394): 190–191.

LeBlanc, A., Schneider, V., Shackelford, L., West, S., Oganov, V., Bakulin, A. & Voronin, L. (2000). Bone mineral and lean tissue loss after long duration space flight., *Journal of musculoskeletal & neuronal interactions* **1**: 157–160.

Lee, S.-P., Smith, J. A., Kimber, M. & Houk, K. (2018). Insertion and presence of fine-wire intramuscular electrodes to the lumbar paraspinal muscles do not affect muscle performance and activation during high-exertion spinal extension activities, *PM&R* **10**(11): 1192–1197.

Leeuw, M., Goossens, M. E. J. B., Linton, S. J., Crombez, G., Boersma, K. & Vlaeyen, J. W. S. (2006). The fear-avoidance model of musculoskeletal pain: Current state of scientific evidence, *Journal of Behavioral Medicine* **30**(1): 77–94.

Legroux-Gerot, I., Lormeau, C., Boutry, N., Cotten, A., Duquesnoy, B. & Cortet, B. (2004). Long-term follow-up of vertebral osteoporotic fractures treated by percutaneous vertebroplasty, *Clinical Rheumatology* **23**(4).

Li, Q. Y., Kim, H.-J., Son, J., Kang, K.-T., Chang, B.-S., Lee, C.-K., Seok, H. S. & Yeom, J. S. (2017). Biomechanical analysis of lumbar decompression surgery in relation to degenerative changes in the lumbar spine – validated finite element analysis, *Computers in Biology and Medicine* **89**: 512–519.

Little, J. P., Visser, H. D., Pearcy, M. J. & Adam, C. J. (2008). Are coupled rotations in the lumbar spine largely due to the osseo-ligamentous anatomy?—a modeling study, *Computer Methods in Biomechanics and Biomedical Engineering* **11**(1): 95–103.

Liu, C.-L., Zhong, Z.-C., Hsu, H.-W., Shih, S.-L., Wang, S.-T., Hung, C. & Chen, C.-S. (2011). Effect of the cord pretension of the dynesys dynamic stabilisation system on the biomechanics of the lumbar spine: a finite element analysis, *European Spine Journal* **20**(11): 1850–1858.

Liu, X. S., Sajda, P., Saha, P. K., Wehrli, F. W., Bevill, G., Keaveny, T. M. & Guo, X. E. (2007). Complete volumetric decomposition of individual trabecular plates and rods and its morphological correlations with anisotropic elastic moduli in human trabecular bone, *Journal of Bone and Mineral Research* **23**(2): 223–235.

Liu, X. S., Sajda, P., Saha, P. K., Wehrli, F. W. & Guo, X. E. (2006). Quantification of the roles of trabecular microarchitecture and trabecular type in determining the elastic modulus of human trabecular bone, *Journal of Bone and Mineral Research* **21**(10): 1608–1617.

Liu, X. S., Zhang, X. H. & Guo, X. E. (2009). Contributions of trabecular rods of various orientations in determining the elastic properties of human vertebral trabecular bone, *Bone* **45**(2): 158–163.

Longo, U. G., Loppini, M., Berton, A., Laverde, L., Maffulli, N. & Denaro, V. (2014). Degenerative changes of the sacroiliac joint after spinal fusion: an evidence-based systematic review, *British Medical Bulletin* **112**(1): 47–56.

Macintosh, J. E. & Bogduk, N. (1986). The biomechanics of the lumbar multifidus, *Clinical Biomechanics* **1**(4): 205–213.

Macintosh, J. E. & Bogduk, N. (1987). 1987 volvo award in basic science. the morphology of the lumbar erector spinae., *Spine* **12**: 658–668.

Macintosh, J. E. & Bogduk, N. (1991). The attachments of the lumbar erector spinae., *Spine* **16**: 783–792.

Madureira, M. M., Takayama, L., Gallinaro, A. L., Caparbo, V. F., Costa, R. A. & Pereira, R. M. R. (2006). Balance training program is highly effective in improving functional status and reducing the risk of falls in elderly women with osteoporosis: a randomized controlled trial, *Osteoporosis International* **18**(4): 419–425.

Maganaris, C. N. (2004). Imaging-based estimates of moment arm length in intact human muscle-tendons, *European Journal of Applied Physiology* **91**(2-3): 130–139.

Maganaris, C. N., Baltzopoulos, V., Ball, D. & Sargeant, A. J. (2001). In vivo specific tension of human skeletal muscle, *Journal of Applied Physiology* **90**(3): 865–872.

Maillot, C. & Wolfram-Gabel, R. (1993). Pedicles of lumbar vertebrae, *Surgical and Radiologic Anatomy* **15**(4): 295–300.

Mayer, T. G., Gatchel, R. J., Kishino, N., Keeley, J., Capra, P., Mayer, H., Barnett, J. & Mooney, V. (1985). 1985 volvo award in clinical sciences: Objective assessment of spine function following industrial injury, *Spine* **10**(6): 482–493.

McGill, S. (2004). *Ultimate Back Fitness and Performance*, Stuart McGill, PhD.

McGill, S., Juker, D. & Kropf, P. (1996). Quantitative intramuscular myoelectric activity of quadratus lumborum during a wide variety of tasks., *Clinical biomechanics (Bristol, Avon)* **11**: 170–172.

McGill, S. & Norman, R. (1988). Potential of lumbodorsal fascia forces to generate back extension moments during squat lifts, *Journal of Biomedical Engineering* **10**(4): 312–318.

McGregor, A. H., Anderton, L., Gedroyc, W. M., Johnson, J. & Hughes, S. P. (2001). Assessment of spinal kinematics using open interventional magnetic resonance imaging., *Clinical orthopaedics and related research* pp. 341–348.

McGregor, A. H. & Hukins, D. W. L. (2009). Lower limb involvement in spinal function and low back pain., *Journal of back and musculoskeletal rehabilitation* **22**: 219–222.

Meakin, J. R., Gregory, J. S., Aspden, R. M., Smith, F. W. & Gilbert, F. J. (2009). The intrinsic shape of the human lumbar spine in the supine, standing and sitting postures: characterization using an active shape model, *Journal of Anatomy* **215**(2): 206–211.

Melton, L. J., Chrischilles, E. A., Cooper, C., Lane, A. W. & Riggs, B. L. (2009). Perspective how many women have osteoporosis?, *Journal of Bone and Mineral Research* **7**(9): 1005–1010.

Milanovic, Z., Jorgić, B., Trajković, N., Sporis, Pantelić, S. & James (2013). Age-related decrease in physical activity and functional fitness among elderly men and women, *Clinical Interventions in Aging* p. 549.

Modenese, L., Phillips, A. & Bull, A. (2011). An open source lower limb model: hip joint validation, *Journal of biomechanics* **44**(12): 2185–2193.

Mondal, A., Nguyen, C., Ma, X., Elbanna, A. E. & Carlson, J. M. (2019). Network models for characterization of trabecular bone, *Physical Review E* **99**(4).

Morlock, M., Schneider, E., Bluhm, A., Vollmer, M., Bergmann, G., Muller, V. & Honl, M. (2001). Duration and frequency of every day activities in total hip patients, *Journal of Biomechanics* **34**(7): 873–881.

Mottram, S. & Comerford, M. (1998). Stability dysfunction and low back pain, *Journal of Orthopaedic Medicine* **20**(2): 13–18.

Mukhopadhyay, B., Shukla, R., Mukhopadhyay, M., Mandal, K., Haldar, P. & Benare, A. (2012). Spectrum of human tails: A report of six cases, *Journal of Indian Association of Pediatric Surgeons* **17**(1): 23.

Muller, R. (2004). Long-term prediction of three-dimensional bone architecture in simulations of pre-, peri- and post-menopausal microstructural bone remodeling, *Osteoporosis International* **16**(S02): S25–S35.

Nabhani, F. & Wake, M. (2002). Computer modelling and stress analysis of the lumbar spine, *Journal of Materials Processing Technology* **127**(1): 40–47.

Nachemson, A. (1965). The effect of forward leaning on lumbar intradiscal pressure, *Acta Orthopaedica Scandinavica* **35**(1-4): 314–328.

Nachemson, A. (1966). Electromyographic studies on the vertebral portion of the psoas muscle:with special reference to its stabilizing function of the lumbar spine, *Acta Orthopaedica Scandinavica* **37**(2): 177–190.

Nachemson, A. (1968). The possible importance of the psoas muscle for stabilization of the lumbar spine, *Acta Orthopaedica Scandinavica* **39**(1-3): 47–57.

Nagele, E., Kuhn, V., Vogt, H., Link, T. M., Muller, R., Lochmuller, E. M. & Eckstein, F. (2004). Technical considerations for microstructural analysis of human trabecular bone from specimens excised from various skeletal sites, *Calcified Tissue International* **75**(1): 15–22.

Nakamura, T. (2003). Low back pain accompanying osteoporosis, *Japan Medical Association Journal* **46**(10): 445–451.

Nakashima, D., Kanchiku, T., Nishida, N., Ito, S., Ohgi, J., Suzuki, H., Imajo, Y., Funaba, M., Chen, X. & Taguchi, T. (2018). Finite element analysis of compression fractures at the thoracolumbar junction using models constructed from medical images, *Experimental and Therapeutic Medicine* .

Nazer, R. A., Lanovaz, J., Kawalilak, C., Johnston, J. & Kontulainen, S. (2012). Direct in vivo strain measurements in human bone—a systematic literature review, *Journal of Biomechanics* **45**(1): 27–40.

Nelson, M. E., Rejeski, W. J., Blair, S. N., Duncan, P. W., Judge, J. O., King, A. C., Macera, C. A. & Castaneda-Sceppa, C. (2007). Physical activity and public health in older adults: recommendation from the american college of sports medicine and the american heart association., *Medicine and science in sports and exercise* **39**: 1435–1445.

Németh, G. & Ohlsén, H. (1985). In vivo moment arm lengths for hip extensor muscles at different angles of hip flexion, *Journal of Biomechanics* **18**(2): 129–140.

Newell, N., Little, J., Christou, A., Adams, M., Adam, C. & Masouros, S. (2017). Biomechanics of the human intervertebral disc: A review of testing techniques and results, *Journal of the Mechanical Behavior of Biomedical Materials* **69**: 420–434.

Ng, J. K., Kippers, V. & Richardson, C. A. (1998). Muscle fibre orientation of abdominal muscles and suggested surface emg electrode positions., *Electromyography and clinical neurophysiology* **38**: 51–58.

Ordway, N. R., Fayyazi, A. H., Abjornson, C., Calabrese, J., Park, S.-A., Fredrickson, B., Yonemura, K. & Yuan, H. A. (2008). Twelve-month follow-up of lumbar spine range of motion following intervertebral disc replacement using radiostereometric analysis, *International Journal of Spine Surgery* **2**(1): 9–15.

Pahr, D. H. & Zysset, P. K. (2009). A comparison of enhanced continuum FE with micro FE models of human vertebral bodies, *Journal of Biomechanics* **42**(4): 455–462.

Pal, P., Milosavljevic, S., Sole, G. & Johnson, G. (2007). Hip and lumbar continuous motion characteristics during flexion and return in young healthy males., *European spine journal : official publication of the European Spine Society, the European Spinal Deformity Society, and the European Section of the Cervical Spine Research Society* **16**: 741–747.

Panjabi, M., Abumi, K., Duranceau, J. & Oxland, T. (1989). Spinal stability and intersegmental muscle forces, *Spine* **14**(2): 194–200.

Panjabi, M. M., Goel, V. K. & Takata, K. (1982). Physiologic strains in the lumbar spinal ligaments, *Spine* **7**(3): 192–203.

Panjabi, M., Yamamoto, I., Oxland, T. & Crisco, J. (1989). How does posture affect coupling in the lumbar spine?, *Spine* **14**: 1002–1011.

Papi, E., Bull, A. M. & McGregor, A. H. (2019). Spinal segments do not move together predictably during daily activities, *Gait & Posture* **67**: 277–283.

Papi, E., Koh, W. S. & McGregor, A. H. (2017). Wearable technology for spine movement assessment: A systematic review, *Journal of Biomechanics* **64**: 186–197.

Park, W. M., Kim, K. & Kim, Y. H. (2013). Effects of degenerated intervertebral discs on intersegmental rotations, intradiscal pressures, and facet joint forces of the whole lumbar spine, *Computers in Biology and Medicine* **43**(9): 1234–1240.

Pearcy, M. J. & Bogduk, N. (1988). Instantaneous axes of rotation of the lumbar intervertebral joints., *Spine* **13**: 1033–1041.

Phillips, A. (2009). The femur as a musculo-skeletal construct: A free boundary condition modelling approach, *Medical Engineering & Physics* **31**(6): 673–680.

Phillips, A., Pankaj, P., Howie, C., Usmani, A. & Simpson, A. (2007). Finite element modelling of the pelvis: Inclusion of muscular and ligamentous boundary conditions, *Medical Engineering & Physics* **29**(7): 739–748.

Phillips, A. T. (2019a). Modelling trabecular bone as a voronoi network, *Bone Research Society Annual Meeting, 5th Joint Meeting with the British Orthopaedic Research Society* .

Phillips, A. T. M. (2012). Structural optimisation: biomechanics of the femur, *Proceedings of the Institution of Civil Engineers - Engineering and Computational Mechanics* **165**(2): 147–154.

Phillips, A. T. M. (2019b). Structural modelling of trabecular bone adaptation using a voronoi network, *XXVII Congress of the International Society of Biomechanics* .

Phillips, A. T. M. (2019c). Structural modelling of trabecular bone adaptation using a voronoi network, *17th Symposium on Computer Simulation in Biomechanics* . **URL:** *http://hdl.handle.net/10044/1/72722*

Phillips, A. T., Villette, C. C. & Modenese, L. (2015). Femoral bone mesoscale structural architecture prediction using musculoskeletal and finite element modelling, *International Biomechanics* **2**(1): 43–61.

Phillips, S., Mercer, S. & Bogduk, N. (2008). Anatomy and biomechanics of quadratus lumborum, *Proceedings of the Institution of Mechanical Engineers, Part H: Journal of Engineering in Medicine* **222**(2): 151–159.

Pillastrini, P., Gardenghi, I., Bonetti, F., Capra, F., Guccione, A., Mugnai, R. & Violante, F. S. (2012). An updated overview of clinical guidelines for chronic low back pain management in primary care, *Joint Bone Spine* **79**(2): 176–185.

Pizzolato, C., Lloyd, D. G., Sartori, M., Ceseracciu, E., Besier, T. F., Fregly, B. J. & Reggiani, M. (2015). Ceinms: A toolbox to investigate the influence of different neural control solutions on the prediction of muscle excitation and joint moments during dynamic motor tasks, *Journal of Biomechanics* **48**(14): 3929–3936.

Polikeit, A., Ferguson, S. J., Nolte, L. P. & Orr, T. E. (2003). Factors influencing stresses in the lumbar spine after the insertion of intervertebral cages: finite element analysis, *European Spine Journal* **12**(4): 413–420.

Pollock, M. L., Mengelkoch, L. J., Graves, J. E., Lowenthal, D. T., Limacher, M. C., Foster, C. & Wilmore, J. H. (1997). Twenty-year follow-up of aerobic power and body composition of older track athletes., *Journal of applied physiology (Bethesda, Md. : 1985)* **82**: 1508–1516.

Pothuaud, L., Rietbergen, B. V., Charlot, C., Ozhinsky, E. & Majumdar, S. (2004). A new computational efficient approach for trabecular bone analysis using beam models generated with skeletonized graph technique, *Computer Methods in Biomechanics and Biomedical Engineering* **7**(4): 205–213.

Raabe, M. E. & Chaudhari, A. M. (2016). An investigation of jogging biomechanics using the full-body lumbar spine model: Model development and validation, *Journal of Biomechanics* **49**(7): 1238–1243.

Rabi, I. I., Zacharias, J. R., Millman, S. & Kusch, P. (1938). A new method of measuring nuclear magnetic moment, *Physical Review* **53**(4): 318–318.

Rajagopal, A., Dembia, C. L., DeMers, M. S., Delp, D. D., Hicks, J. L. & Delp, S. L. (2016). Full-body musculoskeletal model for muscle-driven simulation of human gait, *IEEE Transactions on Biomedical Engineering* **63**(10): 2068–2079.

Reginster, J.-Y. & Burlet, N. (2006). Osteoporosis: A still increasing prevalence, *Bone* **38**(2): 4–9.

Reznikov, N., Shahar, R. & Weiner, S. (2014). Bone hierarchical structure in three dimensions, *Acta Biomaterialia* **10**(9): 3815–3826.

Rho, J.-Y., Kuhn-Spearing, L. & Zioupos, P. (1998). Mechanical properties and the hierarchical structure of bone, *Medical Engineering & Physics* **20**(2): 92–102.

Ritzel, H., Amling, M., Posl, M., Hahn, M. & Delling, G. (1997). The thickness of human vertebral cortical bone and its changes in aging and osteoporosis: A histomorphometric analysis of the complete spinal column from thirty-seven autopsy specimens, *Journal of Bone and Mineral Research* **12**(1): 89–95.

Roberto, K. (1989). Stress and adaptation patterns of older osteoporotic women, *Women & Health* **14**(3-4): 105–119.

Robling, A. G., Burr, D. B. & Turner, C. H. (2001). Recovery periods restore mechanosensitivity to dynamically loaded bone., *The Journal of experimental biology* **204**: 3389–3399.

Robling, A. G., Castillo, A. B. & Turner, C. H. (2006). Biomechanical and molecular regulation of bone remodeling., *Annual review of biomedical engineering* **8**: 455–498.

Rohlmann, A., Graichen, F. & Bergmann, G. (2000). Influence of load carrying on loads in internal spinal fixators, *Journal of Biomechanics* **33**(9): 1099–1104.

Rohlmann, A., Graichen, F., Kayser, R., Bender, A. & Bergmann, G. (2008). Loads on a telemeterized vertebral body replacement measured in two patients, *Spine* **33**(11): 1170–1179.

Rohlmann, A., Pohl, D., Bender, A., Graichen, F., Dymke, J., Schmidt, H. & Bergmann, G. (2014). Activities of everyday life with high spinal loads, *PLoS ONE* **9**(5): e98510.

Rontgen, W. C. (1896). On a New Kind of Rays, *Science* **3**(59): 227–231.

Rosatelli, A. L., Ravichandiran, K. & Agur, A. M. (2008). Three-dimensional study of the musculotendinous architecture of lumbar multifidus and its functional implications, *Clinical Anatomy* **21**(6): 539–546.

Rossini, M., Adami, S., Bertoldo, F., Diacinti, D., Gatti, D., Giannini, S., Giusti, A., Malavolta, N., Minisola, S., Osella, G., Pedrazzoni, M., Sinigaglia, L., Viapiana, O. & Isaia, G. C. (2016). Guidelines for the diagnosis, prevention and management of osteoporosis, *Reumatismo* **68**(1): 1.

Rozumalski, A., Schwartz, M. H., Wervey, R., Swanson, A., Dykes, D. C. & Novacheck, T. (2008). The in vivo three-dimensional motion of the human lumbar spine during gait., *Gait & posture* **28**: 378–384.

Rucci, N. (2008). Molecular biology of bone remodelling., *Clinical cases in mineral and bone metabolism : the official journal of the Italian Society of Osteoporosis, Mineral Metabolism, and Skeletal Diseases* **5**: 49–56.

Rybicki, E., Simonen, F. & Weis, E. (1972). On the mathematical analysis of stress in the human femur, *Journal of Biomechanics* **5**(2): 203–215.

Saidu, I. A., Maduagwu, S. M., Abbas, A. D., Adetunji, O. O. & Jajere, A. M. (2011). Lumbar spinal mobility changes among adults with advancing age., *Journal of mid-life health* **2**: 65–71.

Santaguida, P. L. & McGill, S. M. (1995). The psoas major muscle: a three-dimensional geometric study., *Journal of biomechanics* **28**: 339–345.

Sato, K., Kikuchi, S. & Yonezawa, T. (1999). In vivo intradiscal pressure measurement in healthy individuals and in patients with ongoing back problems., *Spine* **24**: 2468–2474.

Schmidt, H., Galbusera, F., Rohlmann, A., Zander, T. & Wilke, H.-J. (2010). Effect of multilevel lumbar disc arthroplasty on spine kinematics and facet joint loads in flexion and extension: a finite element analysis, *European Spine Journal* **21**(S5): 663–674.

Schultz, A., Andersson, G., Ortengren, R., Haderspeck, K. & Nachemson, A. (1982). Loads on the lumbar spine. validation of a biomechanical analysis by measurements of intradiscal pressures and myoelectric signals., *The Journal of bone and joint surgery. American volume* **64**(5): 713–720.

Senteler, M., Weisse, B., Rothenfluh, D. A. & Snedeker, J. G. (2015). Intervertebral reaction force prediction using an enhanced assembly of opensim models., *Computer Methods in Biomechanics and Biomedical Engineering* **19**(5): 538–548.

Shirazi-Adl, A. (1994). Biomechanics of the lumbar spine in sagittal/lateral moments., *Spine* **19**: 2407–2414.

Shum, G. L. K., Crosbie, J. & Lee, R. Y. W. (2007). Movement coordination of the lumbar spine and hip during a picking up activity in low back pain subjects., *European spine journal : official publication of the European Spine Society, the European Spinal Deformity Society, and the European Section of the Cervical Spine Research Society* **16**: 749–758.

Sinaki, M., Pfeifer, M., Preisinger, E., Itoi, E., Rizzoli, R., Boonen, S., Geusens, P. & Minne, H. W. (2010). The role of exercise in the treatment of osteoporosis, *Current Osteoporosis Reports* **8**(3): 138–144.

Smith, R. M., Pool, R. D., Butt, W. P. & Dickson, R. A. (1991). The transverse plane deformity of structural scoliosis., *Spine* **16**: 1126–1129.

Solomonow, M., Baratta, R., Bernardi, M., Zhou, B., Lu, Y., Zhu, M. & Acierno, S. (1994). Surface and wire emg crosstalk in neighbouring muscles, *Journal of Electromyography and Kinesiology* **4**(3): 131–142.

Speirs, A. D., Heller, M. O., Duda, G. N. & Taylor, W. R. (2007). Physiologically based boundary conditions in finite element modelling, *Journal of Biomechanics* **40**(10): 2318–2323.

Splendiani, A., Perri, M., Grattacaso, G., Tunno, V. D., Marsecano, C., Panebianco, L., Gennarelli, A., Felli, V., Varrassi, M., Barile, A., Cesare, E. D., Masciocchi, C. & Gallucci, M. (2015). Magnetic resonance imaging (MRI) of the lumbar spine with dedicated g-scan machine in the upright position: a retrospective study and our experience in 10 years with 4305 patients, *La radiologia medica* **121**(1): 38–44.

Spoor, C. & van Leeuwen, J. (1992). Knee muscle moment arms from MRI and from tendon travel, *Journal of Biomechanics* **25**(2): 201–206.

Steele, J., Bruce-Low, S. & Smith, D. (2014). A reappraisal of the deconditioning hypothesis in low back pain: review of evidence from a triumvirate of research methods on specific lumbar extensor deconditioning, *Current Medical Research and Opinion* **30**(5): 865–911.

Steele, K. M., DeMers, M. S., Schwartz, M. H. & Delp, S. L. (2012). Compressive tibiofemoral force during crouch gait, *Gait & Posture* **35**(4): 556–560.

Stilwell, D. L. (1962). Structural deformities of vertebrae. bone adaptation and modeling in experimental scoliosis and kyphosis., *The Journal of bone and joint surgery. American volume* **44-A**: 611–634.

Stokes, I. A. & Gardner-Morse, M. (1999). Quantitative anatomy of the lumbar musculature., *Journal of biomechanics* **32**: 311–316.

Takahashi, I., Kikuchi, S.-i., Sato, K. & Sato, N. (2006). Mechanical load of the lumbar spine during forward bending motion of the trunk-a biomechanical study., *Spine* **31**: 18–23.

Tarantino, U., Fanucci, E., Iundusi, R., Celi, M., Altobelli, S., Gasbarra, E., Simonetti, G. & Manenti, G. (2012). Lumbar spine MRI in upright position for diagnosing acute and chronic low back pain: statistical analysis of morphological changes, *Journal of Orthopaedics and Traumatology* **14**(1): 15–22.

Tella, S. H. & Gallagher, J. C. (2014). Prevention and treatment of postmenopausal osteoporosis, *The Journal of Steroid Biochemistry and Molecular Biology* **142**: 155–170.

Teng, G. G., Curtis, J. R. & Saag, K. G. (2008). Mortality and osteoporotic fractures: is the link causal, and is it modifiable?, *Clinical and experimental rheumatology* **26**: S125–S137.

Thelen, D. G. (2003). Adjustment of muscle mechanics model parameters to simulate dynamic contractions in older adults, *Journal of biomechanical engineering* **125**(1): 70–77.

Tsouknidas, A., Michailidis, N., Savvakis, S., Anagnostidis, K., Bouzakis, K.-D. & Kapetanos, G. (2012). A finite element model technique to determine the mechanical response of a lumbar spine segment under complex loads, *Journal of Applied Biomechanics* **28**(4): 448–456.

Tsubota, K., Adachi, T. & Tomita, Y. (2003). Effects of a fixation screw on trabecular structural changes in a vertebral body predicted by remodeling simulation, *Annals of Biomedical Engineering* **31**(6): 733–740.

Turner, C. H., Forwood, M. R. & Otter, M. W. (1994). Mechanotransduction in bone: do bone cells act as sensors of fluid flow?, *The FASEB Journal* **8**(11): 875–878.

Turner, C. H., Rho, J., Takano, Y., Tsui, T. Y. & Pharr, G. M. (1999). The elastic properties of trabecular and cortical bone tissues are similar: results from two microscopic measurement techniques, *Journal of Biomechanics* **32**(4): 437–441.

Turner, M. J., Clough, R. W., Martin, H. C. & Topp, L. J. (1956). Stiffness and deflection analysis of complex structures, *Journal of the Aeronautical Sciences* **23**(9): 805–823.

Uppin, A. A., Hirsch, J. A., Centenera, L. V., Pfiefer, B. A., Pazianos, A. G. & Choi, I. S. (2003). Occurrence of new vertebral body fracture after percutaneous vertebroplasty in patients with osteoporosis, *Radiology* **226**(1): 119–124.

van Arkel, R. J., Modenese, L., Phillips, A. & Jeffers, J. R. (2013). Hip abduction can prevent posterior edge loading of hip replacements, *Journal of Orthopaedic Research* **31**(8): 1172–1179.

van Lenthe, G., Stauber, M. & Muller, R. (2006). Specimen-specific beam models for fast and accurate prediction of human trabecular bone mechanical properties, *Bone* **39**(6): 1182–1189.

van Rijsbergen, M., van Rietbergen, B., Barthelemy, V., Eltes, P., Lazáry, Á., Lacroix, D., Noailly, J., Tho, M.-C. H. B., Wilson, W. & Ito, K. (2018). Comparison of patient-specific computational models vs. clinical follow-up, for adjacent segment disc degeneration and bone remodelling after spinal fusion, *PLOS ONE* **13**(8): e0200899.

Vanti, C., Andreatta, S., Borghi, S., Guccione, A. A., Pillastrini, P. & Bertozzi, L. (2017). The effectiveness of walking versus exercise on pain and function in chronic low back pain: a systematic review and meta-analysis of randomized trials, *Disability and Rehabilitation* **41**(6): 622–632.

Vasavada, A. N., Li, S. & Delp, S. L. (1998). Influence of muscle morphometry and moment arms on the moment-generating capacity of human neck muscles., *Spine* **23**: 412–422.

Verbunt, J. A., Smeets, R. J. & Wittink, H. M. (2010). Cause or effect? deconditioning and chronic low back pain, *Pain* **149**(3): 428–430.

Villette, C. C. (2016). *Structural meso and microscale finite element based approaches for the prediction of bone architecture and fracture*, PhD thesis, Imperial College London.
URL: *http://hdl.handle.net/10044/1/68280*

Villette, C. C. & Phillips, A. T. M. (2015). Informing phenomenological structural bone remodelling with a mechanistic poroelastic model, *Biomechanics and Modeling in Mechanobiology* **15**(1): 69–82.

Villette, C. C. & Phillips, A. T. M. (2017). Microscale poroelastic metamodel for efficient mesoscale bone remodelling simulations, *Biomechanics and Modeling in Mechanobiology* **16**(6): 2077–2091.

Villette, C. & Phillips, A. (2018). Rate and age-dependent damage elasticity formulation for efficient hip fracture simulations, *Medical Engineering & Physics* .

Vlaeyen, J. W. & Linton, S. J. (2000). Fear-avoidance and its consequences in chronic musculoskeletal pain: a state of the art, *Pain* **85**(3): 317–332.

Vlaeyen, J. W., Seelen, H. A., Peters, M., de Jong, P., Aretz, E., Beisiegel, E. & Weber, W. E. (1999). Fear of movement/(re)injury and muscular reactivity in chronic low back pain patients: an experimental investigation., *Pain* **82**: 297–304.

Wagner, D. W., Divringi, K., Ozcan, C., Grujicic, M., Pandurangan, B. & Grujicic, A. (2010). Combined musculoskeletal dynamics/structural finite element analysis of femur physiological loads during walking, *Multidiscipline Modeling in Materials and Structures* **6**(4): 417–437.

Wall, P. D. (1979). On the relation of injury to pain the john j. bonica lecture, *Pain* **6**(3): 253–264.

Wang, J., Zhou, B., Parkinson, I., Thomas, C. D. L., Clement, J. G., Fazzalari, N. & Guo, X. E. (2013). Trabecular plate loss and deteriorating elastic modulus of femoral trabecular bone in intertrochanteric hip fractures, *Bone Research* **1**(4): 346–354.

Ward, S. R., Tomiya, A., Regev, G. J., Thacker, B. E., Benzl, R. C., Kim, C. W. & Lieber, R. L. (2009). Passive mechanical properties of the lumbar multifidus muscle support its role as a stabilizer, *Journal of Biomechanics* **42**(10): 1384–1389.

Weiner, D. K., Haggerty, C. L., Kritchevsky, S. B., Harris, T., Simonsick, E. M., Nevitt, M. & and, A. N. (2003). How does low back pain impact physical function in independent, well-functioning older adults? evidence from the health ABC cohort and implications for the future, *Pain Medicine* **4**(4): 311–320.

White, A. A., Panjabi, M. M. et al. (1978). *Clinical biomechanics of the spine*, Vol. 2, Lippincott Philadelphia.

White, D. R., Griffith, R. V. & Wilson, I. J. (1992). Report 46, *Journal of the International Commission on Radiation Units and Measurements* **os24**(1): NP–NP.

Wilke, H. J., Neef, P., Caimi, M., Hoogland, T. & Claes, L. E. (1999). New in vivo measurements of pressures in the intervertebral disc in daily life., *Spine* **24**: 755–762.

Wilke, H.-J., Wolf, S., Claes, L. E., Arand, M. & Wiesend, A. (1996). Influence of varying muscle forces on lumbar intradiscal pressure: An in vitro study, *Journal of Biomechanics* **29**(4): 549–555.

Wilke, H., Neef, P., Hinz, B., Seidel, H. & Claes, L. (2001). Intradiscal pressure together with anthropometric data–a data set for the validation of models., *Clinical biomechanics (Bristol, Avon)* **16 Suppl 1**: S111–S126.

Wilkenfeld, A. J., Audu, M. L. & Triolo, R. J. (2006). Feasibility of functional electrical stimulation for control of seated posture after spinal cord injury: A simulation study., *Journal of rehabilitation research and development* **43**: 139–152.

Winter, D. A. (2009). *Biomechanics and Motor Control of Human Movement*, Wiley John + Sons.

Winter, D. A., Sidwall, H. & Hobson, D. A. (1974). Measurement and reduction of noise in kinematics of locomotion, *Journal of Biomechanics* **7**(2): 157–159.

Winter, D., Fuglevand, A. & Archer, S. (1994). Crosstalk in surface electromyography: Theoretical and practical estimates, *Journal of Electromyography and Kinesiology* **4**(1): 15–26.

Wong, K. W. N., Luk, K. D. K., Leong, J. C. Y., Wong, S. F. & Wong, K. K. Y. (2006). Continuous dynamic spinal motion analysis, *Spine* **31**(4): 414–419.

Wu, G., Siegler, S., Allard, P., Kirtley, C., Leardini, A., Rosenbaum, D., Whittle, M., D'Lima, D. D., Cristofolini, L., Witte, H., Schmid, O., Stokes, I., Standardization & of the International Society of Biomechanics, T. C. (2002). Isb recommendation on definitions of joint coordinate system of various joints for the reporting of human joint motion–part i: ankle, hip, and spine. international society of biomechanics., *Journal of biomechanics* **35**: 543–548.

Wu, G., van der Helm, F. C., Veeger, H. D., Makhsous, M., Roy, P. V., Anglin, C., Nagels, J., Karduna, A. R., McQuade, K., Wang, X., Werner, F. W. & Buchholz, B. (2005). ISB recommendation on definitions of joint coordinate systems of various joints for the reporting of human joint motion—part II: shoulder, elbow, wrist and hand, *Journal of Biomechanics* **38**(5): 981–992.

Yang, P. F., Bruggemann, G.-P. & Rittweger, J. (2011). What do we currently know from in vivo bone strain measurements in humans?, *Journal of musculoskeletal & neuronal interactions* **11**: 8–20.

Yeager, M. S., Cook, D. J. & Cheng, B. C. (2015). In VitroComparison of dynesys, PEEK, and titanium constructs in the lumbar spine, *Advances in Orthopedics* **2015**: 1–8.

Zaharie, D. T. & Phillips, A. T. (2019). A comparative study of continuum and structural modelling approaches to simulate bone adaptation in the pelvic construct, *Applied Sciences* **9**(16): 3320.

Zaharie, D. T. & Phillips, A. T. M. (2018). Pelvic construct prediction of trabecular and cortical bone structural architecture, *Journal of Biomechanical Engineering* **140**(9): 091001.

Zajac, F. E. (1989). Muscle and tendon: properties, models, scaling, and application to biomechanics and motor control., *Critical reviews in biomedical engineering* **17**: 359–411.

Zander, T., Rohlmann, A. & Bergmann, G. (2009). Influence of different artificial disc kinematics on spine biomechanics, *Clinical Biomechanics* **24**(2): 135–142.

Zanjani-Pour, S., Meakin, J. R., Breen, A. & Breen, A. (2018). Estimation of in vivo intervertebral loading during motion using fluoroscopic and magnetic resonance image informed finite element models, *Journal of Biomechanics* **70**: 134–139.

Zapata-Cornelio, F. Y., Day, G. A., Coe, R. H., Sikora, S. N. F., Wijayathunga, V. N., Tarsuslugil, S. M., Mengoni, M. & Wilcox, R. K. (2017). Methodology to produce specimen-specific models of vertebrae: Application to different species, *Annals of Biomedical Engineering* **45**(10): 2451–2460.

Zhu, R., Zander, T., Dreischarf, M., Duda, G. N., Rohlmann, A. & Schmidt, H. (2013). Considerations when loading spinal finite element models with predicted muscle forces from inverse static analyses, *Journal of Biomechanics* **46**(7): 1376–1378.

Zienkiewicz, O. C. (1977). *The finite element method*, Vol. Volume 3, McGraw-Hill.

Zienkiewicz, O. C. & Taylor, R. L. (2000). *Finite Element Method: Solid Mechanics*, Vol. Volume 2, Butterworth-Heinemann.

Zienkiewicz, O. & Cheung, Y. (1967). *The finite element method in structural and continuum mechanics: numerical solution of problems in structural and continuum mechanics*, Vol. Volume 1 of *European civil engineering series*, McGraw-Hill.

Publications

Journal papers

Favier, C.D., Deane, J.A., McGregor, A.H., Phillips, A.T.M (2019). Design and preliminary testing of a low-cost balance perturbation system for the evaluation of real life postural adjustment on public transport, *Journal of Medical Engineering and Technology*

Conference oral presentations

Favier, C.D., McGregor, A.H., Phillips, A.T.M. (2019). Subject specific multiscale modelling for the study of lumbar pathologies. *17th International Symposium on Computer Simulation in Biomechanics*

Favier, C.D., McGregor, A.H., Phillips, A.T.M. (2019). Full body subject specific musculoskeletal model for complex spine movements, *XXVII Congress of the International Society of Biomechanics*

Favier, C.D., McGregor, A.H., Phillips, A.T.M. (2018). Subject specific multiscale modelling of the lumbar spine, *14th Annual Bath Biomechanics Symposium*

Favier, C.D., McGregor, A.H., Phillips, A.T.M. (2018). Combined musculoskeletal and structural finite element modelling of the lumbar spine, *8th World Congress of Biomechanics*

Favier, C.D., McGregor, A.H., Phillips, A.T.M. (2017). Development of a combined MSK and FEA model of the lower back, *13th Annual Bath Biomechanics Symposium*

Favier, C.D., Phillips, A.T.M. (2017). Musculoskeletal model of lumbar spine and lower limb, *XXVI Congress of the International Society of Biomechanics*

Conference posters

Favier, C.D., McGregor, A.H., Phillips, A.T.M. (2019). Multiscale subject-specific modelling for the investigation of structural adaptation in the lumbar spine. *Bone Research Society Annual Meeting, 5th Joint Meeting with the British Orthopaedic Research Society*

Appendix A

Ethical approval letters

A.1 NHS Health Research Authority approval

NHS
Health Research Authority

Mr Clement Favier
Office 326, Skempton building
South Kensington Campus
London
SW7 2AZ

Email: hra.approval@nhs.net

17 February 2017

Dear Dr Phillips

Letter of HRA Approval

Study title:	**Computational modelling of the lumbar spine and investigation of low back pain development patterns**
IRAS project ID:	**211500**
REC reference:	**17/HRA/0465**
Sponsor	**Imperial College London**

I am pleased to confirm that **HRA Approval** has been given for the above referenced study, on the basis described in the application form, protocol, supporting documentation and any clarifications noted in this letter.

Participation of NHS Organisations in England

The sponsor should now provide a copy of this letter to all participating NHS organisations in England.

Appendix B provides important information for sponsors and participating NHS organisations in England for arranging and confirming capacity and capability. **Please read *Appendix B* carefully**, in particular the following sections:

- *Participating NHS organisations in England* – this clarifies the types of participating organisations in the study and whether or not all organisations will be undertaking the same activities
- *Confirmation of capacity and capability* - this confirms whether or not each type of participating NHS organisation in England is expected to give formal confirmation of capacity and capability. Where formal confirmation is not expected, the section also provides details on the time limit given to participating organisations to opt out of the study, or request additional time, before their participation is assumed.
- *Allocation of responsibilities and rights are agreed and documented (4.1 of HRA assessment criteria)* - this provides detail on the form of agreement to be used in the study to confirm capacity and capability, where applicable.

Further information on funding, HR processes, and compliance with HRA criteria and standards is also provided.

It is critical that you involve both the research management function (e.g. R&D office) supporting each organisation and the local research team (where there is one) in setting up your study. Contact details

Figure A.1: NHS Health Research Authority - Letter of approval.

A.2 Imperial College Research Ethics Committee approval

Imperial College Research Ethics Committee
Imperial College London
Room 221
Medical School Building
St Marys Campus
London
W2 1PG
Tel: +44 (0)207 594 9484

researchethicscommittee@imperial.ac.uk

Dr Andrew Phillips
Imperial College London
433 Skempton Building
South Kensington Campus
SW7 2AZ

31/03/17

Dear Dr Phillips,

Study Title: Computational modelling of the spine and lower limb and investigation of low back pain development patterns.

ICREC reference: 17IC3811.

The above study was approved by your Head of Department on 14/12/16 and by the Joint Research Compliance Office on 16/03/17.

Under the Imperial College Research Ethics Committee process, a study that has been reviewed by the Joint Research Compliance Office and Head of Division/Department (or Principal), where no significant ethical issues have been identified in the protocol or ethics application, can be approved without requiring it to go to full committee.

Documents
The documents reviewed were:

- ICREC Application form
- Protocol (v127/02/17)
- Participant info sheet (v2 17/02/17)
- Consent form (v2 17/02/17)
- Data collection sheet (v1 27/02/17)
- Recruitment poster (v1 27/02/17)
- Sponsorship and Indemnity form

Yours sincerely,

Gary Roper,
Head of Regulatory Compliance,
Imperial College London

Figure A.2: Imperial College Research Ethics Committee - Letter of approval.

Appendix B

Supplementary material for the musculoskeletal model

B.1 Inertial properties of the body segments in the musculoskeletal model

Table B.1: Inertial properties of musculoskeletal model segments.

		Mass center			Inertia tensor					
	Mass	**X**	**Y**	**Z**	**Ixx**	**Iyy**	**Izz**	**Ixy**	**Ixz**	**Iyz**
	(kg)	(m)	(m)	(m)	($kg.m^2$)	($kg.m^2$)	($kg.m^2$)	($kg.m^2$)	($kg.m^2$)	($kg.m^2$)
Pelvis	5.753	-0.084204	-0.023234	-0.000729	0.037034	0.039757	0.021241	-0.002347	0.000135	0.00076
Right femur	9.325	-0.002247	-0.199388	0.002801	0.169555	0.029937	0.170279	-0.005371	0.000789	0.007951
Right patella	0.039	0.000417	-0.02176	-0.000797	1e-05	5e-06	6e-06	0	0	0
Right tibia	2.501	-0.010173	-0.176519	-0.003662	0.030653	0.00284	0.030214	-0.000354	4.8e-05	0.002418
Right hind foot	1.180	0.061979	-0.032793	0.003263	0.000937	0.004461	0.004581	-0.000174	-4e-05	-6.5e-05
Left femur	9.245	-0.000524	-0.199953	-0.004492	0.164198	0.029368	0.165236	-0.005403	-0.00071	-0.009058
Left patella	0.034	0.001084	-0.016234	-0.001537	8e-06	5e-06	4e-06	0	0	0
Left tibia	2.363	-0.010778	-0.173164	-0.001315	0.025167	0.002492	0.024991	-0.000155	-8e-05	-0.000929
Left hind foot	1.184	0.057747	-0.051519	-0.000722	0.001185	0.004304	0.004667	-0.000553	0.00012	5.5e-05
L5	1.905	0.007448	0.024571	-0.001532	0.010821	0.013164	0.004533	0.001547	8.7e-05	8.4e-05
L4	1.733	0.008156	0.025285	0.004564	0.009087	0.011896	0.003453	0.000329	8.8e-05	2e-06
L3	1.661	0.004839	0.024545	-0.001006	0.008073	0.011474	0.003825	0.000277	0.00011	7.1e-05
L2	1.949	0.018247	0.025451	-0.001255	0.009407	0.014221	0.005353	0.000219	1.1e-05	0.000118
L1	1.641	0.017764	0.019844	-0.005278	0.008588	0.013062	0.004741	-4e-05	-6.5e-05	3.2e-05
Torso bottom	6.726	0.002612	0.059899	-0.001809	0.059043	0.06765	0.02912	-0.001284	-0.00038	-0.000564
Torso top	7.993	0.029228	0.065109	-0.000582	0.100805	0.109454	0.034519	0.000279	0.000308	-0.000698
Head	6.972	0.007815	0.142349	0.001358	0.063748	0.034148	0.065473	0.004073	0.000309	0.000151
Right humerus	1.544	0	-0.15698	0	0.008267	0.002852	0.009280	0	0	0
Right ulna	0.461	0	-0.134669	0	0.002810	0.000586	0.003048	0	0	0
Right radius	0.461	0	-0.134669	0	0.002810	0.000586	0.003048	0	0	0
Right hand	0.347	0	-0.0656669	0	0.000630	0.000386	0.000947	0	0	0
Left humerus	1.544	0	-0.15698	0	0.008267	0.002852	0.009280	0	0	0
Left ulna	0.461	0	-0.134669	0	0.002810	0.000586	0.003048	0	0	0
Left radius	0.461	0	-0.134669	0	0.002810	0.000586	0.003048	0	0	0
Left hand	0.347	0	-0.0656669	0	0.000630	0.000386	0.000947	0	0	0

B.2 Musculotendon actuator properties

Table B.2: Musculotendon actuator properties. These properties are the same on the left and right sides.

	Maximum isometric force (N)	**Optimal fiber length** (mm)	**Tendon slack length** (mm)	**Pennation angle** (°)
Ps_L1_VB	210.9	18.757	6.592	0.0
Ps_L1_TP	60.9	18.512	6.507	0.0
Ps_L1_L2_IVD	120.0	16.898	5.935	0.0
Ps_L2_TP	210.9	16.235	5.703	0.0
Ps_L2_L3_IVD	119.0	14.637	5.143	0.0
Ps_L3_TP	101.0	14.150	4.974	0.0
Ps_L3_L4_IVD	36.0	12.518	4.399	0.0
Ps_L4_TP	160.9	12.092	4.250	0.0
Ps_L4_L5_IVD	79.0	10.068	3.541	0.0
Ps_L5_TP	173.0	10.421	3.658	0.0
Ps_L5_VB	191.0	9.064	3.182	0.0
rect_abd	571.7	22.682	1.723	0.0
IL_L1	108.7	5.412	11.446	13.8
IL_L2	154.3	3.919	8.301	13.8
IL_L3	182.6	2.633	5.577	13.8
IL_L4	189.1	1.803	3.818	13.8
IL_R5	23.9	15.787	22.099	13.8
IL_R6	30.4	15.086	18.246	13.8
IL_R7	39.1	15.650	15.505	13.8
IL_R8	34.8	14.074	13.235	13.8
IL_R9	50.0	15.716	8.478	13.8
IL_R10	100.0	13.227	6.990	13.8
IL_R11	123.9	11.697	5.100	13.8
IL_R12	147.8	9.014	3.704	13.8
LTpT_T1	28.3	10.344	24.460	12.6
LTpT_T2	56.5	10.701	25.766	12.6
LTpT_T3	56.5	10.780	25.905	12.6
LTpT_T4	21.7	10.787	25.926	12.6
LTpT_T5	21.7	10.181	24.467	12.6
LTpT_T6	32.6	10.424	23.857	12.6
LTpT_T7	39.1	11.971	22.630	12.6
LTpT_T8	63.0	12.766	20.209	12.6
LTpT_T9	73.9	12.578	21.318	12.6
LTpT_T10	80.4	11.358	17.357	12.6
LTpT_T11	82.6	9.918	15.116	12.6
LTpT_T12	69.6	7.898	12.037	12.6
LTpT_R4	21.7	13.689	20.863	12.6
LTpT_R5	21.7	12.829	19.552	12.6
LTpT_R6	32.6	13.718	18.678	12.6
LTpT_R7	39.1	13.115	19.661	12.6
LTpT_R8	63.0	10.737	20.082	12.6
LTpT_R9	73.9	9.259	21.040	12.6
LTpT_R10	80.4	10.851	16.763	12.6
LTpT_R11	82.6	10.577	13.289	12.6
LTpT_R12	69.6	6.421	12.477	12.6
LTpL_L5	115.2	5.209	0.101	12.6
LTpL_L4	110.9	4.324	4.672	12.6
LTpL_L3	102.2	5.871	6.377	12.6
LTpL_L2	91.3	7.107	7.805	12.6

Table B.2 continued from previous page

	Maximum isometric force (N)	Optimal fiber length (mm)	Tendon slack length (mm)	Pennation angle (°)
LTpL_L1	78.3	8.496	9.868	12.6
QL_post_I1-L3	39.6	3.938	3.304	7.4
QL_post_I2-L4	52.6	2.197	1.843	7.4
QL_post_I2-L3	30.7	4.994	4.190	7.4
QL_post_I2-L2	19.1	3.474	1.907	7.4
QL_post_I3-L1	28.1	8.487	4.408	7.4
QL_post_I3-L2	29.6	4.921	4.128	7.4
QL_post_I3-L3	50.4	3.417	2.867	7.4
QL_mid_L3-12_3	12.6	5.468	2.840	7.4
QL_mid_L3-12_2	14.3	5.784	3.004	7.4
QL_mid_L3-12_1	23.9	6.291	3.268	7.4
QL_mid_L2-12_1	20.0	3.998	2.077	7.4
QL_mid_L4-12_3	11.7	7.343	3.814	7.4
QL_ant_I2-T12	15.4	10.490	5.449	7.4
QL_ant_I3-T12	29.0	10.306	5.353	7.4
QL_ant_I2-12_1	10.2	9.894	5.139	7.4
QL_ant_I3-12_1	19.3	9.686	5.031	7.4
QL_ant_I3-12_2	12.8	9.126	4.740	7.4
QL_ant_I3-12_3	14.8	8.576	4.450	7.4
MF_m1s	40.0	4.825	2.006	0.0
MF_m1t_1	42.0	7.742	2.322	0.0
MF_m1t_2	36.0	9.740	2.921	0.0
MF_m1t_3	60.1	10.402	3.119	0.0
MF_m2s	39.0	4.676	1.809	0.0
MF_m2t_1	39.0	6.605	2.008	0.0
MF_m2t_2	99.0	8.259	2.511	0.0
MF_m2t_3	99.0	9.426	2.866	0.0
MF_m3s	54.0	4.107	1.707	0.0
MF_m3t_1	52.2	11.033	3.674	0.0
MF_m3t_2	52.2	9.202	3.064	0.0
MF_m3t_3	52.2	9.198	3.063	0.0
MF_m4s	45.7	3.780	2.392	0.0
MF_m4t_1	46.5	5.571	2.258	0.0
MF_m4t_2	46.5	8.139	3.299	0.0
MF_m4t_3	46.5	9.381	3.803	0.0
MF_m5s	22.5	1.487	0.658	0.0
MF_m5t_1	22.5	7.672	3.110	0.0
MF_m5t_2	22.5	5.735	2.325	0.0
MF_m5t_3	22.5	4.071	0.716	0.0
MF_m1_laminar	19.2	3.223	1.224	0.0
MF_m2_laminar	22.2	2.773	1.053	0.0
MF_m3_laminar	23.1	2.694	1.023	0.0
MF_m4_laminar	16.7	2.939	1.116	0.0
MF_m5_laminar	36.1	3.526	1.339	0.0
EO1	195.7	3.762	5.975	0.0
EO2	231.7	3.994	5.809	0.0
EO3	243.2	4.042	4.902	0.0
EO4	234.8	4.123	4.699	0.0
EO5	273.0	4.793	5.249	0.0
EO6	397.4	5.670	5.731	0.0
IO1	185.3	3.847	5.820	0.0
IO2	224.3	4.006	6.074	0.0
IO3	226.0	4.942	7.492	0.0
IO4	267.6	7.390	4.980	0.0
IO5	234.8	6.172	4.159	0.0

Table B.2 continued from previous page

	Maximum isometric force (N)	Optimal fiber length (mm)	Tendon slack length (mm)	Pennation angle (°)
IO6	207.2	5.810	3.915	0.0
TR1	347.8	6.967	4.199	0.0
TR2	137.0	14.304	11.211	0.0
TR3	137.0	14.318	7.546	0.0
TR4	137.0	14.340	7.848	0.0
TR5	413.0	7.045	3.185	0.0
ADD_BREV_PROS_1	190.0	9.676	0.000	0.0
ADD_BREV_PROS_2	190.0	9.680	0.000	0.0
ADD_BREV_MID_1	175.0	10.464	0.000	0.0
ADD_BREV_MID_2	175.0	10.464	0.000	0.0
ADD_BREV_DIST_1	160.0	11.080	0.000	0.0
ADD_BREV_DIST_2	160.0	11.076	0.000	0.0
ADD_LONG_1	251.7	10.676	0.000	0.0
ADD_LONG_2	251.7	10.652	0.000	0.0
ADD_LONG_3	251.7	10.626	0.000	0.0
ADD_LONG_4	251.7	10.599	0.000	0.0
ADD_LONG_5	251.7	10.573	0.000	0.0
ADD_LONG_6	251.7	10.548	0.000	0.0
ADD_MAG_DIST_1	883.3	10.235	3.980	0.0
ADD_MAG_DIST_2	883.3	10.281	3.998	0.0
ADD_MAG_DIST_3	883.3	10.373	4.034	0.0
ADD_MAG_MID_1	368.3	9.468	0.000	0.0
ADD_MAG_MID_2	368.3	9.471	0.000	0.0
ADD_MAG_MID_3	368.3	9.610	0.000	0.0
ADD_MAG_MID_4	368.3	9.622	0.000	0.0
ADD_MAG_MID_5	368.3	9.748	0.000	0.0
ADD_MAG_MID_6	368.3	9.761	0.000	0.0
ADD_MAG_PROX_1	125.0	10.252	0.000	0.0
ADD_MAG_PROX_2	125.0	9.926	0.000	0.0
ADD_MAG_PROX_3	125.0	10.049	0.000	0.0
ADD_MAG_PROX_4	125.0	10.171	0.000	0.0
BIC_FEM_CL_1	2720.0	8.278	12.661	29.9
BIC_FEM_CB_1	393.3	9.206	3.136	0.0
BIC_FEM_CB_2	393.3	9.233	3.145	0.0
BIC_FEM_CB_3	393.3	9.280	3.161	0.0
EXT_DIG_LONG_1	180.0	6.355	31.881	8.3
EXT_DIG_LONG_2	180.0	6.358	31.894	8.3
EXT_DIG_LONG_3	180.0	6.359	31.902	8.3
EXT_HAL_LONG_1	203.3	6.340	18.808	14.4
EXT_HAL_LONG_2	203.3	6.347	18.829	14.4
EXT_HAL_LONG_3	203.3	6.352	18.845	14.4
FLEX_DIG_LONG_1	220.0	4.032	17.614	28.5
FLEX_DIG_LONG_2	220.0	4.030	17.607	28.5
FLEX_DIG_LONG_3	220.0	4.029	17.599	28.5
FLEX_HAL_LONG_1	1036.7	2.751	24.759	30.1
FLEX_HAL_LONG_2	1036.7	2.749	24.738	30.1
FLEX_HAL_LONG_3	1036.7	2.746	24.710	30.1
GASTR_LAT_1	2400.0	6.040	24.796	25.4
GASTR_MED_1	4380.0	6.355	22.453	10.8
GEM_INF_1	410.0	3.749	0.000	0.0
GEM_SUP_1	410.0	3.573	0.000	0.0
GLUT_MAX_SUP_1	828.3	13.852	0.000	0.0
GLUT_MAX_SUP_2	828.3	13.549	0.000	0.0
GLUT_MAX_SUP_3	828.3	13.315	0.000	0.0
GLUT_MAX_SUP_4	828.3	13.826	0.000	0.0

Table B.2 continued from previous page

	Maximum isometric force (N)	Optimal fiber length (mm)	Tendon slack length (mm)	Pennation angle (°)
GLUT_MAX_SUP_5	828.3	13.559	0.000	0.0
GLUT_MAX_SUP_6	828.3	13.336	0.000	0.0
GLUT_MAX_INF_1	375.0	16.238	0.000	0.0
GLUT_MAX_INF_2	375.0	15.981	0.000	0.0
GLUT_MAX_INF_3	375.0	15.603	0.000	0.0
GLUT_MAX_INF_4	375.0	16.304	0.000	0.0
GLUT_MAX_INF_5	375.0	16.053	0.000	0.0
GLUT_MAX_INF_6	375.0	15.637	0.000	0.0
GLUT_MED_ANT_1	631.7	4.604	0.000	0.0
GLUT_MED_ANT_2	631.7	4.594	0.000	0.0
GLUT_MED_ANT_3	631.7	4.582	0.000	0.0
GLUT_MED_ANT_4	631.7	4.577	0.000	0.0
GLUT_MED_ANT_5	631.7	4.566	0.000	0.0
GLUT_MED_ANT_6	631.7	4.536	0.000	0.0
GLUT_MED_POST_1	1013.3	5.476	3.651	15.9
GLUT_MED_POST_2	1013.3	5.345	3.563	15.9
GLUT_MED_POST_3	1013.3	5.149	3.432	15.9
GLUT_MED_POST_4	1013.3	5.480	3.654	15.9
GLUT_MED_POST_5	1013.3	5.338	3.559	15.9
GLUT_MED_POST_6	1013.3	5.203	3.468	15.9
GLUT_MIN_ANT_1	1000.0	3.286	8.566	0.0
GLUT_MIN_MID_1	810.0	3.932	8.442	0.0
GLUT_MIN_POST_1	740.0	4.188	8.263	0.0
GRACILIS_1	245.0	17.934	13.872	0.0
GRACILIS_2	245.0	18.089	13.992	0.0
ILIACUS_LAT_1	220.0	11.886	13.040	26.5
ILIACUS_LAT_2	220.0	11.775	12.919	26.5
ILIACUS_LAT_3	220.0	11.686	12.820	26.5
ILIACUS_MID_1	433.3	6.057	13.162	0.0
ILIACUS_MID_2	433.3	6.016	13.074	0.0
ILIACUS_MID_3	433.3	5.966	12.965	0.0
ILIACUS_MED_1	253.3	10.310	17.955	0.0
ILIACUS_MED_2	253.3	10.257	17.864	0.0
ILIACUS_MED_3	253.3	10.146	17.671	0.0
OBT_EXT_SUP_1	820.0	2.853	3.057	0.0
OBT_EXT_SUP_2	820.0	2.821	3.023	0.0
OBT_EXT_SUP_3	820.0	2.827	3.029	0.0
OBT_INT_1	846.7	2.348	9.170	0.0
OBT_INT_2	846.7	2.324	9.075	0.0
OBT_INT_3	846.7	2.312	9.028	0.0
PECTINEUS_1	170.0	11.914	0.000	0.0
PECTINEUS_2	170.0	11.885	0.000	0.0
PECTINEUS_3	170.0	11.856	0.000	0.0
PECTINEUS_4	170.0	11.921	0.000	0.0
PERONEUS_BREV_1	633.3	2.884	6.837	23.1
PERONEUS_BREV_2	633.3	2.886	6.841	23.1
PERONEUS_BREV_3	633.3	2.888	6.846	23.1
PERONEUS_LONG_1	796.7	3.629	16.971	15.8
PERONEUS_LONG_2	796.7	3.630	16.975	15.8
PERONEUS_LONG_3	796.7	3.631	16.980	15.8
PERONEUS_TERT_1	206.7	4.572	10.632	19.1
PERONEUS_TERT_2	206.7	4.573	10.635	19.1
PERONEUS_TERT_3	206.7	4.574	10.637	19.1
PIRIFORME_1	810.0	4.204	1.725	0.0
PLANTARIS_1	240.0	5.082	37.056	0.0

Table B.2 continued from previous page

	Maximum isometric force (N)	Optimal fiber length (mm)	Tendon slack length (mm)	Pennation angle (°)
POPLITEUS_1	535.0	2.554	1.064	0.0
POPLITEUS_2	535.0	2.553	1.064	0.0
QUAD_FEM_1	365.0	3.469	0.000	0.0
QUAD_FEM_2	365.0	3.471	0.000	0.0
QUAD_FEM_3	365.0	3.476	0.000	0.0
QUAD_FEM_4	365.0	3.483	0.000	0.0
RECTUS_FEM_1	1445.0	8.041	9.897	22.0
RECTUS_FEM_2	1445.0	8.048	9.906	22.0
SARTORIUS_PROS_1	590.0	35.954	8.185	0.0
SARTORIUS_DIST_1	590.0	36.045	8.206	0.0
SEMIMEMB_1	1710.0	7.816	15.149	25.0
SEMITEND_1	1470.0	13.972	23.319	0.0
SOLEUS_MED_1	3143.3	2.548	9.024	64.5
SOLEUS_MED_2	3143.3	2.549	9.027	64.5
SOLEUS_MED_3	3143.3	2.549	9.029	64.5
SOLEUS_LAT_1	2863.3	2.761	9.027	58.7
SOLEUS_LAT_2	2863.3	2.762	9.029	58.7
SOLEUS_LAT_3	2863.3	2.762	9.031	58.7
TENS_FASC_L_1	440.0	9.851	0.000	0.0
TENS_FASC_L_2	440.0	9.889	0.000	0.0
TIBIALIS_ANT_1	886.7	4.885	24.957	9.6
TIBIALIS_ANT_2	886.7	4.884	24.952	9.6
TIBIALIS_ANT_3	886.7	4.882	24.940	9.6
TIBIALIS_POST_MED_1	720.0	2.551	11.691	25.2
TIBIALIS_POST_MED_2	720.0	2.550	11.687	25.2
TIBIALIS_POST_MED_3	720.0	2.549	11.681	25.2
TIBIALIS_POST_LAT_1	720.0	2.550	11.688	43.1
TIBIALIS_POST_LAT_2	720.0	2.549	11.681	43.1
TIBIALIS_POST_LAT_3	720.0	2.546	11.669	43.1
VASTUS_INTERM_1	635.0	7.789	12.746	11.8
VASTUS_INTERM_2	635.0	7.776	12.725	11.8
VASTUS_INTERM_3	635.0	7.762	12.701	11.8
VASTUS_INTERM_4	635.0	7.812	12.783	11.8
VASTUS_INTERM_5	635.0	7.788	12.744	11.8
VASTUS_INTERM_6	635.0	7.768	12.711	11.8
VASTUS_INTERM_7	635.0	7.835	12.821	11.8
VASTUS_INTERM_8	635.0	7.826	12.806	11.8
VASTUS_LAT_INF_1	178.3	4.177	9.548	0.0
VASTUS_LAT_INF_2	178.3	4.228	9.664	0.0
VASTUS_LAT_INF_3	178.3	4.234	9.677	0.0
VASTUS_LAT_INF_4	178.3	4.229	9.667	0.0
VASTUS_LAT_INF_5	178.3	4.229	9.666	0.0
VASTUS_LAT_INF_6	178.3	4.226	9.660	0.0
VASTUS_LAT_SUP_1	2950.0	9.160	9.664	0.0
VASTUS_LAT_SUP_2	2950.0	9.165	9.669	0.0
VASTUS_MED_INF_1	490.0	7.487	9.457	0.0
VASTUS_MED_INF_2	490.0	7.511	9.487	0.0
VASTUS_MED_MID_1	1160.0	7.625	9.632	0.0
VASTUS_MED_MID_2	1160.0	7.652	9.666	0.0
VASTUS_MED_SUP_1	448.3	8.356	9.664	0.0
VASTUS_MED_SUP_2	448.3	8.379	9.692	0.0
VASTUS_MED_SUP_3	448.3	8.355	9.664	0.0
VASTUS_MED_SUP_4	448.3	8.371	9.682	0.0
VASTUS_MED_SUP_5	448.3	8.359	9.669	0.0
VASTUS_MED_SUP_6	448.3	8.359	9.669	0.0

B.3 Musculotendon actuator paths

Musculotendon actuator paths and insertions were adjusted in the musculotendon model to match the MRI scans of the healthy volunteer. This Section presents musculotendon actuators of the lumbar spine in Opensim (Delp et al. 2007) overlaying the segmented muscle geometry.

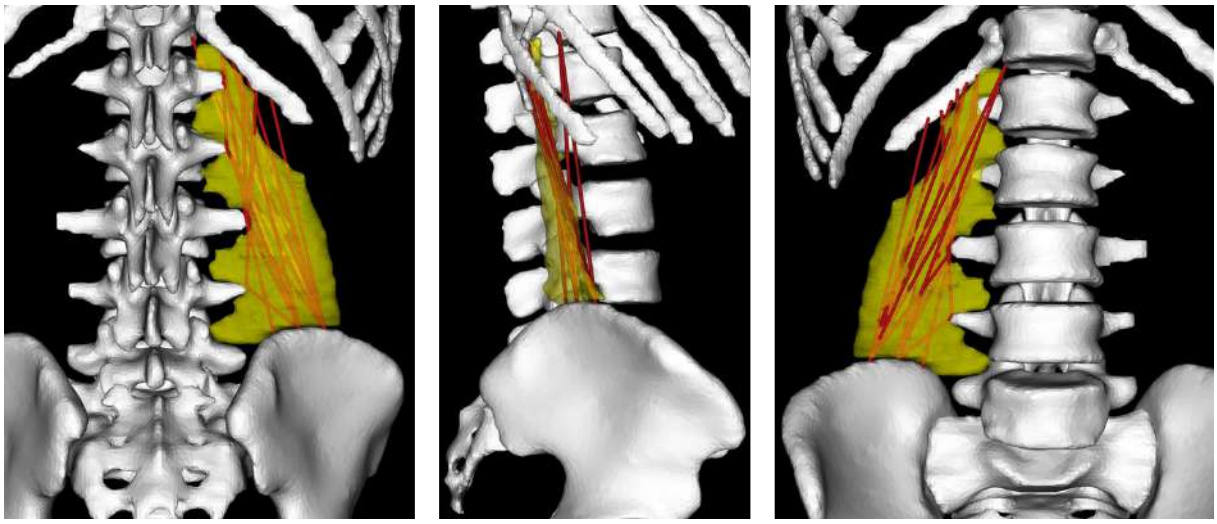

Figure B.1: Dorsal (left), lateral (middle) and frontal (right) views of the right quadratus lumborum musculotendon actuators.

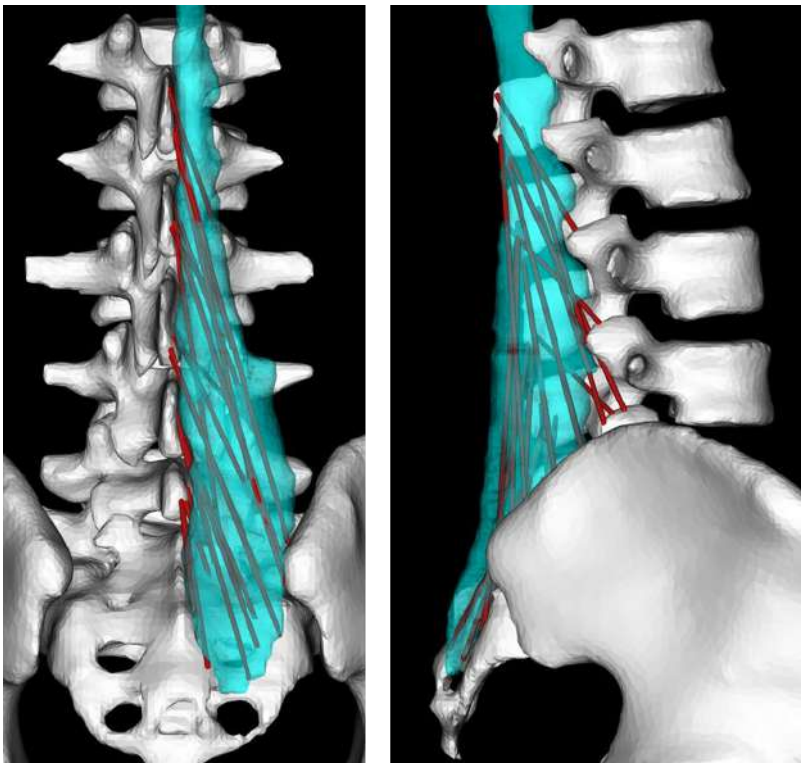

Figure B.2: Dorsal (left) and lateral (right) views of the multifidus musculotendon actuators.

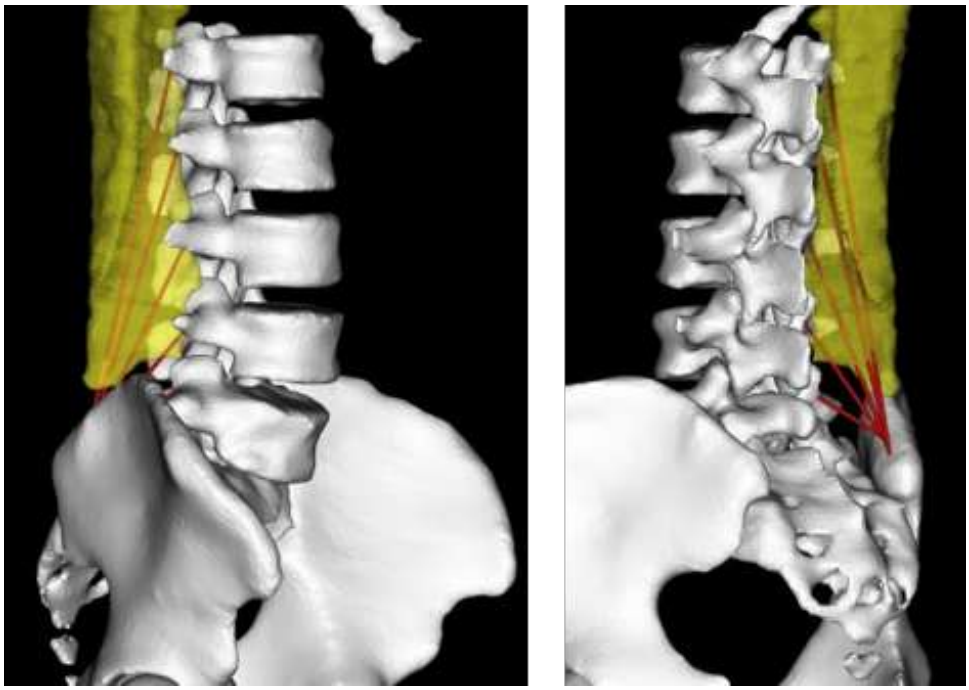

Figure B.3: Anterolateral (left) and dorsolateral (right) views of the longissimus musculotendon actuators attaching to the lumbar vertebrae.

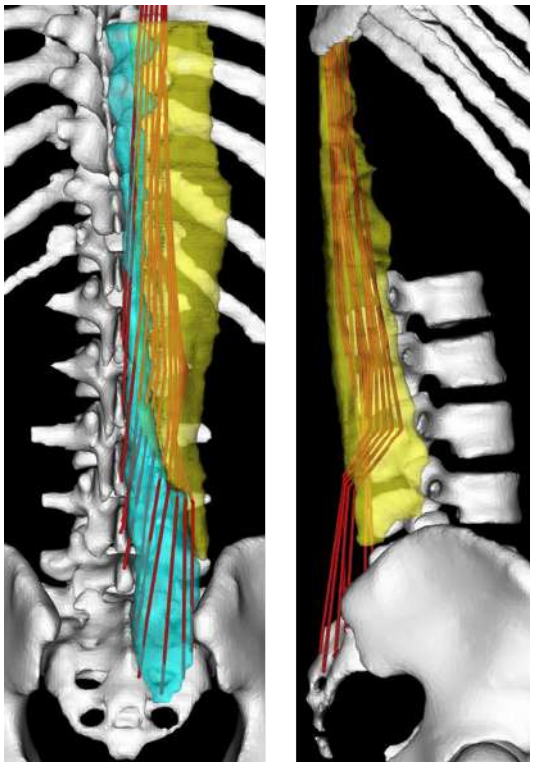

Figure B.4: Dorsal (left) and lateral (right) views of the longissimus musculotendon actuators attaching to the thoracic vertebrae.

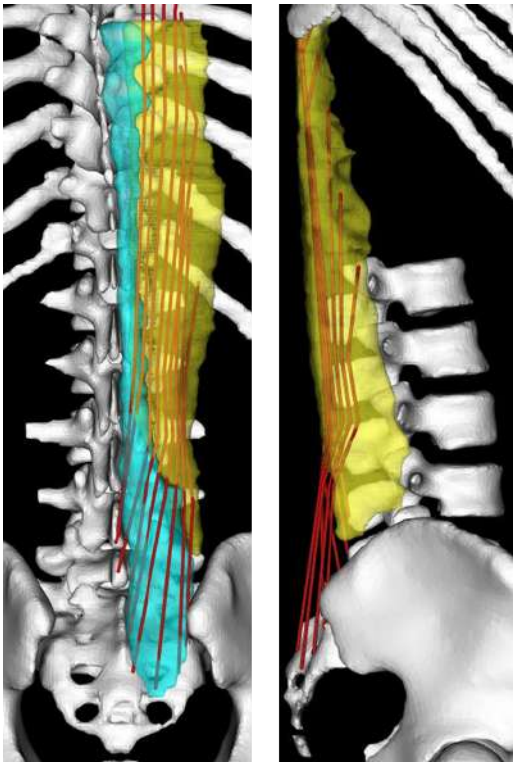

Figure B.5: Dorsal (left) and lateral (right) views of the longissimus musculotendon actuators attaching to the ribcage.

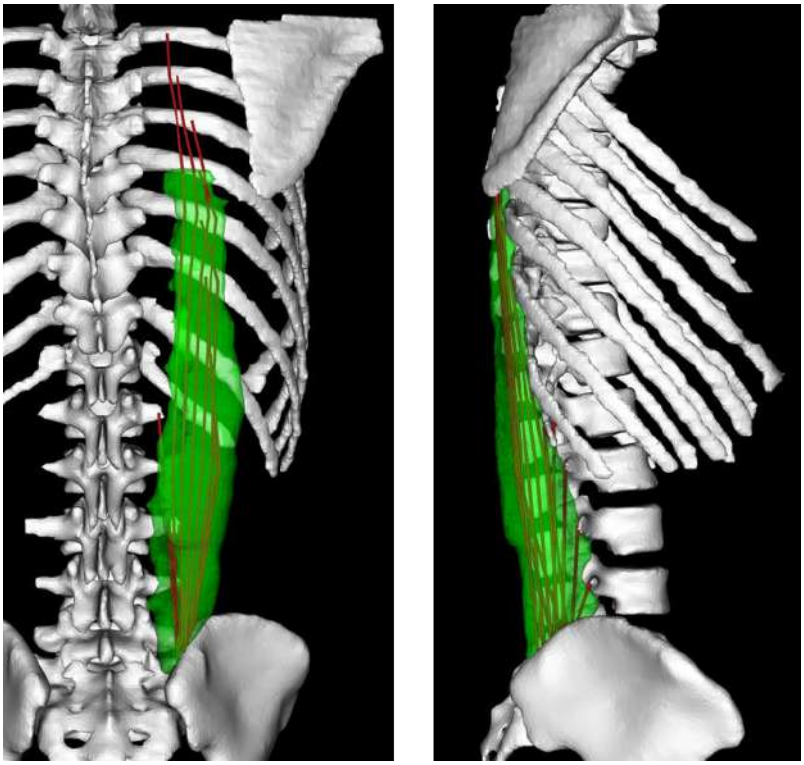

Figure B.6: Dorsal (left) and lateral (right) views of the iliocostalis musculotendon actuators.

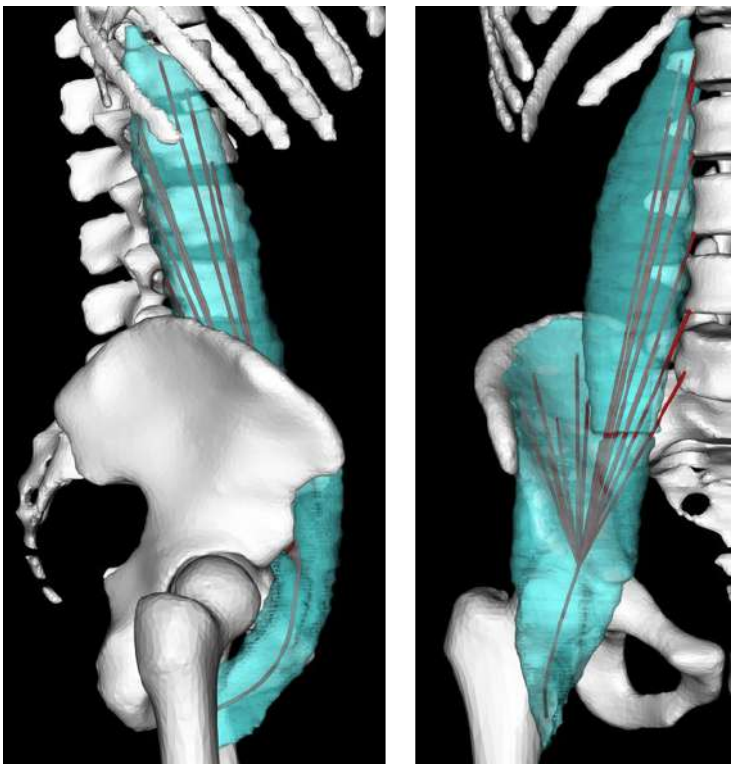

Figure B.7: Lateral (left) and frontal (right) views of the right ilipsoas musculotendon actuators.

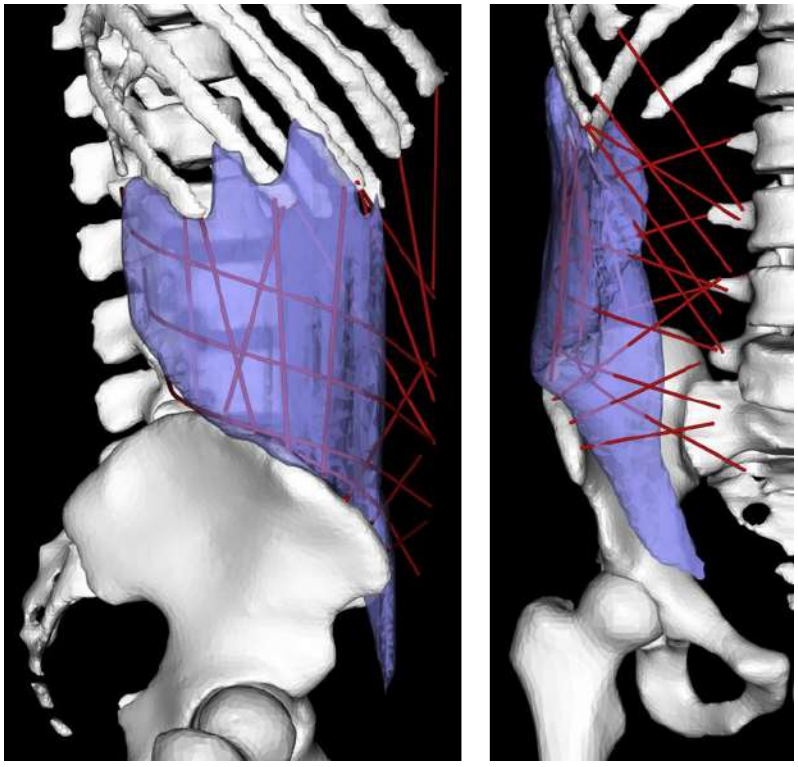

Figure B.8: Lateral (left) and frontal (right) views of the musculotendon actuators representing the right internal obliques, external obliques and transverse abdominis.

B.4 Inverse kinematics marker weighting coefficients

Table B.3: Inverse kinematics (IK) weighting coefficients for all markers.

Body segment	Marker name	IK weighting	Body segment	Marker name	IK weighting
Pelvis	RASIS	100	Pelvis	LASIS	100
	RPSIS	100		LPSIS	100
Right femur	RTHI1	5	Left femur	LTHI1	5
	RTHI2	5		LTHI2	5
	RTHI3	5		LTHI3	5
	RTHI4	5		LTHI4	5
	RKCOL	0		LKCOL	0
	RKCOM	0		LKCOM	0
	RKFIB	0		LKFIB	0
Right tibia	RSHA1	5	Left tibia	LSHA1	5
	RSHA2	5		LSHA2	5
	RSHA3	5		LSHA3	5
	RSHA4	5		LSHA4	5
	RANTI	0		LANTI	0
	RANFI	0		LANFI	0
Right foot	RHEEL	5	Left foot	LHEEL	5
	RMET1	5		LMET1	5
	RMET5	5		LMET5	5
	RTOE	5		LTOE	5
L3	TL31	0	L2	FL21	0
	TL32	0		FL22	0
	TL33	0		FL23	0
Lower thoracic	FT121	20	Upper thoracic	FT51	10
	FT122	20		FT52	10
	FT123	20		FT53	10
	TT101	20		TT31	10
	TT102	20		TT32	10
	TT103	20		TT33	10
	FT81	20		FT11	10
	FT82	20		FT12	10
	FT83	20		FT13	10
Head	NOSE	20		CERV7	100
	RTEMP	20		STERN	0
	LTEMP	20		RACRO	0
				LACRO	0

Appendix C

Supplementary material for the five mesoscale structural finite element models of the lumbar vertebrae

Supplementary material is accessible online:
https://imperialcollegelondon.box.com/v/ClementFavier-DigitalAppendix